

**ON THE NANOSTRUCTURE OF
BIOGENIC AND BIO-INSPIRED
CALCIUM CARBONATE**

As studied by electron microscopy techniques

Renée van de Locht

PhD

University of York

Physics

March 2014

“There is grandeur in this view of life, with its several powers, having been originally breathed into a few forms or into one; and that, whilst this planet has gone cycling on according to the fixed law of gravity, from so simple a beginning endless forms most beautiful and most wonderful have been, and are being, evolved.”

Charles Darwin (1808 - 1882) in *‘The Origin of Species’*

“What I cannot create, I do not understand”.

Richard P. Feynman (1918 - 1988)

ABSTRACT

Most biominerals in nature are formed from both organic and inorganic (mineral) compounds, and are thus by definition a *composite* material. They are hierarchically ordered from the nanoscale and often have superior mechanical properties compared to synthetic ceramics [1].

This study focuses on the structural characterisation of aragonite and calcite biominerals, combined with the investigation of formation mechanisms through the synthesis of *bio-inspired* or *biomimetic* crystals. To this end a multi-length scale study of aragonite and calcite based minerals is presented, based primarily on electron microscopy techniques and supported by Raman spectroscopy and chemical analysis of the organic compounds.

Aragonite skeletal material from corals is studied in detail from the nano-to microscale. This is compared to calcium carbonate crystals precipitated in the presence of organic molecules with *hydroxyl-groups*, namely ethanol. Secondly, we look at the calcite based system of coccolithophores (marine algae) which precipitate their exoskeleton intracellularly. Such crystals formed in confinement are compared to the structure of synthetically produced calcite nanowires, grown in track-etch membranes.

The coral's *spherulites* (roughly 10-20 μm in size) were found to consist of three distinct crystalline phases. This microstructural sequence could for the first time be directly correlated to diurnal growth bands observed in optical transmission images and are linked to a light enhanced calcification process. The synthetic CaCO_3 precipitation experiments showed that increasing ratios of ethanol resulted in a shift of crystal phase and morphology from single crystal rhombohedral calcite to branched polycrystalline aragonite, the latter being similar to the coral.

The calcite coccoliths of *Rhabdosphaera clavigera* exhibit centrally positioned, several micrometre long five-fold symmetric spines. The spines are made up of spiral staircase arrangements of {104} single crystal calcite rhombohedra. However the rim of the coccolith has complex shaped, *kinked*, crystal elements. It was found that such unconventional crystal shapes can be promoted by external anisotropic surface stresses as was seen for the calcite nanowires investigated in this study.

CONTENT

<u>ABSTRACT</u>	<u>I</u>
<u>CONTENT</u>	<u>III</u>
<u>LIST OF FIGURES</u>	<u>VII</u>
<u>LIST OF TABLES</u>	<u>XIII</u>
<u>ACKNOWLEDGEMENTS</u>	<u>XV</u>
<u>DECLARATION</u>	<u>XVII</u>
<u>1. INTRODUCTION</u>	<u>1</u>
1.1 MOTIVATION AND SCIENTIFIC BACKGROUND	2
1.2 RESEARCH OBJECTIVES AND EXPERIMENTAL APPROACH	5
1.3 OUTLINE OF THE THESIS	7
1.4 BIOMINERALISATION OF CALCIUM CARBONATE	8
1.4.1 NUCLEATION, GROWTH AND MORPHOLOGY	8
1.4.2 ORGANISATION AND PROPERTIES	10
1.4.3 CRYSTAL STRUCTURE OF CALCIUM CARBONATES	11
<u>2. MATERIAL AND EXPERIMENTAL BACKGROUND</u>	<u>17</u>
2.1 MATERIAL SYSTEMS	18
2.1.1 SCLERACTINIAN CORALS	18

2.1.2	ARAGONITE PRECIPITATED IN THE PRESENCE OF ETHANOL	23
2.1.3	COCCOLITHS	25
2.1.4	CALCITE NANOWIRES GROWN IN CONFINEMENT	28
2.2	EXPERIMENTAL TECHNIQUES	31
2.2.1	OUTLINE OF APPLIED EXPERIMENTAL TECHNIQUES	31
2.2.2	TRANSMISSION ELECTRON MICROSCOPY	32
2.2.3	SCANNING ELECTRON MICROSCOPY	51
2.2.4	RAMAN MICROSCOPY	55
2.2.5	REVERSE PHASE HIGH PERFORMANCE LIQUID CHROMATOGRAPHY	61
3.	<u>ARAGONITE BASED MINERALS</u>	67
3.1	MICROSTRUCTURE OF CORAL SPHERULITES	69
3.1.1	THE MINERAL FRACTION	69
3.1.2	THE ORGANIC FRACTION	82
3.2	SYNTHETIC ARAGONITE FORMATION VIA ORGANIC ADDITIVES	93
3.3	ORGANIC ADDITIVES AND ARAGONITE CRYSTAL GROWTH	99
4.	<u>CALCITE BASED MINERALS</u>	105
4.1	COCCOLITH ULTRASTRUCTURE	107
4.1.1	RESULTS OF THE EM CHARACTERISATION	107
4.1.2	INTERPRETATION OF COCCOLITH STRUCTURE	114
4.2	CALCITE NANOWIRES	121
4.2.1	RESULTS OF THE EM CHARACTERISATION	122
4.2.2	INTERPRETATION AND COMPARISON WITH SIMULATION	128
4.3	CONFINEMENT AND CALCITE CRYSTAL GROWTH	131

5. DISCUSSION & CONCLUSIONS	135
5.1 IMPACT OF THE CRYSTALLISATION ENVIRONMENT	136
5.1.1 LOCAL CARBONATE CHEMISTRY	136
5.1.2 ORGANIC ADDITIVES: STABILISING CRYSTAL FACETS AND POLYMORPH SELECTION	141
5.1.3 MINERALISATION IN CONFINEMENT: SHAPING CRYSTALS	147
5.2 SUMMARY OF THE CONCLUSIONS	152
5.3 OUTLOOK	155
APPENDIX A	161
APPENDIX B	165
APPENDIX C	171
LIST OF ABBREVIATIONS	175
BIBLIOGRAPHY	179

LIST OF FIGURES

Figure 1.1 Hierarchical structure of Scleractinian corals.....	4
Figure 1.2 Flowchart representation of the structure of this thesis.....	8
Figure 1.3 Schematic representation of: A) the orthorhombic lattice, B) the hexagonal lattice which shows how four bases of a trigonal lattice combine can describe the hexagonal symmetry.	12
Figure 1.4 Schematic representation of the unit cell of aragonite with its atomic arrangement.	13
Figure 1.5 Schematic representing the unit cell of calcite with its atomic arrangement.	15
Figure 2.1. Simplified physiological model for coral calcification (A) and coral skeletal components (B).....	19
Figure 2.2. SEM micrographs of heterococcoliths.	26
Figure 2.3. Schematic drawing of the V/R structure model for coccoliths.	27
Figure 2.4. Schematic drawing the gas diffusion method (courtesy of Andreas Verch, Department of Physics, University of York and Anna Schenk, School of Chemistry, University of Leeds).	29
Figure 2.5. A) SEM image of the 200 nm calcite nanowires. B) TEM bright field image of the 200 nm calcite nanowires.	30
Figure 2.6 Schematic of the overview of techniques used for structural and chemical characterisation of the CaCO ₃ material systems.	31
Figure 2.7. The ray diagram provides an overview of the imaging and diffraction modes in TEM. Objective Lens (OL), Selected Area aperture (SA), Projector Lens (PL).	33
Figure 2.8 HAADF-STEM image of the side of a coccolith spine (<i>R. Clavigera</i>) showing beam damage induced during a line scan for EELS analysis..	34
Figure 2.9 A) TEM bright field image taken before high resolution imaging.	35

Figure 2.10. Left: <i>Bright-field</i> imaging mode; directly transmitted light contributes to the image contrast. Right: off-axis <i>dark-field</i> imaging mode; a diffracted beam is selected by using the objective aperture.....	37
Figure 2.11. Diffraction from a set of crystal planes a distance d_{hkl} apart.	41
Figure 2.12 Schematic representation of the effect of crystal tilt, twist and bending on the position of the Laue circle in the diffraction pattern and the rotation of the diffraction spots.	45
Figure 2.13 Series of simulated diffraction patterns for aragonite in [010] zone axis.....	46
Figure 2.14. TEM sample preparation stages.....	50
Figure 2.15. The different signals generated in an scanning electron microscope by inelastic scattering processes and their relative origins in the sample volume.	52
Figure 2.16. Schematic drawing of the ASEM.	53
Figure 2.17. Spectrum of photon transition from ground state to virtual levels.....	57
Figure 2.18. Schematic representation of the experimental setup of the Micro-Raman spectrometer.....	57
Figure 2.19 Jablonksi diagram for the occurrence of fluorescence.....	58
Figure 2.20 Schematic 2D representation of the carbonate ion and two of its characteristic stretching modes that result in specific Raman peaks.....	58
Figure 2.21 Raman spectra from geological calcite and aragonite mineral, the intensity is in arbitrary units.	59
Figure 2.22. Diagram depicting the general features and setup of a HPLC instrument with chromatograms as data output showing concentration of amino acids (pmoles/mg of sample) versus retention time (s).....	64
Figure 3.1 SEM micrographs of <i>Porites sp.</i>	70
Figure 3.2 SEM micrographs of an etched <i>S. siderea</i> specimen.	70
Figure 3.3. A) Optical micrograph providing the context of the sample area, the position of the FIB lamella is indicated by the white rectangle and encompasses a COC in <i>P. lobata</i>	72
Figure 3.4. TEM micrographs of <i>P. lobata</i>	73

Figure 3.5. A) TEM BF micrograph of <i>P. lobata</i> showing a stack of partly aligned nanocrystals, the circles indicate the positions of the SAED aperture.	74
Figure 3.6. A) TEM bright field micrograph of stacked nanocrystalline area: the red circle indicates the position and approximate area size of the SA aperture. B) Diffraction pattern indicating a polycrystalline structure. C) TEM bright field micrograph of large acicular crystals, the red circle indicates the position and approximate area size of the SA aperture. D) Diffraction pattern indicating a single crystalline structure with a [211] zone axis.	75
Figure 3.7 HRTEM micrograph of a nanocrystalline area from the blue square in Figure 3.3B, showing two adjacent grains from two neighbouring stacks with a different crystal orientation as shown by the FFT's in B and C.	75
Figure 3.8 A) SEM micrograph of large acicular crystals protruding from a spherulite of <i>P. lobata</i>	77
Figure 3.9 A) TEM micrograph of a bundle of acicular crystals in a spherulite of <i>S. siderea</i> . B) HRTEM micrograph showing two adjacent acicular crystals within the same bundle, squares indicate the areas used for FFT analysis. C and D) FFT's of two adjacent crystals in B.	78
Figure 3.10 Analysis of image 3.9B.	78
Figure 3.11 TEM bright field micrographs of <i>S. siderea</i> showing strain contrast where acicular crystal bundles of different orientation meet.	79
Figure 3.12 <i>A. millepora</i> larva, 5 days after onset of mineralisation, cultivated at ambient 390 ppm CO ₂ and 29°C.	81
Figure 3.13 SEM micrographs of organic material extracted from <i>P. lobata</i> bulk skeleton sample.	83
Figure 3.14 SEM micrographs of adult coral, surface-etched specimens.	83
Figure 3.15 Raman spectra of three adult coral species from the non-porous acicular crystal bundles confirming that the crystal phase is aragonite.	85
Figure 3.16 Raman spectroscopy of <i>P. lobata</i> . polished specimen surface.	85
Figure 3.17 Optical image of a <i>P.lobata</i> fibre (A) with Raman spectra (B-C) taken over two data ranges with two different lasers.	87

Figure 3.18 Optical images of <i>S.siderea</i> fibre bundles (A and C) with corresponding Raman spectra (B and D, 532 nm laser).....	88
Figure 3.19 Pie-charts showing relative percentages of amino acid concentrations for three coral species.	90
Figure 3.20 SEM images of CaCO ₃ crystals precipitated in ClairScope dishes.	94
Figure 3.21 SEM images of CaCO ₃ crystals precipitated in ClairScope dishes.	94
Figure 3.22 Sequence of ASEM images showing the growth of aragonite from a {104} calcite facet in the presence of ethanol (15 vol%), directly after mixing.	95
Figure 3.23 Graph showing measurements of crystal growth over time.....	96
Figure 3.24 A) TEM bright field micrograph of fragments of aragonite bundles precipitated with 25 vol% ethanol, matured for 1 hour. B) SAED pattern of the right-hand fragment in A, taken with a large selected area aperture (approx. 500 nm area size), showing a polycrystalline symmetry for the overall stack.	97
Figure 3.25 Aragonite precipitated with 25 vol% ethanol, matured for 1 hour.	97
Figure 3.26 Proposed growth model linking light enhanced calcification and the related abundance of organics to the microstructural patterns observed in adult Scleractinian corals.....	102
Figure 4.1 SEM images of <i>Rhabdosphaera clavigera</i>	108
Figure 4.2 SEM micrographs of coccolith disk.....	109
Figure 4.3 SAED patterns accompanying the TEM bright field micrograph, white circles indicate the position of the selected area aperture.	111
Figure 4.4 A) SEM image of the tip of the spine. B) TEM bright field image of the side view of a crystal panel showing the position of the acute angle at the outer edge of the crystal panel. C) Schematic drawing of {104} calcite rhombohedra with obtuse and acute angles of 102° and 78°, respectively. D) Calcite unit cell with (104) planes indicated by the green coloured areas on the left, the dashed line indicates the edge of the unit cell and does not relate to angles in the crystal facets.	112
Figure 4.5 3D STEM tomography reconstruction of the spine tip.....	113
Figure 4.6 Schematic of ultrastructure of the spine.....	115

- Figure 4.7 Schematic 2D representation of two coccolith disk cross sections. 116
- Figure 4.8 A) SEM micrograph of ~70 nm diameter calcite nanowires, the inset clearly shows that they are cylindrical in shape. B) TEM bright field image of a ~70 nm diameter calcite nanowire, arrows indicate notches on the surface. C) TEM dark field image using the (0 0 12) reflection, the contrast changes imply high amounts of lattice rotation..... 122
- Figure 4.9 TEM bright field images of a ~70 nm diameter calcite nanowire. 123
- Figure 4.10 A) TEM bright field image of a ~70 nm diameter calcite nanowire. B) SAED patterns, the white arrow indicates the growth direction of the wire..... 123
- Figure 4.11 Graphs representing the evaluation of the twist (α , black), out-of plane bending (β , red) and in-plane bending (γ , blue) as a function of position along the length axis of the nanowires shown in Figure 4.10 and Figure 4.8 respectively. 125
- Figure 4.12 A) SAED pattern series along the length of a ~200 nm diameter calcite nanowire shown in B, the white arrow indicates the projected growth orientation of the wire, which is close to [21 11 23], the zone axis is [8-2 1]. B) TEM bright field image, dots indicate the position of the SA aperture (area size approximately 125 nm), the numbers correspond to the diffraction patterns in A. 127
- Figure 4.13 A) TEM bright field image of a ~250 nm nanowire, the red dots indicate the position of the SA aperture. B) SAED series corresponding to the positions in A.. 127
- Figure 4.14 A and B show the results of the finite element calculations for nanowires with orientations similar to those shown in Figure 4.11 A and B, respectively, applied with a homogenous 10 Nm^{-1} surface stress. C shows the model used for the calculations in the presence of surface notches and D displays the results of the calculations for twist and bend as a function of position on a nanowire identified on the nanowire with a growth direction close to [20 4 -1]..... 130
- Figure 4.15 The calculated rotations (α : twist (black), β : out of plane bending (red) and γ : in plane rotation (blue)) as a function of the position along the nanowire for (A) a surface stress of 2 Nm^{-1} oriented along the wire on one side and 0.7 Nm^{-1} on the opposite side for a wire orientation corresponding to the one shown in Figure 4.11A. (B) an anisotropic, surface stress with principal components of magnitudes 2 Nm^{-1}

and 1 Nm ⁻¹ , oriented 30° and 120° to the axis of a nanowire orientated as in Figure 4.11B.	130
Figure 5.1 Schematic representing crystal morphology and structure variations as a function of the distance from the reaction equilibrium and the strength of the crystallization driving force.....	139
Figure 5.2 Schematic of simplified relation between the amount of organic additives present at time of precipitation (low (+) to high (+++) in the biogenic system and 15-50 % of water/alcohol ratio in the bio-inspired system) and resulting crystal phase and morphology in adult Scleractinian corals (biogenic) and CaCO ₃ precipitated in the presence of ethanol (bio-inspired).....	143
Figure 5.3 SEM images of <i>Emiliana huxleyi</i>	149
Figure 5.4 SEM micrograph of <i>R. clavigera</i> spine with its typical five-fold chiral symmetry and discrete crystal elements, the different tip elements are indicated in colour. ...	158

LIST OF TABLES

Table 1-1 Aragonite and calcite lattice parameters used in our analyses.....	13
Table 3-1. List of analysed amino acids by RP-HPLC of coral inter-crystalline organics and extracted fibres, with their respective acronyms and characteristics. Source for attributed properties: the Institute of Chemistry, Department of Biology, Chemistry and Pharmacy, FU Berlin.....	89
Table 5-1 Summary of the results combined with information from literature as described in previous chapters.	153

ACKNOWLEDGEMENTS

I would like to thank a few people who have made this work possible:

First and foremost I want to thank Roland Kröger for all his help and guidance throughout the course of this research, and for not giving up on a Geoarchaeologist wanting to be a Physicist.

I would like to thank Andreas Verch for all the hours spent together at the microscopes and interpreting the data, providing invaluable advice and a never ending supply of Lindt chocolates.

I greatly thank Jeremy Mitchell for teaching me the basics of TEM sample preparation and his patience dealing with my tantrums about computers and Physics.

Many thanks are due to Judy Mitchell for all the hours spent proofreading the manuscript and I am indebted to Lisette Kootker for helping me with the layout of the thesis.

Lastly, I am indebted to my parents, Pim and Madeleine van de Locht and my sister Saskia van de Locht for their unfailing support and encouragement.

DECLARATION

The work presented in this thesis is based on original research performed at the Department of Physics, University of York, between October 2010 and March 2014 under the supervision of Dr. Roland Kröger of the Nano- and Biomaterials Physics Group. Where other studies are referenced it is explicitly stated in the text and I confirm that none of this research has previously been submitted for any other qualification.

Renée van de Locht

Publications

- Van de Locht R.*, Slater T., Verch A., Young J., Haigh S., and Kröger R.*, *Ultrastructure and crystallography of nanoscale calcite building blocks in Rhabdosphaera clavigera coccolith spines*. Journal of Crystal Growth and Design **14** (4) (2014) 1710-1718.
- Verch A., Côté, A., Darkins R., Van de Locht R., Kim Y.Y., Meldrum M.C., Duffy D. and Kröger R.* *Anisotropy and lattice distortion in calcium carbonate nanowires grown in confinement*, Small (2014) In press.
- Verch A., Morission I. E.G., Van de Locht R., Kröger R.*, *In situ electron microscopy studies of calcium carbonate precipitation from aqueous solution with and without organic additives*. Journal of Structural Biology **183** (2013) 270-277.
- Van de Locht R.*, Verch A., Saunders M., Dissard D., Rixen T., Moya A. and Kröger R.*, *Microstructural evolution and nanoscale crystallography in Scleractinian coral spherulites*. Journal of Structural Biology **183** (2013) 57-65.

To Daniëlle, my dear friend, whose battle against a severe illness puts writing a thesis into perspective.

1. INTRODUCTION

The motivation of the study of biomineralising systems is twofold. On the one hand many marine organisms that are vital for the oceans primary production and the oceans ecosystems, are under threat of global environmental and climate change. Yet their calcification mechanisms are poorly understood and their crystal structure is often not described in detail. On the other hand, these biocomposite materials often have strong mechanical properties, and a complex assembled architecture. Therefore, it would be beneficial to achieve reproduction of similar synthetic materials for both medical and industrial purposes.

This has inspired a detailed study of the most commonly available biomineral: calcium carbonate in two of its naturally occurring anhydrous polymorphs: aragonite and calcite. Both are studied in their biogenic form and as a synthetic derivative to gain understanding of the parameters influencing the crystal formation and morphology.

In this chapter an introduction to biomineralisation will be given by a short literature review in light of the motivation for this doctoral work. This is followed by a description of the experimental approach, thesis setup and an overview of some key concepts relevant to this study.

1.1 MOTIVATION AND SCIENTIFIC BACKGROUND

Despite the abundance and variety of calcium carbonate precipitating organisms within diverse phyla, the characterisation and understanding of the mineral accretion process remains under debate [2-5]. Given the potential impact of climate change on this process, understanding the calcifying mechanism has become increasingly important for conservation purposes. Anthropogenic increase in atmospheric carbon dioxide causes ocean acidification and this will affect many aspects of marine life such as algae blooms (calcitic coccolithophores) and particularly coral reefs [6, 7]. Numerous studies have reported negative impacts on biomineralising organisms, such as decreasing calcification rates and decalcification [8-10].

The formation mechanisms, structural characteristics and most importantly, the control of crystallisation processes have been intensively studied both in academic and industrial disciplines. However, the fabrication of crystalline and biocomposite materials with well-defined properties remains a challenge in Materials Science to this day. In contrast, organisms have developed ways to produce functional hard materials through millions of years of evolution, adapting to their environment and specific function [1]. They achieve exceptional mechanical properties [11] (e.g. hard but flexible instead of brittle), considering the often weak constituents from which they are assembled [1], examples are bone, shell and coral, to name but a few. An impressive example of adaptation to specific function is the enhanced hardness by chemical composition regulation in the teeth of the skeleton of sea urchins by their high magnesium content. This enables the structure to be hard enough to scrape rocks for feeding [12].

Materials Science research started in the 1950's and developed into three main directions: metals, polymers and ceramics [1]. From the 1990's onwards, biological materials started to get more interest and are now one of its primary foci [1], although the field of biomineralisation itself is by no means new, as the first book on the subject was published in 1924 by W.J Schmidt [13]. The renewed interest is

mainly because these biominerals, although formed from a restricted amount of available elements and under ambient conditions with respect to temperature, pH and pressure, often outperform synthetic materials made from the same components [14]. Across scientific disciplines there is interest in understanding the versatility, formation mechanisms and structure of biominerals. Materials Science is specifically focussed on the fabrication of bio-inspired materials by processes common in biological systems, such as nanoscale, self-assembled, hierarchical structures. The latter means a structural organisation over several length scales, which has been recognised as a key concept for the formation of biogenic minerals [1, 11]. Another important part of biomineral formation is the role played by organic molecules. Mineral accretion is often (partly) controlled by organic components [15, 16], which can influence size, morphology and even polymorph selection of the mineral [17-19].

Inspired by such biogenic controlled structures, Materials Science and nanotechnology have been able to fabricate some promising materials such as synthetic nacre [20] and synthetic bone grafts [21]. However, the processes guiding biomineralisation itself are yet poorly understood. This includes the interplay between inorganic (kinetic) controlled and organic controlled reactions leading to mineral precipitation, and the role of specific organic compounds in shaping the crystals and forming the structural hierarchy. The most abundant biomineral, due to its low solubility in water and the global abundance of available calcium [22], is calcium carbonate [23]. Calcium carbonate has three crystalline polymorphs: calcite, aragonite and vaterite. The first two are dominant in diverse marine phyla. An example of the hierarchical structure of aragonite in Scleractinian corals is shown in Figure 1.1 below. This figure shows the coral skeleton at its apex level: the colony (A) with its living membrane (only several millimetres thick) on top of a large aragonite exoskeleton dome. Its surface consists of individual polyps (B), the mineral below the polyps consists of branches of CaCO_3 (C), and each branch consists of spherulitic domains (D). These domains are made up of a granular crystal centre (E) and outward radiating, crystal needles (F), these aragonite needles are single crystalline and grow in the [001] direction (G).

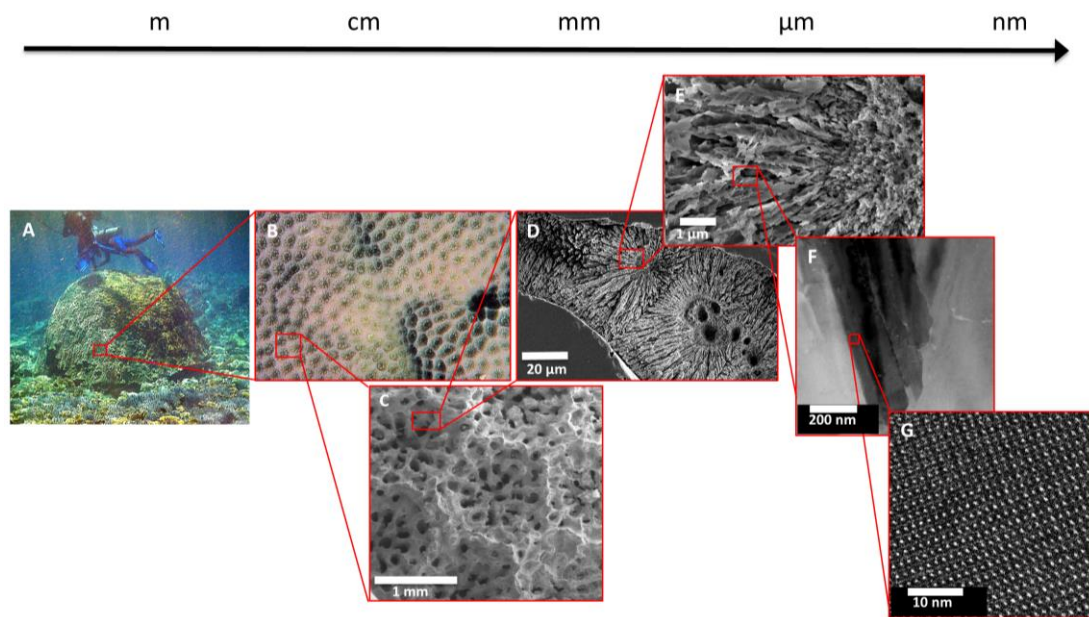


Figure 1.1 Hierarchical structure of Scleractinian corals. A) Photograph of a mushroom head shaped dome of a live *Porites lobata* colony (Image provided by Tim Rixen, Centre of Marine Tropical Ecology in Bremen, Germany). B) Photograph of the surface of live *Porites lobata* with individual polyps. C) SEM image of *Porites sp.* surface after the live membrane is removed, showing individual corallites. D) SEM image of a surface etched cross section of a skeletal branch in a corallite showing spherulites. E) SEM image of a close-up of a spherulite with granular crystals at the centre of calcification followed by elongated crystals fanning outward. F) TEM bright-field micrograph of a bundle of elongated crystals. G) High-resolution TEM micrograph of the crystal bundle showing regular two dimensional aragonite lattice spacings.

The difference between the three anhydrous polymorphs of calcium carbonate is their thermodynamic stability, with vaterite being the least stable and calcite the most stable. Precipitation from a supersaturated solution at ambient conditions, however usually starts with an amorphous transient phase: amorphous calcium carbonate (ACC) [24]. This phase is thermodynamically unstable and easily transforms to crystalline calcium carbonate. Some experiments have shown that this can in first instance be vaterite and as the saturation levels decrease it transforms to calcite at temperatures under 40°C and to aragonite at temperatures above 40°C [25, 26]. There is much discussion about how ACC forms and subsequently transforms to a crystalline phase. Views range from the classical ion by ion model to pre-nucleation clusters [27]. It is also unclear whether a crystalline phase directly forms from ACC or that ACC dissolves prior to precipitation of a crystalline phase [28].

Although ACC and vaterite are unstable phases and aragonite is metastable, they are found in nature as biominerals [3, 29-31]. Organisms have mechanisms to promote and stabilise mineral polymorphs and morphologies that are not energetically advantageous. Additionally, they can grow single crystals in round or curved shapes instead of polyhedral crystal facets [32]. The main factors that are thought to be influential are: organic additives [12, 22, 33], crystallisation within confined spaces [34, 35] and the seawater chemistry (i.e. the abundance of Mg) [36].

This study is motivated by the unique properties of biogenic minerals and the potential for the fabrication of biomimetic materials [37, 38] – as well as by a lack of fundamental understanding of the controlling factors in the formation processes thereof. This inspired a nano- to microscale investigation of coral and coccolithophore skeletal structures and the role of organics and the crystallisation environment associated with them. To this end an aragonite and a calcite based synthetic system was designed to isolate particular parameters that may influence the crystal growth.

1.2 RESEARCH OBJECTIVES AND EXPERIMENTAL APPROACH

In the study presented here aragonite and calcite mineral systems - both biogenic and bio-inspired - are investigated structurally by a multi-method approach to access different levels of length scales. This involves structural characterisation by various electron microscopy techniques, light microscopy and analytical techniques. For the millimetre to micrometre scale a combination of optical imaging and Raman spectroscopy on thin sections or whole crystals is used to determine large scale features and the distribution of different crystal polymorphs and organic materials. Subsequently, scanning electron microscopy (SEM) is performed on the thin sections after a surface etching process, to reveal the

microstructure. Specimens of (sub)micrometre dimensions, such as coccoliths and synthetically grown crystals, are imaged by SEM as a whole, without creating thin sections and applying surface etching. Energy Dispersive X-ray Spectroscopy (EDX) is used at this stage for elemental analysis.

The smallest reoccurring skeletal units, often termed building blocks, are localised by optical imaging and SEM after which focussed ion beam preparation of these units is applied where necessary (i.e. the corals), to create electron transparent, thin sections (ideally < 100 nm thick [39]). A nanoscale investigation is then performed by transmission electron microscopy (TEM), determining the crystal morphology, structure, orientation and grain sizes, by a combination of bright-field imaging, dark-field imaging and selected area diffraction. The latter is analysed by comparing experimental diffraction patterns with simulated patterns. Crystal lattice spacings, defects and strain contrast are investigated using high resolution TEM. Electron energy-loss spectroscopy (EELS) is used to probe elemental compositions in nanoscale features.

One of the main foci of this study is the coral aragonite skeleton, its microstructural evolution throughout its smallest building blocks (roughly 20 μm diameter) – *the spherulites* – and the correlation to the diurnal growth bands and the imbedded skeletal organic matrix. The latter compelled a detailed investigation of an aragonite bio-inspired system: calcium carbonate precipitated with ethanol as an organic additive to mimic coral mineralisation in the presence of OH-group containing organics. The organic fraction within the coral mineral skeleton itself is additionally investigated chemically, by extracting the organics and determining the amino acid composition of several species by high performance liquid chromatography (HPLC).

The second part of the study focusses on the crystallographic properties and ultrastructure in calcite systems: coccolithophores are marine algae producing calcite exoskeletons consisting of a nanoscale assembly of small single crystal units. To gain a better understanding of the intracellular calcification processes involved here, this system is compared to synthetically fabricated single crystal calcite

nanowires, grown from confinement in track-etch membranes. Part of the coccolithophore structure (i.e. a five-fold symmetric spine) is additionally investigated by scanning transmission electron tomography to create a three dimensional reconstruction.

The primary objective of this thesis is to obtain a detailed, nanoscale structural characterisation of complex calcium carbonate structures and to gain a better understanding of how the crystallisation environment, inter alia: local carbonate chemistry of the calcifying fluid (saturation state), external mechanical stresses (confinement) and organic additives, influence the end product in terms of crystal phase (i.e. polycrystalline versus single crystalline), polymorph selection and crystal morphology.

1.3 OUTLINE OF THE THESIS

This thesis will start with a general introduction, highlighting key issues and principals relevant to this work and the wider field of biomineralisation. This is followed by a detailed description of the investigated material systems and the experimental methods used. Subsequently two results chapters detailing the experimental findings on the aragonite based systems and the calcite based systems are presented respectively. These two chapters are again divided in sections dealing with the four individual subsystems, see Figure 1.2. The thesis is concluded by a last chapter discussing the results, comparing the aragonite and calcite based systems and deriving general parameters influencing calcium carbonate crystal phase, morphology, and polymorph selection.

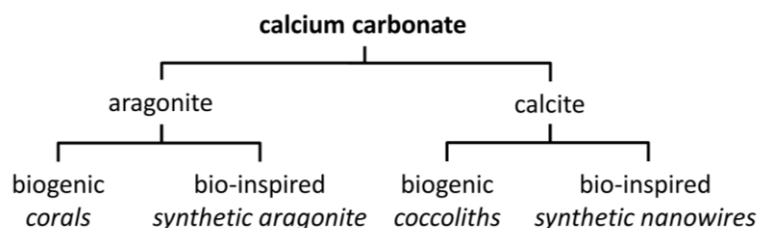


Figure 1.2 Flowchart representation of the structure of this thesis.

1.4 BIOMINERALISATION OF CALCIUM CARBONATE

1.4.1 NUCLEATION, GROWTH AND MORPHOLOGY

Nucleation and growth of crystalline material in biomineral systems can only occur when there is a space or compartment where a sufficient supersaturation state is maintained [23]. Such a space is usually realised in biomineralising organisms by having a physical barrier isolating the mineralising site from the environment, this can be in the form of tissue layers (extracellular, as in corals) or within vesicles (intracellular, as in coccolithophores). The dimensions of such compartments are often unclear, but it is generally thought that these compartments limit diffusion in and out of the system [23] and that targeted ions (i.e. calcium) are purposefully transported into these regions. Ion transport (in or out) is generally controlled in two ways: active pumping associated with certain organic molecules (e.g. acidic polysaccharides in coccolithophores [40]) that can attach ions, or by passive diffusion rates [23]. Several organisms (e.g. marine algae [41], marine and freshwater molluscs [42]) were found to have calcifying fluids with significant ionic strengths (>600 for marine molluscs), which implies an important role of total ion activity in affecting the supersaturation state, besides simply the concentration of the ions that will ultimately precipitate as minerals [23].

The growth of biominerals has been traditionally divided into two different processes: *biologically induced* [43] and *biologically controlled* [44]. The first is described in terms of the organism only providing nucleation sites (e.g. cell surfaces). After that the organism has little control over the type and morphology of the deposited minerals, although it does control the calcifying fluid in terms of pH, pCO₂ and organic secretion products (e.g. [4, 45]). Biominerals precipitated via such a process are often heterogeneous in their crystal shapes, grain sizes and porosity [23]. Corals are an example of *biologically induced* mineralisation although it is unclear where the nucleation sites exactly are located and what they consist of. This study shows that adult corals have three different crystal morphologies within the spherulites with different levels of ordering.

The second type of biomineralisation – *biologically controlled* – is characterised by the organism using cellular activities to direct the nucleation, growth, morphology and location of the mineral phase [23]. An example is the intricate skeletal structure of *R. clavigera* coccoliths, investigated in this study, consisting of single crystal calcite units, where each group of units making up the whole have exceptionally consistent shapes and sizes.

The crystal morphology or polymorph that is precipitated is a result of kinetic favourability. The kinetic favourability of a CaCO₃ structure is determined by the carbonate chemistry (the supersaturation state and the presence of trace elements like Mg etc.), the presence of organic molecules [1], and the nature of the medium in which crystal nucleation and growth takes place (e.g. fluid viscosity, vesicle dimensions etc.). Mann (2001) [22] discusses that the activation energies for the mineral forming reactions can be influenced by organic molecules present in the calcifying fluid, by differences in affinity to varying crystal surface structures. When the activation energy of a certain structure is further lowered in comparison to the other, than that structure will precipitate preferentially. How the kinetic favourability is influenced by organic molecules, genetic, metabolic and environmental processes, is often discussed in the framework of biomineralisation, but not much hard evidence is given for the actual mechanism.

1.4.2 ORGANISATION AND PROPERTIES

In a way all materials are hierarchically structured, but in biominerals it is key to the design and function at different length scales. Different length scales have different controlling factors or forces acting on the structure and thus hierarchical levels of ordering are induced [46]. At the macroscopic scale, skeletal features are influenced by forces such as mechanical loading and gravity, whereas the microstructure is subject to positioning and local activity of cells, membranes and organic molecules [46]. At the nanometre scale interfacial bonding strengths between crystal surfaces and between crystal surfaces and organics are vital [46]. This results in materials with ordered layers/units of crystal and organics making up the base building blocks and the assembly of these building blocks again constitute the whole. For example, abalone shells have a hierarchical structure starting at the nanoscale with organic layers of 20-30 nm thick, followed by single crystals of aragonite of 0.5-10 μm which are interlocked and form long flat plates. The plates are each separated by those thin organic layers thus building up the shell [1].

Another key aspect of biocomposites is that they consist of two very different constituents: a mineral and an organic part. The mineral will provide the rigidity and strength of the system, whereas the organic component provides ductility [1]. Ashby plots presented by Wegst and Ashby (2004) [47] of strength and Young moduli versus density respectively, of biological materials, shows that biominerals have the highest strength/density ($\sim 100 \text{ (MPa)}/3 \text{ (Mg/m}^3\text{)}$) and highest Young moduli/density ($\sim 100 \text{ (GPa)}/3 \text{ (Mg/m}^3\text{)}$) ratios of all the biological materials (e.g. natural cellular materials, natural polymer composites etc.). This shows that they are rigid structures, which can absorb relatively high energy impact before yielding and they have superior mechanical properties to monolithic minerals [1].

1.4.3 CRYSTAL STRUCTURE OF CALCIUM CARBONATES

Calcite, aragonite and vaterite are anhydrous polymorphs of CaCO_3 with identical chemical composition, but varying in the arrangement of the constituting ions. This leads to different crystal geometry. Under ambient conditions calcite is the stable polymorph. Vaterite and aragonite can be subject to diagenetic deterioration to calcite, as they are metastable under ambient conditions [48].

The smallest repeatable unit within a crystal is termed the *unit cell*. A unit cell is defined by a set of *base lattice vectors*, which describe the position of the atoms in the unit cell in three-dimensional space. These distances represent fractional displacements along the three axial directions x , y and z [49].

The *crystal structure* is defined as a regular arrangement of atoms in a periodic, three-dimensional lattice. The lattice is defined as a set of points which is created by all integer linear combinations of the three *base vectors*: $\bar{\mathbf{a}}$, $\bar{\mathbf{b}}$ and $\bar{\mathbf{c}}$ [50] from an arbitrary origin. The lattice vector ($\bar{\mathbf{R}}$) can be written as:

$$\bar{\mathbf{R}} = u\bar{\mathbf{a}} + v\bar{\mathbf{b}} + w\bar{\mathbf{c}} \quad \text{Eq. 1}$$

with (u, v, w) being an arbitrary triplet of integers. By definition, the entire lattice can be created by periodic repetition of the unit cell. The *lattice parameters* (\mathbf{a} , \mathbf{b} , \mathbf{c}) determine the unit cell in terms of *Bravais lattice* and represent the *lengths* of the sides of the cube/hexagon/etc. of the crystal geometry (i.e. they are not vectors).

Bragg (1924)[51] was the first to study the structure of aragonite, this and later work resolved that aragonite has an orthorhombic crystal structure [52]. Calcite has a trigonal structure but can be described by the hexagonal lattice by combining several trigonal unit cells (Figure 1.3). The structure of vaterite is not well understood until this day, but appears in large parts hexagonal.

An orthorhombic lattice has its three bases intersect at 90° angles, such that the three lattice vectors are mutually orthogonal. However the lengths of the $\bar{\mathbf{a}}$, $\bar{\mathbf{b}}$ and $\bar{\mathbf{c}}$ vectors are distinct (Figure 1.3).

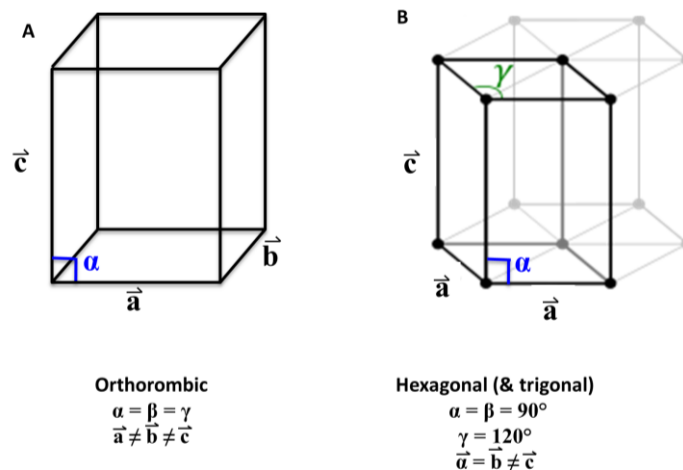


Figure 1.3 Schematic representation of: A) the orthorhombic lattice, B) the hexagonal lattice which shows how four bases of a trigonal lattice combine can describe the hexagonal symmetry.

A hexagonal crystal structure has \vec{a} and \vec{b} lattice vectors of equal length, but it has a longer \vec{c} , and the lattice vectors are not positioned orthogonally, in other words; the angles between the bases are distinct (Figure 1.3).

Symmetries of crystals are described by their space group, this is the complete group of crystal symmetry operations that generate the three-dimensional lattice [49]. Aragonite is usually placed within the Pnma space group. However, Bragg (1924)[51] expressed some concerns that aragonite may in fact not belong in this space group. This was investigated by Bevan *et al.*, (2002) [53], by means of diffraction pattern analysis, and they concluded that aragonite could indeed either belong to the Pnma or P1 space group, the latter being a space group of a triclinic system. To make matters more confused, aragonite is currently usually referred to as having a Pmcn space group in geological and biomineral studies. Pmcn is a simple permutation of Pnma of the lattice parameters (**a b c**):

Pnma = **a b c**; for example [10 -1 -4] zone axis orientation, becomes:

Pmcn = **b c a**; for example [-1 -4 10] zone axis orientation

In this study we will use the Pmcn space group notation for aragonite, to facilitate comparison with other studies. Calcite belongs to space group R-3 2/c and vaterite is allocated to the P 6₃/mmc space group.

Table 1-1 Aragonite and calcite lattice parameters used in our analyses.

Mineral	Lattice	a/nm	b/nm	c/nm
Aragonite	Orthorhombic	0.57407	0.49611	0.79672
Calcite	Hexagonal	0.4999	0.4999	1.7061

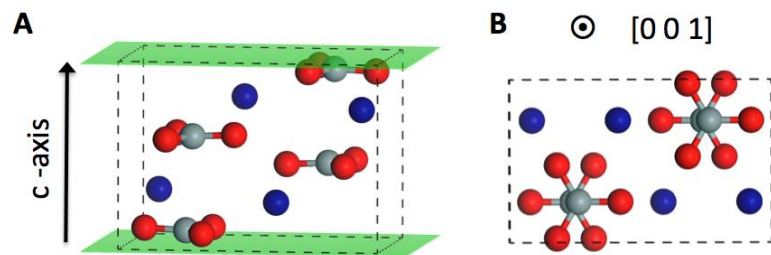


Figure 1.4 Schematic representation of the unit cell of aragonite with its atomic arrangement. A) The {001} lattice planes are indicated as green plates, and B) shows the view along the c-axis or [001] direction. Atom colours are as follows: blue is calcium, grey is carbon and red is oxygen.

Due to a preferred growth direction along the c-axis, and random growth distributions along its a- and b-axes, aragonite crystals usually form acicular (needle-like) crystals [54, 55]. We define the c-axis as being the axis with the largest lattice parameter, the values for aragonite and calcite are given below.

In Figure 1.4 and Figure 1.5, a *lattice plane* is defined by three lattice points and can be described by a triplet of Miller indices (hkl). These Miller indices correspond to the reciprocals of the intercepts $|\bar{a}|/h, |\bar{b}|/k, |\bar{c}|/l$ of the respective plane in real space. The indices of a family of planes $\{hkl\}$ lying midway in between and all parallel to each other, are by convention derived from the plane located closest to the origin of the coordinate system. In the figure above the unit cell of aragonite is depicted with the {001} lattice planes indicated in green. Similarly this is shown for the calcite unit cell and the {104} lattice planes in Figure 1.5.

Scattering from a crystal

The amplitude \mathbf{A}_{cell} of a wave scattering from a unit cell can be described by

$$\mathbf{A}_{cell} = \frac{\exp(2\pi i k r)}{r} \sum_i f_i(\theta) \exp(-2\pi i \vec{\mathbf{K}} \cdot \vec{\mathbf{R}}) \quad \text{Eq. 2}$$

Where $f_i(\theta)$ is the atomic scattering amplitude from atom i and the factor $2\pi i \vec{\mathbf{K}} \cdot \vec{\mathbf{R}}$ is the phase difference of a wave scattered from a point i relative to that of the origin (distance r) and $\vec{\mathbf{R}}$ is the lattice vector which defines the location of each atom in the unit cell. $\vec{\mathbf{K}}$ is equal to $\vec{\mathbf{G}}$, the reciprocal lattice vector, for an infinite perfect crystal.

$$\vec{\mathbf{G}} = h\vec{\mathbf{a}}' + k\vec{\mathbf{b}}' + l\vec{\mathbf{c}}' \quad \text{Eq. 3}$$

In which $\vec{\mathbf{a}}'$, $\vec{\mathbf{b}}'$ and $\vec{\mathbf{c}}'$ are the reciprocal base lattice vectors. So when we consider the atoms stacked in a regular fashion in a crystal we can introduce the *structure factor* $F(\theta)$

$$F(\theta) = \sum_i^{\infty} f_i \exp 2\pi i(hx_i + ky_i + lz_i) \quad \text{Eq. 4}$$

The amplitude (and therefore its square, the intensity) of the scattering is determined by the type of atom, the position of the atom in the unit cell (x,y,z) and specific atomic planes (hkl) that make up the crystal structure. From this equation it follows that in certain circumstances the amplitude will be zero and thus no reflection will appear in the diffraction pattern.

A reflection will only occur when:

$$\vec{\mathbf{G}} \cdot \vec{\mathbf{R}} = 0 \text{ or an integer} \quad \text{Eq. 6}$$

For a more detailed discussion on diffraction pattern formation and analysis see section 2.2.2.

As mentioned earlier, aragonite is often found in nature, both biogenic and non-biogenic, as acicular crystals with preferential growth along the c-axis. This results in the dominant growth front exposing the (001) plane. It has been suggested that the (001) plane in aragonite easily binds to organic molecules that bind Ca^{2+}

ions, such as aspartic acid-rich proteins [1, 56-58], due to the atomic arrangement at this crystal plane. This may facilitate crystalline-organic composite mineral formation in biogenic systems.

In calcite the {104} rhombohedral cleavage plane is thermodynamically most stable and it is therefore commonly expressed in crystal growth [59]. It has been found that organic molecules with OH-groups, such as ethanol preferentially bind to this surface and even displace water [59]. This may provide biomineralising organisms with a way to control crystal growth and prevent recrystallisation on specific crystal facets.

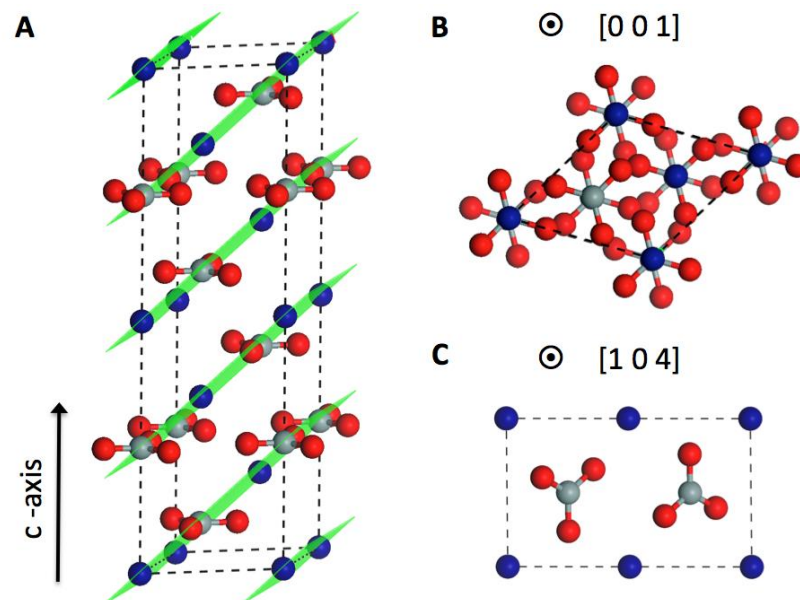


Figure 1.5 Schematic representing the unit cell of calcite with its atomic arrangement. A) The {104} lattice planes are indicated as green plates, B) shows the view along the c-axis or [001] direction, and C) shows the view along the [104] direction. Atom colours are as follows: blue is calcium, grey is carbon and red is oxygen.

2. MATERIAL AND EXPERIMENTAL BACKGROUND

This chapter comprises a description of the two material systems investigated in this study: aragonite and calcite based minerals. These are divided into four subunits, dealing respectively with biogenic (coral) and bio-inspired (CaCO_3 precipitated in the presence of ethanol) aragonite, and biogenic (coccolithophores) and bio-inspired (nanowires) calcite. Each of these sections will include an introduction to the respective material systems and a short review of the literature relevant to this work.

The second part of this chapter describes the methods used to characterise the above mentioned materials together with the sample preparation needed for each method and the data analysis involved.

2.1 MATERIAL SYSTEMS

2.1.1 SCLERACTINIAN CORALS

Scleractinian corals, or stony corals, accrete hard exoskeletons and are thus distinguished from the soft corals (Octocorallia and Antipatheria) [4]. Scleractinian corals can be divided into two groups; the reef builders and the non-reef builders. We focus our research on the microstructure of reef building corals. The results of the electron microscopy, micro-Raman and HPLC investigation of the mineral and organic skeletal fraction are presented in section 3.1.

Most stony corals are colonial and host symbiotic algae named zooxanthellae. These single-celled algae live within the cells of the coral polyp upper tissue layers [4]. The algae provide the majority of the corals nutrition by sacrificing 78-98% of their photosynthetic products (glycerol and glucose) [60, 61] to the coral, as well as nitrogen from waste products for amino acid assemblage, in return for structural protection. Due to the photosynthetic nature of the zooxanthellae, stony corals exhibit light enhanced calcification. This faster form of calcification results in the build-up of coral reefs [2] and induces a diurnal banding as seen in optical thin sections of the skeletal microstructure [4]. The 'living' part of the coral, the polyp, inhabits only the upper few millimetres of the coral skeleton, leaving beneath it an expanse of bare CaCO_3 . It has been widely accepted that controlled skeletogenesis or biomineralisation occurs at the interface between the polyps inner layer of soft tissue, composed of calicoblastic cells, and the mineral skeleton [62], see Figure 2.1B at the black arrow.

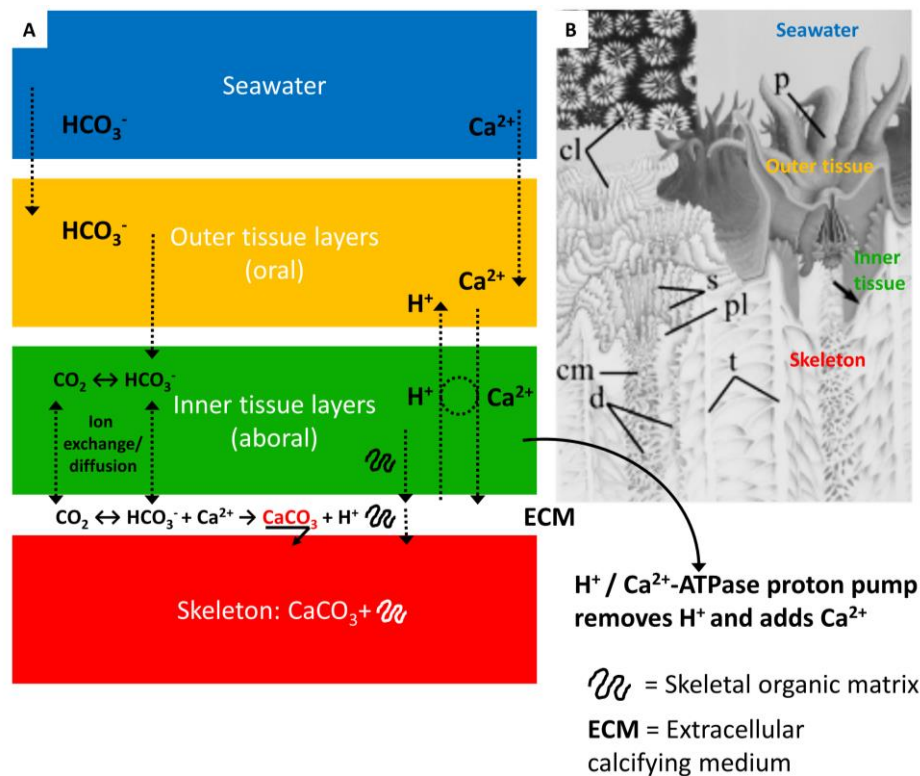


Figure 2.1. Simplified physiological model for coral calcification (A) and coral skeletal components (B). A) The model shows the hypothetical organisation of ion transport, carbonate chemistry control and secretion of skeletal organic matrix into the EMC [4, 63, 64]. B) The major skeletal components are labelled: (p) the polyp, (cl) the corallite, (t) the theca, (s) the septa, (pl) paliform lobes (outgrowths of the septa), (cm) columella and the (d) dissepiment (Figure B is adapted from Veron (1986) [65] and Cohen & McConnaughey (2003) [4]).

The generally accepted physiological model of carbonate accretion in corals consists of two mechanisms: 1) control of carbonate chemistry by ion transport and diffusion, and 2) secretion of a skeletal organic matrix into the Extracellular Calcifying Medium (ECM) [63, 64, 66], see Figure 2.1. Both these processes are heavily dependent on the availability of Adenosine-5'-triphosphate (ATP) molecules, the coral's 'energy source'. This enables a 'proton pump' mechanism to remove H^+ and add Ca^{2+} to the ECM to enhance carbonate supersaturation with respect to seawater for fast calcification, and the production of organic molecules that help guide nucleation and crystallisation. In the ECM calcium and carbonate ions react to form CaCO_3 . It is unknown how wide the ECM area is and whether it is a fully- or semi-closed system with respect to the environment [63].

Many decades of study have not revealed the exact process of mineral accretion within corals. Despite this lack of understanding there is general agreement about the structural characteristics of the Scleractinian skeleton on the macroscale. A coral colony consists of a collection of individual skeletons, also called corallites, of its resident polyps [4]. The corallite looks like a tube, called the theca, intercepted by radiating vertical partitions, the septa (Figure 2.1). The lower part of the polyp sits on a thin horizontal sheet called the dissepiment. The surface of the corallite grows as the polyp pulls itself up along the walls of the theca, leaving the old dissepiment sheet behind, after which – on a monthly basis - a new dissepiment layer is formed a few millimetres above, sealing the living tissue off from the now unoccupied skeleton beneath [4]. From this it follows that only the upper few millimetres of a coral colony is occupied by living tissue and that this is the only place where biomineralisation takes place. Although the lower, by far larger skeletal mass is still in direct contact with seawater and abiogenic aragonite crystals continue to grow slowly, within pores previously occupied by gastrovascular canals and tissue [4].

Interestingly, the non-biogenic crystals are distinct in morphology, growth rate and chemical composition from the biogenic crystals grown at the tissue skeleton interface [67]. This implies that the organism has extensive influence over the mineralisation mechanism.

This study concentrates on the biogenic minerals formed at the polyp-mineral skeleton interface and aims to describe the crystalline skeleton on the nano- and microscale and to provide a better understanding of the mineralisation process (es). The species investigated here are adult *Porites lobata*, *Siderastrea siderea*, *Montastrea annularis* and juvenile *Acropora millepora*.

Centres of calcification (COCs)

The basic building blocks of the aragonite coral skeleton on the microscale are bundles of fan-like acicular crystals situated around a so-called centre of calcification [4]. Ogilvie (1896) [68] described these as *spherulites*, grouped into

fishscale-shaped bundles termed fascicles. Different coral species show different diameters and morphologies of individual aragonite needles. Bundles of spherulites growing upward together in a certain plane develop into a vertical spine called a trabecula, subsequently groups of trabeculae - sometimes intercepted by pores depending on the coral species - form the septa, and thus the primary structure of the coral skeleton [4].

The centres of calcification form the origin of the bundles of crystal needles and were first recognised showing up as dark patches in optical microscope thin-sections of coral skeleton in transmitted light by Ogilvie (1896) [68]. These COCs are traditionally considered to be nucleation sites for the growth of aragonite acicular crystals and thus fundamental to any model for coral mineralisation [69-72]. Within these supposed nucleation centres, crystals with a granular morphology have been observed [4, 70]. Our aim is to further resolve the structure of COCs and the surrounding needle-like crystals using EM methods, combined with Raman characterisation and chemical analysis. By these methods we aim to reveal the components present in these features, as both structural and compositional information are essential to make any progress towards a model of nucleation and growth in corals.

The study of juvenile corals as well as adult coral skeletons is essential in this approach, since it allows the study of the early stage of the crystallisation in comparison to the fully developed skeleton.

State of the art: nanostructure

Studies on coral skeletal structure and its calcifying mechanism are numerous (e.g. [2, 4, 55, 63, 73, 74]), but not much is known at a nanoscale level, particularly encompassing whole spherulites. Benzerara *et al.*, (2011) [75] were the first to present a detailed TEM and scanning transmission X-ray microscopy study of the COCs in *Porites* coral. They concluded that it consisted of clusters of 100 nm aragonite grains that were crystallographically aligned over several micrometres with a fan-like distribution and with properties of single crystals at the mesoscale.

They also found that the rest of the skeleton consists of aragonite single crystal fibres that are in crystallographic continuity with the grains making up the centre.

Organic matrix in corals

Within the field of biomineralisation in corals two main contradictory views concerning the mineral nucleation and growth of corals seem to persist. Geologists consider mineralisation as being a 'physico-chemically dominated process' headed by the influential paper of Bryan and Hill (1941) [76]. In this work it is suggested that 'a single crystal of aragonite' is the basic element of the coral skeleton and that it is formed without biological control [71]. In contrast biologists follow the 'organic matrix' concept [77]. This model was first supported by TEM and SEM structural images of organic materials associated with the coral mineral phase, in the study of Johnston (1980) [78].

In Scleractinian corals it has been shown by bicarbonate or amino acid labelling that organic matrix synthesis is a prerequisite step in the calcification process [79, 80]. More recently, Clode and Marshall (2002) [81] made the suggestion that organic matter acts as a sheath to inhibit or direct CaCO_3 deposition, or otherwise serve as a structural framework. Cuif and Dauphin (2005) [74] proposed a model where the mineralisation begins with the secretion of an organic matrix layer of proteoglycans (i.e. proteins with attached polysaccharide chains), followed by simultaneous formation of needle like crystals and centres of calcification. In more detail, Puvarel *et al.*, (2005) [82] suggested that since there is a dominance of acidic amino acids and especially aspartic acid, that the organic matter can bind calcium and serve to concentrate and deliver calcium when needed for calcification. In contrast, it was put forward that particular molecules with high calcium binding affinity act as templates or nucleation sites for CaCO_3 [83]. Another suggestion by Teng *et al.*, 1998 [84] was that aspartic acid changes the crystal growth surfaces by alteration of the thermodynamic equilibrium.

Galaxin is one of the sole proteins to have been fully characterised and recognised as part of the skeletal organic matrix [83]. This protein, however, does not bind calcium and its role remains unclear. It is possible that due to high

abundance of cysteine residues this molecule is highly cross-linked through intermolecular sulphide bonds and thus forms a structural framework [83]. It has also been proposed that the skeletal organic matrix acts as a catalyst as it has carbonic anhydrase activity [85, 86] which could eliminate the kinetic barrier to the inter-conversion of inorganic carbon at the nucleation site [63]. Nakata *et al.*, 2002 [87] and Ichikawa (2007) [88] therefore suggested that carbonic anhydrase could directly hydrate CO_2 and form CO_3^{2-} .

Overall it is assumed that the skeletal organic matrix plays a vital role in the morphology of skeletal features since the structure, composition and quantity is taxon specific [89-91]. In this study we aim to improve characterisation of the organic fraction and especially determine its location within the mineral to correlate changes in crystal morphology with the spatial distribution of organics.

2.1.2 ARAGONITE PRECIPITATED IN THE PRESENCE OF ETHANOL

As stated above, the zooxanthellae provide the coral with nutrients, mostly in the form of glycerol and with traces of glucose [92]. Extracellular acidic polysaccharides are part of the 'coral organic matrix' at mineralising sites and probably originate from the coral's calicoblast cells (i.e. a layer of cells situated just above the mineral accretion zone) [93]. Additionally, protein bundles are known to be present in the coral mineral, see paragraph 3.1.2. These organic compounds have in common the presence of OH-groups.

The pathways in which organisms can control the morphology of biomineral formation are further explored in this study by investigating the effect of OH-containing compounds with aragonite formation on the nano- to microscale in a controlled system with well-defined parameters. This system is used as a simplified scenario to compare with coral mineral formation.

Molecular dynamic (MD) simulation studies have shown that some saccharides bind to CaCO_3 mineral surfaces through OH [94], and the OH of ethanol has been

observed to preferentially bind to calcite {104} facets compared to water [95]. This behaviour can lead to the promotion or inhibition of certain crystal facets. We aim to determine how high amounts of OH-group containing molecules in a system influences crystal morphology and polymorph selection as compared to no or low ratios of OH-group containing additives. This will then be compared to the coral microstructural with the aim of isolating the effect of the organics on crystal formation and morphology from other influential parameters such as saturation state.

Here we investigate the crystal formation from 0.1 M CaCl₂ solution with 0.1 M Na₂CO₃ solution in the presence of ethanol. This work is the result of a collaboration with Dr. Karina Sand from the Nano-Science Centre, Department of Chemistry, University of Copenhagen, Denmark. Karina Sand prepared the solutions, the electron microscopy and data analyses were performed by Dr. Andreas Verch from the Department of Physics, University of York and this author.

This study is a continuation of the experiments described in Sand *et al.*, (2011) [96], where different percentages (10 vol%-50 vol%) of OH containing additives (i.e. ethanol, 1-propanol and 2-propanol) were mixed with a 25mM CaCO₃ solution under varying shaking speeds and time intervals. One of the main findings of that study was that higher amounts of ethanol enhances the amount of initial aragonite formation in favour of calcite and that the aragonite is stabilised and does not convert to calcite over longer periods of time. The aragonite formed in the presence of ethanol consisted of bundles of needle-like crystals, with the individual needles made up of small segments separated by well expressed, perpendicular grooves [96]. Similar experiments are conducted in this study, however the crystallisation process is observed *in-situ* with a JEOL ClairScope atmospheric SEM instrument. It enables us to view samples in aqueous solutions, under atmospheric conditions, in real time, through a thin SiN window situated at the bottom of a petri dish (see paragraph 2.2.3). The specimens were subsequently studied by conventional SEM and TEM. Analogous specimens are also analysed in detail by TEM and SAED, the results are presented in section 3.2.

2.1.3 COCCOLITHS

Coccoliths are calcitic exoskeletons produced by coccolithophores, which are a group of unicellular marine algae or phytoplankton. Phytoplankton consist of microscopic organisms that obtain energy by photosynthesis and hence live in the upper sunlit region of the water column with a global distribution. Phytoplankton are primary producers, they create organic compounds from dissolved CO₂ in seawater and are vital for the aquatic food web [98]. In this study the structure of *Rhabdosphaera clavigera* is described and the results are presented in section 4.1.

Coccoliths are of substantial geological and environmental importance as they occur in abundance, forming a significant proportion of the global carbon fixation and primary marine production, mainly in open ocean environments [99]. Coccoliths are used in geologic studies as marker fossils to determine the age of sedimentary rocks. More recent studies have focused on satellite imaging of large coccolithophore blooms and their impact on the global carbon cycle and marine ecosystem (e.g. Thierstein & Young 2004 [100]).

A characteristic feature in the formation of exoskeletons by coccolithophores is the occurrence of two very distinct types of biomineralisation modes within a single species, related to two phases in the life cycle of a coccolithophore [99]. The two life cycles consists of a diploid phase (Mitosis) and a haploid phase (after Meiosis of diploid cells), both phases calcify and produce heterococcoliths and holococcoliths respectively [99].

The most common types of coccoliths are heterococcoliths, disk-shaped structures formed by radially arranged, interlocking calcite crystals. These disks usually have diameters of 2 – 10 μm, depending on the species. The separate disks, or coccoliths, interlock to form a hollow sphere, called the coccosphere. Hence, the individual coccoliths often have a concave proximal (inner) surface (Figure 2.2).

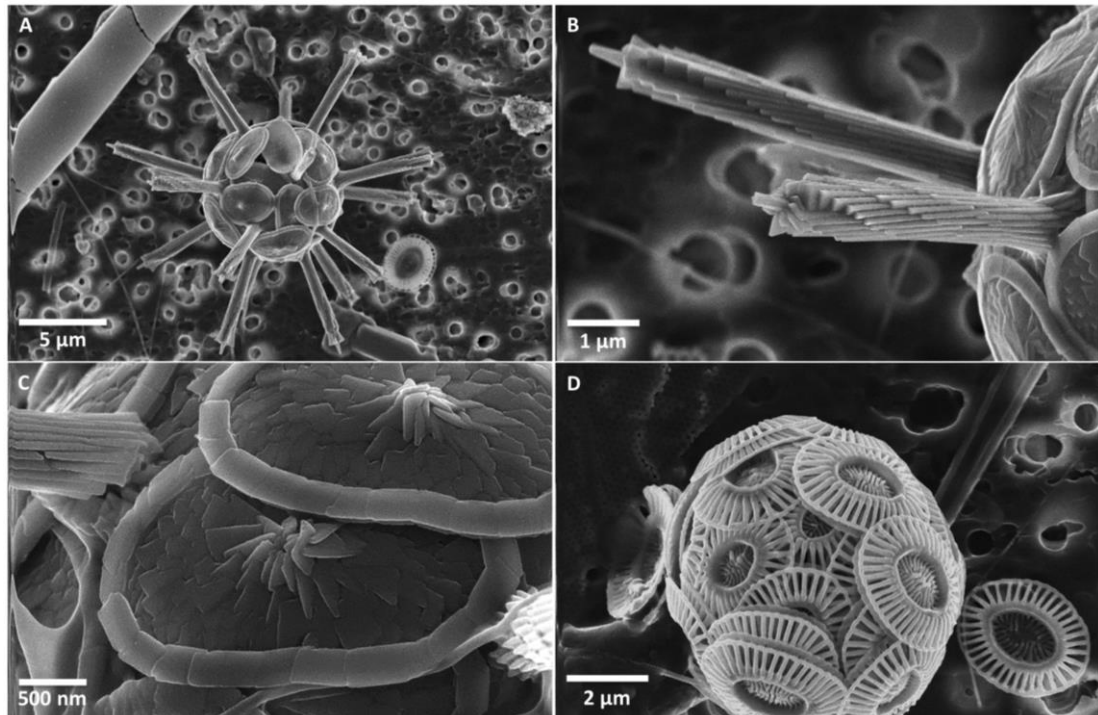


Figure 2.2. SEM micrographs of heterococcoliths. A) *Rhabdosphaera clavigera*: complete coccosphere. B) *R. Clavigera* detail of spine structures. C) *R. Clavigera* detail of coccolith plates without spine structure. D) *Emiliana Huxleyi* complete coccosphere.

Previous studies, using polarised light, scanning electron microscopy and cytological (study of cells) transmission electron microscopy have shown that the coccoliths are formed within intracellular Golgi-derived vesicles with growth commencing by nucleation of a ‘proto-coccolith ring’ of minute crystallites with alternating crystallographic orientation, probably controlled by an organic template. Subsequently these crystallites grow and interlock to form the elaborate final coccolith morphologies. After this process the coccolith vesicle migrates to the edge of the cell and merges with the cell membrane resulting in the expulsion (exocytosis) of the coccolith [101, 102].

Young *et al.*, (1992-1993) suggested a model of coccolith crystal ultrastructure which can be applied to most heterococcoliths: the *V/R* model [103, 104]. It is based on the observation that the coccolith rims are characteristically formed of two cycles of interlocking crystal units, one with sub-vertical *c*-axes, termed *V*-units, and the other with sub-radial *c*-axes, *R*-units (Figure 2.3). These originate as alternating nuclei in the proto-coccolith ring. However, the central area of the coccoliths may

show rather different structures. *Rhabdosphaera clavigera* is a dramatic example of this, exhibiting a central area of spiral cycles of small units with a five-fold, several micrometre long, symmetric spine, with diameters of approximately 0.5 μm . Crystals are arranged radially along the longitudinal axis of the spine, protruding from the centre of the concave disks constituting the coccosphere (Figure 2.2A-C). The rim of the disk in *Rhabdosphaera clavigera* does comply with the V/R structure model. It has been suggested that the central area and the spine are both separately nucleated [105] or caused by a different mineralization mode, but not much is known about the crystallographic orientation of its crystal units and ultrastructure. This characteristic biomineral structure, starting with the growth of a ring of calcite crystallites with alternating orientations, has no parallel in any other biogenic system and has remained constant through more than 200 million years of evolution, as demonstrated by Young *et al.*, 1992 [104] and Young *et al.*, 1999 [105]. The complex structure of the mineral shows little resemblance to inorganic mineral calcite and it is not yet possible to reproduce such a complex nanocrystal assembly synthetically. Coccoliths are exceptional in being able to fully control both c- and a-axis orientation. Such stark control in creating functional structures motivates a detailed study of the microstructure, with the aim of unveiling fundamental aspects of nanocrystal assembly in biological systems.

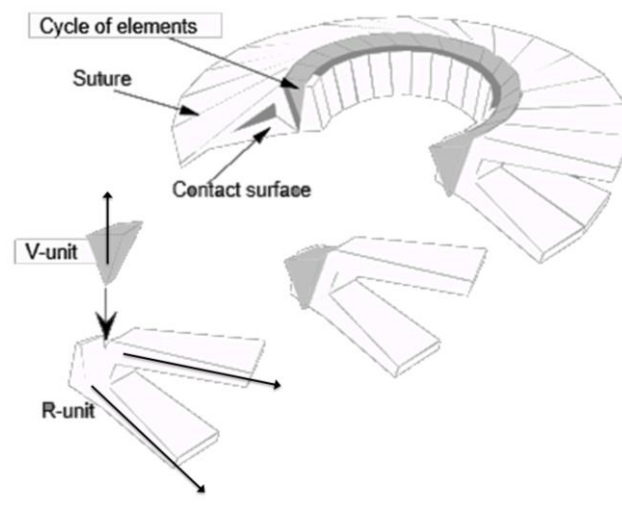


Figure 2.3. Schematic drawing of the V/R structure model for coccoliths, image provided by Jeremy Young, University College London, Department of Earth Sciences.

2.1.4 CALCITE NANOWIRES GROWN IN CONFINEMENT

One of the great difficulties in the study of the fundamental mineralisation processes in biological systems is the lack of control and understanding of the numerous parameters (e.g. external parameters such as pH, $p\text{CO}_2$, available nutrients, salinity and temperature, but also internal parameters such as metabolism, intra- or extracellular mineral growth, the organics involved, conditions within mineralising fluid, etc.). A way to facilitate the study of certain aspects of a biological system is to find a simplified analogous synthetic system, which is designed to mimic certain biogenic parameters.

Here we are investigating calcite nanowires grown in confinement from amorphous calcium carbonate (ACC). The calcite nanowires are later compared to fundamental aspects of intracellular calcite nanocrystal formation in coccoliths, where the vesicle membrane tightly envelopes the crystal formation and can thus induce external stresses. In nanostructures, surface stress has been found to be an important factor as the ratio of surface area to bulk volume is decreased to such a large extent that the surface stress causes bulk distortion. This has been shown to result in twisting of nanoribbons [106, 107] and deformation of nanowires and nanocantilevers [108-110].

Dr. Yi-Yeoun Kim from the School of Chemistry, University of Leeds, has been instrumental in producing the calcite nanowires. The electron microscopy and data analyses were performed by Dr. Andreas Verch from the Department of Physics, University of York and this author. The results are presented in section 4.2.

The ACC is precipitated in track etch (TE) membranes with approximately 50 nm and 200 nm pore diameter. To extend the lifetime of ACC, a gas diffusion method using an additive poly(acrylic acid) (pAA) or poly(aspartic acid) (pAsp), named the polymer-induced liquid precursor (PILP) method is used. Additives are used to stabilise ACC as it naturally immediately crystallises under ambient conditions [35].

The track etch membranes

The CaCO_3 is precipitated in a polycarbonate track etch membrane (Isopore, Millipore) with a smooth, flat glass-like surface with 50 and 200 nm diameter pores measured at pore entrance. After precipitation the membranes are dissolved by three cycles of sonication in dichloromethane/centrifugation and exchange of solvent for fresh. The isolated nanowires are then rinsed with methanol and washed with ethanol and pipetted onto TEM grids.

Polymer-induced liquid precursor (PILP) method

In this method the track etch membranes were directly immersed in 10 mM CaCl_2 with pAA or pAsp (10ppm) and left overnight to achieve a homogenous distribution of the solution over the membranes. Afterwards, the membranes in solution were placed in a vacuum desiccator together with a source of $(\text{NH}_4)_2\text{CO}_3$ – vapour. CO_2 diffuses into the Ca-solution and CaCO_3 precipitates (Figure 2.4). This method resulted in complete filling of the membrane pores and yielded nanowires with aspect ratios of ≈ 50 [35]. SEM and TEM bright field images of the resulting nanowires after deposition on a TEM lacy carbon grid are shown in Figure 2.5.

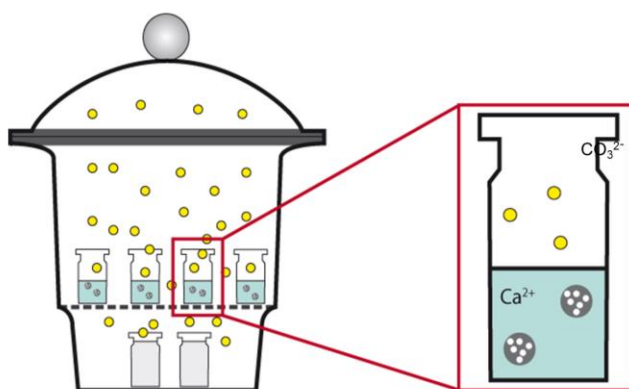


Figure 2.4. Schematic drawing the gas diffusion method (courtesy of Andreas Verch, Department of Physics, University of York and Anna Schenk, School of Chemistry, University of Leeds).

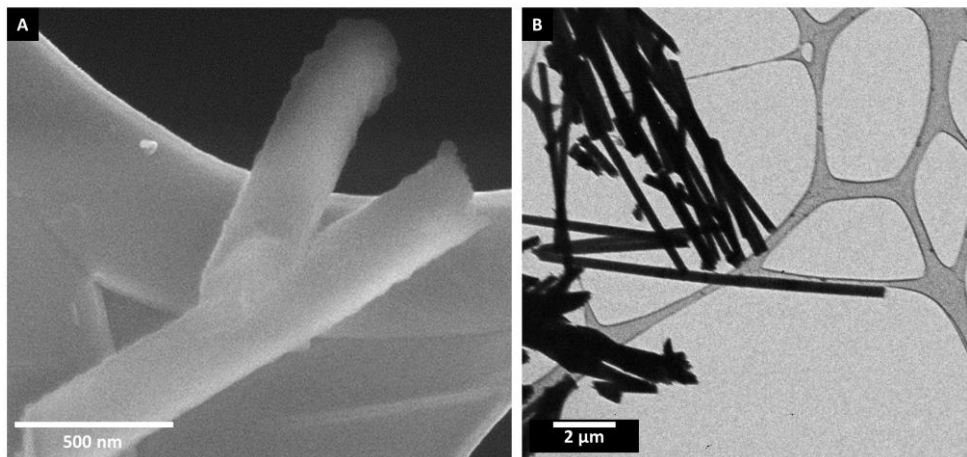


Figure 2.5. A) SEM image of the 200 nm calcite nanowires. B) TEM bright field image of the 200 nm calcite nanowires.

2.2 EXPERIMENTAL TECHNIQUES

2.2.1 OUTLINE OF APPLIED EXPERIMENTAL TECHNIQUES

When studying biogenic or bio-inspired minerals it is necessary to study the mineral at several different hierarchical levels in order to get a complete understanding of the structure. Therefore this study uses experimental methods that provide structural information at different length-scales. Furthermore complementary chemical data are obtained, also for a range of scales from bulk analysis to targeted microscale features.

The main focus of this study is structural characterisation from the nanometre to the micrometre length-scale and therefore predominantly electron microscopy based techniques, such as conventional TEM and SEM, were used. An overview of the used techniques and their resolution scope are given in the graph below (Figure 2.6).

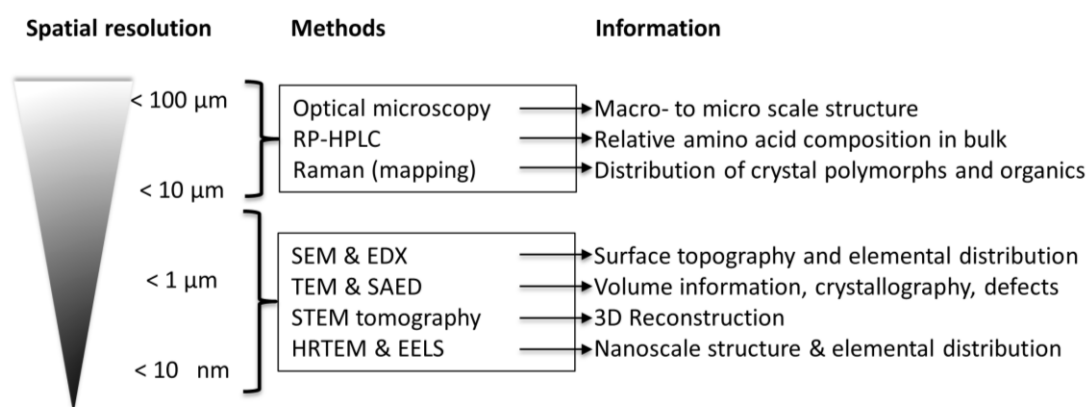


Figure 2.6 Schematic of the overview of techniques used for structural and chemical characterisation of the CaCO_3 material systems.

2.2.2 TRANSMISSION ELECTRON MICROSCOPY

The great advantage of transmission electron microscopy over conventional optical (light) microscopy is the shorter wavelength of electrons compared to photons, which enables us to obtain a much higher resolution. An estimate for the wavelength of an electron in a TEM operating at an accelerating potential of 200 kV is 2.5 pm (2.5×10^{-12} m) (via the De Broglie equation and taking relativistic effects into account for the velocity of the electrons generated by the acceleration potential). In optical microscopes the wavelength of visible (green) light is typically assumed to be 550 nm (5.5×10^{-7} m). In practice this results in TEM being able to image at an atomistic level whereas optical microscopes at best achieve a 200 nm resolution.

The general concept of image formation in TEM is that an almost parallel coherent beam of electrons is scattered by a thin specimen. In *bright-field* (BF) TEM the image is formed by electrons passing straight through and any low angle inelastic scattering. Thus the contrast is a result of variations in intensities of diffracted electrons (who do not contribute to the image) from different parts of the sample and is therefore called *diffraction contrast* [111]. In *dark-field* (DF) TEM the image is constructed using electrons that undergo diffraction within a crystalline sample.

It is of utmost importance that TEM specimens are electron transparent (≤ 100 nm) so that no multiple scattering events occur (see TEM sample preparation below). TEM images are extremely difficult to interpret as there are many different sources of contrast that can contribute to the final image. By keeping the specimen thin we limit the number of sources of contrast in the final image. In fact, a 'truly' thin specimen is rarely obtained; hence we need to take more complex scattering processes into account when interpreting TEM images.

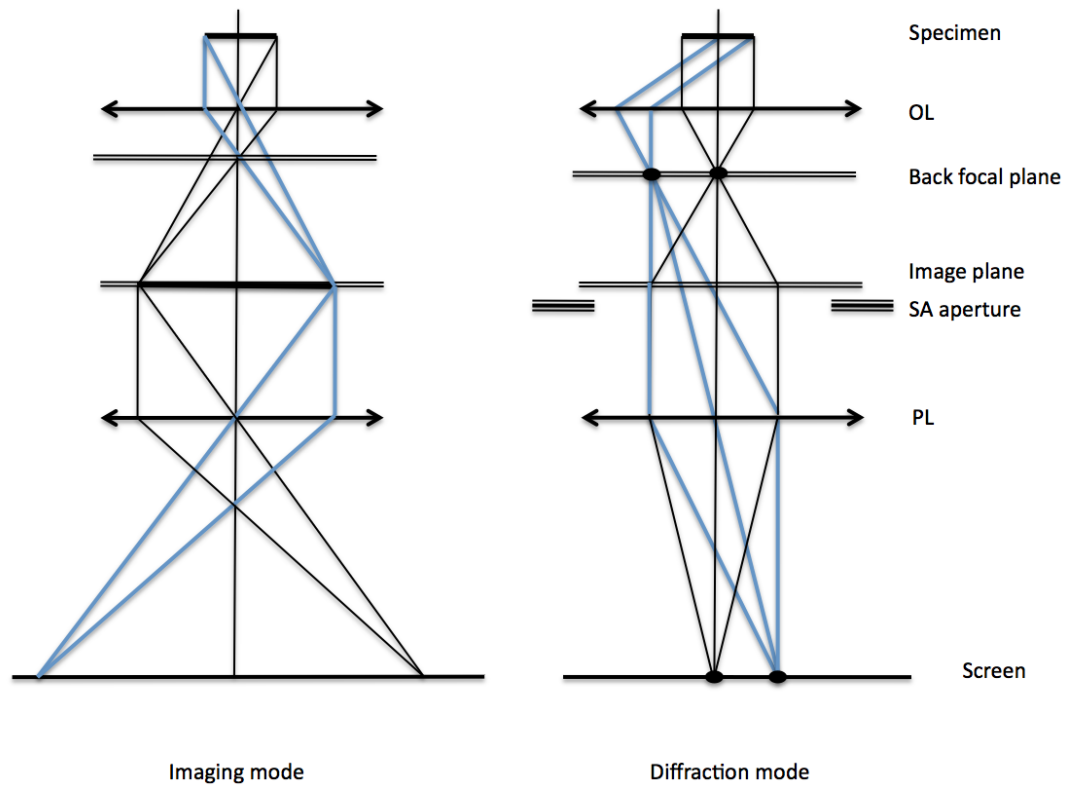


Figure 2.7. The ray diagram provides an overview of the imaging and diffraction modes in TEM. Objective Lens (OL), Selected Area aperture (SA), Projector Lens (PL).

The most important operation modes in TEM are imaging and diffraction (Figure 2.7). Within the imaging mode we make use of bright field imaging (BF) conditions, dark field imaging (DF) conditions and high resolution (HRTEM).

Additionally, most transmission electron microscopes have analytical capabilities to explore the chemical composition and distribution on the nano- and microscale of the specimen such as energy dispersive x-ray spectroscopy (EDX) and electron energy-loss spectroscopy (EELS).

Microscope conditions and beam damage

Damage caused by inelastic interactions can affect the original structure and/or chemistry of the specimen by a variety of phenomena. This includes the breaking of chemical bonds, the displacement of atoms, creating point defects or simply the heating caused by phonons interacting with the sample [39]. Contamination is caused by the deposition of carbonaceous material due to hydrocarbons that are

present in the TEM chamber reacting with electrons from the beam forming hydrocarbon ions and condensing on the irradiated specimen surface [112]. In the case of biogenic samples a hydrocarbon organic film is often naturally present on the specimen itself, which greatly enhances this phenomenon. Especially during analytical EM: EDX and EELS, beam damage is problematic as the beam is often condensed on a spot for several tens of seconds' acquisition time (see Figure 2.8). This can cause severe structural damage: removal of material, and re-deposited together with the previously mentioned hydrocarbons on the specimen surface. Beam damage also occurs during high resolution imaging as the high magnification (>400 000 x) requires a high illuminating brightness and the electron beam is focused onto a small area of the sample (Figure 2.9).

Calcium carbonate/organic composite materials are particularly prone to beam damage compared to other purely crystalline materials, as can be derived from the nature of the *critical ionisation energy* (E_c). An atom will be ionised (i.e. acquiring a negative/positive charge by gaining/losing electrons) when the electron beam transfers an amount of energy (E_0) significantly greater than a certain value to the inner shell electron [39] (p.57).

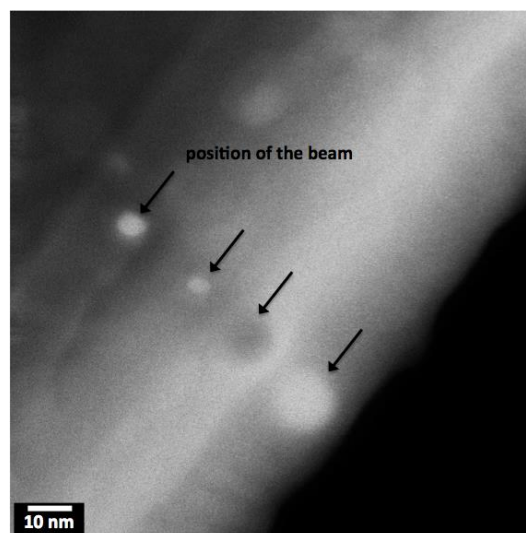


Figure 2.8 HAADF-STEM image of the side of a coccolith spine (*R. Clavigera*) showing beam damage induced during a line scan for EELS analysis. Reduced contrast implies the removal of material, whereas increased contrast implies re-deposition or contamination.

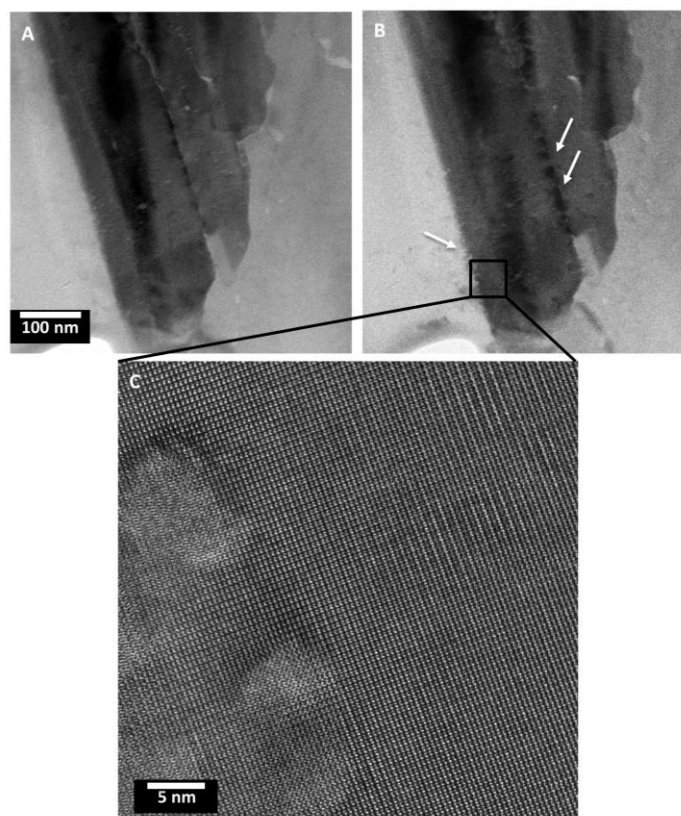


Figure 2.9 A) TEM bright field image taken before high resolution imaging. B) TEM bright field image taken after high resolution imaging, the arrows indicate areas that have been affected by the beam. C) HRTEM image of area affected by the beam showing disruption of the lattice fringes.

The critical ionisation energy increases with Z as the electrons in higher Z atoms are more tightly bound due to the increasing nuclear charge. Since organic molecules often consist primarily of H ($Z=1$), C ($Z=6$) and O ($Z=8$) atoms, its E_c will be low and therefore easily ionised by the electron beam.

To reduce beam damage, imaging and diffraction is predominantly performed using a TEM with a LaB₆ filament rather than a higher brightness aberration corrected field emission TEM. Specimens were observed over time to determine optimum imaging conditions, and we found that the current density is the dominant factor in causing beam damage: the higher the current density to more severe the beam damage. A field emission gun has a current density approximately three orders of magnitude higher than a LaB₆ crystal (Williams and Carter (2009) [39], Table 5.1, p.74). In order to reduce the current density, the smallest condenser apertures (40 and 20 μm for condenser aperture n. 3 and 4 respectively JEM 2200 FS, and 20 and 10 μm for the JEM 2011) and smallest spot sizes (~ 2 nm) were used at all

times. The disadvantage of these measures is reduced beam intensity and less contrast in the image. Both TEMs were operated at 200kV.

Bright Field and Dark Field imaging

Transmission electron imaging has two important modes, which can be employed by selecting between the transmitted/forward scattered and diffracted beams. By only allowing the non-scattered electrons to contribute to the image contrast, one images in *bright-field* (BF) mode (Figure 2.10A). The contrast in the image is a direct result of the changing amplitude of the transmitted beam due to absorption and scattering by the specimen.

For *dark-field* (DF) imaging the objective aperture is displaced so that the image is formed by a diffracted beam instead of the incident beam (Figure 2.10B). This figure shows how this would be achieved by shifting the position of the objective aperture. However, another way of achieving DF is by leaving the objective aperture aligned with the centre of the lens and tilting the incident beam so that the position of the diffracted beam aligns with the objective aperture. An advantage of this method is that the beam you are using to make the image goes through the centre of the lenses and is thus less affected by distortions.

The DF image thus shows which areas of the specimen are contributing to the diffracted beam, therefore providing an alternative to selected area diffraction as a means of correlating the diffraction pattern to the image [111] (p.295). This mode is predominantly used for defect analysis and allows for the determination of crystals of similar orientation in a polycrystalline material. The bright areas in a DF image indicate the areas in the specimen which contribute most to the selected diffracted beam, hence it tells you which areas in the specimen are aligned with that particular diffraction spot. For instance a *screw dislocation* would show some contrast in a BF image, but results in an apparent maximum or minimum under DF conditions.

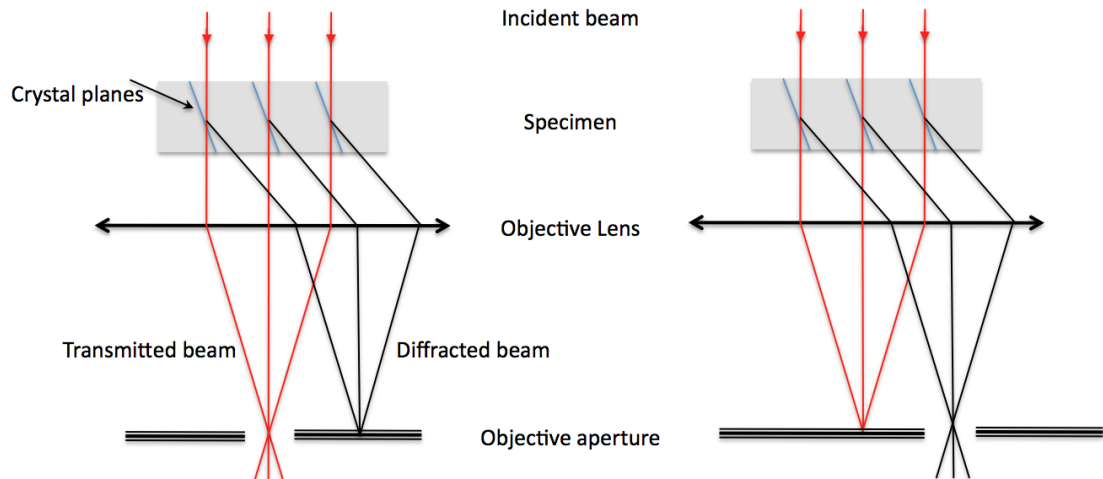


Figure 2.10. Left: *Bright-field* imaging mode; directly transmitted light contributes to the image contrast. Right: off-axis *dark-field* imaging mode; a diffracted beam is selected by using the objective aperture.

High-resolution transmission electron microscopy (HRTEM)

For HRTEM no objective aperture is inserted therefore multiple beams contribute to the image, creating a phase-contrast image instead of a diffraction contrast image. Generally, the greater the number of beams contributing to an image the higher the resolution [39] (p. 389). Phase-contrast images form as a result of the interference of non-scattered electrons with those that have had their phase altered by the crystal potential. Since this contrast is in fact the result of constructive or destructive interference at the image plane from multiple scattered beams the image cannot be directly related to the structure [113]. Furthermore, the image contrast is heavily dependent on specimen thickness and the defocus value. To directly interpret the image, contrast exit-wave reconstructions are necessary requiring a defocus series. However, the high sensitivity of the biogenic minerals and composites are detrimental to this approach since a defocus series at high-resolution will, even under optimum conditions, lead to modifications of the structure during the imaging due to beam damage.

HRTEM and TEM lenses are by no means perfect and suffer from aberrations due to the inhomogeneity of the magnetic field line distribution. As a result some frequencies above a cut-off given by the respective contrast-transfer function are not

transmitted to the imaging plane. The predominant source of aberration in an uncorrected microscope is *spherical aberration* and causes the spreading out of information from a single point, this is termed *delocalisation*.

Z-contrast HAADF STEM tomography (coccolith specimen only)

Z-contrast is the high resolution imaging of mass-thickness of a specimen. Mass-thickness contrast is formed by incoherent elastic scattering (Rutherford scattering) of electrons and is a strong function of the atomic number (Z) and the thickness of a specimen [39] (p.373). A high-angular annular dark field detector (HAADF) is used to detect electrons that have been diffracted under high angles (50-150 mrad or $\sim 9^\circ$), which means that no diffraction contrast (BF or DF) contributes to the image and the intensity of the beams is only dependent on the Z-value [39] (p.373, 379-381). Since the scattering coefficient of electrons scales with atomic number, heavier atoms will appear brighter in the image because they produce more scattering.

Scanning Transmission Electron Microscopy (STEM) does not use a broad parallel beam for illumination, but focuses the beam to a small spot. This spot is then rastered across the sample. Due to the different illumination method STEM allows the user to select much smaller areas of the sample to investigate when performing EDX or EELS than is possible with HRTEM.

STEM tomography was performed on an FEI Tecnai F30 operating at 300kV using a Fischione 2020 single tilt tomography holder and a HAADF detector. The tilt series was acquired using Xplore3D acquisition software at angular increments of 2° from -60° to $+60^\circ$ and 1° between $\pm(60^\circ$ to $70^\circ)$. Alignment and reconstruction were performed using the IMOD software package [114]. The tilt series was aligned using cross correlation and a patch tracking method before reconstruction using weighted back-projection. Visualization was performed using ImageJ and Avizo software. This experiment was performed as part of a collaboration project with Thomas Slater and Sarah Haigh of the School of Materials, University of Manchester.

TEM data analysis

In Abbe's theory the (TEM) specimen is assumed to act as a diffraction grating, coupled with the fact that coherent illumination will diffract from the condenser aperture. Therefore every point in the sample, together with all points in the aperture can contribute to the complex interference at all points in the image plane. To address this problem Abbe's theory models the lenses as a double Fourier transform of the specimen function. This Fourier transform enables us to access the reciprocal space. Subsequently *aperture*, *envelope* (i.e. the curve outlining the extremities in amplitude of a varying wave) and *aberration* functions are applied, after which the resultant Fourier is transformed again to obtain an image. The function, which describes the ability of the imaging system to transfer spatial frequencies from the object plane to the imaging plane, is known as the *contrast transfer function*.

The spacing between lattice fringes and the angle between intersecting lattice fringes is characteristic for the crystal structure. By taking a Fourier transform of an image of a crystalline structure we are able to access the spatial frequencies that make up the image and therefore the characteristic information relating to the crystal structure.

The Fourier transform

A Fourier transform expresses a function in terms of the individual frequencies that comprise it. In other words, it expresses a function in reciprocal units. For example, a *sine* wave described in terms of distance and amplitude would be described in terms of its frequency and intensity.

There are several different conventions when using the Fourier transform, we will use the one most commonly applied in crystallography, where the Fourier transform F of a function $f(\vec{\mathbf{R}})$ is defined as

$$F(\vec{\mathbf{G}}) = F[f(\vec{\mathbf{R}})] \equiv \int_{-\infty}^{\infty} f(\vec{\mathbf{R}}) e^{2\pi i \vec{\mathbf{G}} \cdot \vec{\mathbf{R}}} d\vec{\mathbf{R}} \quad \text{Eq. 7}$$

Where $\bar{\mathbf{R}}$ is the lattice vector and $\bar{\mathbf{G}}$ is the reciprocal lattice vector. The inverse Fourier transform F^{-1} is defined as

$$f(\bar{\mathbf{R}}) = F^{-1}[F(\bar{\mathbf{G}})] \equiv \int_{-\infty}^{\infty} f(\bar{\mathbf{G}}) e^{-2\pi i \bar{\mathbf{G}} \cdot \bar{\mathbf{R}}} d\bar{\mathbf{G}} \quad \text{Eq. 8}$$

Often the fast Fourier transform (FFT) algorithm is implemented. This is an example of the use of the discrete Fourier transform (DFT), as we can't use the continuous Fourier transform shown above for processing a set of images.

Diffraction

To obtain a diffraction pattern (DP) the back focal plane of the objective lens is projected onto the viewing screen instead of the image plane (Figure 2.7). By using a small aperture (Selected Area aperture) particular crystals or domains on a specimen can be selected to contribute to the DP.

Diffraction in TEM can be used to determine if the specimen is crystalline or amorphous, and what its crystallographic characteristics are such as lattice parameters and symmetry. For this study it is important to determine which polymorphs of CaCO_3 are present in a single specimen. Is the specimen single or polycrystalline? If it is not single crystalline, what is the grain size and morphology, and what are the crystallographic orientations and relations between the different grains or domains?

Diffraction spots appear when the electron waves are diffracted constructively by a set of parallel lattice planes with Miller indices hkl , when the path difference between waves diffracted by different planes is a multiple of the wavelength (λ). This condition is only met at a certain angle of the incident beam with respect to the crystal planes. This angle is called the Bragg angle (θ_B) (Figure 2.11). If this angle is not met the waves will interfere destructively and will cancel out so no diffraction spot will form.

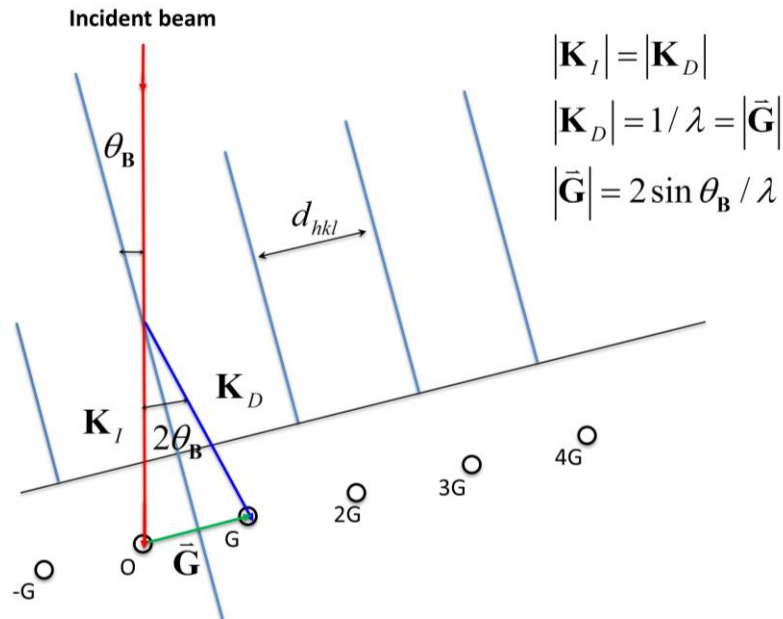


Figure 2.11. Diffraction from a set of crystal planes a distance d_{hkl} apart. The planes are orientated to fulfil the Bragg condition (θ_B is the incident angle). The vector $\bar{\mathbf{G}}$ from the origin O (000) to the first diffraction spot G (hkl) is normal to the diffraction plane (Image adapted from Williams and Carter (2009) [39] Figure 11.7, p. 202). See also appendix A.

To be able to analyse a DP it is important to tilt the sample into a (preferably low index) zone axis this requires the incident beam to be perpendicular to the reciprocal lattice plane. When the DP is close to zone axis orientation it will have equal illumination on all sides of the origin (O).

Data analysis

From the geometry of Figure 2.11 we can derive Bragg's law:

$$n\lambda = 2d_{hkl} \sin \theta_B \quad \text{Eq. 9}$$

Where n is an integer, λ is the wavelength, d_{hkl} is the lattice spacing of (hkl) and θ_B is the angle of the incoming wave with the lattice plane. The relationship between d_{hkl} and θ_B reflects that the closer the atomic planes are stacked, the greater the distance of the diffraction spots from the central beam-spot; hence this is a direct representation of the reciprocal or Fourier space. The positions of the diffraction

spots contain information about the size and shape of the crystal unit cell and its symmetry.

In order to understand and index electron diffraction patterns we use the concept of the reciprocal lattice. A crystal can be thought of as having two lattices: 1) the real lattice; the arrangement of the unit cells of atoms in the crystal, and 2) the reciprocal lattice; an array of points which is uniquely defined for any given crystal, where each point is associated with a particular set of planes in the crystal [39].

The reciprocal lattice vector \vec{G} is defined as:

$$\vec{G} = h\vec{a}' + k\vec{b}' + l\vec{c}' \quad \text{Eq. 10}$$

where h , k and l are the Miller indices and together define the plane (hkl) and $|\vec{G}| = 1/d_{hkl}$ which is normal to the set of lattice planes. \vec{a}' , \vec{b}' and \vec{c}' are the reciprocal base lattice vectors. This means that \vec{G} must be perpendicular to the zone axis

$$\vec{R} = u\vec{a} + v\vec{b} + w\vec{c} \quad \text{Eq. 11}$$

where \vec{a} , \vec{b} and \vec{c} are the base lattice vectors and \vec{R} is the lattice vector, with uvw an arbitrary triplet of integers (repetition of Eq. 1 in chapter 1).

By using a generalised dot product this gives

$$\vec{G} \cdot \vec{R} = 0 = uh + vk + wl \quad \text{Eq. 12}$$

High-symmetry structures are relatively easy to index, however for the orthorhombic and hexagonal systems it is useful to employ auto-indexing software for initial pattern identification. In this study we use JEMS [115]. With this software a custom crystal is generated, by using a set of well-established parameters. The experimental diffraction pattern is then compared to the model and thus indexed, see the section below.

From the diffraction patterns the growth orientation of the calcite nanowires, aragonite nanocrystalline bundles and coral crystals were determined by the following DP analysis method:

- 1) Determination of the zone axis by measuring the $1/d$ distances of the spots to the origin in the experimental pattern in ImageJ. Thus the possible known (hkl) planes for the calcite and aragonite crystal are found.
- 2) By calculating the cross product of two (hkl) planes a candidate zone axis is found. This can be entered into JEMS software and is directly compared to the experimental DP. When a match is found the experimental DP can be indexed.
- 3) The growth plane is then determined by superimposing the BF image of the nanowire, crystal needle or stack onto the DP. The longitudinal axis of the nanowire/needle/stack will cut through a row of diffraction spots which corresponds to the growth plane. Similarly, the coordinates of the centre of Laue circle placed along the length of the crystal nanowire/stack/needle corresponds to the growth plane.
- 4) The growth direction $[UVW]$ can then be calculated from the growth plane (hkl) by using the following equations [116] for calcite:

$$\mathbf{U} = 2h + k \quad \text{Eq. 13}$$

$$\mathbf{V} = h + 2k \quad \text{Eq. 14}$$

$$\mathbf{W} = l \left(\frac{3}{2} \right) \cdot \left(\frac{\mathbf{a}}{\mathbf{c}} \right)^2 \quad \text{Eq. 15}$$

Where \mathbf{a} and \mathbf{c} are the lattice parameters mentioned in table 1-1 in section 1.4.3 for calcite.

- 5) Then convert the $[UVW]$ to fourfold notation for the trigonal system.

$$(hkl) = (h, k, (-h - k), l) \quad \text{Eq. 16}$$

A full example of this method, starting from experimental DP and going through the analysis steps is shown in appendix A. Steps 4 and 5 are only applied to calcite, since aragonite is orthorhombic.

One important assumption we make while using this DP analysis method is that the calcite nanowires and aragonite crystal stacks are positioned perpendicular to the electron beam. Furthermore, it should be noted that there is an image rotation

of 6.5° between the BF-TEM image using magnification settings of 10-30 K and the DP for the JEOL 2011 TEM. This has been taken into consideration during the SAED analysis (see appendix A).

As well as the zone axis and growth direction determination, DP indexing with JEMS software enables the analysis of crystal tilt (vertical motion, out of plane), twist (rotation along the crystal longitudinal axis), and bending (horizontal motion, in plane around the zone axis) see Figure 2.12. This behaviour can occur within a single crystal rod, wire or needle, or within a stack of nanocrystals and will result in shifts in intensity distribution of the diffraction spots and rotation of the pattern, as illustrated by Figure 2.13. Tilting *in* and *out of plane* results in a shift or *opening up* of the Laue circle parallel to the longitudinal axis of the rod, whereas 'twisting' causes a shift along the perpendicular axis of the rod. 'In plane bending' results in the rotation of the diffraction pattern along the patterns origin ($O, 000$). The Laue circle is the intersection with the Ewald sphere, which is a geometric construct of a sphere with a radius of $1/\lambda$ passing through the origin (O) of the reciprocal lattice (see appendix A). When a crystal is in 'perfect' zone axis the centre of the Laue circle is at (000) or origin, and the intensity distribution in the diffraction spots is equal on all sides. However, when due to a change in crystal orientation (e.g. tilt, twist and/or bending) the Laue circle will shift its centre point outwards (i.e. way from (000)); the Laue circle's radius increases with the amount of deviation from 'perfect' zone axis.

Tilt, twist and rotation angles can be measured in absolute degrees from the diffraction patterns. They are systematically analysed by tilting the extremity of a crystalline rod or stack into zone axis and subsequently taking diffraction patterns along the length of the feature without further manual tilting of the specimen. Simulated diffraction patterns of aragonite in $[010]$ zone axis are shown in Figure 2.13 and demonstrate the effects of tilt and twist. The tilt is depicted with a large angle resulting in an 'opening up' of the Laue circle with diffraction spots along its circumference. The twist is shown with a relatively small angle resulting only in a shift of intensity of diffraction spots in the direction perpendicular to the rod's length axis.

Errors

The intensity distributions of diffraction spots in the experimental patterns are compared with simulated kinematic patterns [115] at different angles to obtain *twist* ($\pm 0.1^\circ$), *out of plane* ($\pm 0.1^\circ$) and *in plane* bending ($\pm 0.5^\circ$) for every recorded DP. The angles were then plotted as a function of the position across the nanowire long axis (Figure 4.11). The error in *in-plane bending* is larger as it is affected by lens aberrations. Errors in growth direction are estimated to be roughly $\pm 1.0^\circ$ and are minimised by performing repeats ($n=10$).

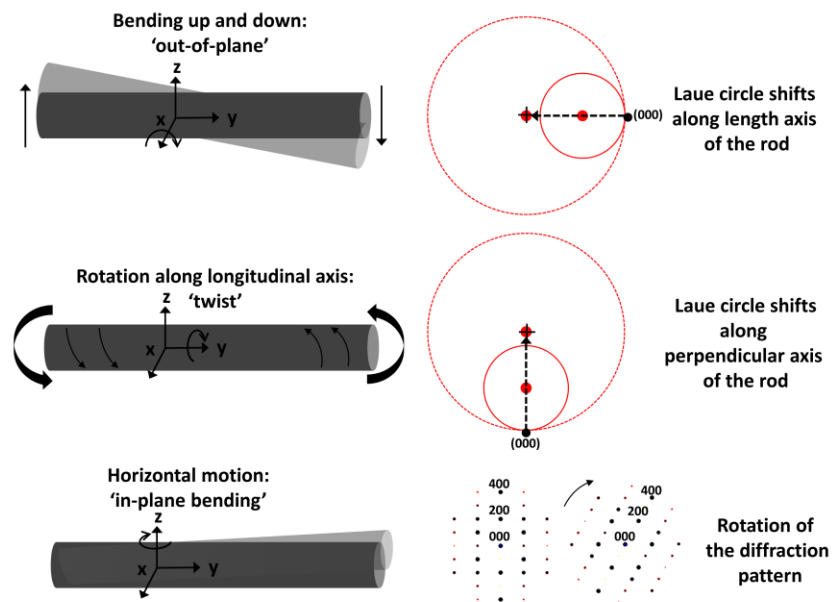


Figure 2.12 Schematic representation of the effect of crystal tilt, twist and bending on the position of the Laue circle in the diffraction pattern and the rotation of the diffraction spots. The beam orientation relative to the rods is along the z-axis. Diffraction spots will appear where the Laue circle intersects the Ewald sphere (appendix A), the larger the circle radius the further 'away' from zone axis a crystal is which results in an unequal intensity distribution of the diffraction spots relative to (000). The red dots indicate the centres of the Laue circles. See also Figure 2.13 below.

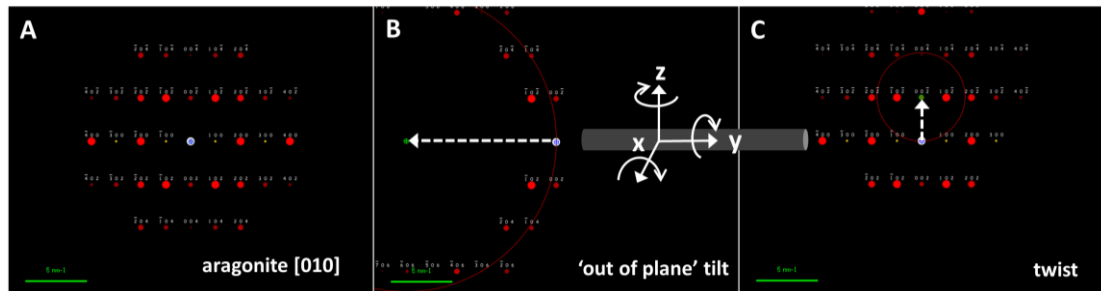


Figure 2.13 Series of simulated diffraction patterns for aragonite in [010] zone axis. A) In zone axis: the centre of the Laue circle is (000), equal intensity distribution of diffraction spots on all sides of the origin (000). B) Relative to A: a widening of the Laue circle, with the centre shifting along the length axis of the crystal rod, as would be caused by 'out of plane bending'. C) Relative to A: a widening of the Laue circle with a shift of its centre along the perpendicular axis of the crystal rod as would be caused by a twisting effect.

Analytical TEM: EDX and EELS

Analytical TEM can be performed in a regular TEM, but becomes more powerful and accurate in scanning transmission electron microscopes (STEM). In contrast to regular TEM, STEM uses a convergent beam that scans over the specimen. This intense beam can be used as a probe for analytical applications such as EDX and EELS and generates a higher signal that results in a better signal to noise ratio. A drawback of this method is the possible sample damage as a high intensity beam is concentrated on a very small specimen surface area. This can easily result in 'burning' holes through the sample and/or re-depositing carbohydrates (originating from the specimen itself or surrounding carbon grid) in and around the area of interest often referred to as contamination.

Energy dispersive X-ray spectroscopy (EDX)

Characteristic X-rays are generated when the incident electron beam excites an atomic inner shell electron, which is subsequently ejected from its shell, thus creating an electron hole. An outer shell (higher energy shell) electron falls back into the created electron hole. The difference in energy between the outer and inner shell is released in the form of an X-ray characteristic for that particular energy difference. This energy is electron-shell and element specific. For example, when an

electron from the M-shell falls back to an electron hole in the K shell (two shells difference), a $K\beta$ X-ray is emitted, whereas if an electron from the L-shell falls back to the K-shell (one shell difference) a $K\alpha$ X-ray is emitted.

Electron energy-loss spectroscopy (EELS)

Electrons with a narrow energy range (the incident beam) pass through a specimen and undergo inelastic scattering; they lose energy. Inelastic interactions include phonon excitations, inter- and intra-band transitions, plasmon excitations and inner shell ionisations.

The inner-shell ionisations are particularly useful for detecting the elemental components of a material. The electron beam emerging from the specimen can be passed through a magnetic prism (or an in-column omega filter), which causes the flight path of the electrons to vary depending on their energy, this can be observed in the energy dispersion plane and recorded by a CCD detector.

EELS data result in a spectrum showing particular ionisation edges and thus showing which elements are dominant in the targeted specimen area. Furthermore, the appearance of the ionisation edges, the 'fine structure', can be used to determine the phase of a particular material (e.g. amorphous, or crystalline polymorph discrimination). EELS is relatively slow (10s of seconds acquisition time) but has a high energy resolution (1-2eV).

Instrumentation

TEM samples were predominantly analysed at the York JEOL Nanocentre utilising a JEM 2011 (LaB₆ heated filament with an EDX detector for elemental analysis) and a JEM 2200 FS (field emission, double Cs aberration corrected with EDX detector for elemental analysis and an in-column omega filter for EELS and EFTEM) TEM operated at 200kV. The optimum resolution of the JEM 2011 is 1.94 Å (0.194 nm) and 1Å (0.1 nm) for the JEM 2200 FS in optimum conditions (JEOL instrument specifications).

Additionally TEM analysis was performed at the Centre for Microscopy, Characterisation and Analysis (CMCA) at the University of Western Australia using a JEM 2100 TEM (LaB₆ heated filament with an 11M pixel Gatan Orius digital camera and a Gatan Tridiem energy filter for EELS) operated at 120 and 200 kV and a JEM 3000 F FEGTEM (field emission with a 1M pixel Gatan 694 MSC digital camera and a Gatan GIF2000 energy filter for EELS and EFTEM) operated at 300 kV. The resolution under optimum conditions of this instrument is similar to the JEM 2011; 1.94 Å.

A word on statistics

An often problematic characteristic of TEM analysis is the lack of a representable sample population, or *poor statistics* due to the difficulties in preparing successful thin lamellae by FIB milling or other methods. In this study we obtained three high quality coral FIB lamellae (two adult and one juvenile specimen) as well as one thin lamella prepared by PIPS (adult specimen) during previous work by Elisabeth Brown. Although this is not a large number the TEM data could be directly correlated to features in SEM and optical images of which we have numerous (>20 per coral species; four tropical stony coral species are investigated from diverse localities including Western Australia, Indonesia, the Andaman and the Caribbean Sea) and thus be extrapolated with good certainty.

The coccolith TEM data originates from three TEM specimens, this did not involve FIB preparation, but deposition of singular coccospheres on TEM grids by micromanipulator. *R. clavigera* has been shown to have exact reoccurring crystal morphologies over a large collection of SEM images (>40) by this author and by Jeremy Young, comprising more than 50 *R. clavigera* coccospheres within the SEM image collection of the Natural History Museum London. This included specimens from diverse localities in the North and South Atlantic, Pacific Ocean, Caribbean, and the Mediterranean Sea. We are therefore confident that this study's TEM data set is representative for this coccolithophore species.

The synthetically prepared aragonite bundles and calcite nanowires had no preparation constraints as they are simply pipetted onto a TEM grid and dried, thus the sample population investigated here is much larger. The TEM data from the aragonite bundles involve three different batches of precipitated aragonite bundles matured over 1 hour, 4 hours and 4 months respectively, each TEM grid contained >15 crystal bundles. Lastly, over 40 nanowires (from 50 and 200 nm track-etch membranes) were investigated in detail using SAED.

Sample preparation

Coral specimens

To investigate the polyp-mineral interface the soft tissue of the polyp consisting of the calcicoblastic ectoderm, mesoglea and epidermis, is removed by immersion in fresh water, followed by mechanical brushing and drying. Besides adult specimen skeletal material of coral larvae is also investigated. For this purpose new coral recruits were cultivated in filtered seawater at 390 ppm and 750 ppm atmospheric CO₂ at 29°C at the aquaculture facilities, James Cook University, Australia. Corallite cross-sections of approx. 1 × 3 mm in size were cut from the cores perpendicular to the growth direction using a diamond cut-off wheel for TEM analysis (adult specimen only). The cross sections or complete larvae were then immersed in Gatan G1 epoxy resin and allowed to cure at 140°C on a hot-plate for 30 minutes to fill up the coral pores increasing the stability of the samples. The samples were manually polished down to approximately 50 µm thickness using diamond lapping pads (30 - 0.1 µm) and a tripod holder. Ultimately a bevel is applied, resulting in a sample edge thickness of approximately 20 µm. A molybdenum TEM slot is attached to the sample to provide structural support.

Focused ion beam milling

FIB lamellae are created on the thin polished sample edge using a FEI nova 200 Dual Beam FIB/SEM from the Leeds Electron Microscopy and Spectroscopy centre. The lamellae are created by applying the h-bar method: a platinum layer is

deposited at the edge of the coral sidewall, perpendicular to the general alignment direction of the acicular crystals related to the targeted COC. An approximately 15 x 30 μm lamella is then excavated with a 30 kV Ga⁺ beam. Bulk milling is performed at 20 nA after which cleaning cross sections are applied at 5 nA and 0.30 nA. The final polish is performed with a 10 kV beam at an angle of 3° at 50 pA. The lamella is milled down to a 100 nm thin section and no lift out is performed to retain specimen context as well as structural support (Figure 2.14).

Coccoliths

Coccoliths were caught at sea using a filter paper in water column system by Jeremy Young from The Natural History Museum in London. For TEM the specimen of interest were extracted from the filter paper with a glass needle attached to a manually controlled micro-manipulator under the optical microscope. Once on the needle the specimen is deposited on a TEM carbon film grid (200 μm mesh).

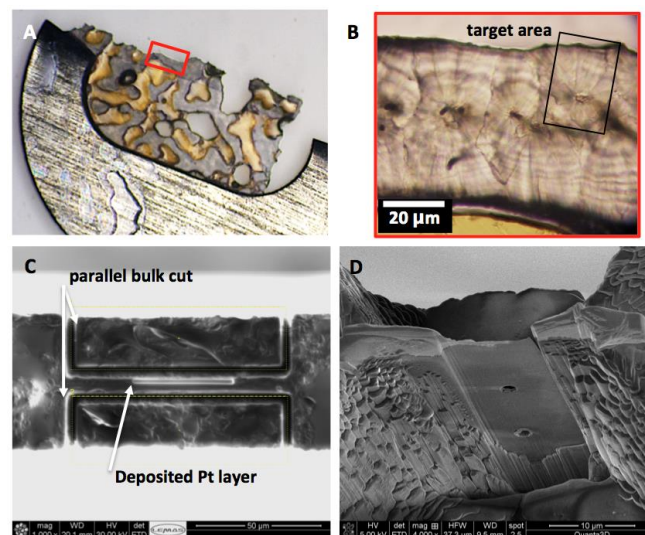


Figure 2.14. TEM sample preparation stages. A) Optical image of a manually polished coral thin section via the tripod method (see paragraph ‘Sample preparation-coral specimen’) attached to a molybdenum halfring. B) Optical image of the thin sample edge and targeted area for FIB milling. C) Top view SEM image of the thin edge in an early stage of the FIB milling process. D) SEM image of completed FIB lamella.

Calcite nanowires

Yi-Yeoun Kim from the Leeds University, School of Chemistry, grew the calcite nanowires in confinement from ACC. By rehydrating the nanowires in an eppendorf tube with ethanol we could pipette a droplet onto lacy carbon TEM grids (200 μm mesh) leaving it 2-3 minutes to dry in air.

2.2.3 SCANNING ELECTRON MICROSCOPY

A Scanning Electron Microscope (SEM) has the great advantage of having a large depth of field and being able to obtain elaborate surface information at higher magnifications compared to a light microscope. Furthermore, an SEM can analyse large surface areas, which is often a very useful primary step in any investigation of a new specimen.

In SEM the electron beam is focussed on the sample instead of illuminating it with a parallel beam as in a TEM. The electrons from the focussed beam interact with the atoms in the specimen and are scattered either elastically or inelastically. With elastic scattering the electron path changes, but it loses little, if any energy. Alternatively, inelastic scattering causes the incident electron to change its kinetic energy and velocity, but its path is only moderately altered. This is caused by interaction with orbital electrons of the atoms of the specimen. Inelastic scattering causes a range of signals: Secondary Electrons (SE), Backscattered Electrons (BSE), Cathodeluminescence (CL), continuum X-ray radiation (bremsstrahlung), characteristic X-ray radiation and phonons (heat) (Figure 2.15).

The two main signals we use in the SEM are SE and X-rays. The latter is used for elemental analysis and has been discussed previously (see paragraph 3.1.2 section on EDX). Secondary Electrons are generated when an incident electron beam penetrates the surface of a specimen and interacts with atomic electrons. The atomic electrons that are knocked out of their orbit and leave the specimen are collected by a detector and are used to form the image.

Atmospheric scanning electron microscope (ASEM)

A particular powerful tool in our studies of bio-mimetic materials is the atmospheric SEM. In regular SEM and TEM instruments all specimen are by definition kept under conventional vacuum and are dry. Understandably, this is not a good comparison to real life biomineralising systems that precipitate their exoskeletons in an aqueous environment at atmospheric pressures.

The JEOL ClairScope offers the possibility to fulfil both these requirements, as samples are precipitated *in-situ* from aqueous solutions under atmospheric conditions. Electron beam imaging is performed in real time through a thin SiN window situated at the bottom of the ClairScope petri dishes (Figure 2.16). With this setup we investigate the nucleation and growth of calcite, vaterite and aragonite crystals from oversaturated solutions in the presence of different organic additives, especially ethanol.

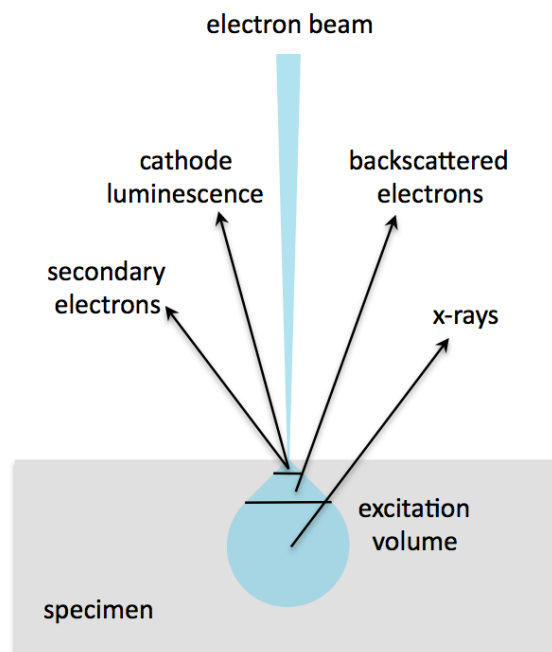


Figure 2.15. The different signals generated in an scanning electron microscope by inelastic scattering processes and their relative origins in the sample volume.

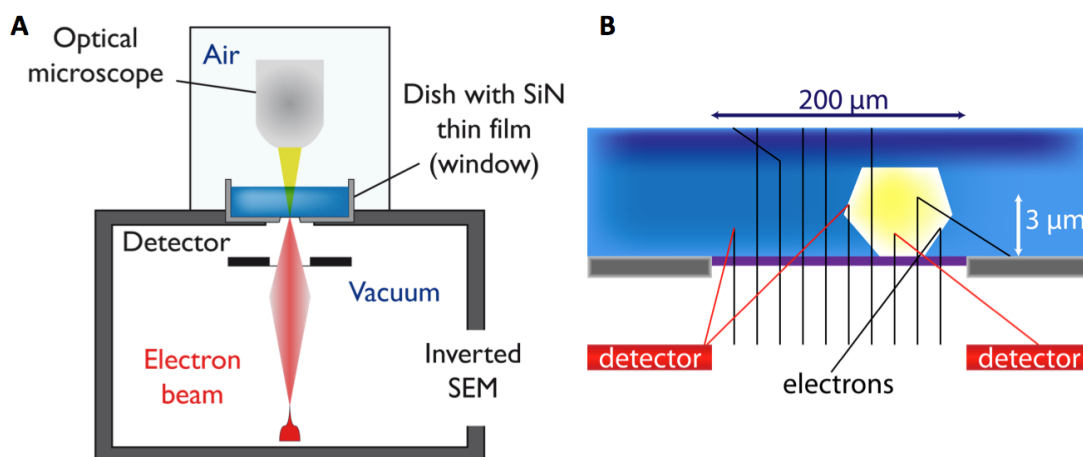


Figure 2.16. Schematic drawing of the ASEM. A) Instrumental setup with an inverted electron beam combined with a regular optical microscope. Samples are situated in a dish in liquid environment with a SiN window. B) Detail of the SiN window and approximation of the electron detection limits in water due to scattering at 30 kV of 3 μm . Images by courtesy of Andreas Verch.

Instrumentation

In this study a FEI Sirion S-FEG FESEM (field emission, high resolution SEM) was used at the York JEOL Nanocentre and operated at 5 kV for imaging and 12kV for EDX analysis. This instrument is coupled with a Noran EDX system which uses an Oxford INCA analysis system and a 30 mm 2 light element Silicon-Lithium (SiLi) detector. The resolution of this microscope under optimum conditions is < 2 nm (FEI instrument specifications) but in practise a 5 nm resolution is more common (E. Boyes, personal communication).

The ASEM is a JEOL JASM-6200 ClairScope, operational at 10, 20 and 30 kV with a high sensitivity colour CCD, combined with an Olympus optical microscope (40x liquid immersion lens). The optimum resolution of the ASEM in dry conditions is 8 nm (JEOL instrument specifications), however in liquid the best achievement has been found to be distinguishable 20 nm gold beads (I.E.G.Morrison, personal communication). This instrument is made available to us by the Bioscience Technology Facilities of the University of York, by courtesy of Peter O'Toole.

Sample preparation

Specimen preparation for SEM is usually much quicker and less involved as compared to TEM specimen preparation as the samples need not be electron transparent. Since there is a limit to the depth of field and we are interested in the cross section perpendicular to the growth direction of coral skeletons, a bulk cut followed by polishing is performed to a thickness of approximately 100-200 μm using the tripod polishing method, but without applying a bevel. This particular thickness range makes the specimen light transparent, which enables us to combine transmission optical microscope data with surface SEM data.

Specimens are subsequently lightly etched with deionised water (coral larvae) and dilute acetic acid-water mixture (adult coral specimen) to reveal the microstructure. Biogenic samples are routinely treated with a sputter coater (carbon or Pt/Pd 5 nm coating) to reduce charging effects [39].

ASEM specimens

Calcite, vaterite and aragonite crystals are precipitated *in-situ* from 5 ml 0.1 M Ca^{2+} (CaCl_2) and 5 ml 0.1 M CO_3^{2-} (Na_2CO_3) solutions in 15-35% ethanol-water mixtures. The liquid phases can be inserted by manual syringe injection into the ClairScope petri dishes or via a syringe pump mechanism at determined flow rates. In this study the Ca and CO_3 solutions are premixed, shaken 5x by hand and left to stand for 1-5 hrs, after which it is introduced to the petri dish. The petri dishes are pre-treated by plasma cleaning to augment its hydrophilic properties, to increase probability of crystal nucleation directly onto the SiN window to improve electron imaging.

2.2.4 RAMAN MICROSCOPY

In certain biomineralising organisms more than one polymorph of CaCO_3 has been recorded by Raman spectroscopy analysis [117]. Often these findings challenge earlier optical and SEM based work, as it is difficult to distinguish between calcite, aragonite and vaterite on appearance alone. It could be argued that such information can be easily derived using TEM diffraction analysis, however sample preparation for Raman spectroscopy is much quicker and simpler and allows in addition to cover much larger specimen areas in a short time span. Furthermore, Raman spectroscopy enables us to localise areas within the mineral phase with high organic content as this results in an elevated fluorescence or background signal.

Raman Microscopy has the capability of obtaining analytical quality Raman spectra with a $1\ \mu\text{m}$ spatial resolution [118]. In Raman spectroscopy we use the scattering of monochromatic light, often produced by a laser, by matter. Raman enables us to study the vibrational modes, called phonons for crystal lattice vibrations, and is based on inelastic scattering (Raman scattering) of the incident laser photons. As the laser beam interacts with the electron cloud and the bonds of the molecules in the specimen, a photon can gain a discrete amount of energy due to annihilation of a phonon or molecule vibration, this is called anti-Stokes Raman scattering (Figure 2.17). More common is the loss off of energy due to the creation of a phonon or molecule vibration called Stokes Raman scattering (Figure 2.17). The change in energy between an incident and scattered laser photon corresponds exactly to the energy of the involved phonon. This result in an energy shift between the laser photons and the scattered photons and is characteristic for each chemical species, as it is dependent on the mass of the atoms in the specimen as well as their binding strength and coordination [119]. Stokes Raman scattering causes the wavelengths to increase, whereas anti-Stokes Raman scattering causes a wavelength to decrease. This shift is expressed by the Raman shift in wavenumbers

$$\Delta\tilde{\nu}(\text{cm}^{-1}) = \left(\frac{1}{\lambda_0(\text{nm})} - \frac{1}{\lambda_s(\text{nm})} \right) \times 10^7 \quad \text{Eq. 17}$$

where $\Delta\tilde{\nu}$ is the Raman shift, λ_0 is the incident beam wavelength and λ_s is the scattered beam wavelength.

$$\Delta\tilde{\nu} = \nu_0 - \nu_m \quad \text{Eq. 18}$$

$$\Delta\tilde{\nu} = \nu_0 + \nu_m \quad \text{Eq. 19}$$

Equations 15 and 16 show the formulas for the Stokes and anti-Stokes lines respectively, where ν_0 is the frequency of the incident beam and ν_m is the vibrational frequency of a molecule.

Fluorescence

Sample impurities and/or organics can absorb the laser radiation and reemit it as fluorescence; it can be as much as 10^4 greater than the Raman signal. Fluorescence occurs when electrons in a molecule are excited to a discrete electronic state, instead of a virtual level, and decay to the lowest vibrational level through radiation-free transitions and then emit radiation as photons [118]. This reemitted light is of lower energy, and thus longer wavelength than the laser light, because of the decay through radiation-free transitions before photon emission. Organic compounds often contain fluorophores, this can be a hindrance as it may interfere with the Raman peaks, or it can be used to map the spatial distribution of this non-mineral fraction, which may contain important structural information.

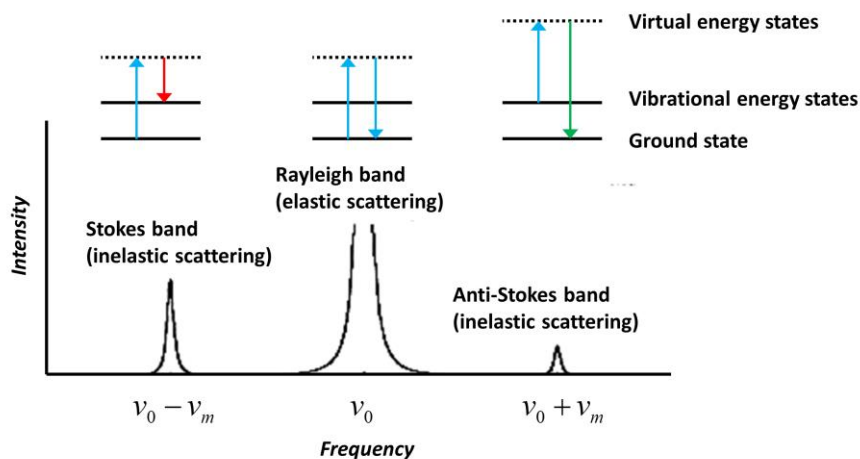


Figure 2.17. Spectrum of photon transition from ground state to virtual levels.

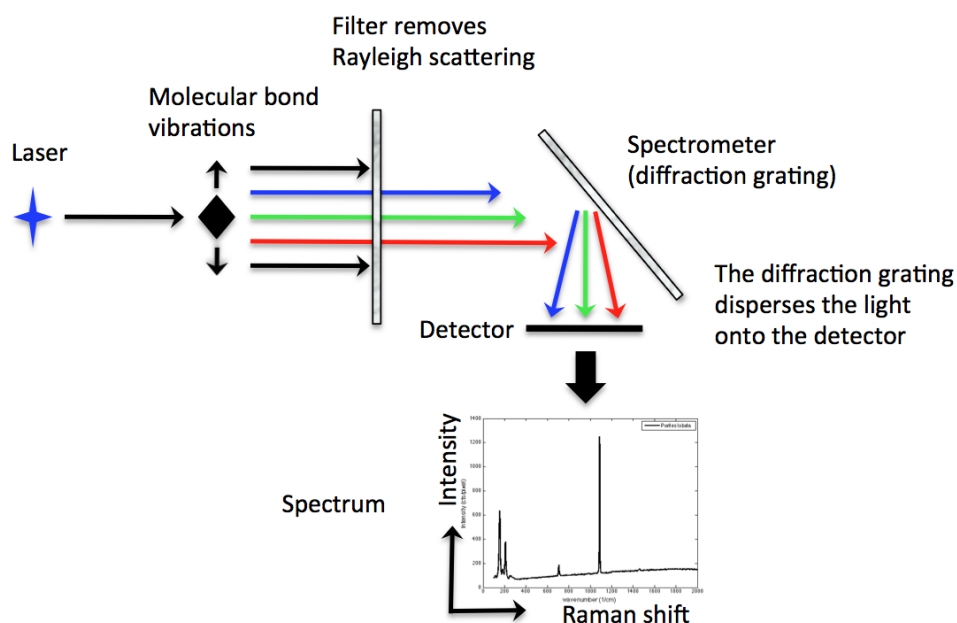


Figure 2.18. Schematic representation of the experimental setup of the Micro-Raman spectrometer. The filter removes elastically scattered light, this signal can be up to 10^6 larger than the Raman signal. The spectrometer or diffraction grating disperses the light onto a detector creating a spectrum of Intensity (counts/pixel) versus the Raman shift in wavenumber (cm^{-1}).

Raman peaks in calcium carbonate structures

In mineral carbonate structures there are two main sub-units that cause vibrational modes resulting in specific Raman peaks: the isolated CO_3^{2-} groups or ‘molecular carbonate ions’ and the crystal unit cell symmetry (e.g. calcite or

aragonite crystal unit cell) [31]. The ‘free’ CO_3^{2-} ion has several vibrational modes, the most characteristic ones being the symmetric stretching mode (ν_1) and the in-plane bending mode (ν_4) (Figure 2.20). Furthermore characteristic ‘lattice modes’ are caused by vibrational modes of the crystal unit cell configuration.

The Raman peaks characteristic for calcite and aragonite are depicted in Figure 2.21, although some peaks are common to both structures, several distinct peaks make it relatively easy to distinguish them. Depending on the instrument used, the local conditions (i.e. temperature) and the provenance of the specimens, small spectra shifts ($\pm 5 \text{ cm}^{-1}$) can occur between datasets of different research groups, but the general succession of peaks or ‘fingerprint’ should be identical for each mineral type or organic compound.

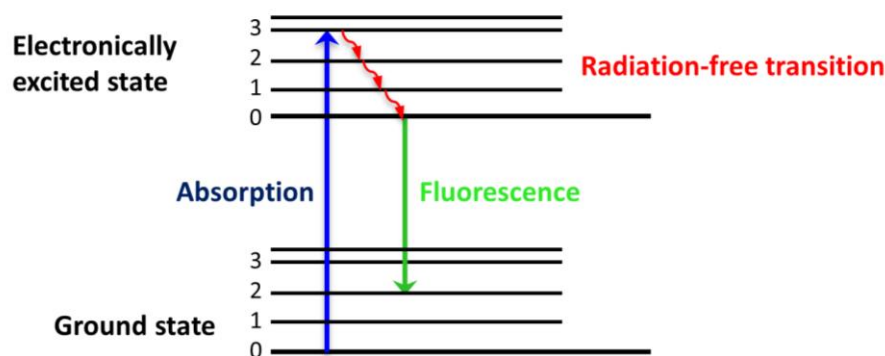


Figure 2.19 Jablonski diagram for the occurrence of fluorescence.

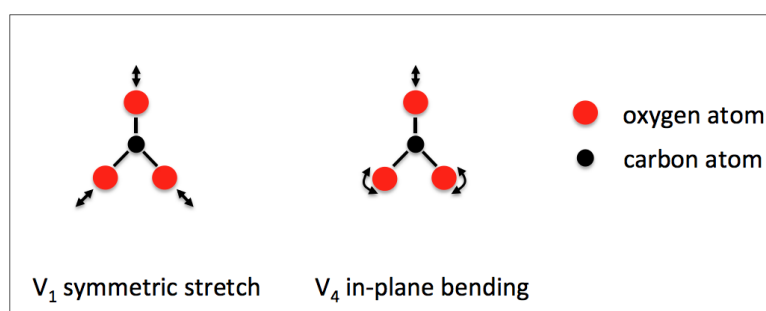


Figure 2.20 Schematic 2D representation of the carbonate ion and two of its characteristic stretching modes that result in specific Raman peaks.

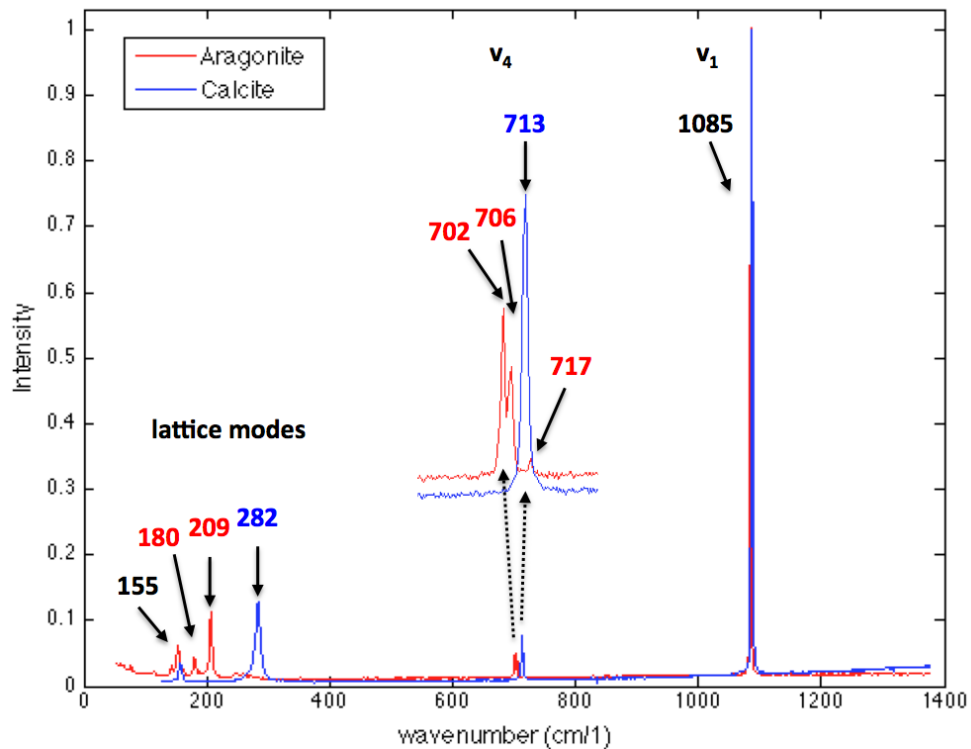


Figure 2.21 Raman spectra from geological calcite and aragonite mineral, the intensity is in arbitrary units. Numbers indicate Raman peaks, red for aragonite, blue for calcite and black for shared peaks. The data was obtained from the free online reference database 'Handbook of Raman spectra' of the Laboratoire de géologie de Lyon, ENS-Lyon, France.

Instrumentation

The Micro-Raman system of the Physics department of York University consists of an Horiba XPLORA Raman spectroscope (1 μm in XY and $< 2\mu\text{m}$ in Z spatial resolution) with three available lasers and correlated filters (532 nm, 638 nm and 785 nm) in combination with an Olympus BX41 Optical microscope (10x, 50x and 100x objectives) and a CCD (1650x200) camera. The spectral resolution of the instrument is approximately 0.8 cm^{-1} wavenumber using the 1800 grating (derived from experimental findings and personal communication with K. Chatzipanagis (Department of Physics, University of York) and T. Jones (Horiba Scientific, UK)).

Data acquisition conditions

The Raman point spectra acquired from coral mineral specimen were taken with a 532 nm laser and a 50 x objective lens for 2-5 seconds acquisitions time, with 5 to 10 repeats per spectra to minimise the error ($\pm 1 \text{ cm}^{-1}$). The use of the green laser was preferentially selected because although Raman peak position is not dependent on excitation wavelength, the scattering intensity is inversely proportional to λ^4 , therefore the 532 nm laser generates a stronger Raman signal than the 633 and 785 nm lasers [120].

The filter was set to 10 - 25% to reduce local heating which can cause sample damage, the grating to 1800 (grooves/mm), the hole to 100-300 (μm) and the slit to 100 (μm), to obtain the best signal to noise ratio. A typical data range of 150 - 3000 cm^{-1} was acquired. Mapping was performed using the same general settings, but with 1 second acquisition time and 2 repeats per data point, with distance increments of 0.1 - 0.5 μm in x and y direction.

Organic material extracted from demineralised coral skeleton was analysed via point spectra measurements with 532 and 638 nm laser frequencies, the 100x objective lens for 10 seconds with 5 repeats per spectra. The filter was set to 25%, the grating to 2400 (grooves/mm), the hole to 100 (μm), and the slit to 100 (μm). A data range of 200 - 3800 cm^{-1} was explored.

Sample preparation

Mineral specimens

The sample preparation is equivalent to that described for SEM in paragraph 3.1.3. Although for Raman spectroscopy we do not perform the etching step, as a polished surface is required. Raman spectroscopy has a very small depth of field and thus cannot perform well on highly topographic samples.

Organic specimens

Organic residue is extracted from coral skeletal material to analyse the Raman signal. The coral skeleton is first treated with bleach (sodium hydroxide) to remove external debris after which the mineral is gently dissolved in EDTA.

Dissolution protocol:

- powder the coral sample (mortar & pestle): 20-30 mg coral powder
- bleach with 1 M NaOH for 2 hrs on rotation wheel/gentle shaker (50 μ l/mg sample)
- centrifuge and rinse 4x with ultrapure water
- add 50 μ l/mg sample 0.5 M EDTA (pH 7.8)
- vortex, leave overnight
- vortex if not dissolved, leave again for 12 hrs
- repeat until fully dissolved

To separate soluble-insoluble:

- centrifuge 15min 4000 rpm
- filter using a Whatman 90 mm Φ filter paper

Work under sterile conditions: between two open flames, using sterile equipment.

2.2.5 REVERSE PHASE HIGH PERFORMANCE LIQUID CHROMATOGRAPHY

In this study we want to investigate the compounds present in the organic fibres, (containing proteins) which are observed in coral skeletons and are thought to play an important role within the biomineralisation process. By performing RP-HPLC analyses on the extracted organic fraction we investigate its amino acids composition, and what their absolute and relative concentrations are in three different species of adult Scleractinian corals.

Liquid chromatography is the separation of mixtures by passing an analyte dissolved in a *mobile phase (eluent)* through a solid *stationary phase*, separating the different components on the basis of their differential affinities with the phases. The

partitioning coefficients of the different compounds are essential as they result in different retention times on the stationary phase. Quantification of the concentrations of the different analytes is achieved by calibration with known-concentration standards. Reverse - phase chromatography uses a non-polar stationary phase, 'a non-polar column', and a polar mobile phase, 'a polar solvent', with a gradient from more polar to less polar. Therefore, more polar compounds are eluted first as they have higher chemical affinity with the polar mobile phase. In general, compounds are eluted as a function of their mass, hydrophobicity and structure.

RP-HPLC analysis and instrumentation

This study adopts a modified analytical method of Kaufman and Manley (1998) [121] for an automated system of RP-HPLC, described in Penkman (2005) [122].

This has been developed for the separation of chiral amino acids, i.e. D- and L-amino acids, and therefore uses a derivatisation step, but in this study L' and D-enantiomers were considered together for the calculation of the concentrations. The derivatisation of the enantiomers is performed automatically (and prior to the injection of the samples in the analytical column) by mixing online a solution volume of 2 μL of sample with 2.2 μL of derivatising reagent (260 mM N-Isobutyryl- L-cysteine (IBLC), 170 mM o-phthaldialdehyde (OPA) in 1 M potassium borate buffer, adjusted to pH 10.4 with KOH).

The resulting enantiomeric derivatives are then separated on Hypersil C18 BDS column (sphere d. 5 μm ; 5x250 mm) at 25°C, using a linear gradient of three solvents: sodium acetate buffer (23 mM sodium acetate try-hydrate, 1.3 μM Na₂EDTA, 1.5 mM sodium azide, adjusted to pH 6.00 \pm 0.01 with 10% acetic acid and sodium hydroxide), methanol and acetonitrile on an integrated Agilent 1100 liquid chromatograph (Agilent, USA). This gradient allows the elution time to be kept below 120 minutes.

The separated amino acids are then detected by the fluorescence detector (Ex = 230 nm, Em = 445 nm) and each elution is recorded as separate peaks on a chromatogram. Under the conditions used the area under each peak is directly proportional to the concentration of the amino acids, which is then normalised to the internal standard (L-h-Arg). The technique allows detection in the sub-picomole range: Kaufman and Manley (1998) [121] found that the limit of quantifiable detectability was as low as 0.1 pmol.

Ten amino acids (D and L- isomers) were routinely analysed (in order of retention time): aspartic acid (L-Asp, D-Asp), glutamic acid (L-Glu, D-Glu), serine (L-Ser, D-Ser), threonine (L-Thr), histidine (L-His), glycine (Gly, which co-elutes with D-Thr and D-His), arginine (L-Arg, D-Arg), alanine (L-Ala), L-homo-arginine (LhArg; internal standard), D-Ala, tyrosine (L-Tyr), Valine (L-Val), methionine (L-Met, D-Met), D-Val, phenylalanine (L-Phe), isoleucine (L-Ile), D-Phe, leucine (L-Leu), D-Ile and D-Leu. During preparative hydrolysis both asparagine and glutamine undergo rapid irreversible deamination to aspartic acid and glutamic acid respectively [123]. It is therefore not possible to distinguish between these acidic amino acids and their derivatives and they are reported together as Asx and Glx. It is also important to note that some common amino acids like cysteine have the tendency to rapidly degrade and are thus often undetectable.

Quantification of individual amino acids was achieved by comparison with the standard amino acid mixtures. External standards containing a variety of D- and L-amino acids were analysed at the beginning and end of every run, and one standard was analysed every ten samples. This provides a reference for the identification of the individual compounds on the chromatograms. Procedural blanks were randomly interspersed amongst the samples. A schematic of the HPLC setup is shown (Figure 2.22).

Sample preparation

In order to analyse separate amino acids the peptide bonds must be hydrolysed, this is achieved by adding 7M HCl and leaving the sample at high

temperature for a certain amount of time. However, prior to hydrolysis two sample pre-treatments have been performed to compare different portions of the coral skeletal organic matter and to evaluate the effect of pre-treatment protocols on the RP- HPLC results.

Pre-hydrolysis treatments

- 1) Bleaching: removal of surface organics and analysis of the organics directly associated with the skeletal crystals [124]: 50 mL 12% NaOCl (l) per mg of powdered coral sample was added at room temperature. The powders were left to soak for 48 hours, and vortexed after 24 hours to ensure complete penetration of the bleaching agent.
- 2) Dissolution of the mineral skeleton in a weak acid under a light microscope and manual isolation of the organic fibres with the aide of vacuum tweezers. Via this method the RP-HPLC analysis is focussed on the large isolated organic fibres or 'inter-crystalline organics' that can be seen protruding from COCs in the coral skeleton (see section 3.1.2).

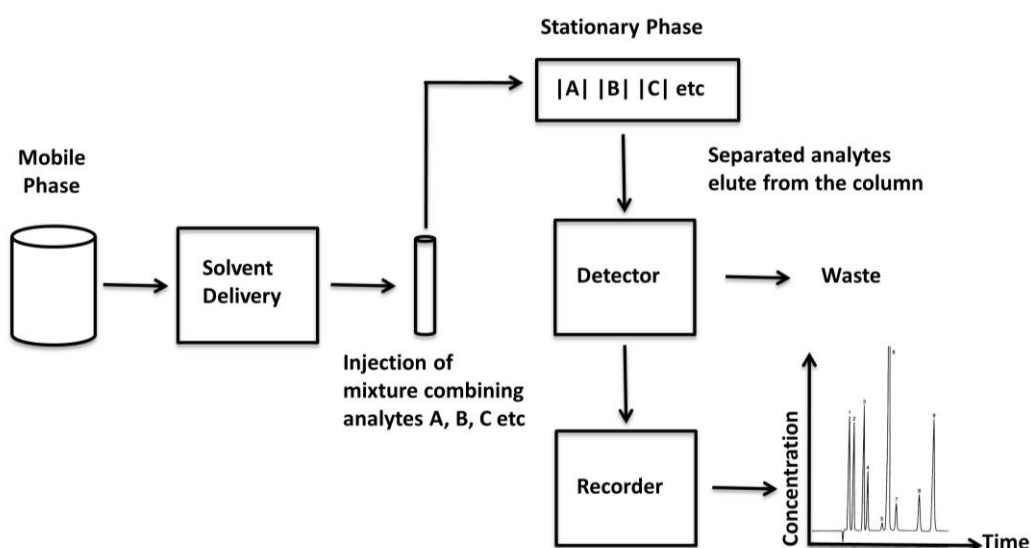


Figure 2.22. Diagram depicting the general features and setup of a HPLC instrument with chromatograms as data output showing concentration of amino acids (pmoles/mg of sample) versus retention time (s).

Hydrolysis is achieved by the following steps:

- 1) Add 7M HCl (20 μ L per mg powder).
- 2) Flush the samples with N₂ (g) minimise oxidation.
- 3) Place in an oven at 110°C for 24hrs.
- 4) Dry the samples in an evaporator centrifuge for 24hrs.
- 5) Rehydrate with L-homo arginine (LhArg, internal standard) rehydration fluid and vortex.

3. ARAGONITE BASED MINERALS

Characterisation and interpretation

In this chapter the crystal structures of two aragonite systems will be described based on experimental results. The microstructure of aragonite based Scleractinian corals will be discussed. Subsequently the results from the analysis of aragonite bundles precipitated in the presence of ethanol will be presented. In the last part of this chapter the observations in both systems will be discussed in comparison.

It was found that the smallest building blocks in the coral skeleton, the *spherulites*, consist of three distinct crystal morphologies. At the centre of calcification (COC) there is a porous and disordered granular crystal phase, this is followed by stacks of regular sized nanocrystals grown preferentially in [001] direction. Subsequently a transition into large single crystal acicular needles occurs, which consistently grow in the [001] direction and radiate outwards. This succession in microstructure could for the first time be directly correlated to a diurnal growth pattern induced by the photosynthetic zooxanthellae that live in symbiosis with the coral and provide its host with nutrients. It was also shown that organic material is especially concentrated at the COC and that it does contain protein bundles, although not all organic components could be positively identified.

Following the synthetic calcium carbonate precipitation experiments (in collaboration with Karina Sand of the University of Copenhagen), this author and Andreas Verch (University of York, Department of Physics) found that aragonite in the form of sheaf-shaped bundles of crystalline needles precipitate preferentially in

comparison to calcite and vaterite at high ethanol (25-50 vol%) concentrations. With less ethanol (≤ 15 vol%) the dominant crystal phase is expressed as calcite {104} rhombohedra.

The aragonite needles in the sheaf-shaped bundles are up to tens of microns long, sometimes hexagonal in shape and have a segmented surface. They consist of stacks of nanocrystals, with individual grains of 100 to 150 nm in size and grow in the [001] direction, very similar to the stacked crystal phase in the coral.

It is suggested that OH-group containing organic additives, such as sugars, proteins and ethanol, drives the crystallinity towards polycrystalline, branching morphologies and that it may promote and/or stabilise certain crystallographic facets.

3.1 MICROSTRUCTURE OF CORAL SPHERULITES

The stony coral aragonite skeleton is hierarchically ordered from the nanometre to the macroscopic scale. This has frequently been observed in other biominerals [11]. It is generally accepted that the fundamental structure of the aragonite coral skeleton consists of bundles of needle-like or acicular crystals situated around a 'centre of calcification' (COC) [125, 126] or 'early mineralization zone' [127, 128] forming a three dimensional fan-like structure or *spherulite* [4], as discussed in paragraph 2.1.1, and as shown in Figure 3.1 and Figure 3.2.

The two main substructures within a spherulite are [68, 125, 126, 129]; 1) a centre with granular aragonite submicron crystals (the COC), and 2) aragonite crystal needles radiating from this centre. Furthermore radial contrast bands have been observed by optical microscopy investigations within spherulites and have been interpreted as daily growth bands (Figure 3.3A) [130, 131].

A subset of the data presented in this section was published in Van de Locht *et al.*, (2013) [132].

3.1.1 THE MINERAL FRACTION

SEM investigation of etched coral specimens confirms the findings of these earlier studies. Figure 3.1 shows the spherulites found in a *Porites lobata* and Figure 3.2 shows a spherulite in *Siderastrea Siderea*. The centre consists of granular crystals, followed by elongated crystals radially arranged around the central granular area which are limited in extension by adjacent spherulites.

TEM analysis of a thin FIB lamella of a spherulite in *Porites lobata* shows three crystallographically distinct regions, which can be correlated to the above-mentioned morphological substructures (Figure 3.3 and Figure 3.4):

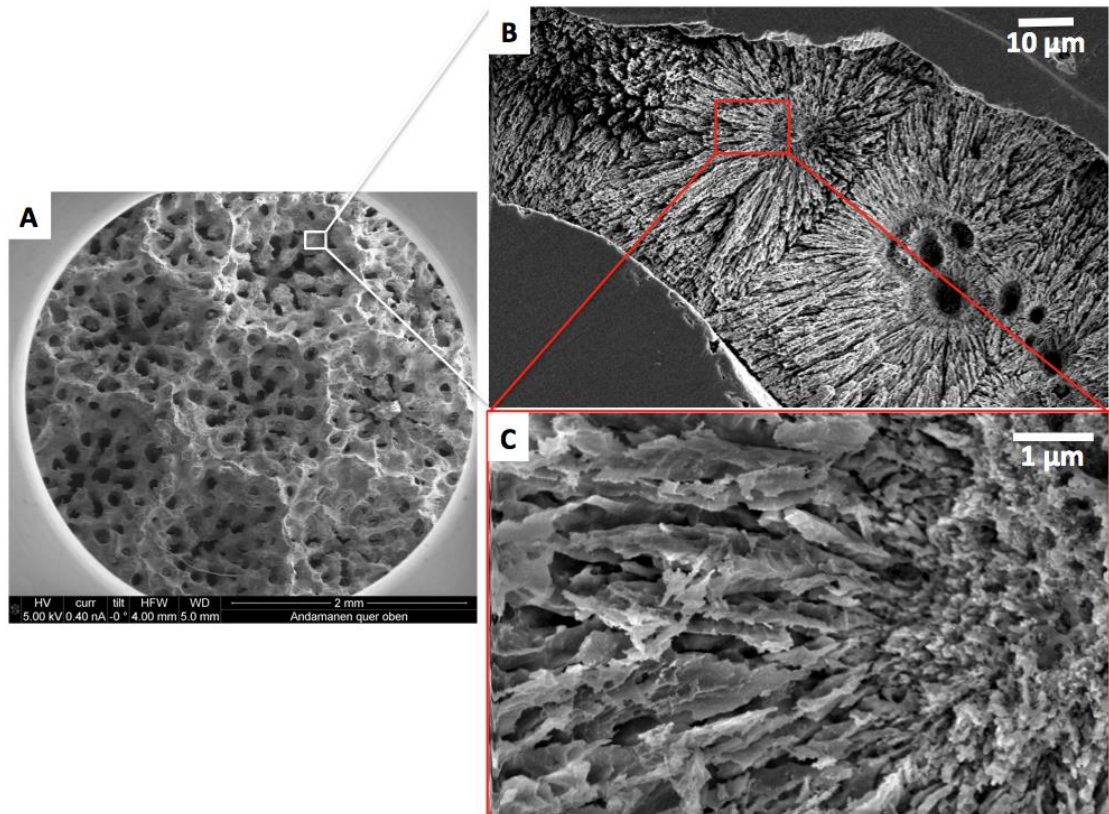


Figure 3.1 SEM micrographs of *Porites* sp. A) Macroscale overview of the coral surface with the live membrane removed by submersion in fresh water and manual brushing. The individual former polyp locations are visible. B) Detail of *P. lobata* etched cross section, showing individual spherulites around COCs. C) Close-up of part of a spherulite with granular crystal morphology at the centre followed by large elongated crystals fanning out towards the edges where they meet neighbouring crystal bundles.

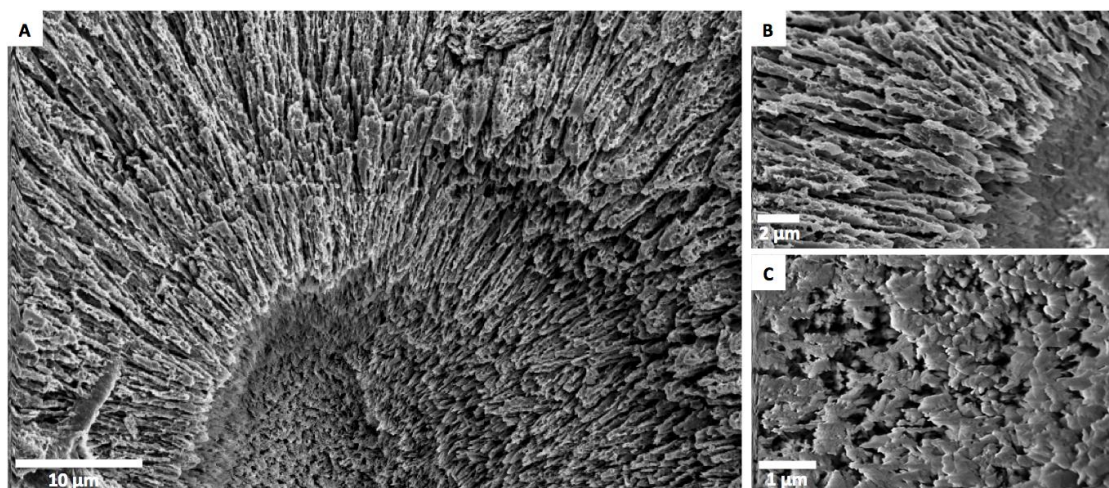


Figure 3.2 SEM micrographs of an etched *S. siderea* specimen. A) Part of a spherulite, where the etching process reveals several bands, showing up as 'steps' within the acicular crystal areas. B) Acicular crystals. C) Granular crystals from the COC.

- 1) Randomly orientated nanocrystals of 50 – 100 nm in size with high intergranular porosity. This crystalline type is found directly at the centre of the spherulite, the COC.
- 2) Partly orientated nanocrystals of 50 - 70 nm in size forming stacks with high porosity between individual stacks. This crystalline type is positioned adjacent to the randomly orientated nanocrystals and within the dark 'daily' contrast bands.
- 3) Densely packed large acicular crystals with diameters of approximately 300 - 500 nm and several μm in length, fanning out of the COC creating the spherulitic appearance. The acicular phase is found 'growing out' of the stacked nanocrystalline phase and is again interrupted by this nanocrystalline type of morphology forming the next granular band.

The different morphologies within the spherulite could be directly correlated with optical transmission images, showing that the nanocrystalline areas are correlated to the dark regions indicating COCs and the subsequent dark contrast bands (Figure 3.3). Enhanced light scattering in the porous nanocrystalline parts causes this dark appearance, whereas the 'light' bands are directly correlated to the densely packed large acicular crystal regions.

As mentioned earlier, the dark-light optical contrast bands occurring in spherulites are thought to be diurnal growth bands. From these results it follows that the diurnal growth cycle is clearly expressed at the nanoscale with a systematic change in crystallographic morphology.

At the centre of the targeted spherulite, the optical image shows a feature which appears as a round-shaped hole in the TEM micrograph. From optical, SEM and Raman data it is concluded that the COCs contain a high density of soft organic material which is very sensitive to beam damage and thus is preferably removed during the ion milling process. The organic inclusions in the coral aragonite mineral will be discussed in detail in paragraph 3.1.2.

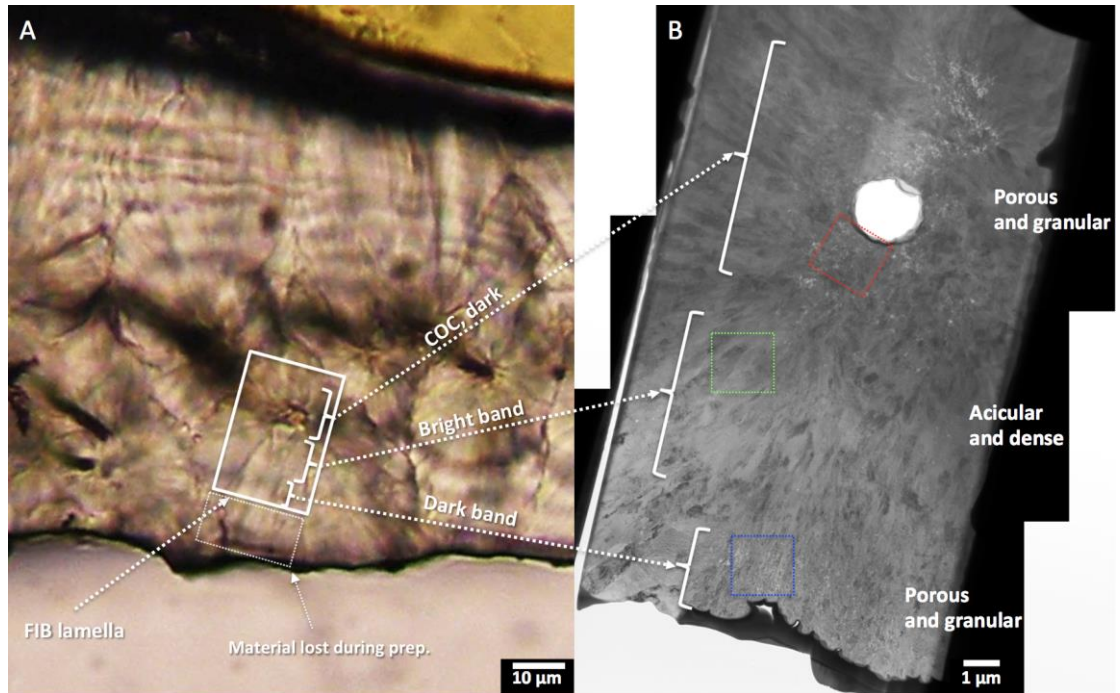


Figure 3.3. A) Optical micrograph providing the context of the sample area, the position of the FIB lamella is indicated by the white rectangle and encompasses a COC in *P. lobata*. Dashed lines are drawn to indicate correlating contrast bands in the optical image with distinct microstructural areas in the TEM micrographs. B) Compilation of three BF TEM micrographs of the *Porites lobata* FIB lamella. An area of granular crystals with a porous texture can be seen surrounding the original position of an organic fibre (which was largely removed as a result of the FIB milling) at the COC. The adjacent band consists of a dense area with large crystal domains, which is followed again by a band of granular crystals with higher porosity. The coloured rectangles indicate the location of the detailed areas in Figure 3.4. Reprinted from Van de Locht *et al.*, (2013) [132] with permission. Elsevier Copyright Clearance Center (license number 3345260883340).

Structure and orientation of the nanocrystalline regions

Throughout the extension of the FIB lamella we observed the gradual transition from the centre of the spherulite with randomly orientated nanocrystals (Figure 3.4 A,B) through to stacked (partly aligned) nanocrystals (Figure 3.4 C,D) and to large acicular crystals (Figure 3.4 E,F).

The diffraction patterns of nanocrystals within the stacked arrangement indicate that the different grains in one stack share a common zone axis orientation, as shown in Figure 3.5.

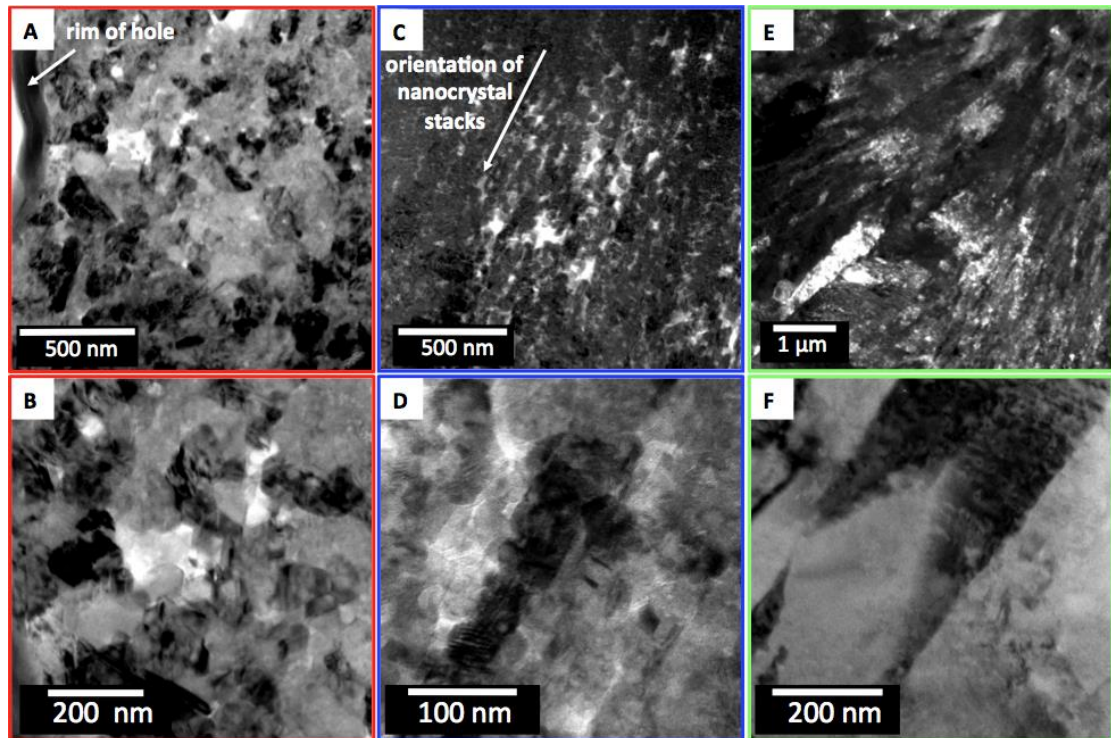


Figure 3.4. TEM micrographs of *P. lobata*. A-B) BF images of the porous area with disordered granular crystals at the COC. C-D) BF images of the granular band with stacking of nanocrystals. E) DF image of the dense acicular crystals from the bright middle band in the optical image in Figure 3.3. F) BF image with higher magnification taken from this area. Reprinted from Van de Locht *et al.*, (2013) [132] with permission. Elsevier Copyright Clearance Center (license number 3345260883340).

This was repeated for several areas within the stacked nanocrystalline area of the lamella and showed that most nanocrystals within individual stacks retain a common zone axis over approximately 200-300 nm. Although the nanocrystals retain a specific crystallographic orientation along the stack length axis, successive individual crystals show misalignment resulting in an increasing divergence from the zone axis as a function of position along the stack (Figure 3.5). The growth direction of the stack shown in Figure 3.5 is found to be $[001]$, as determined by projecting the prolongation or growth axis of the stack onto the reciprocal space – the diffraction plane – where it crosses the $\{002\}$ reflections (taking into account the 6.5° image rotation as discussed in Chapter 2). The stack orientation in $[001]$ direction seems preferential in both the nanocrystalline stacks as well as the acicular crystals (Figure 3.8).

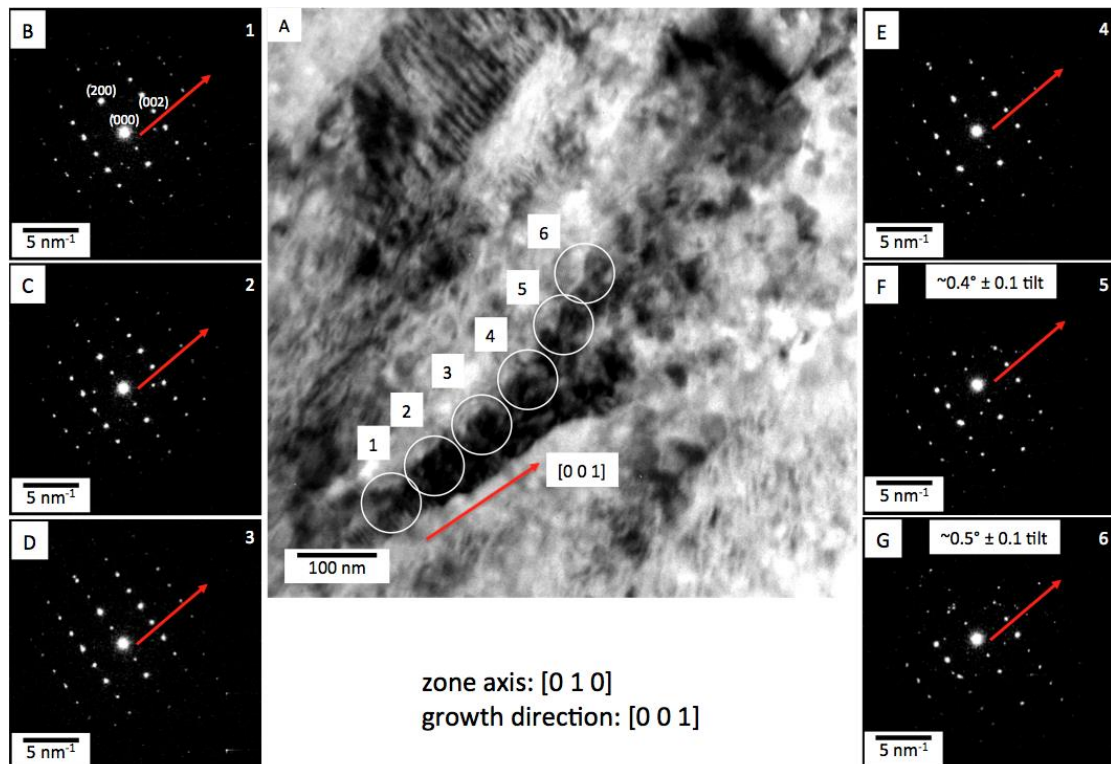


Figure 3.5. A) TEM BF micrograph of *P. lobata* showing a stack of partly aligned nanocrystals, the circles indicate the positions of the SAED aperture. The red arrow indicates the growth direction of the stack. B-E) Selected area diffraction series (aperture has an area size of approximately 30 nm) along the stack of partly aligned nanocrystals, in the [010] zone axis orientation. The indexed reflections are shown in B. The SAED patterns of position 4 and 5 indicate an increasing off-zone axis tilting of the crystals along the stack axis. Reprinted from Van de Locht *et al.*, (2013) [132] with permission. Elsevier Copyright Clearance Center (license number 3345260883340).

The partly aligned stacks of nanocrystals have porous spaces between individual stacks along the longitudinal axis, but pores can also be observed cutting across stacks prolonged in the same general direction. The pores in the randomly orientated nanocrystalline area at COC are unevenly distributed and vary in size, showing pores up to $\sim 150 \times 300$ nm, followed by areas with relatively small pores ($\sim 50 \times 80$ nm) or none at all. The large pores are predominantly located directly surrounding the hole where it is speculated that organic material present during the crystal formation was situated.

Diffraction patterns recorded with a larger SA aperture, encompassing several stacks (Figure 3.6) - as opposed to DPs of individual grains within a single stack discussed previously - showed a polycrystalline pattern.

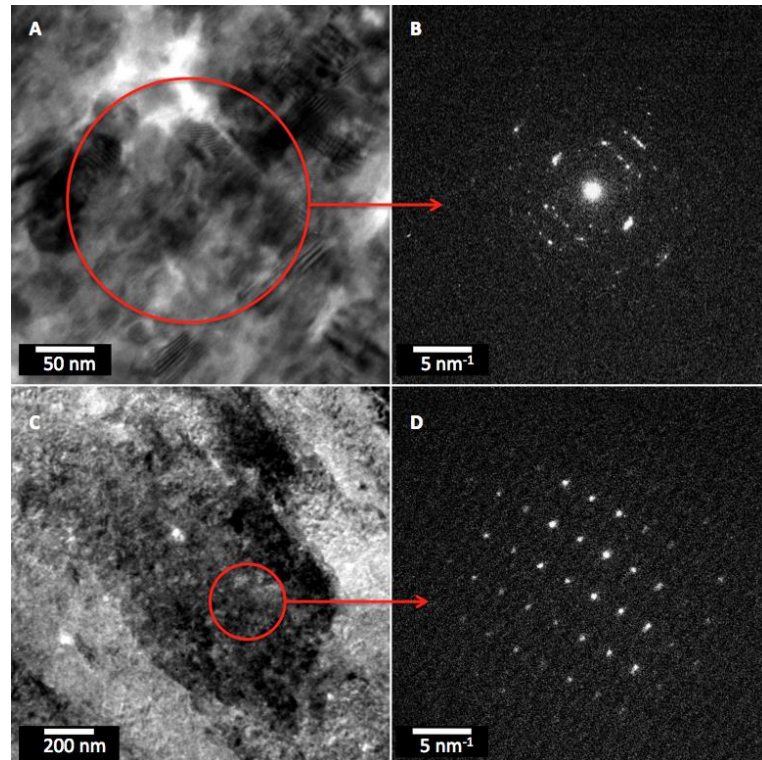


Figure 3.6. A) TEM bright field micrograph of stacked nanocrystalline area: the red circle indicates the position and approximate area size of the SA aperture. B) Diffraction pattern indicating a polycrystalline structure. C) TEM bright field micrograph of large acicular crystals, the red circle indicates the position and approximate area size of the SA aperture. D) Diffraction pattern indicating a single crystalline structure with a [211] zone axis.

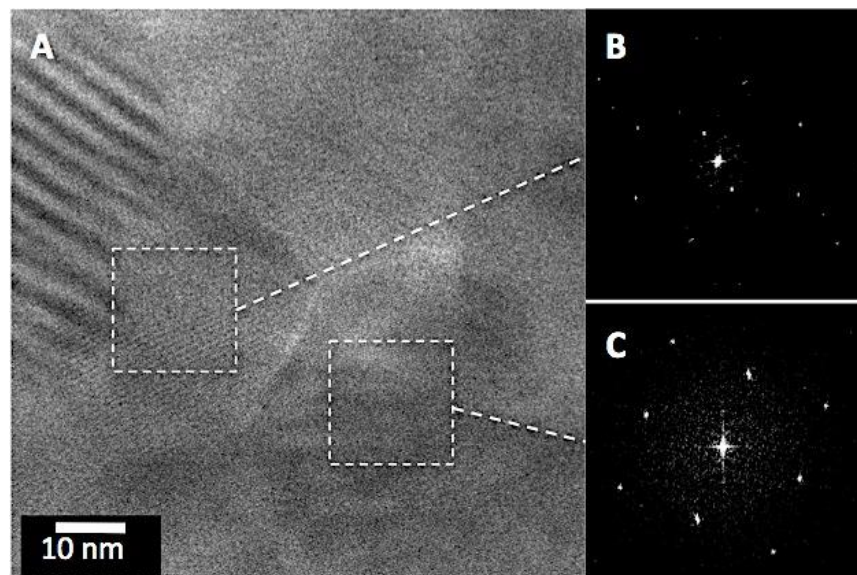


Figure 3.7 HRTEM micrograph of a nanocrystalline area from the blue square indicated in Figure 3.3B, showing two adjacent grains from two neighbouring stacks with a different crystal orientation as shown by the FFT's in B and C.

This supports the observation that the stacks are only partly aligned and do not generate a single crystalline DP on the micrometre scale as suggested for mesocrystals [133]. In contrast the acicular crystal region does generate a single crystalline diffraction pattern using a similar size SA aperture. HRTEM images were taken from crystal boundaries in the stacked nanocrystalline parts as shown in Figure 3.7. The two adjacent nanocrystals belong to two neighbouring stacks of grains and have a different crystallographic orientation, as demonstrated by the FFT analysis.

Structure and orientation of the acicular crystal phase

Acicular crystals were analysed in three TEM specimens from two different coral species: *Porites lobata* and *Siderastrea Siderea* (see Figure 3.8, Figure 3.9 and Figure 3.11).

SEM data at the micrometre scale (Figure 3.1 and Figure 3.2) show that within a single spherulite the acicular crystal bundles are all fanning out from the centre and the crystal growth is terminated at the boundary with a neighbouring spherulite. We have established that the acicular crystal bundles are interrupted along their length by bands consisting of partly aligned nanocrystals (Figure 3.4 and Figure 3.5) and that they consist - in contrast to these - of large elongated (300 - 500 nm wide by several μm in length), densely packed, single crystals, as was shown by SA diffraction (Figure 3.6). HRTEM data confirms the single crystalline nature and demonstrates that the [001], or c-axis, is the preferred crystal growth orientation of this phase in both investigated coral species (Figure 3.8 and Figure 3.9).

It is observed that some acicular crystals growing within the same bundle have 'extra' reflections present in the FFT pattern taken from the HRTEM image, in relation to their direct neighbours, without exhibiting a change in crystal orientation and growth direction. The extra reflections occur as a systematic row in the FFT of the right hand crystal of Figure 3.9. The inverse FFTs of selected reflections from the FFT of Figure 3.9B, along two systematic rows representing particular crystal planes: [001] and [-110], demonstrate that these lattice planes are consistent across

the grain boundary, confirming continuation of the crystal orientation over larger areas. Grain boundary related contrast is present; showing some blurring and decreased intensity due to overlap and stepping effects (Figure 3.10 A, B). The inverse FFT of the 'extra' or forbidden reflections (Figure 3.10 C) shows that these reflections are more prominent in the crystal positioned on the right side. Double diffraction occurs due to the rediffraction of a diffracted beam within the crystal [39]. Such reflections are often weak in intensity and their occurrence becomes more prominent with increasing specimen thickness. This is caused, for example, by the stacking of multiple crystal layers. The lattice spacings related to this effect were found to be $9.2 \pm 0.1 \text{ \AA}$ as calculated from the intensity profile, which is not a known d-spacing for aragonite.

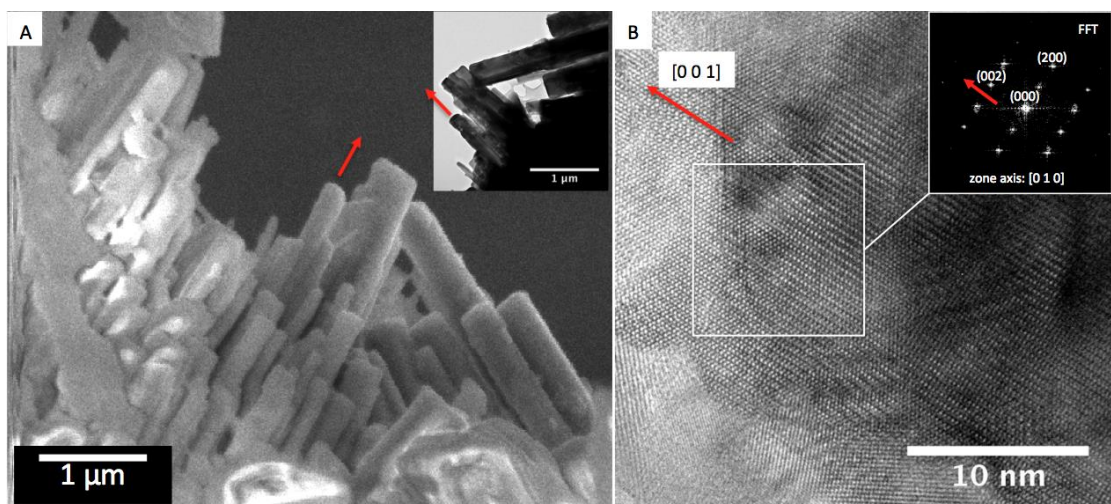


Figure 3.8 A) SEM micrograph of large acicular crystals protruding from a spherulite of *P. lobata*. The red arrows indicate the growth direction of the crystal analysed in B. Inset shows a TEM bright field micrograph of the protruding acicular crystals. B) HRTEM micrograph of one of the protruding acicular crystals, showing the aragonite lattice, the red arrow indicates the direction of growth and the square indicates the area used for Fast Fourier Transform (FFT) analysis. The inset shows the FFT, the red arrow indicates the projection of the growth direction in reciprocal space, indicating an [001] growth direction. *Elisabeth Brown prepared this TEM specimen by ion milling (no FIB) for her Master thesis project (2010) at the University of York, UK. Reprinted from Van de Locht et al., (2013) [132] with permission. Elsevier Copyright Clearance Center (license number 3345260883340).*

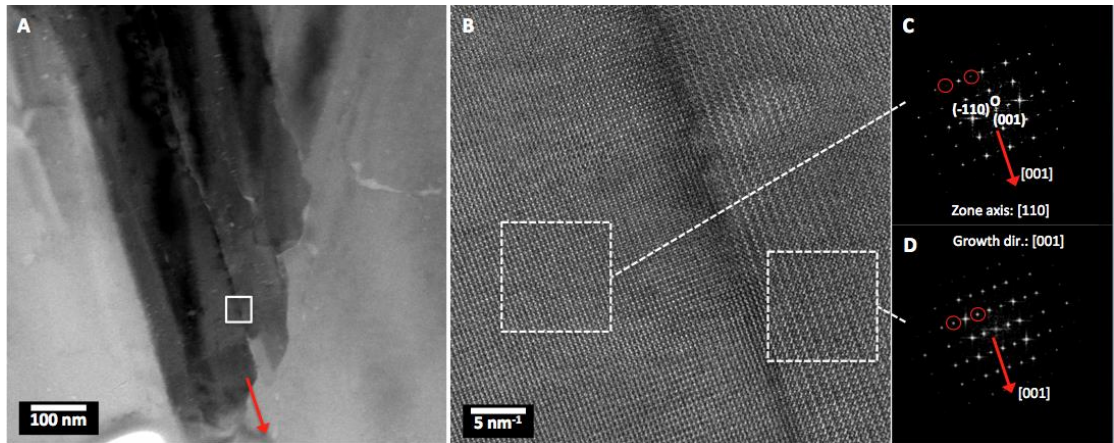


Figure 3.9 A) TEM micrograph of a bundle of acicular crystals in a spherulite of *S. siderea*. The red arrow indicates the crystal growth direction. The square indicates the region shown in high resolution in B. B) HRTEM micrograph showing two adjacent acicular crystals within the same bundle, squares indicate the areas used for FFT analysis. C and D) FFT's of two adjacent crystals in B. The red circles indicate positions of reflections, which are present in the right crystal but lacking in the left crystal.

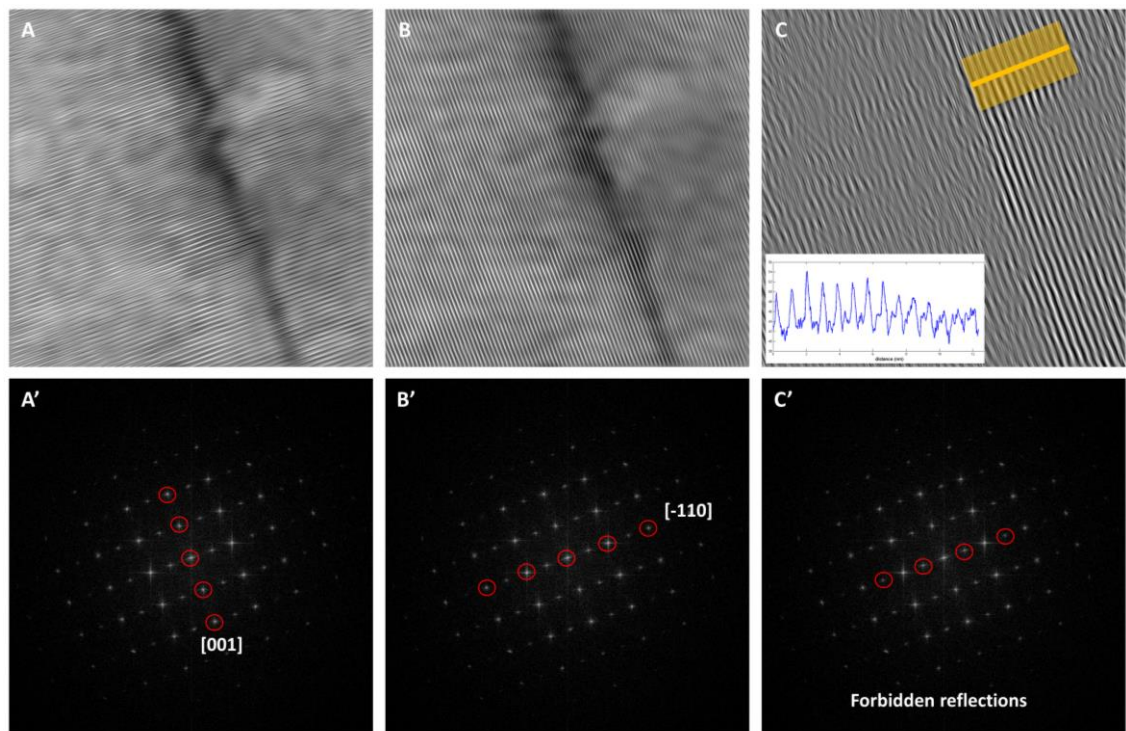


Figure 3.10 Analysis of image 3.9B. A) Inverse FFT of A' from selected reflection of the (001) plane. B) Inverse FFT of B' from selected reflections of the (-110) plane. C) Inverse FFT of C' of a systematic row of forbidden reflections, the inset shows an intensity plot along the yellow line averaged over the indicated area.

Crystal strain

Interestingly, strain (causing dark bands in bright-field TEM imaging) has been observed in multiple specimens, but only in areas with the large acicular crystals. This occurs infrequently along grain boundaries within crystal bundles of the same orientation, but mostly at the point where crystal bundles of one spherulite encounter another (Figure 3.11). Figure 3.11 C demonstrates that the strain contrast originates at the grain boundary, implying that it is not caused by internal defects of the crystal but by an external force; namely the pressure applied by the top crystal. Compression strain is the most likely explanation for the bending contrast seen at the contact points between crystals of differently orientated bundles.

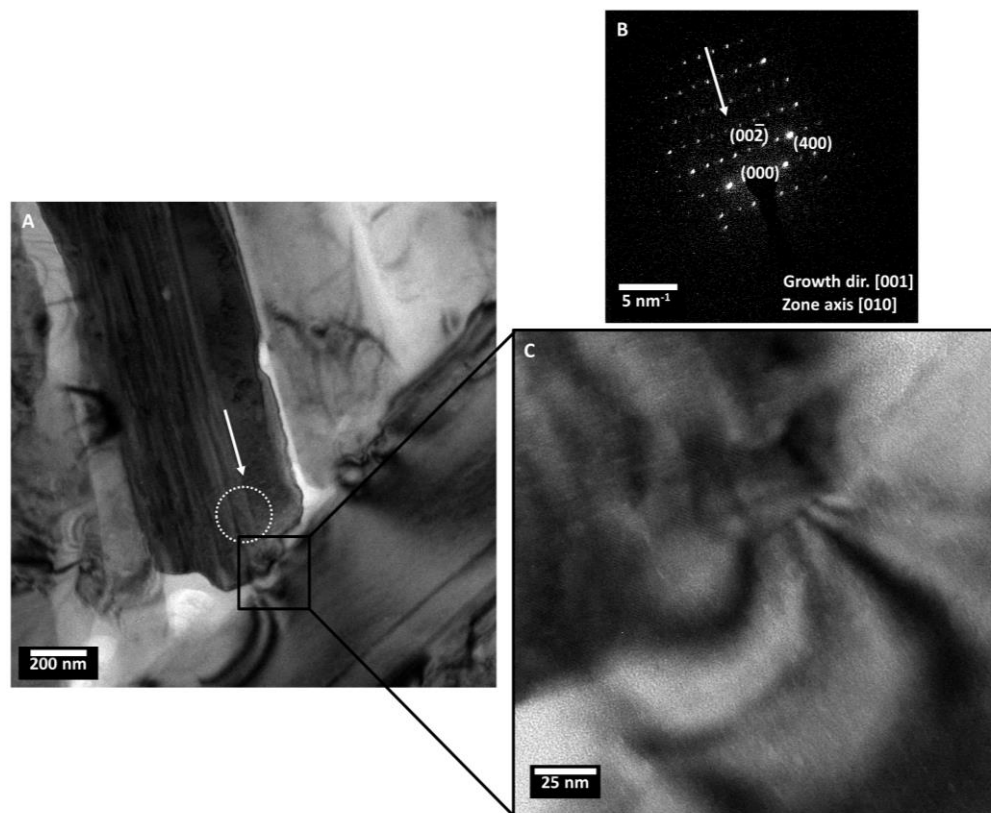


Figure 3.11 TEM bright field micrographs of *S. siderea* showing strain contrast where acicular crystal bundles of different orientation meet. A) Overview, circle indicates the position and approximate size of the selected area aperture and the arrow indicates the growth direction of the crystal. Amorphous material can be observed between the differently orientated crystal bundles. B) SAED pattern of the crystal in A, the arrow indicates the growth orientation projected in reciprocal space, showing a [001] growth direction. C) Detail of strain contrast.

Microstructure in juvenile coral specimens

SEM micrographs of recruited (aquarium-grown) *Acropora millepora* larvae show a structure often referred to as “fish-scale” morphology on the skeletal surface, consisting of aragonite acicular crystals organized in discrete bundles, called fasciculi (see Fig. 8B). These features together with randomly oriented fusiform crystals at the growth front have been observed in several studies of *Acropora* coral recruits [72, 134].

TEM data from a FIB lamella show several distinct features along a succession of aragonite acicular crystal domains (Figure 3.12). The acicular crystals measure up to 500 nm in width and to several μm in length, similar to the adult *Porites lobata* and *Siderastrea Siderea* specimens. Acicular crystals form larger domains with neighbouring crystals of the same c-axis orientation, of up to 2-3 μm in width. Differences in angle between adjacent acicular domains have been measured up to $\sim 28^\circ \pm 0.5$, where neighbouring spherulites meet. Furthermore, narrow porous bands ($\sim 50 - 100$ nm) can be observed interrupting the acicular crystal domains. Individual acicular crystals, as well as extended domains, maintain their orientation across these porous bands. Furthermore, it was found that nanocrystalline material of the type observed in the adult *Porites lobata* was not present within these bands.

Summary of coral microstructure results

Adult corals show three distinct crystal morphologies within the spherulites: 1) nanocrystalline randomly oriented and porous, 2) nanocrystalline stacked and porous and 3) large, acicular densely-packed single crystals occurring in bundles. These phases are directly correlated with daily contrast bands observed in optical images.

The nanocrystalline areas consist of individually aligned stacks, following an unaligned nanocrystalline phase directly at the centre of calcification (COC).

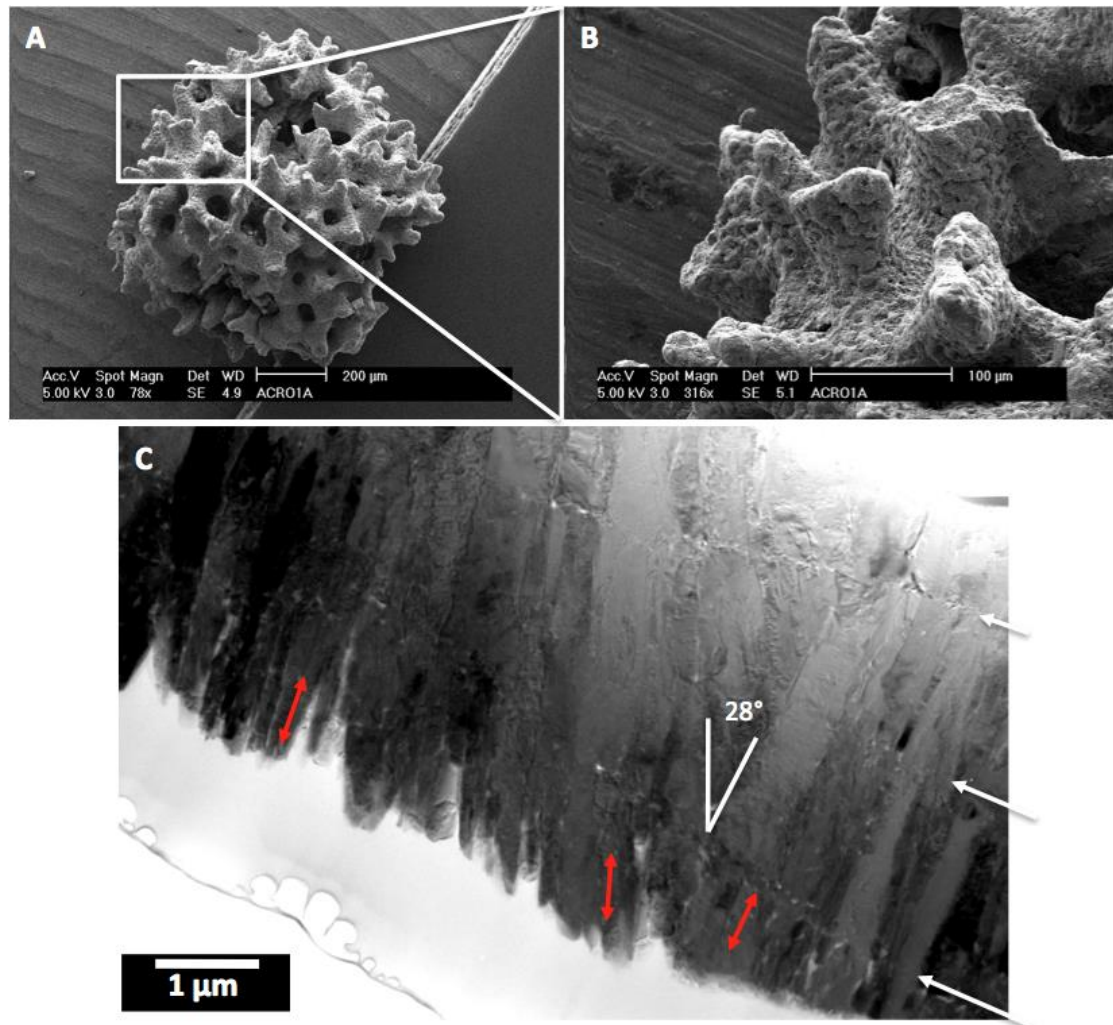


Figure 3.12 A. *millepora* larva, 5 days after onset of mineralisation, cultivated at ambient 390 ppm CO₂ and 29°C. A) SEM micrograph of the complete specimen. B) SEM micrograph of a detail of the surface of the skeleton showing the typical fish-scale morphology formed by the aragonite fibre bundles. C) Bright field TEM micrograph, red arrows indicate the c-axis direction (growth orientation) of the acicular crystals. The white arrows indicate boundaries with pores across these bundles that seem to 'interrupt' the crystal domains. Reprinted from Van de Locht *et al.*, (2013) [132] with permission. Elsevier Copyright Clearance Center (license number 3345260883340).

The aligned nanocrystalline stacks are also present in the subsequent granular band separated from the COC by the dense acicular crystal phase. The individual nanocrystals are 50-70 nm in size. The nanocrystalline stacks show imperfect alignment in growth orientation with the individual grains being similarly oriented, but with misalignments over greater distances. Different stacks show no orientation correlation between each other, resulting in overall polycrystalline morphology on

the micrometre scale, as compared to the extended single crystal domains characteristic of the acicular phase. The growth orientations derived from SAED and FFT data show that both the acicular crystals and the nanocrystalline stacks (over small distances) are preferentially aligned in [001] direction. Apparent super-lattice effects have been observed due to specimen thickness variation. Strain contrast appears regularly in the acicular crystal areas at the contact point between spherulites, probably caused by compression stress from one crystal bundle to the other.

The studied juvenile specimens show similar acicular crystal domains, but these were interrupted – not by bands of stacked nanocrystals – but by linear bands of pores. Crystal orientation in the acicular phase is maintained across these porous bands.

3.1.2 THE ORGANIC FRACTION

As mentioned in section 2.1.1, Johnston (1980) [78], Gautret *et al.* (2000) [76] and others show the presence of organic compounds at the growth front and in deeper parts of the coral skeleton. They are entrapped between, and possibly within crystals (the inter- and intra-crystalline organics respectively). The presence of organics in the skeleton has been unambiguously proven, but their role, spatial distribution and composition are still far from being resolved.

Isolation of the organic fraction from the mineral phase was achieved through slow demineralisation (72 hrs) by gentle, chemical dissolution (0.5 M EDTA, see paragraph 2.2.4) to prevent deterioration of the organics themselves. SEM imaging revealed three different morphologic organic compounds: sheet-like material (>50 x 100 μm), fibrous bundles (individual fibres are approximately 100nm x 5 μm) and isolated fibres (> 2 x 30 μm) (Figure 3.13). Some of the loose fibres could have originated from the bundles, although a wide size variation was observed and most exceeded fibre bundle dimensions, implying different components.

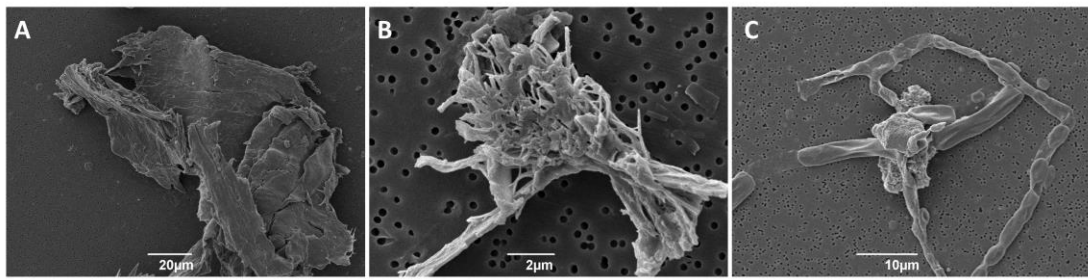


Figure 3.13 SEM micrographs of organic material extracted from *P. lobata* bulk skeleton sample. A) Sheet-like material. B) Bundle of (submicron) fibres. C) Large isolated fibres.

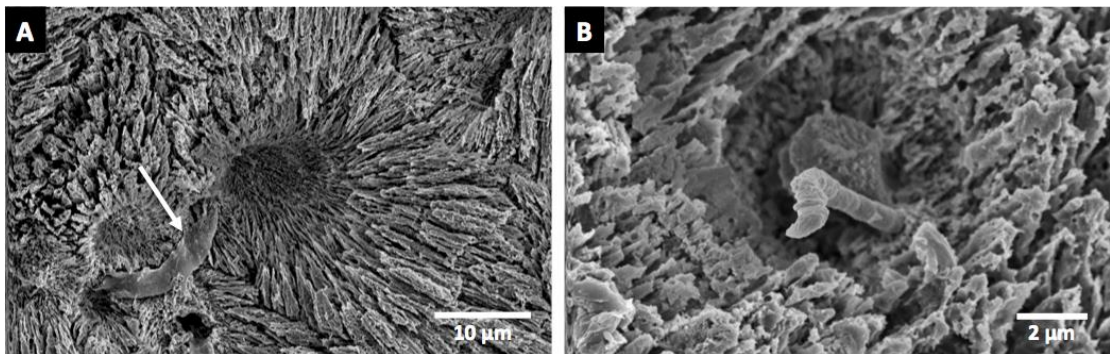


Figure 3.14 SEM micrographs of adult coral, surface-etched specimens. A) *P. lobata* spherulite with sheet-like organic fragments at the COCs. B) A *S. siderea* COC with extruding organic fibre.

The sheets and large isolated fibres were also observed at the surface of the coral skeleton after etching by SEM (Figure 3.14), these features seem often located in proximity or at the centre of the COCs.

The small fibre bundles would fit in 100's of nanometre to micron-sized pores at spherulite boundaries and at the COC in the highly porous randomly oriented crystalline phase. Amorphous material was detected in such contexts by TEM (Figure 3.3 and Figure 3.11). It is likely that these bundles are part of the inter-crystalline organic phase, the so-called intra-crystalline organics may be too small or fragmented to be observed as discrete features by SEM. The large sheets and isolated fibres could be remnants of external/contaminant sources, as they are too large to fit in between crystals. It is however intriguing that they appear to be connected to the COC locations.

EDX measurements show an enhanced carbon to calcium signal from the COCs with granular crystal morphologies as opposed to the acicular crystal bundles that

radiate from the COCs (see Appendix B). This suggests the presence of organics at the COCs, not only in the bulk fraction as was shown in the SEM images above, but also on the smaller, possibly at the nanometre scale in the form of inter- and intra-crystalline components. Additionally, previous (unpublished) EDX data collected by Roland Kröger in 2009 from *in-situ* fibres in *Porites lutea* coral partly overgrown with aragonite crystals at the mineral/living membrane interface, show a distinct organic composition with enhanced nitrogen, magnesium, phosphorus and sulphur ratios (see Appendix B).

The difference in chemical signature between mineral and organic fraction is further investigated by Raman spectroscopy. Raman spectra from three coral species confirmed that the mineral phase consists exclusively of aragonite crystal with no occurrences of calcite or vaterite polymorphs (Figure 3.15). The typical aragonite triplet peak of the ν_4 vibration of the carbonate ion could be identified, as well the characteristic lattice mode vibrations at approximately 180 and 206 cm^{-1} which are seen in aragonite but not in calcite and vaterite [31, 135]. The 155 and 1086 cm^{-1} are common peaks in CaCO_3 structures and cannot be used to distinguish between mineral polymorphs.

Mineral structures with dimensions above the μm range with low levels of impurities will generate a spectrum with well-defined and sharp peaks. In contrast organic compounds give rise to an enhanced background signal due to *fluorescence* (see paragraph 3.2.4). Figure 3.16B shows point spectra taken from an area with dense acicular crystals and an area at the COC with a granular porous morphology. As expected from preliminary EDX measurements, the Raman spectrum at the COC shows a much increased background signal, with the aragonite peaks superimposed on this signal.

To determine the spatial extent of the fluorescent signal Raman mapping was applied on several tens of micrometre scale areas around COCs, an example is shown in Figure 3.16 for *P. lobata*. The Raman intensity of the carbonate ion symmetric vibration peak (ν_1) was extracted and compared to a map of the extracted fluorescence intensity (Figure 3.16C, D).

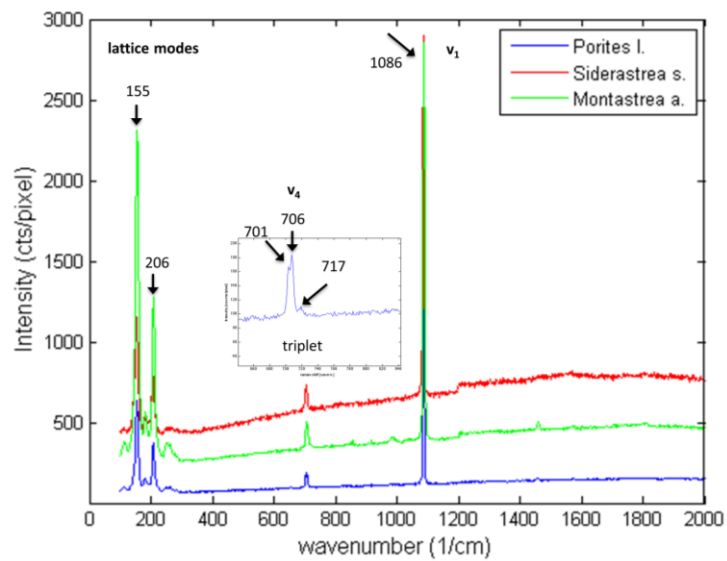


Figure 3.15 Raman spectra of three adult coral species from the non-porous acicular crystal bundles confirming that the crystal phase is aragonite.

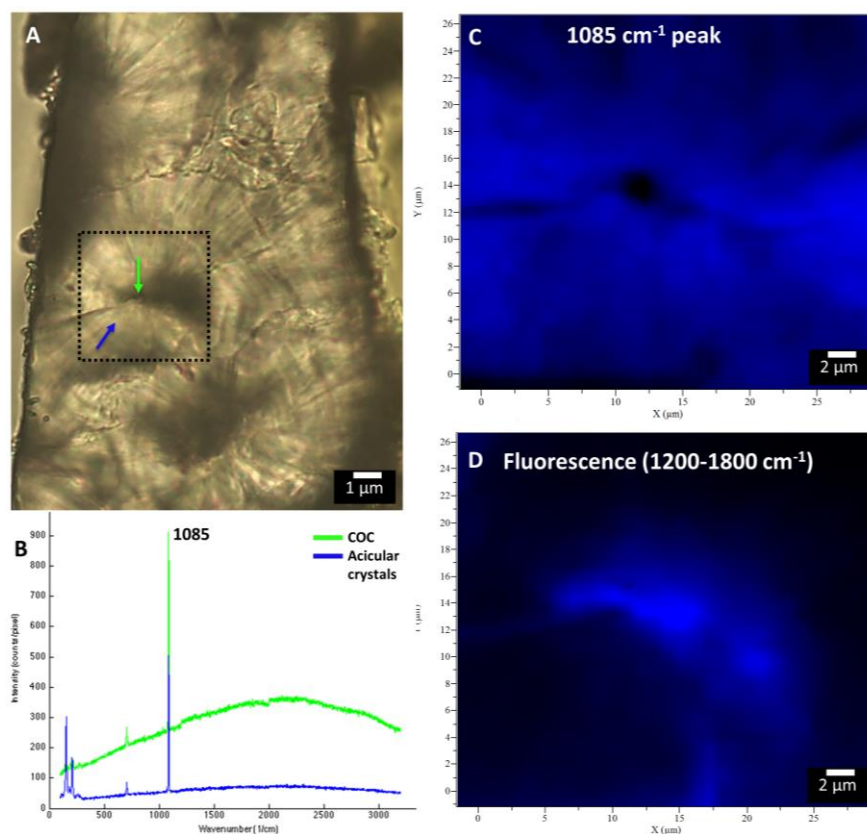


Figure 3.16 Raman spectroscopy of *P. lobata*. polished specimen surface. A) Optical transmission image of the specimen surface, square indicates the scanned area for mapping and the arrows indicate the point spectra locations in corresponding colours. B) Point spectra of the COC and acicular crystal bundles (raw data). C) Intensity distribution map of the v_1 CaCO_3 stretching mode (baseline corrected). D) Intensity distribution map of the background signal.

This shows a clear concentration of fluorophores, i.e. organics, at the COC and a gradual decrease towards the dense acicular crystal bundles. Furthermore, some underlying linear features with high fluorescence seem to extend toward the exterior: this could be the previously observed fibres (Figure 3.14). It is noteworthy that the carbonate distribution is relatively homogenous except at the strict centre of the COC where the mineral phase seems to be depleted, as well as across the linear features. Also, a slight variation in fluorescence occurs at the first dark contrast band outside of the COC. The fluorescent signal increases marginally, implying higher organic content in the granular daily growth band as opposed to the acicular crystal band. This phenomenon is shown and discussed in much more detail by Wall & Nehrke *et al.*, 2012 [136] for a *Porites lutea* coral.

Chemical characterisation of the coral organic compounds

Above, three different morphological types of extracted organic compounds could be identified after demineralisation; sheet-like material, bundles with small fibres and large isolated fibres (Figure 3.13 and Figure 3.14). Raman spectra could be successfully obtained from the latter two (Figure 3.17 and Figure 3.18). The sheet-like organics only generated a noisy background signal, possibly due to laser sensitivity of this substrate. The Raman data demonstrates that the organic compounds are chemically dissimilar. The fibre bundles most likely consist of proteins, as many individual amino acid Raman peaks could be identified. The isolated fibres however, show some generic organic vibrational modes, but no positive identification towards a particular compound could be made at this point.

Interestingly, both the isolated fibres and fibre bundles show peaks at approximately 1460 cm^{-1} and between $2880\text{--}2950\text{ cm}^{-1}$ commonly attributed to CH and CH_2 vibrational modes in general, such as in glycerol [137], indicating that this material could be present in the background or as a coating/residue. Additionally a broad peak between $3000\text{--}3600\text{ cm}^{-1}$ is attributed to water or any OH-bonds, which is likely to originate from the remnants of the demineralisation fluid.

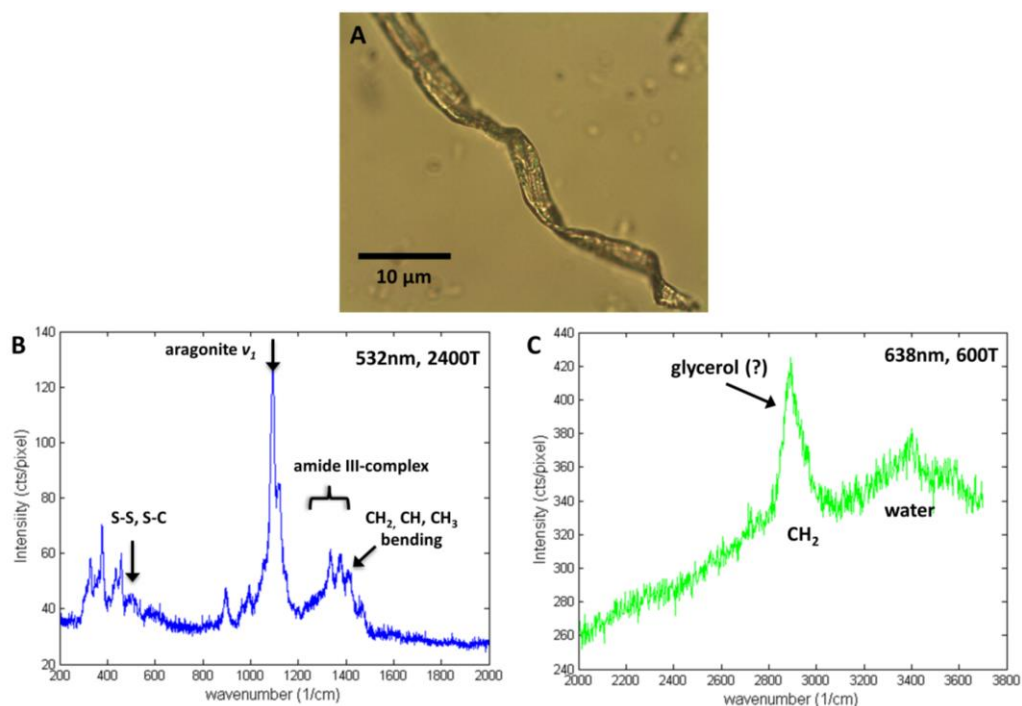


Figure 3.17 Optical image of a *P.lobata* fibre (A) with Raman spectra (B-C) taken over two data ranges with two different lasers. The 200-2000 (B) and 2000-3000 cm^{-1} (C) data ranges show several peaks recognised as vibrational modes in organic molecules. Peaks were labelled using comparative data from several studies: Wall and Nehrke (2012) [136], Zhang *et al.*, (2011) [138], Perrin and Smith (2007) [139], Mudalige and Pemberton (2007) [137] and Kaczorowska *et al.*, (2003) [140].

It should be noted that peak identification of complex materials or mixtures can be problematic as some peaks may be superimposed and thus not recognised or wrongly labelled.

To discriminate between the large fibres and the inter/intra-crystalline organics (e.g. the small fibre bundles) the samples were pre-treated according to two different methods: 1) bleaching of the powdered coral skeletal mineral to remove all external organics and retain the inter/intra-crystalline fraction, 2) demineralisation of the bulk skeletal coral and isolation of large fibres by use of a micro-manipulator (see paragraph 2.2.5). The results show that the inter/intra-crystalline organics of three different coral species are predominately made up of aspartic acid (incl. asparagine) (Asx), glycine (Gly) and glutamic acid (incl. glutamine) (Glx), see Figure 3.19. All three species follow the same general trend in amino acid composition, although *P.lobata* has a much higher Asx concentration relative to the other two dominant amino acid species.

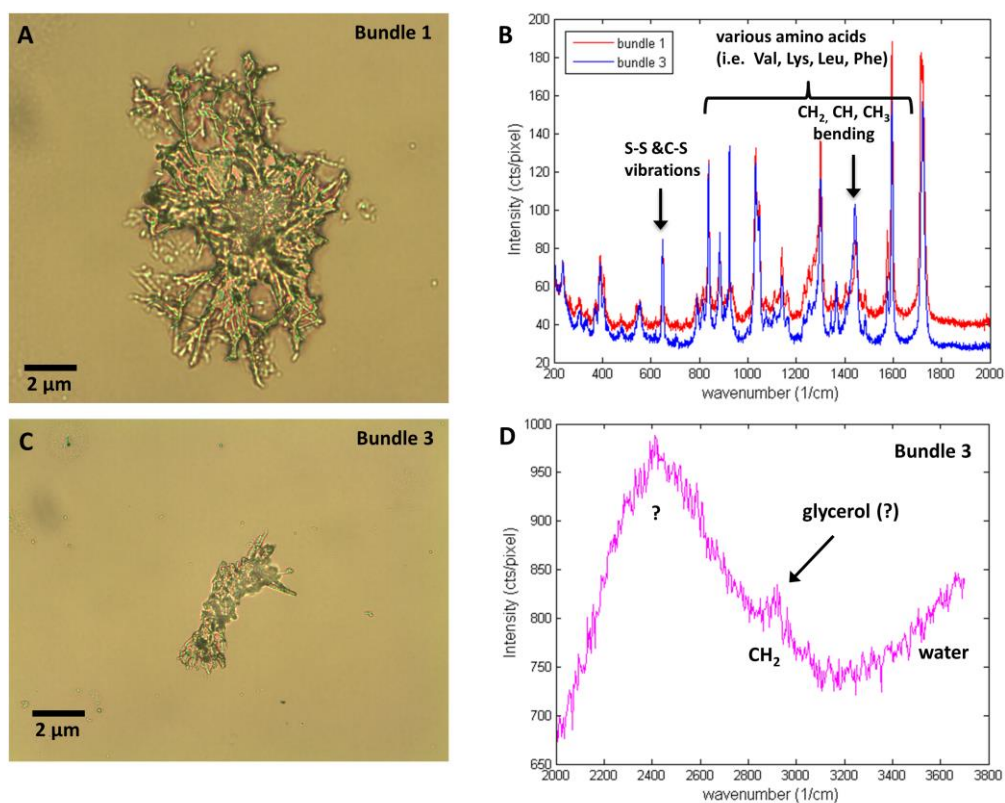


Figure 3.18 Optical images of *S.siderea* fibre bundles (A and C) with corresponding Raman spectra (B and D, 532 nm laser). Sharp peaks could be identified in the 200-2000 cm^{-1} range, mostly corresponding to vibrational modes in amino acids. In the 2000-3600 cm^{-1} range broad peaks appear which could be identified with some uncertainty. Peaks were labelled using comparative data from several studies: Wall and Nehrke (2012) [136], Zhang *et al.*, (2011) [138], Perrin and Smith (2007) [139], Kaczorowska *et al.*, (2003) [140] for Raman peaks from organics in coral and Mudalige and Pemberton (2007) [137] for Raman peaks of glycerol.

Table 3-1 summarises the amino acids species, their acronyms and general properties. Unfortunately, under the acidic hydrolysis conditions, which are necessary to break down the amide bonds and analyse the bulk amino acid composition, the basic Asn and Gln undergo irreversible deamination to the acidic Asp and Glu. Hence, no distinction can be made between the basic and the acidic residues and the detected species are called Asx and Glx, respectively. Therefore, we cannot conclude from this preliminary dataset if the general protein trend in the studied coral species represents acidic or basic residues. Another experimental approach should be considered, such as zeta potential measurements, where information about the surface charge is obtained. The experiment could be run at different pH values, so as to determine whether the protein is rather basic or acidic.

Table 3-1. List of analysed amino acids by RP-HPLC of coral inter-crystalline organics and extracted fibres, with their respective acronyms and characteristics. Source for attributed properties: the Institute of Chemistry, Department of Biology, Chemistry and Pharmacy, FU Berlin.

Acronym	Amino acid	Group	Characteristics
Asx	aspartic acid + asparagine	-	-
Asp	aspartic acid	acidic	negatively charged
Asn	asparagine	basic	positively charged
Glx	glutamic acid + glutamine	-	-
Glu	glutamic acid	acidic	negatively charged
Gln	glutamine	basic	positively charged
Ser	serine	polar	hydrophilic, non-charged
L-Thr	threonine	polar	hydrophilic, non-charged
Gly	glycine	polar	hydrophilic, non-charged
L-His	histidine	basic	positively charged
L-Arg	L-homo arginine	basic	<i>added standard</i>
Ala	alanine	non-polar	hydrophobic
Val	valine	non-polar	hydrophobic
Phe	phenylalanine	non-polar	hydrophobic
Leu	leucine	non-polar	hydrophobic
Ile	Isoleucine	non-polar	hydrophobic

Previous studies on the biochemical composition of the organic fraction in Scleractinian coral skeletal material have reported the presence of chitin, although this seems limited to certain species [79, 141], as well as lipids for several species [79, 85, 142]. But most papers have reported the presence of proteins [79, 82, 85, 141, 143, 144], and polysaccharides [82, 127, 143], with the protein to sugar ratio varying between species [82, 144].

Targeted analysis of the coral skeletal organic matrix *proteins* showed that it is enriched in aspartic acid, and to some lesser extent glutamic acid and glycine [82, 145-147], which is in accordance with the results presented here (bearing in mind that this study cannot differentiate between Asp/Asn and Glu/Gln). Acidic amino acids have been shown to impact the crystal morphology in synthetic CaCO₃ precipitation experiments [59] and to interact with coral CaCO₃ during skeleton formation in several scleractinians [148-150]. It is hypothesised that acidic macromolecules play a role in the biomineralisation process possibly by way of

templating [151, 152], i.e. by attracting positively charged Ca^+ ions to create stable nucleation sites.

In the past it has been suggested that the coral organic matrix consisted fully or predominantly of acidic proteins [143], which follows from bulk analyses (similar to this study). Recently however, Ramos-Silva *et al.*, (2013)[153] have characterised 36 proteins from *Acropora millepora* and concluded that this view is far too simplistic. They found that there is a wide range of proteins present with different functionalities, and that although acidic proteins remain a key player in calcification, they are not exclusive to that role.

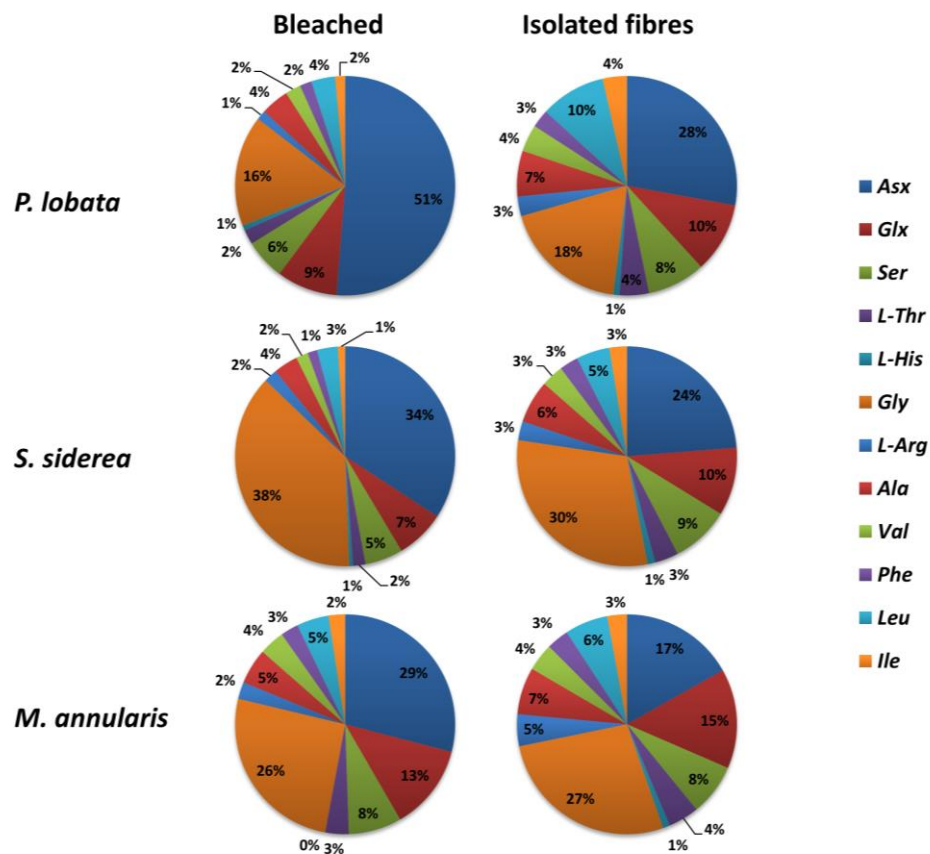


Figure 3.19 Pie-charts showing relative percentages of amino acid concentrations for three coral species. The bleached samples represent the inter-crystalline organics, the isolated fibres represent the large fibres extracted after demineralisation. Average standard deviations (σ) per sample category averaged over 12 amino acid types are: *P. lobata* bleached $\sigma = 1.23\%$, fibres $\sigma = 0.72\%$; *S. siderea* bleached $\sigma = 2.03\%$, fibres $\sigma = 0.50\%$; *M. annularis* bleached $\sigma = 1.62\%$, fibres $\sigma = 2.01\%$ (see appendix A).

Another finding of the HPLC study is that there is a clear difference in composition between the inter/intra-crystalline organics and the isolated fibres, complementing the results from the Raman spectroscopy. Although the large fibres do contain amino acids, and thus proteins, which was not evident from the Raman analysis, they are less rich in Asx and Glx. Instead, there is a more even distribution between amino acids, and Gly is the largest contributor in two out of the three coral species (Figure 3.19).

Chemical analysis as well as imaging suggests that the large fibres are of different origin as compared to the inter/intra-crystalline organic fraction. The fibre size may suggest this is not original to the coral skeleton, but possibly from an external contamination source. Burrowing organisms such as fungi are known to invade corals and possibly affect crystal growth by way of a triggered defence mechanisms against the invading species [154]. However, this may not prevent them from playing a structural role in the coral biomineralisation process, as they are regularly found at COC (see Figure 3.14). Further analysis, such as polymerase chain reaction (PCR) to amplify DNA is needed to verify whether this material belongs to the coral itself or may be from a different organism.

The composition and origin of the large sheets remain unclear as Raman spectroscopy was unsuccessful due to the laser sensitivity of the material. Additionally, we assume that the HPLC data does not encompass this material as external organic materials are removed by the bleaching process.

Summary of coral organic compound analyses

Non-crystalline material was observed, in SEM images of etched coral surfaces *in-situ* (in the coral spherulites) as well as in inter-crystalline pores in TEM images and after demineralisation as a residue. The organic material appears to be associated predominantly with the COC and the crystal growth front between spherulite boundaries. Raman mapping confirmed the former, as well as suggesting an increase in organic content in the granular porous bands as compared to the acicular bands. Three morphologically distinct organic types were detected after

extraction: 1) sheet-like material (>50-100 μm), 2) bundles of thin fibres (individual fibres are $\pm 100 \text{ nm} \times 5 \mu\text{m}$) and 3) large isolated fibres (> 2 x 30 μm). Raman analysis showed the small fibre bundles and the large isolated fibres to be dissimilar in composition; the fibre bundles are probably protein bundles, the large fibres show generic organic molecular vibrations but no amino acid peaks. Liquid chromatography confirmed the chemical dissimilarity between the fibre bundles (thought to be inter/intra-crystalline organics) and the large fibres (thought to be from an external source). The former consists of predominantly of Asx (29-51%) with Gly (16-38%) and Glx (7-13%) also being main components, while the latter shows a more even distribution between these dominant amino acid types (Gly: 18-30%, Asx: 17-28% and Glx: 10-15%). Acidic proteins or macromolecules are thought to play an important role in the biomineralisation process by, for example, forming a template to guide nucleation by Ca^{2+} attraction and/or by affecting certain crystal facets [151, 152, 155]. However, in recent studies the contribution of basic proteins to the coral skeletal organic matrix has also been highlighted and it was concluded that the coral skeletal proteins consisted of a complex mixture [153].

The biochemical study presented here is but a preliminary dataset and needs to be further complemented by other chemical analysis techniques. Furthermore, the study would benefit from DNA analysis of the large isolated fibres as they might originate from external contaminant species such as fungi.

3.2 SYNTHETIC ARAGONITE FORMATION VIA ORGANIC ADDITIVES

As mentioned in paragraph 2.1.2, the experiments discussed in this section are a continuation of the work presented by Sand *et al.*, (2011) [96] and a direct collaboration with Dr. Sand. In Sand and co-workers's study, CaCO₃ polymorphs are precipitated from mixing saturated Ca²⁺ and CO₃²⁻ solutions in the presence of OH containing additives to mimic biogenic aragonite mineralisation. An important finding was that a higher ratio of ethanol increases the yield of aragonite, and stabilises aragonite against conversion to calcite. This is significant as calcite is the thermodynamically most stable polymorph of CaCO₃ [97], and an important question is how biomineralising organisms stabilise the less favourable phases to create their skeletons. It has to be noted that current ocean conditions also promote aragonite by having high Mg concentrations, see the discussion in section 5.1.1.

The aragonite formed in the presence of ethanol consisted of bundles of needle-like crystals, with the individual needles made up of small segments separated by well expressed, perpendicular grooves [96].

In this study we focus on the aragonite formation and its crystallographic properties, as it is relevant for coral mineralisation. Below we discuss the results of ASEM, SEM and TEM data on aragonite precipitated in the presence of 15-50 vol% ethanol from mixing 0.1 M CaCl₂ and 0.1 M Na₂CO₃ solutions in bulk at ambient conditions.

The addition of less than 15% ethanol results in precipitation of mostly calcite, some of hopper-type crystal. Hopper crystal formation is triggered by rapid growth as ions are preferentially consumed at the edges of facets, while the inside remains empty [156], see Figure 3.20A. Moreover, small amounts of aragonite needle bundles and cauliflower or dendritic shaped vaterite are observed. All the crystals or crystal aggregates are of medium size ($\leq 20 \mu\text{m}$). By increasing the ethanol concentration the crystal morphology is greatly affected as is shown in Figure 3.21 for ethanol concentrations higher than 35 vol%. Firstly, abundant hopper-type

calcite crystals form, although they remain relatively small ($\leq 2 \mu\text{m}$). The dominant crystal phase is aragonite which forms large bundles of crystalline needles ($\geq 50 \mu\text{m}$, Figure 3.20B). The bundles themselves are shaped like *wheat sheafs* or *hollow sided spherulites*. These results are in agreement with the previous findings of Sand *et al.*, (2011) [96]. We also observed the growth of aragonite crystal bundles from {104} calcite facets. This was recorded *in-situ* during ASEM experiments, and a time-laps series of these recordings is shown in Figure 3.22.

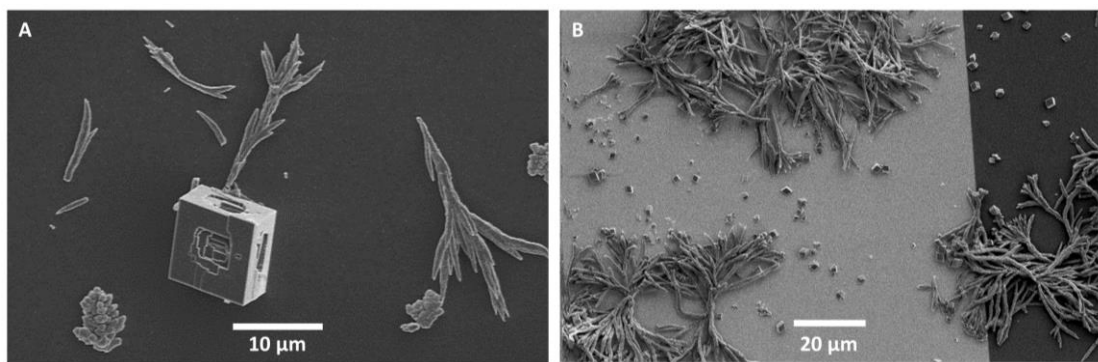


Figure 3.20 SEM images of CaCO_3 crystals precipitated in ClairScope dishes with: A) 35 vol% ethanol, pre-mixed, 0.5 hour matured; mostly calcite rhombohedra (some hopper-type) crystals, with some vaterite (compact bundles) and bundles of elongated aragonite needles. B) 50 vol% ethanol, pre-mixed, 3 hours matured; abundant small calcite crystals ($< 2 \mu\text{m}$) and large bundles of aragonite needles ($\geq 50 \mu\text{m}$).

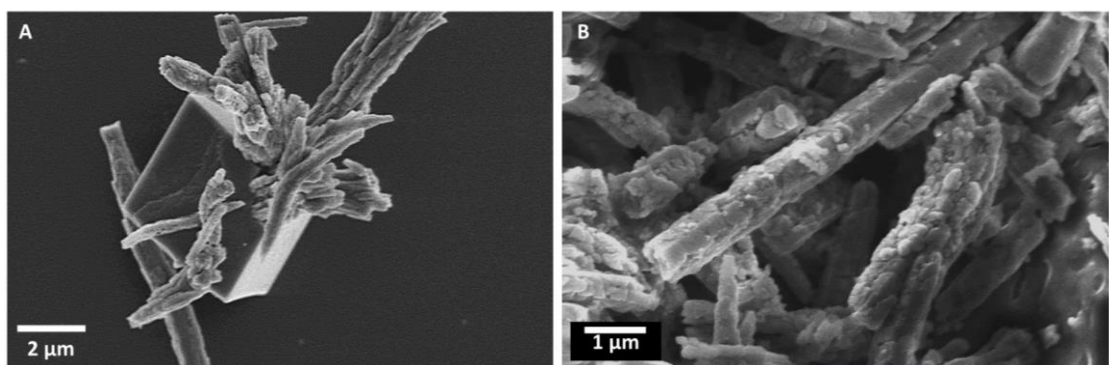


Figure 3.21 SEM images of CaCO_3 crystals precipitated in ClairScope dishes with: A) 35 vol% ethanol, pre-mixed, 0.5 hour matured (same sample as in Figure 3.20 A), bundles of elongated aragonite needles growing out of a {104} calcite rhombohedra. B) 50 vol% ethanol, pre-mixed, 4.5 hours matured (same sample as in Figure 3.20 B), detail of the aragonite needles, showing a surface substructure of small ($< \mu\text{m}$) segments.

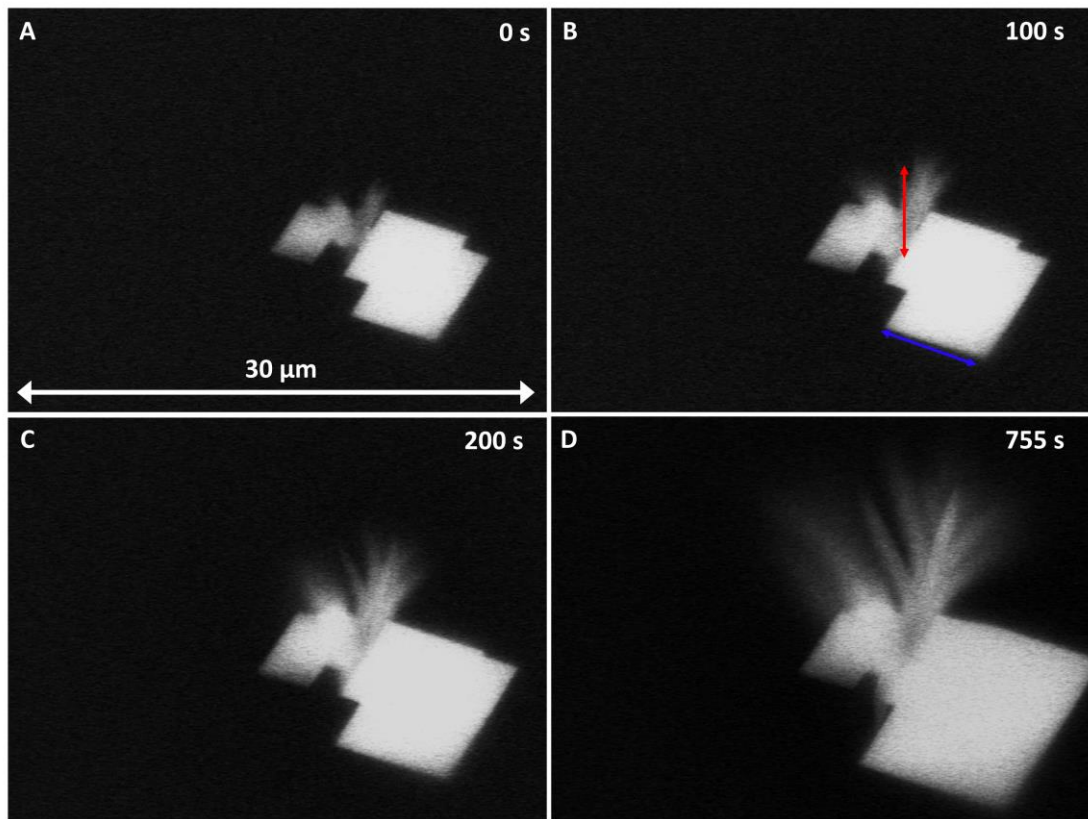


Figure 3.22 Sequence of ASEM images showing the growth of aragonite from a {104} calcite facet in the presence of ethanol (15 vol%), directly after mixing. The Ca^{2+} solution was injected in the ClairScope petri dish to promote crystal attachment to the SiN window. The CO_3^{2-} solution was added after focusing. Aragonite growth started approximately 4 minutes after mixing. The arrows in (B) refer to the length measurements in Figure 3.23.

Backscattered electron SEM images were taken after crystal precipitation from JEOL ClairScope petri dishes during ASEM experiments, which took approximately 50 minutes. Afterwards the liquid was removed by a pipet and a lid was positioned on the dishes to prevent contamination. Later conventional SEM imaging was performed on the dry dishes, observing the crystals from the top instead of the bottom view images provided by the ASEM.

In Figure 3.22 the onset of growth of an aragonite bundle can be seen, while the calcite crystal facets are already fully developed approx. one minute after mixing the solutions. A qualitative comparison of growth rates of the aragonite bundle length and calcite fore facing facet is shown in a graph in Figure 3.23. No absolute growth rates could be recorded as the viewing direction is not perpendicular to the crystal facets.

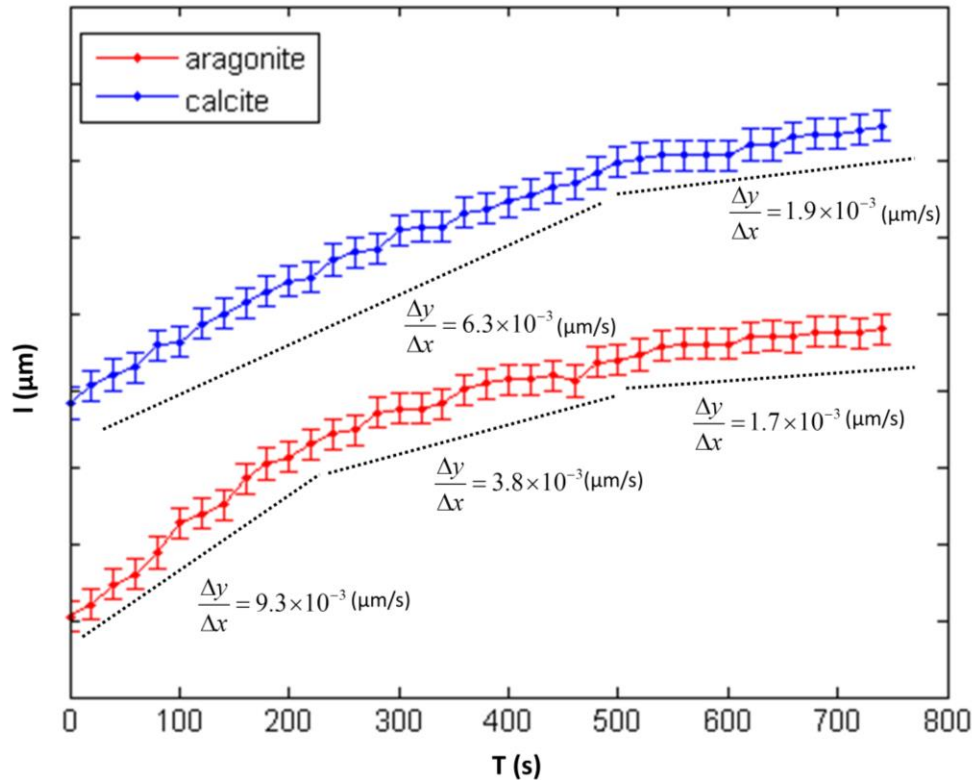


Figure 3.23 Graph showing measurements of crystal growth over time. As a size measure the length of the front edge of the calcite crystal and the length of central aragonite needle in Figure 3.22 are measured over 20 seconds intervals.

The graph shows that initially the aragonite bundle extends the fastest (in length), however the relative calcite crystal facet growth rate catches up and decreases less in time than the growth rate of the aragonite bundle.

A detailed TEM and SAED analysis of the aragonite bundles shows that they are polycrystalline (Figure 3.24) consisting of stacks of nanocrystals which are roughly 100-150 nm in size (Figure 3.24 and Figure 3.25). This phenomenon explains the segmented surface appearance of the crystal needles as seen by SEM. It was found that the nanocrystals share a common crystal orientation throughout the stack. The growth directions of the stacks were determined to be preferentially aligned along the [001] or c-axis orientation. This was determined for multiple ($n = 5$) stacks from different aragonite bundles by projecting the length axis of the stack onto the respective diffraction pattern, for additional data see appendix B. The association between crystals is however imperfect and misalignments of $\geq 3.5^\circ \pm 0.5^\circ$ (Figure 3.25) occur from one grain to the next.

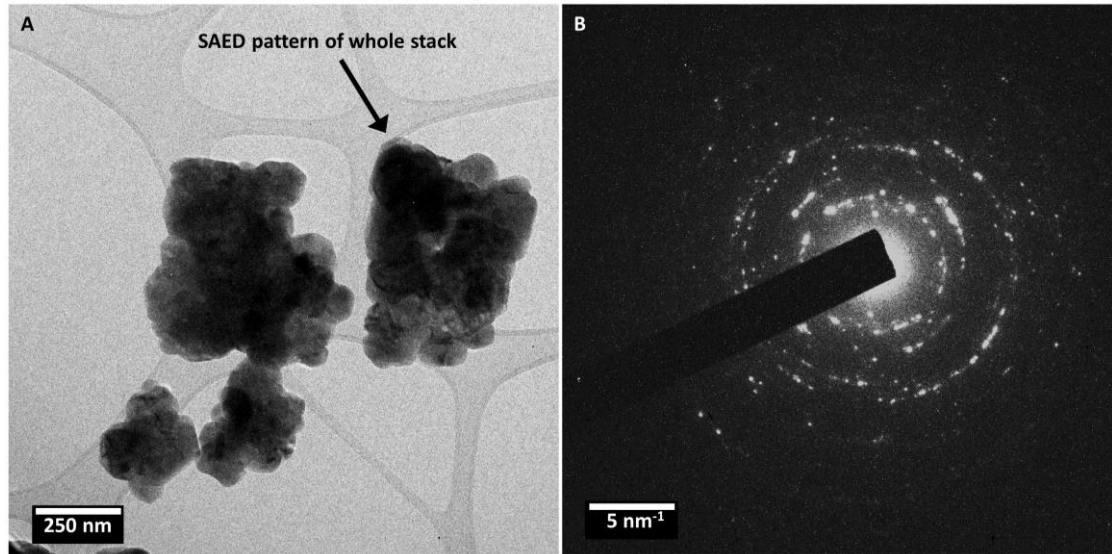


Figure 3.24 A) TEM bright field micrograph of fragments of aragonite bundles precipitated with 25 vol% ethanol, matured for 1 hour. B) SAED pattern of the right-hand fragment in A, taken with a large selected area aperture (approx. 500 nm area size), showing a polycrystalline symmetry for the overall stack.

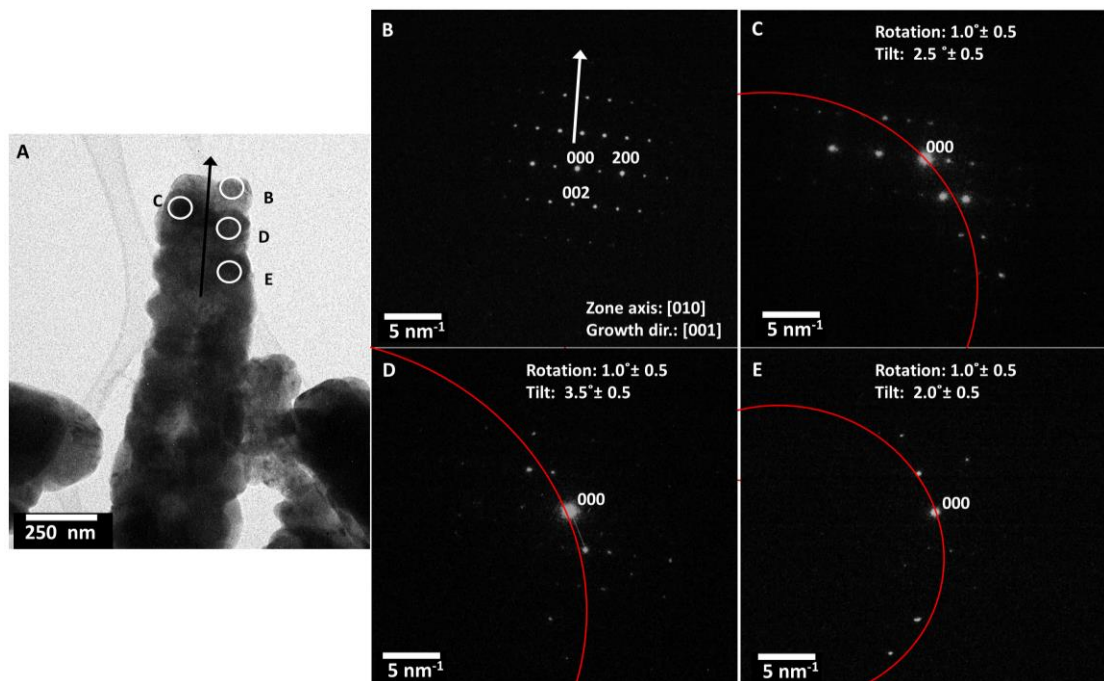


Figure 3.25 Aragonite precipitated with 25 vol% ethanol, matured for 1 hour. A) TEM bright field image, arrow indicates the bundle's overall growth direction, circles indicate the respective positions of the SA aperture. B-E) Diffraction patterns related to SA aperture positions (area size approx. 30 nm) in A. Top crystal grain (B) is manually tilted in a low index zone axis [010], the arrow is the projected growth direction of the bundle in reciprocal space determining a [001] growth orientation. DP's are taken from surrounding grains without further manual tilting. The red line indicates the Laue circle.

This is due to a combination of in and out of plane bending and tilting of grains along the stack's longitudinal axis. This causes the shifting of intensity and rotation of the diffraction pattern away from the ideal zone axis, as can be deduced from the position of the centre of Laue circle and the measure of pattern rotation.

It is observed that the physical appearance and crystallographic behaviour of the aragonite needle-like bundles precipitated in the presence of ethanol and the nanocrystal stacks in adult coral skeletons are remarkably similar. The individual nanocrystals in the bundles are somewhat larger (100 - 200 nm) as compared to the coral's (50 - 70 nm), but the crystal alignment behaviour over several hundred nanometres along stack length axis and the [001] preferential growth orientation are equivalent. Also, both structures do not retain their crystal association over larger areas and thus appear polycrystalline on the micrometre scale. The implication of this correlation will be discussed in detail in section 3.3.

Summary of the findings on EtOH aragonite

We found that aragonite in the form of sheaf-shaped bundles of crystalline needles forms preferentially to calcite and vaterite at high ethanol (25-50 vol%) concentrations from saturated aqueous mixtures of 0.1 M CaCl₂ and 0.1 M Na₂CO₃. At lower ethanol concentrations (≤ 15 vol%) calcite is the dominantly formed crystal phase. This is in agreement with results published by Sand *et al.*, 2011 [96].

The aragonite needles are up to tens of micrometres long, sometimes hexagonal in shape. They always show a segmented surface. TEM analysis demonstrates that these bundles consist of stacks of nanocrystals, with individual grain sizes of 100 to 150 nm in size. SAED analysis was performed over several stacks, and showed that there is a crystal alignment association over several hundred nanometres between grains within discrete stacks. Although there is a common crystal orientation in the [001] direction along the length axis within stacks, the individual grains exhibit misalignments of several degrees from one grain to the next. Overall, on the micrometre scale the stacks are polycrystalline.

3.3 ORGANIC ADDITIVES AND ARAGONITE CRYSTAL GROWTH

In pure systems (no organic additives), at ambient conditions, the first phase to precipitate from a supersaturated solution is usually amorphous calcium carbonate (ACC) [24]. This phase is however thermodynamically unstable at ambient conditions and it transforms to vaterite within minutes [25]. As the saturation level decreases vaterite transforms to calcite at temperatures under 40°C and to aragonite at temperatures above 40°C [25, 26]. Even though ACC and vaterite are unstable phases they are found in nature as biominerals [3, 29-31]. Similarly, aragonite is one of the most abundant biominerals, as it is formed by corals (*Scleractinia*) and mollusc shells (in the nacreous layers) [130, 157, 158]. These organisms must have mechanisms to promote and stabilise mineral polymorphs that are not energetically preferred phases in bulk precipitation under ambient conditions. Factors that are thought to be influential are: the seawater chemistry (e.g. Mg and Ba content)[36], organic additives [12, 22, 33] and effects of crystallisation within confinement [34, 35].

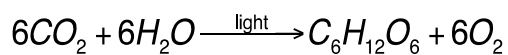
Here we focus on aragonite formation in coral systems and how the organism affects the crystal morphology. The mechanism behind scleractinian mineral formation is highly complex and not well understood. We attempt to link certain known/accepted aspects of the coral calcification fluid dynamics to observations made in this study with respect to the microstructure and organic content.

Generally, models of coral calcification consist of two levels: 1) regulation at a physiochemical level of the ion transport in conjunction with carbonate chemistry control (often called 'the proton pump'), and 2) regulated secretion of a skeletal organic matrix into a hydrogel-like or liquid environment between the calcifying cells and the skeleton. This constitutes the Extracellular Calcifying Medium (ECM) as discussed by Allemand *et al.*, (2011)[63], Tambutté *et al.*, (2011)[66] and Moya *et al.*, (2012) [64].

In this study a striking change in microstructure between the repetitive, relatively narrow bands of a porous nanocrystalline phase (randomly orientated to

partly aligned) and dense large acicular crystals, is shown. Dark (granular and porous) and bright bands (acicular and dense) as observed in optical microscopy correspond to higher and lower porosity respectively, due to increased light scattering by the porous nanocrystalline regions. Many studies suggest that these dark bands are also enriched in organic material [68, 127, 128, 159] and this was also derived here from Raman mapping (see paragraph 3.1.2). This microstructural feature causing dark/bright bands in optical images has also been studied by SEM, linking this pattern to a diurnal growth cycle [130, 131] which is likely to be related to photosynthesis performed by the zooxanthellae. Zooxanthellae are symbiotic algae that live in the upper tissue of the coral in direct contact with seawater and they provide their host (the coral) with nutrients. Although their direct or indirect impact on calcification is still highly debated [63] it is accepted that on the macroscale the algae enhance calcification rates under illumination [160-162]. Additionally a clear saturation level change over light-dark cycles of the internal coral pH has been measured [2]. In order to discuss this relationship the process of photosynthesis has to be discussed in more detail.

Photosynthesis can be described by the reaction equation:



During daylight hours the amount of available oxygen increases to up to >250% of air saturation in the calcifying medium [163]. This, as well as the sugars provided by the zooxanthellae is vital for the production of Adenosine-5'-triphosphate (ATP) molecules and is thus directly linked to the energy available to the coral for calcification. Consequently, this is related to processes such as the removal of H⁺ by proton pumping to maintain high CaCO₃ supersaturation levels. Kulh *et al.* (1995) [163] have found that oxygen levels can be depleted to 2% of air saturation after sunset in the calcifying medium.

It has been observed that the granular growth starts at twilight and is rapid under supersaturation levels (high alkalinity and unlimited O₂ available), with the growth slowing down during the night due to a decrease in supersaturation (Ω)

(and limited O_2 supply) and changing to acicular growth. This acicular growth then speeds up during daylight hours with increasing oxygen, organics and Ω levels (M. Holcomb, personal communication, 2012).

We believe that the rapid calcification at dusk causes the formation of the porous unaligned nanocrystalline phase, which when calcification slows down – due to changing chemistry under darkening conditions – allows for an increased alignment, preferentially in the [001] direction of the nanocrystals – to ultimately form the dense aragonite needles elongated along the c-axis or [001] direction close to sunrise, followed by their prolongation during the day. These concepts are summarised in Figure 3.26.

Another possible explanation for the change in microstructure would be the poisoning of certain crystal facets by organic molecules, which have built up during the day due to photosynthesis (e.g. sugars etc). This could also lead to an interruption of the acicular phase. However, Holcomb *et al.*, (2009) [164] showed that synthetic precipitation of aragonite crystals from seawater with exceptionally high pH levels (i.e. high saturation state Ω) resulted in the growth of spherulites with granular morphology in the centre and acicular needle-shaped crystals radiating outwards, including granular banding, without the presence of organics. This suggests that the diurnal cycle in carbonate chemistry is more likely to be the controlling factor.

Both the synthesis experiments of Holcomb *et al.* (2009) [164] and the microstructure in algae-deprived coral larvae show a general spherulitic growth with banding indicating that this microstructural element in itself is not restricted to a diurnally influenced carbonate chemistry by zooxanthellae. It is likely that a nutritional cycle, influencing the carbonate saturation - whether caused by cyclicity in symbiotic algae productivity, (tidal) currents or other factors - is the direct cause of a change in microstructure.

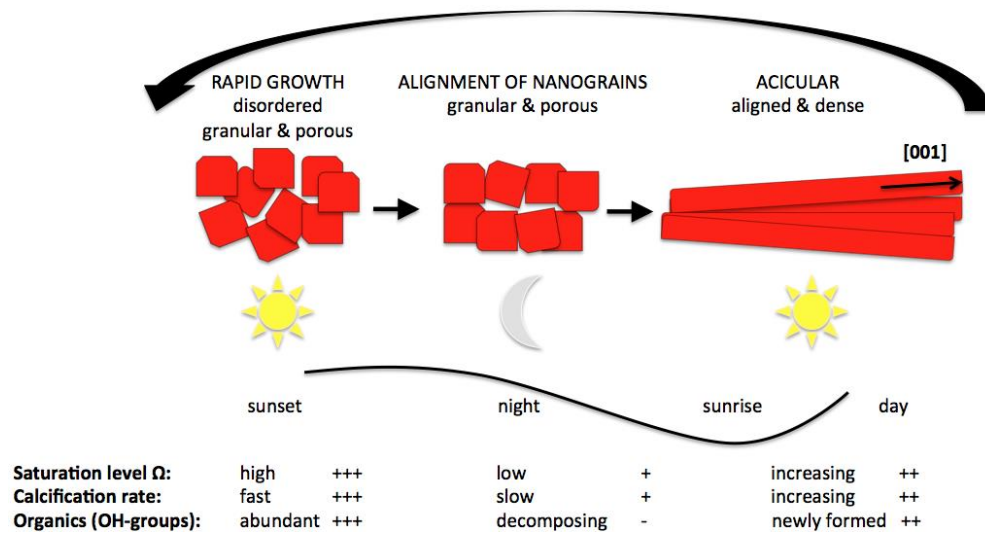


Figure 3.26 Proposed growth model linking light enhanced calcification and the related abundance of organics to the microstructural patterns observed in adult Scleractinian corals. Reprinted from Van de Locht *et al.*, (2013) [132] with permission. Elsevier Copyright Clearance Center (license number 3345260883340).

This needs to be further analysed in future TEM studies investigating the possible presence of a nanocrystalline phase in non-symbiotic adult coral specimens.

Further impacts from organics in crystal arrangement

This study (and many others e.g. [76, 78]) has shown that within the coral skeleton different organic residues are present, especially at the COC, in the nanocrystalline porous bands and at the crystal growth front between spherulites. These organics were found to consist of small fibre bundles, large isolated fibres and sheet like constituents. Raman spectroscopy proved the presence of proteins in the small bundles and indicates the presence of glycerol within these materials was also implied. HPLC demonstrated the presence of serine and threonine amino acids. These organic molecules all bear a large number of OH-groups. Polysaccharides are known to be abundantly present in the coral skeletal organic matrix [82, 127] and also these contain large quantities of OH-groups. To investigate the effect of organic additives with OH-groups on CaCO_3 crystallisation, synthetic experiments were carried out (see section 3.2).

Experiments to evaluate the effect of OH-group containing molecules on carbonate precipitation have shown that increasing ratios of ethanol to water mixtures shift the preferred precipitation from calcite and vaterite to aragonite needle-like bundles ([96]). Furthermore, SEM and TEM data shows that the aragonite bundles do not consist of single crystal needles, but that the individual needles are polycrystalline (Figure 3.24). The needles consist of semi-aligned nanocrystal stacks aligned along the [001] direction (Figure 3.25). This is a striking resemblance to the partly aligned polycrystalline phase seen in the adult *Porites lobata* specimen.

This raises the question whether the role of OH-groups in organics in coral calcification is greater than previously assumed. Sand *et al.* (2010)[59] studied the role of the OH bond in ethanol binding to calcite crystals by a combination of atomic force microscopy (AFM) and molecular dynamics (MD) simulations. They found that ethanol-OH attachment on calcite is stronger than water-OH binding and that the first absorbed layer of ethanol is highly ordered. The strong ordering of the ethanol results in a hydrophobic layer and has therefore a significant impact on mineral growth and dissolution [59]. The end of the ethanol molecule pointing into the solution (CH_3 group) is hydrophobic therefore the water structure is *broken* around it and counter ions; the layer compensates charges and makes the charged crystal surface less accessible. Ethanol has a polar head group (OH) and a non-polar tail (CH_3). If the ethanol is in solution, the water molecules form a more or less rigid *cage* around this non-polar tail, which reduces the entropy, because these H_2O molecules can't move freely anymore. If the ethanol adsorbs on a surface the *cage-interface* is smaller which leads to higher enthalpy in the water (i.e. more water-water bonds) and a higher entropy.

In this system ion transport is confined to specific locations and can influence the entropy and enthalpy of the system, as such it could provide organisms with control over the mineral morphology and crystallographic orientation. However, the outcome will be different if you replace the ethanol by sugars which are more hydrophilic, and further experiments should be designed targeting coral specific organic molecules as additives in synthetic systems.

In conclusion, the nutrients provided by the symbiotic algae in the corals are limited to a light-dark cycle and thus induce a cyclicity to the available energy for skeleton accretion. This causes in a change in carbonate supersaturation (Ω) and thus induces a particular microstructural evolution with diurnal bands of specific crystal morphologies throughout a spherulite. The preferential alignment of the nanocrystals in stacks in the [001] direction are possibly caused by organic additives promoting this particular phenomenon, due to the OH-attachment on crystal surfaces controlling the ion-exchange at the hard/soft matter interface. These concepts and some of the related data were published by this author in Van de Locht *et al.*, (2013) [132].

4. CALCITE BASED MINERALS

Characterisation and interpretation

In this chapter the crystal structures of two calcite based systems will be described based on experimental results. Firstly, the results describing the ultrastructure of a species of coccolithophore (a marine alga) and the crystallographic properties of its individual building blocks will be presented. A subset of the data presented here is published in Van de Locht *et al.*, (2014). [165], the HAADF STEM tomography data was obtained by Thomas Slater and Sarah Haigh of the University of Manchester, School of Materials.

The study showed that the coccoliths of *Rhabdosphaera clavigera* contain a structurally distinct rim structure and central crystal arrangement. The rim was found to conform the V/R model [103], based on other coccolith species and consists of complex-shaped, interlocked calcite crystals. The central arrangement in contrast, consists of simple {104} calcite rhombohedra assembled in a five-fold symmetric spine structure.

In the second part of this chapter the results on synthetically produced calcite nanowires of approximately 70 nm and 250 nm in diameter (samples provided by Yi-Yeoun Kim, University of Leeds, Department of Chemistry) are presented. The experimental results and data analysis of the calcite nanowires are in parts the work of this author and Andreas Verch (University of York, Department of Physics), a subset of the data is published in Verch *et al.*, (2014) [166]. The thin nanowires were found to be single crystalline and to exhibit bend and twist, expressed as crystal

lattice distortions along the longitudinal axis of the wires. From simulation studies it was concluded that this was caused by surface tensile and shear stresses respectively. The thicker nanowires were often polycrystalline and did not show similar bending and twisting behaviour, showing that this is a size-dependent phenomenon.

In the last part of this chapter a comparison between the presented biogenic and biomimetic calcite systems is made and the influence of confinement on calcite crystallisation is discussed. It is concluded that on the nanoscale external surface stresses can cause calcite single crystals to grow in non-crystallographic orientations as seen in the nanowires. It is therefore suggested that a similar process could provide intracellular coccolith calcite formation with a mechanism to control shape and size of its skeletal elements.

4.1 COCCOLITH ULTRASTRUCTURE

Coccolithophores are unicellular marine algae that create an intricate exoskeleton of nanoscale calcite platelets. They control shape, size and crystal orientation to a remarkable degree. The nucleation and growth mechanism in coccoliths is described for 'flat' coccoliths and is called the V/R model [103, 104]. It is based on the observation that the coccolith rims are characteristically formed of two cycles of interlocking crystal units, one with sub-vertical c-axes, termed V-units, and the other with sub-radial c-axes, R-units. These originate as alternating nuclei in the proto-coccolith ring which forms on an organic template. For a more detailed introduction to coccoliths see section 2.1.3.

Some species, however, particularly those from the *Rhabdosphaeraceae* family, show characteristic spine-shaped features protruding from the centre of the coccolith disk and the formation process of these structures is largely unexplained.

In this study, the structure of *Rhabdosphaera clavigera* (Figure 4.1) is described in detail through a combination of electron microscopy techniques, as published in Van de Locht *et al.* (2014). [165].

4.1.1 RESULTS OF THE EM CHARACTERISATION

Coccolith rim and disk

The coccolith rim consists of a circle of interlinking crystal units (ca. 200 nm x 300 nm x 50 nm); these units appear to have an exterior downward kink to interlock with the transitional elements towards the centre as shown in Figure 4.2. A yellow patch in the images indicates the crystal unit. The rim is attached to the central elements via 'transition rods' that can be observed in the bottom view (Figure 4.2 B and C; indicated in green). These rods are inclined by approximately 20° angle relative to the rim units, tilted towards the centre and are approximately 100 nm x

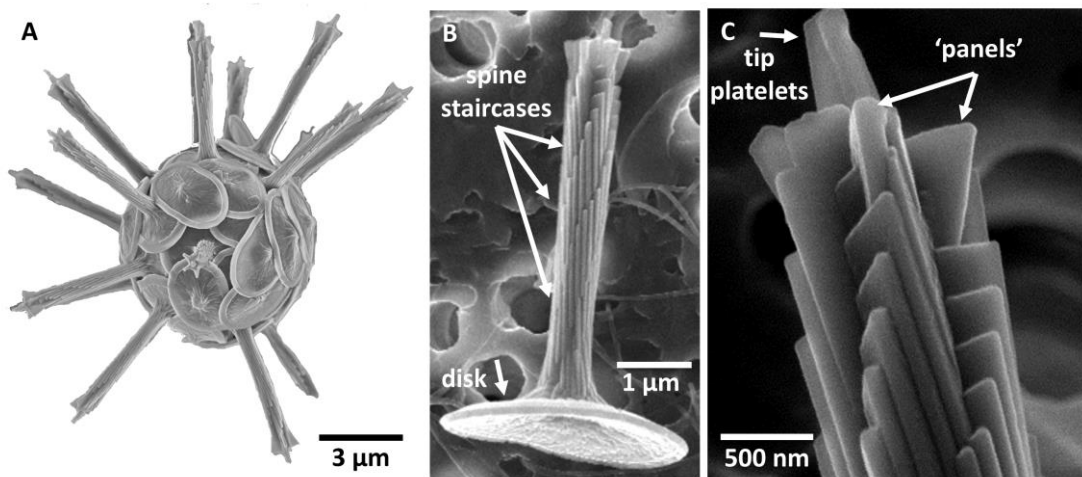


Figure 4.1 SEM images of *Rhabdosphaera clavigera*. A) Complete coccosphere. B) Detached coccolith with spine. C) Side view of the tip of the spine.

300 nm x 50 nm in size. For every rim unit, there is a transition rod. This rim structure is conserved across the Rhabdosphaeraceae [99, 167, 168]. The main rim units are *V*-units and the transition units are thought to be *R*-units. The centre is formed by radial cycles of imbricate tiles, with the left tile consistently overlapping its right-hand neighbour, forming an anti-clockwise spiral towards the centre (Figure 4.2 A; indicated in red). The tiles are almost square-shaped in top view and are about 200 nm x 200 nm x 50 nm, although they show irregularities in both shape and size as well as in overlap step. The innermost central tiles appear to push each other up in a staircase arrangement, forming the spine-base. Surprisingly, the spines are always consistent in quantity (i.e. five equally long staircases and the tip has fifteen units), size and shape of crystal elements, whereas the central parts of the coccolith plate frequently contain irregularities.

Spine morphology

The spine structures protruding from *Rhabdosphaera clavigera* coccoliths in our sample are 5.0 – 5.5 µm in length and have a diameter of approximately 500 nm. A detailed TEM analysis in conjunction with electron diffraction and SEM studies show that the spine consists of single crystal calcite elements (Figure 4.3) that are arranged in a five-fold chiral symmetric structure around its longitudinal axis. The

calcite crystal platelets are organised in five discrete ‘staircase’ structures. The long crystal platelets that comprise the staircase steps are approximately $80 \times 200 \times 1000$ nm and have a $12\text{--}14^\circ$ angle between steps. In total five staircases revolve around the spine’s longitudinal axis and spiral towards the tip, each staircase effecting a near rotation of approximately 280° (Figure 4.1).

The chirality of the spine structure has been observed to be constant over more than 50 *Rhabdosphaera clavigera* coccospheres within the SEM image collection of the Natural History Museum London. These observations were made from diverse samples on which chirality could be determined reliably, including specimens from diverse localities in the North and South Atlantic, Pacific Ocean, Caribbean, and the Mediterranean Sea. Similarly, the tip itself always consists of 5 elements.

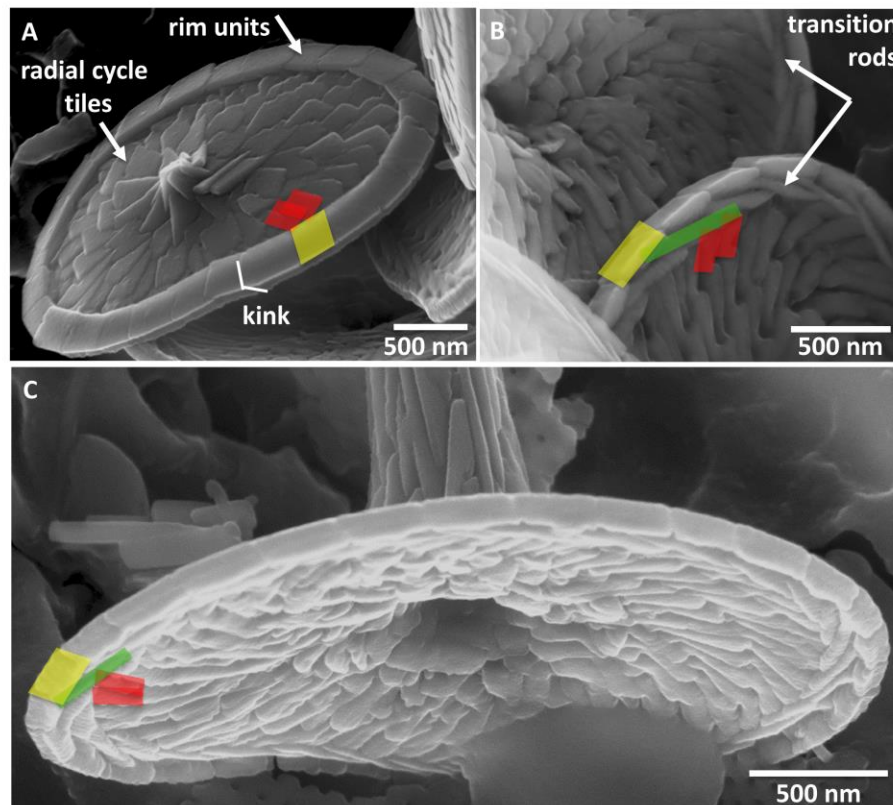


Figure 4.2 SEM micrographs of the coccolith disk. A) Top view of a coccolith without spine, with interlocking crystals in the rim (yellow) and imbricated radial cycles of central crystals (red). B) Detail of the coccolith underside with indicated rim crystals (yellow), transition rods (green) and radial cycles of tile crystals at the centre (red). C) Detached coccolith with spine, viewed from below.

Bright-field transmission electron microscope images show the presence of a homogenous 25 nm thick and apparently amorphous layer surrounding each calcite platelet as shown in Figure 4.4B. We analysed this layer using electron energy loss spectroscopy (EELS low loss spectrum, see appendix C) and found that it does not contain calcium, in contrast to the crystal panel. This suggests that the layer does not consist of amorphous calcium carbonate (ACC). ACC has often been observed as a precursor phase in biomineral systems [29, 30, 169, 170], but has not been observed in coccoliths. We speculate that it consists of organic material presumably related to polysaccharides previously identified in coccoliths [101, 171-173]. Such organic coatings were first observed using TEM in 1955 by Halldal and Markali in decalcified holococcoliths [174].

SEM imaging of the bottom of a detached coccolith (Figure 4.2C) suggests that the spine has a hollow core where it meets the plate. TEM images of the spine tip show a lighter contrast in the centre (Figure 4.3C), suggesting that a hollow or low density non-crystalline centre persists along the length of the spine. Indeed, a 3D tomographic reconstruction using HAADF STEM imaging confirms that the core of the spine consists of a material which has much lower electron density compared to the surrounding crystalline platelets suggesting that it is either hollow or contains lighter most probably organic matter, see Figure 4.5.

Tip of the spine

SEM imaging (Figure 4.4A) combined with tomographic data (Figure 4.5) reveals that the pointed tip of the spine consists of five, roughly 500 nm long intertwining platelets, extended parallel to the long axis of the rod. A cross-section perpendicular to the long-axis direction of the spine, just below the base of the pointed tip crystals, shows that this region consists of fifteen individual elements (Figure 4.5A and Figure 4.6A).

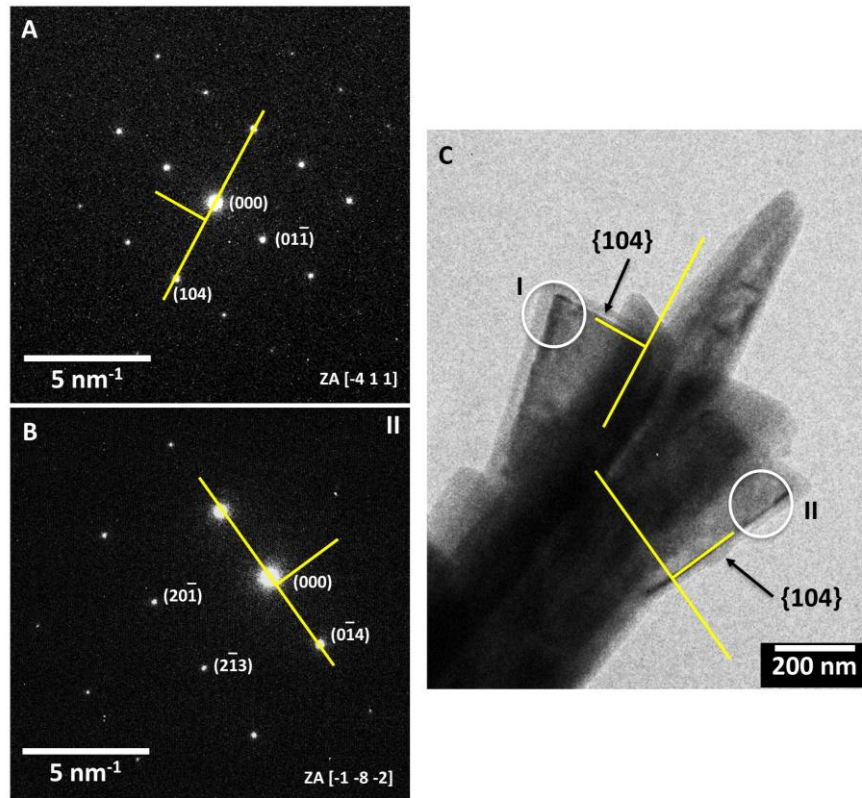


Figure 4.3 SAED patterns accompanying the TEM bright field micrograph, white circles indicate the position of the selected area aperture. A) Diffraction pattern of left panel (I) indicating the $\{104\}$ family of planes in reciprocal space (long yellow line), which is perpendicular to the plane it represents in real space (short yellow line). B) The same is indicated for the right panel (II). C) Projection of the $\{104\}$ planes in reciprocal and real space onto the image shows that the panel crystals are delimited on both top and side edge by the $\{104\}$ family of planes (or $\{10\bar{1}4\}$ in fourfold notation: $(hkl) = (hk, (-h-k), l)$).

Furthest from the core, there are five broad side 'panels' (roughly $100 \text{ nm} \times 200 \text{ nm} \times 400 \text{ nm}$ in size), orientated with their longest edge parallel to the long axis of the spine and inclined such, that they protrude from the core. Closer to the spine core there are five smaller 'leaf' shaped crystals which form the final step of the staircase towards the pointed tip (Figure 4.6A). The side panels and leaf crystals occur in turn at a 90° angle to each other. The panel crystals cut through, or are inter-grown with, the penultimate crystal in each staircase (Figure 4.1C and Figure 4.6B). Closest to the core there are five smaller units, which interconnect the 'panel' and 'leaf' crystals (Figure 4.5A and 4.6A).

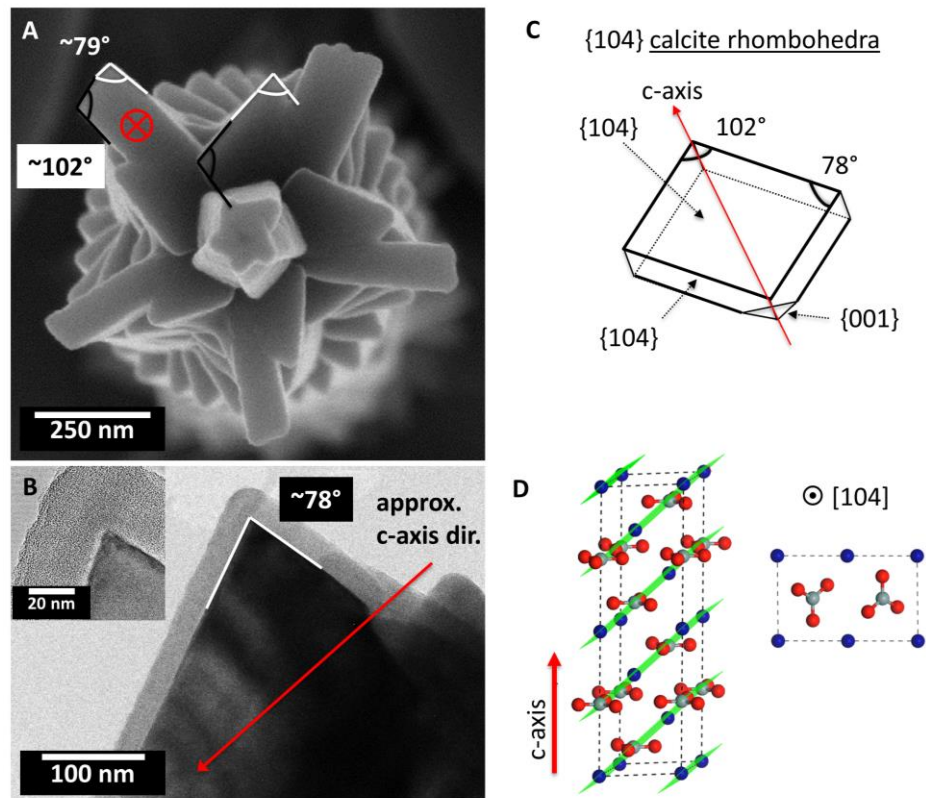


Figure 4.4 A) SEM image of the tip of the spine. The angles between facets were determined with a tolerance of $\pm 5^\circ$ the crossed circle indicates that the c-axis is roughly orientated into the page. B) TEM bright field image of the side view of a crystal panel showing the position of the acute angle at the outer edge of the crystal panel. Surrounding the panel is a homogenous amorphous layer of ± 25 nm as shown in detail in the inset. C) Schematic drawing of $\{104\}$ calcite rhombohedra with obtuse and acute angles of 102° and 78° , respectively. D) Calcite unit cell with $\{104\}$ planes indicated by the green coloured areas on the left, the dashed line indicates the edge of the unit cell and does not relate to angles in the crystal facets. The right schematic shows the atomic arrangement viewed along the $[104]$ direction (Ca: blue, C: grey and O: red).

The tomographic data reveals that these small units are in fact the base of the outer tip crystal platelets which are extended downwards into the core of the spine.

Furthermore, the tomographic cross section along the long-axis of the spine suggests that a similar platelet core structure is present lower down the spine (Figure 4.5C). This appears to be a repeating feature, albeit no tomography data exist for the lower section of the spine.

SAED patterns show that the side panels are delimited by calcite $\{104\}$ planes on the top and side edges. In combination with angle measurements from several

panels over different spines it is concluded that they have a {104} calcite rhombohedra structure (Figure 4.3 and Figure 4.4). Angle measurements from multiple leaf-shaped crystal elements of diverse coccosphere spines exhibit an average obtuse and acute angle, which suggests that the leaves are also {104} rhombohedra (Figure 4.4). The atomic arrangement at this particular crystallographic orientation is shown schematically in Figure 4.4D.

It was not possible to obtain conclusive SAED data from the leaf shaped crystals (i.e. staircase platelets) as well as the outer tip crystals, since they sterically overlapped in beam direction. Hence, an unambiguous analysis of the resulting superimposed diffraction patterns was not possible. A focussed ion beam sample preparation approach could be considered for further analysis of these elements in the future.

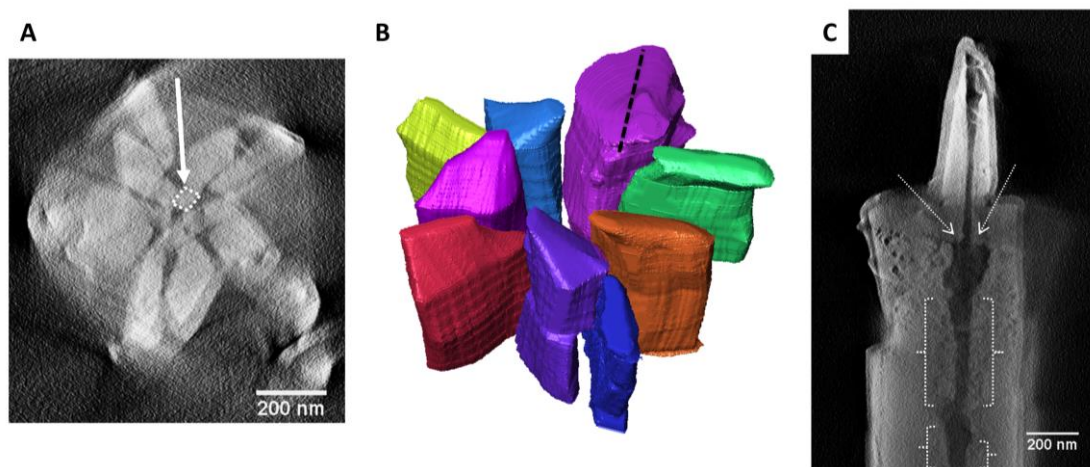


Figure 4.5 3D STEM tomography reconstruction of the spine tip. A) Cross section perpendicular to the long-axis of the spine at the base of the pointed outer-tip crystals, revealing a distinct arrangement of five nanocrystals (assigned by a white arrow, the contour of one of the nanocrystals is highlighted by a dashed line). B) Segmented crystal units forming the lower part of the spine tip. This consists of ten units, however due to tilting limitations of the tomography holder and shadowing from the lacy carbon substrate, only nine elements could be identified using this method. The large purple segment consists of two crystals as can be interpreted from TEM and SEM data and is indicated in the schematic with a dashed line. C) Cross section along the longitudinal axis of the spine, with the darker core revealing a continuous void or presence of less electron dense material at the centre of the spine. The arrows and brackets highlight crystal elements that extend into the core of the structure.

4.1.2 INTERPRETATION OF COCCOLITH STRUCTURE

Summary of the structural characterisation

The coccolith rim and disk are constituted of three structural elements as indicated in Figure 4.1: A rim of interlocking complex-shaped (exterior downward kink) crystals (analogous to *V*-units), connected via transition rods (interpreted as *R*-units) to central imbricated tiles forming an anti-clockwise spiral around the disk centre. At the centre the imbricated tiles push each other up to form a small crest. This acts as the base of the spine - in those coccoliths that exhibit a spine - although the elements are distinct from the spine elements. A schematic drawing of a cross section of the disk is shown in

Figure 4.7. The rim structure conforms to the general V/R growth model and nucleates intracellularly from a proto-coccolith ring as described in [103-105, 175, 176].

In contrast to these complex disk elements the spine is formed from an arrangement of simple calcite {104} rhombohedral building blocks at constant angles to each other in a chiral five-fold symmetric structure, this is drawn schematically in Figure 4.6. Three building blocks can be distinguished as: 1) elongated platelets (80 nm × 200 nm × 1000 nm) making up five staircases (the top crystal looking like a 'leaf' in frontal view), 2) five broad panels (± 100 nm × 200 nm × 400 nm) that protrude into the lateral plane of the tip of the spine like the petals of a flower and 3) five elongated platelets (± 500 nm in length) extending along the longitudinal axis making up the outer tip. The bottommost part of the outer tip crystal platelets appear to form a core structure for the other surrounding crystal units of the tip. It is also suggested that this core-like structure is repeated lower down in the spine as can be observed in the cross-sectional slices through the tomogram. Possibly, these central elongated nano-platelets act as a base onto which the other crystal units have assembled or nucleated, guiding the overall crystal orientation in a similar way as the proto-coccolith ring.

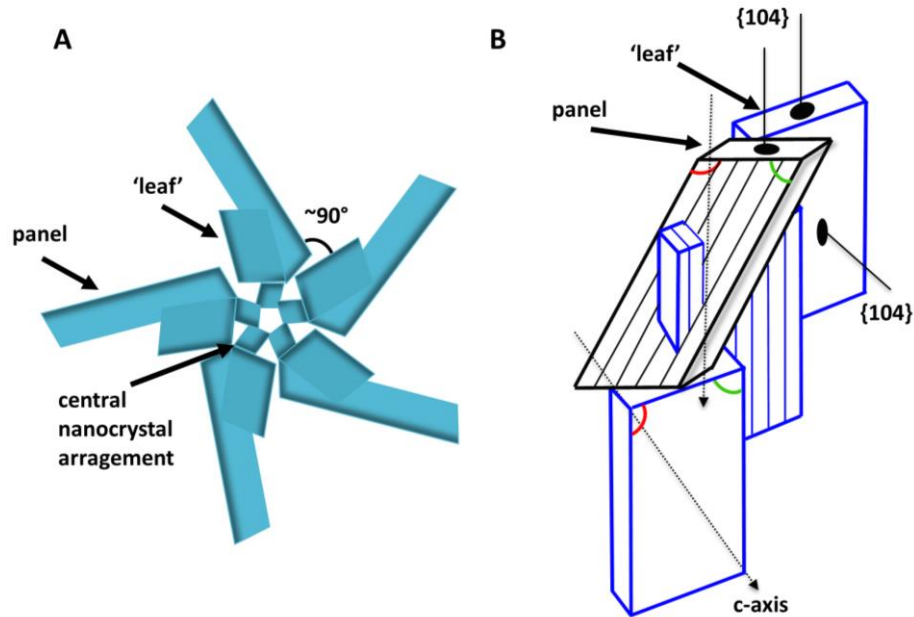


Figure 4.6 Schematic of ultrastructure of the spine. A) Frontal view of tip, without top extension, showing panels, leaf shaped crystals (i.e. top of crystal staircases) and centrally placed nanocrystals. B) Side view of the top of a staircase with the panel crystal intergrown with the penultimate staircase crystal. Crystal surfaces are indexed, the red curve indicates the obtuse angle (102°) and the blue curve the acute angle (78°) in $\{104\}$ calcite facets.

Whether this nano-platelet core structure is in itself guided by an organic template, as has been found for the proto-coccolith rim, remains unclear. It has, however, been observed by light-microscopy, that the coccoliths with attached spines are, like all heterococcoliths, formed within the cell membrane (appendix C).

Properties of the basic building blocks: calcite (104) facets

Synthetic crystals grow from a supersaturated calcium carbonate solution - with no organic additives present - perfect calcite rhombohedra with stable $\{104\}$ faces. However, in coccoliths, like in most other biomineralising systems, the mineralisation is largely controlled by the biochemistry of the organism leading to an intricate nanocrystal assembly thought to be associated with coccolith associated polysaccharides (CAPs) [172].

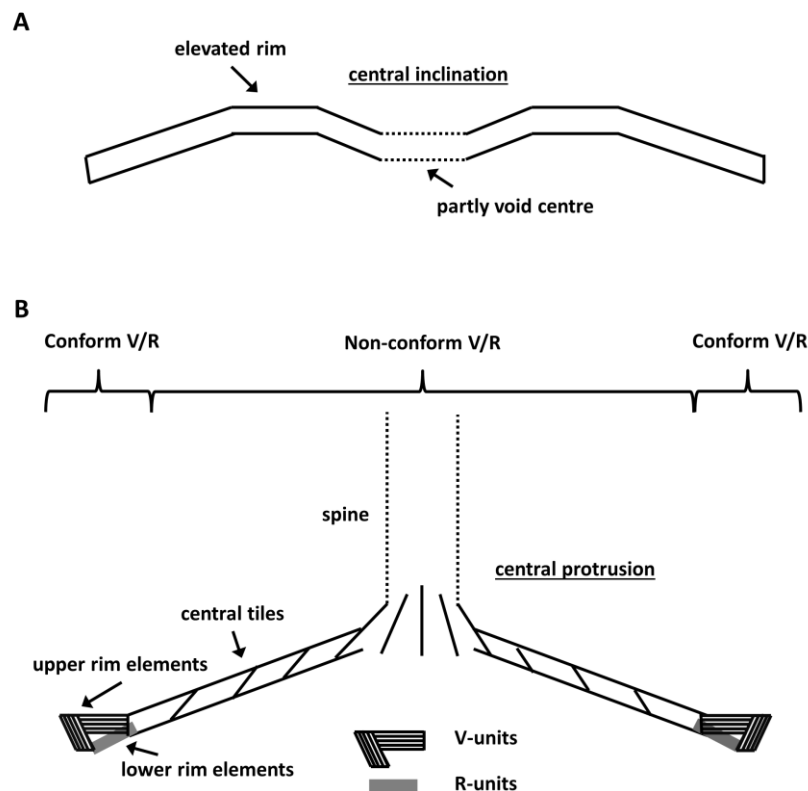


Figure 4.7 Schematic two-dimensional representation of two coccolith disk cross sections. A) A generalised model for species without central spine structures. The coccolith has an overall concave proximal (inner) shape but has a central depression which, depending on the species, is void, partly filled with crystals or completely crystalline. B) A generalized model for *R. clavigera*, the V/R rim units are indicated as well as the central elements that do not conform the V/R growth model. The coccolith has an overall concave proximal shape and has a central protrusion leading to possible spine formation.

Although the exact process is not understood it is commonly accepted that the crystal planes on which biomolecules are preferentially adsorbed are expressed via inhibition of these facets. Hendriksen *et al.* 2004 [172] found that CAPs from *Emiliana huxleyi* interact differently with crystal surface sites defined by acute rather than obtuse angles and that acute sites are blocked during dissolution and growth. In this way the CAPs can lead stable {104} facets to extent on the obtuse edges, thus stimulating the development of faces with lower angles to the c-axis. However in the *R. clavigera* spine the stable 'easy' {104} rhombohedra structure seems to be preferred, even though a homogenous organic coating around each crystal element

is present. Furthermore, no crystal steps were observed on the elements constituting the spine. It appears that beside the complex laterally extended structure the calcite crystals differ significantly from coccolith rims that are growing following the *V/R* model. It seems that the organism compensates the complex lateral structure with the use of simple, stable {104} rhombohedral building blocks, following a five-fold symmetric model.

An explanation for the role of the organic coating on *R. clavigera* spine crystals may be related to the findings of Cooke *et al.* 2010 [95], as the coating does not always seem to enable a surface stepping mechanism. Their work showed, based on molecular dynamics simulations and atomic force microscopy of ethanol/water mixtures with calcite crystals, that a stable and highly ordered organic layer attaches to the {104} calcite face making it difficult for incoming ions to penetrate to the crystal surface. The organic coating on the spine may help to prevent recrystallization on the {104} surface and decrease direct calcite/seawater interactions.

Ultrastructure of *R. clavigera* in context

As already mentioned, the ultrastructure of the *R. clavigera* spine is distinct from that of most coccoliths and does not comply with the *V/R* model. Note, that within the *Rhabdosphaeraceae* family many other species show a disjunct central structure often with elongated central protrusions (e.g. *Algirosphaera*, *Acanthoica*, *Anacanthoica* and *Discosphaera*, amongst others).

Algirosphaera robusta for example, has a central structure in the form of a prominent 'hood' [177]. Probert *et al.* 2007 [177] described the hood as consisting of several sets of elements, amongst which 'tiles' positioned at regular interfaces and angles spiralling to the top of the structure. The inner part of the hood was found to be void. Although having a very different physical appearance there seem to be some similarities between the building blocks. Both the 'tiles' mentioned by Probert *et al.* 2007 [177] and the staircase platelets form a spiral structure along an elongated

axis, albeit with much less pronounced rotation in the case of *A. robusta*. These crystals are found at regular intervals and angles of each other, forming the bulk of the protruding central structure of the coccolith. *A. robusta* was also observed to have vertical rods at its centre and both structures appear to have an inner cavity. It is probable that both species have a similar biomineralisation mode for these central protruding features. A summary of the crystal elements present in both species is given in appendix C.

As mentioned before, the mineralization mode has some strong dissimilarities to the V/R coccolith rim nucleation mechanism, as was also previously observed by Probert *et al.* (2007) [177] for *A. robusta*. Most importantly: the *R. clavigera* spine is formed of discrete simple crystal units instead of complex-shaped intergrown elements. However, there are also correlative features between the spine and the rim structures suggesting an altered but related nucleation mechanism. Firstly, the spine consists of regular spiralling elements. Secondly, a nanocrystal platelet core-structure is observed in the spine, possibly acting as a base for the outer crystalline units, guiding the overall structural and crystallographic orientation. However, this is purely hypothetical at this stage.

Interestingly, only about half the *R. clavigera* coccoliths develop a central spine structure, whilst others do not (Figure 4.1 and Figure 4.2). This is a regular feature of the species and the non-spine bearing coccoliths form an outer layer covering gaps between spine-bearing coccoliths. Thus they fulfill a particular role in the coccosphere architecture and therefore spine development versus spine-inhibition is likely biologically controlled. This could be related to a confinement mechanism or certain organic molecules controlling the ion transport for CaCO₃ precipitation. From the structural and crystallographic investigation of the complex ultrastructure of the spine, it is a feature we can highlight from our observations, but determining a controlling formation mechanism would require an extensive biochemical, cytological and cytoskeletal study.

We can nevertheless conclude from the data on *R. clavigera* and the structure of other well-described species, that a central *protrusion* in the coccolith disk appears to

be a prerequisite for spine formation. Many coccolith species instead, have a central inclination, as for example in *Emiliana huxleyi*. Although *Emiliana* and others have a widely varying physical appearance, in general, they exhibit a central area that forms a depression in the disk, this inclined area can be filled or partly filled with crystal elements, or be void. In contrast, species that form protruding spines, hoods or other features such as in the *Rhabdosphaeraceae*, generally have an 'up-sloping' central area from the rim inwards that culminates in a crest promoting an upwards extending, central canal, around which a central feature may develop. These concepts are illustrated by a schematic in Figure 4.7.

The formation of central protruding features seems therefore to be intimately linked to the ultrastructure of the rim formation itself. This reinforces the argument that both mineralisation modes – that of the V/R rim and the disjunct central area – are related although the crystal units themselves are distinct.

It is interesting to note that the rim structure is conserved across the *Rhabdosphaeraceae*, by contrast the central areas show widely varying structures: spines in *Acanthoica* and *Rhabdosphaera*, a hood in *Algirosphaera* and a trumpet in *Discosphaera*. But all the central individual elements are simple in shape and exceptionally regular in size.

Conclusions

The *R. clavigera* coccolith rim consists of complex-shaped interlinked crystals which conform to the V/R growth model suggested by Young *et al.* (1992) [103]. The central area of the coccolith base is made of imbricated tiles that spiral in an anti-clockwise direction towards its centre, forming the base of the spine. Not all *R. clavigera* coccoliths have spines, some central area spirals only result in a small crest. The spine is constituted by discrete simple {104} calcite rhombohedra, arranged in a winding staircase fashion along a longitudinal axis with a consistent five-fold chiral symmetry. The tip of the spine has a few extra elements, namely laterally protruding side panel crystals and longitudinally extended outer top platelets.

Conversely, the latter may be a reoccurring feature, partway observed lower down in the core of the spine. The discrete simple elements of the spine are dissimilar from complex-shaped intergrown coccolith rim units. Furthermore, the study shows that the spine crystals have a homogenous approximately 25 nm thick organic coating, which does not seem to have promoted the development of faces with lower angles to the c-axis, as has been suggested for other coccoliths [172].

It is hypothesized that the core-platelets in the *R. clavigera* spine may act as a template for the outer crystalline units, guiding the overall structural and crystallographic orientation, like the proto-coccolith ring in the rim structure. As each tip side panel is intergrown with the penultimate corresponding staircase element, it appears that the crystallographic growth direction is pre-determined from the nuclei stage. We conclude, therefore, that the biomineralisation mode for central protruding features in coccolith formation is different from but related to the V/R model.

Additionally, we derive from our data and other well-documented coccolith species that a central protrusion is a prerequisite for spines and other elaborate central protrusions to develop, as coccolith species with a central depression do not develop such structures.

Finally, although a crystal templating mechanism appears to guide the structural assembly in *R. clavigera* and tight size and shape control may be linked to growth in confinement, the data presented here does not allow for a derivation of a detailed formation mechanism.

4.2 CALCITE NANOWIRES

Calcite nanowires grown in a track etch membranes from an ACC precursor phase, are investigated to study the effects of confinement on nanoscale calcite crystallisation. Biomineralising organisms often form their mineral skeletons or shells within a confined space. This can be intracellular and in direct contact with the cell membrane (e.g. coccoliths), or at the interface between the mineral and organic matrices (e.g. coral's Extracellular Calcifying Medium). Such conditions drastically differ from precipitation of minerals out of bulk solutions and show the ability to form complex nanostructures [178].

Within cylindrical pores of track-etch membranes of nominally 50 nm and 200 nm diameter (defined by the manufacturer at the membrane surface), CaCO_3 precipitates in the presence of poly(acrylic acid) (PAA), as described in detail in 2.1.4 and by Kim *et al.*, (2011) [35]. Via this process the pores fill with ACC, which then transforms into crystalline wire-like structures over time. The membrane material is subsequently removed, see Kim *et al.*, (2011) [35], and the nanowires are characterised in detail using TEM and SAED to determine their crystal phase, structure and growth orientation along the long axis and possible lattice distortions are investigated. This information was obtained by taking diffraction patterns at regular intervals (approximately every 100 nm) along 1- 1.3 μm of the wires, starting by tilting the extremity of each wire into a low index zone axis.

The EM characterisation results are compared to finite element simulations performed by Alexander Côté, Robert Darkins and Dorothy Duffy from the Department of Physics and Astronomy, University College London.

4.2.1 RESULTS OF THE EM CHARACTERISATION

Thin nanowires (70-90 nm diameter)

The nanowires that were formed were up to 5 μm in length and the wire diameters were typically 70-90 nm from the 50 nm pore membranes, as the internal channel tends to be larger than the entrance, due to the manufacturing process. In all cases the nanowires were cylindrical in shape, as confirmed by SEM (Figure 4.8A), that is, the calcite wires do not expose low-energy crystal facets as commonly seen in *in-vitro* experiments. Instead the nanowires are moulded to the shape of the membrane pores.

TEM bright field and dark field images show that the brightness is not uniform along the length of the nanowires (Figure 4.8 and Figure 4.9). Frequent changes in contrast occur, with domains of similar brightness of variable width. Inhomogeneities of the surface, that look like *notches*, can be observed along the edge of the wire. These often, but not always co-occur with sudden changes in brightness. Upon closer inspection the notches appear to be dents in the surface which can be local or continuous around the wire's circumference, appearing as *paired notches*, this is illustrated in Figure 4.9. Notches were recorded in all ~ 70 nm diameter wires, but their origin remains unclear. It could be caused by inner surface irregularities of the membrane pores.

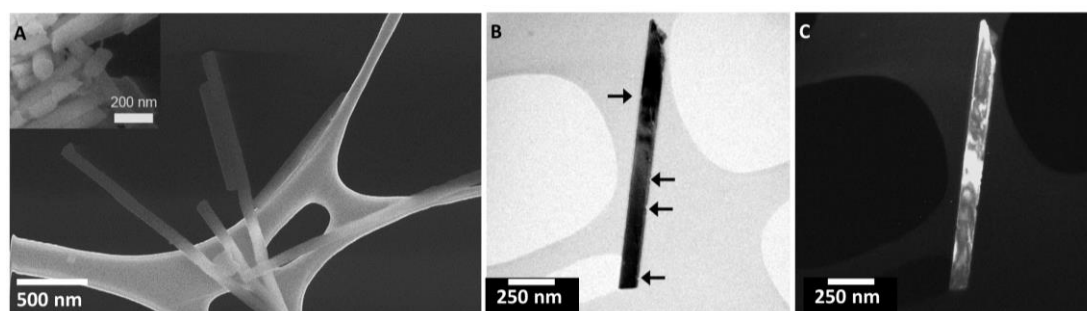


Figure 4.8 A) SEM micrograph of ~ 70 nm diameter calcite nanowires, the inset clearly shows that they are cylindrical in shape. B) TEM bright field image of a ~ 70 nm diameter calcite nanowire, arrows indicate notches on the surface. C) TEM dark field image using the (0 0 12) reflection, the contrast changes imply high amounts of lattice rotation.

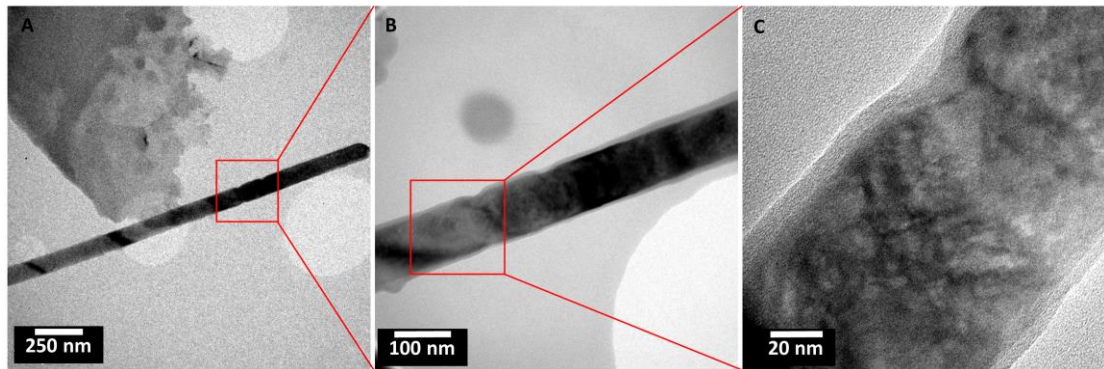


Figure 4.9 TEM bright field images of a ~70 nm diameter calcite nanowire. A) Overview. B-C) Detail of the surface structure resembling ‘notches’.

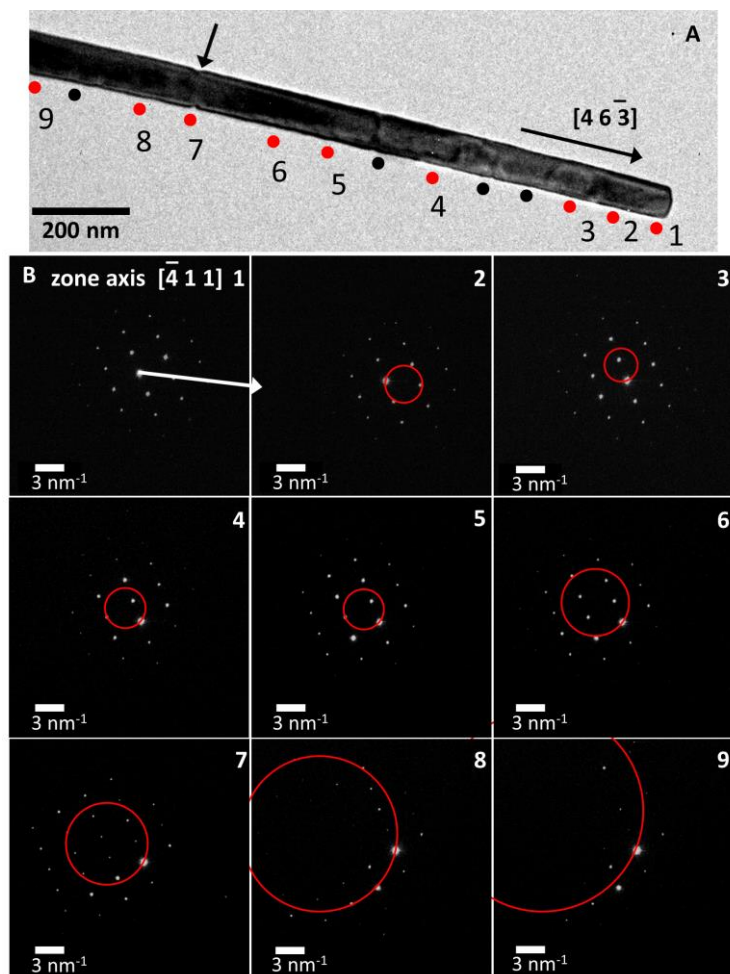


Figure 4.10 A) TEM bright field image of a ~70 nm diameter calcite nanowire. The dots indicate the position of the SA aperture (approximate area size is 125 nm) as projected next to the wire, of the red dots SAED patterns are shown in B. The arrow indicates the position of paired notches in the surface. B) SAED patterns, the white arrow indicates the growth direction of the wire. The shift of the Laue circle (red circle) indicates a tilting out of zone axis relative to point 1. The most dramatic shift occurs at and after point 7, which coincides with surface notches.

The wires also often show an inhomogeneous amorphous outer layer, which could be made up of remnants of the PAA or caused by contamination in the electron beam during imaging (Figure 4.9 B, C).

The SAED pattern series along the long axis of the nanowire in Figure 4.10, shows that it is a calcite single crystal along its entire length. The zone axis is $[-411]$ and the growth direction of the wire is derived to be close to $[46-3]$ by projecting the long axis direction onto the diffraction pattern, as has also been done previously for the coral and synthetic aragonite nanocrystalline stacks. More than thirty individual thin nanowires were investigated following this procedure, and predominantly they were found to be calcite single crystal, with no evidence for the occurrence of polycrystalline regions. A few wires were vaterite. From this and the high aspect ratios of the wires it is inferred that the *nucleation* rate is slow compared to crystallization rate under these growth conditions.

Surprisingly, no preferred growth orientation was found within this large sample population: it appears to be entirely random. This suggests that the membrane surface does not guide the orientation of the crystal nucleus from which the nanowire ultimately develops. Other studies, primarily using electrochemical deposition methods have observed the formation of nanowires from randomly oriented nuclei [179]. However this mainly results in particles with polycrystalline characteristics [180]. See Appendix C for additional images and diffraction pattern series of 70-90 nm diameter nanowires.

Besides the single crystalline nature and the random growth orientation there is another perhaps even more interesting characteristic. From the diffraction pattern series of the nanowires in Figure 4.8 (and see Appendix C) and Figure 4.10 it can be concluded that the lattice orientation changes locally along the wire's length. A change in local crystal orientation causes a gradual shift of the intensity distribution and hence of the position of the centre of the Laue circle in the diffraction pattern. The changes in the intensity distribution are relatively small between positions 1 and 7, between 7 and 8 a more dramatic shift occurs. This indicates a significant relative change in lattice orientation at roughly 900 nm from the wire extremity.

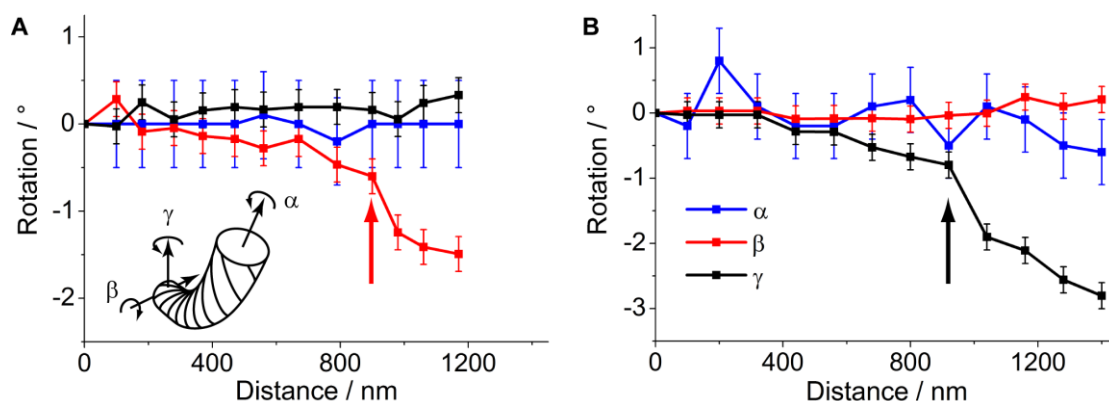


Figure 4.11 Graphs representing the evaluation of the twist (α , black), out-of plane bending (β , red) and in-plane bending (γ , blue) as a function of position along the length axis of the nanowires shown in Figure 4.10 and Figure 4.8 respectively. The arrows indicate the position of dramatic change in lattice orientation due to out-of plane bending (A) and twist (B). Image by courtesy of Andreas Verch.

After each SAED series along a rod, the first position is revisited to make sure the rod has not *rolled* in the beam during the data acquisition.

The lattice rotations were quantified by Andreas Verch (Department of Physics, University of York) by defining three rotational axes in the nanowire's frame of reference (Figure 4.11 inset), this is published in Verch *et al.*, (2014) [166]. The three rotation axes were previously introduced in section 2.2.2 and comprise of: 1) the 'twist' along the long axis of the wire (angle α), 2) the bending across the axis perpendicular to the wire's long axis called out-of-plane bending (angle β), and 3) an in-plane rotation around the zone axis (angle γ). The intensity distributions of diffraction spots in the experimental patterns were compared with simulated kinematic patterns [115] at different angles to obtain α ($\pm 0.1^\circ$), β ($\pm 0.1^\circ$) and γ ($\pm 0.5^\circ$) for every recorded DP. The angles were then plotted as a function of the position across the nanowire long axis (Figure 4.11). The error in γ is larger as it is affected by lens aberrations in contrast to α and β . More results of these analyses are shown in Appendix C.

The graphs in Figure 4.11 show that each wire exhibits a very different rotational behaviour. The nanowire shown in Figure 4.10 has little twist (α) and in-plane bending (γ), but the out-of-plane bending reaches up to 1.5° angle over $1.2 \mu\text{m}$. The large increase of out-of-plane bending is in this particular wire linked to

the position of a pair of notches and indicated by the red arrow in the graph (Figure 4.11). The nanowire shown in Figure 4.8 B and C has a relatively high amount of twist, almost 3° over $1.4 \mu\text{m}$ wire length (α) and much less out-of-plane (β) and in-plane bending (γ). The largest amount of change is reached at approximately 850 nm and indicated by the black arrow in the graph (Figure 4.11). The diffraction pattern series of this wire and additional graphs for different wires from the 50 nm track-etch membranes are shown in Appendix C, which clearly illustrates the variety of lattice rotation behaviour within this sample population.

Thick nanowires (250 nm diameter)

Track-etch membranes with 200 nm pore diameters produced nanowires with diameters of approximately 250 nm. As with the thin nanowires this is caused by the larger channel width compared to the channel entrance at the membrane surface. The formation procedure for the ~ 250 nm wires is identical to the ~ 70 nm wires and similar length nanowires were obtained.

Interestingly a variety of end products is observed. All 250 nm wires were cylindrical in shape, but different crystalline phases and structures were recorded. Firstly, comparable single crystalline calcite nanowires were found. But notably, none of these single crystal calcite thicker wires showed detectable lattice rotations across their length. An example is shown in Figure 4.12. This implies that the lattice distortions consistently observed in the thin nanowires are caused by a size-dependent effect. Otherwise, the thicker nanowires also showed a random growth orientation as observed in the thin wires.

Secondly, some thick wires consist of vaterite and are polycrystalline (Figure 4.13). In some cases a suggestion of *increased alignment* or *development in crystallinity* from vaterite to single crystal calcite could be recorded. In the figure, typical polycrystalline ring patterns can be observed in the first DP, length measurements of the d-spacings correlate with vaterite [181] (red hued markings in the Figure 4.13).

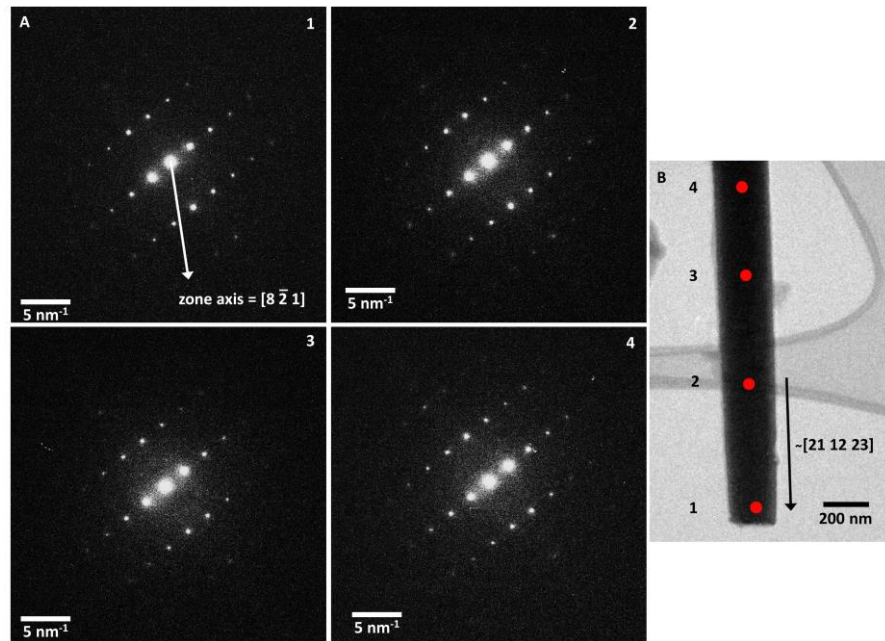


Figure 4.12 A) SAED pattern series along the length of a ~ 200 nm diameter calcite nanowire shown in B, the white arrow indicates the projected growth orientation of the wire, which is close to $[21 11 23]$, the zone axis is $[8\bar{2} 1]$. B) TEM bright field image, dots indicate the position of the SA aperture (area size approximately 125 nm), the numbers correspond to the diffraction patterns in A.

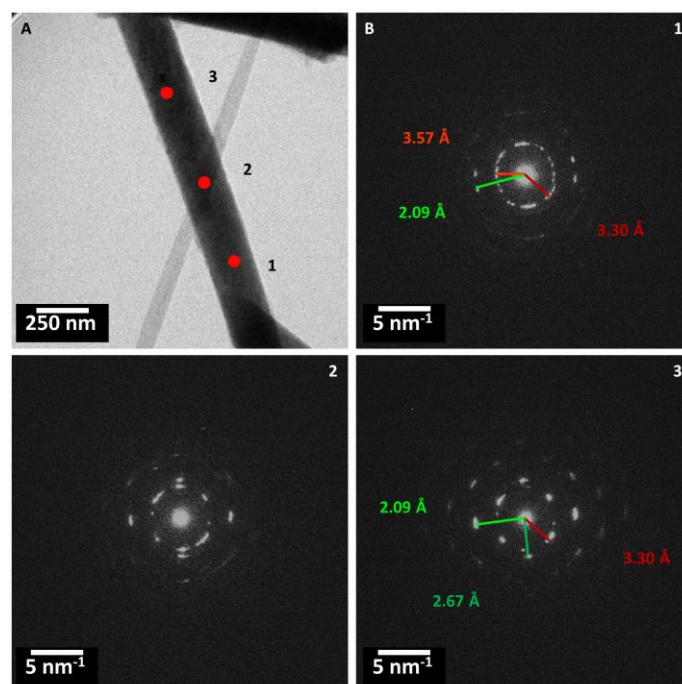


Figure 4.13 A) TEM bright field image of a ~ 250 nm nanowire, the red dots indicate the position of the SA aperture. B) SAED series corresponding to the positions in A. The markings in red hue indicate d-spacings in agreement with vaterite, the green hue markings indicate d-spacings in agreement with calcite.

In the subsequent DP more discrete reflections are present and the third DP shows an almost single crystalline pattern with d-spacings in agreement with calcite (green hued markings in Figure 4.13). However, there are still some reflections present attributed to vaterite, implying a gradual transformation. Though, this data interpretation should be made with reservations. Often, the d-spacings measured in DP's are not accurate enough to differentiate between the polymorphs of calcium carbonate as many are very similar. What can be said with certainty is that there is an increased alignment, or trend from polycrystalline to single crystalline within the vateritic wires. For another example of a polycrystalline vaterite wire which gradually transforms to single crystalline, see Appendix C.

4.2.2 INTERPRETATION AND COMPARISON WITH SIMULATION

The main question that arises from the experimental investigations of the calcite nanowires, is what causes the lattice rotations in the thin single crystal wires. It is probably caused by residual stresses, which could be due to the inherent structure of the nanowires or from defects. In nanostructures the surface structure and surface stress plays an increasingly important role as the surface area to volume ratio increases and therefore the impact of surface structure can result in bulk distortions [15, 182]. It was found that the larger (250 nm diameter) wires did not exhibit this lattice rotation behaviour, reinforcing the size-dependent correlation. Other studies also recorded twisting behaviour in nanoribbons [107, 183], and distortions in nanowires and nanocantilevers were also characterised [184, 185].

To understand what may have caused the lattice rotations in the ~70 nm wires, the experimental data is directly compared with finite element modelling (FEM) performed by Alexander Côté, Robert Darkins and Dorothy Duffy (University College London). The procedure of the modelling and its results are described in Verch *et al.*, (2014) [166]. In general, the nanowires were modelled by wrapping each wire with a 1 nm thick membrane, which was then compressed in the direction of

the wire's long axis to create a surface stress. Different growth directions of wires were used and it was found the impact of the stress was highly dependent on the wire orientation. In addition, they tested systems where the stress was not applied uniformly around the wire but only on one side or two with unequal magnitudes. The high anisotropy of the lattice led to different types of *distortions*: twist (α), out of plane bending (β) and in plane rotation (γ).

The surface stress incurred by the compression of the membrane resulted in a rotatory strain throughout all tested nanowire orientations, but varied in magnitude and axis of rotation, see Figure 4.14. Except for the nanowire oriented in the [001] direction, all nanowires exhibited twist and bend.

The FEM calculations showed that an inhomogeneous surface stress with a larger longitudinal component on one side of the wire compared to the other (e.g. 2 Nm^{-1} and 0.7 Nm^{-1} , stresses applied perpendicular to the wire's long axis, see Figure 4.15A) caused the wires to bend. It should be noted that in the experimental setup surfaces stresses will be at random angles to the wire's long axis and not just parallel or perpendicular. The simulation demonstrated that anisotropic surface stress, at arbitrarily chosen angles to the long axis, for example 2 Nm^{-1} and 1 Nm^{-1} , oriented respectively at 30° and 120° , consistently results in a twisting, see Figure 4.15B. Those particular conditions actually resulted in rotation behaviour very similar to the nanowires shown in Figure 4.11. The FEM calculations for uniform and non-uniform stresses applied to the thin nanowires result in comparable magnitudes and type of rotation behaviour seen in the experimental wires. It also demonstrated that the crystallographic orientation of the wire is a critical factor in the resultant lattice rotation [166].

The FEM simulations were also adapted to fit the experimentally observed *surface notches* in the thin nanowires, by carving small holes in the surfaces of the model nanowires, as shown in Figure 4.14 C. This resulted in a concentration of stress which caused a distinct increase in the calculated twist and bend. The locally increased rotation as a result of concentrated surface stress helps to explain the varied and sometimes abrupt lattice rotation changes along the wire lengths [166].

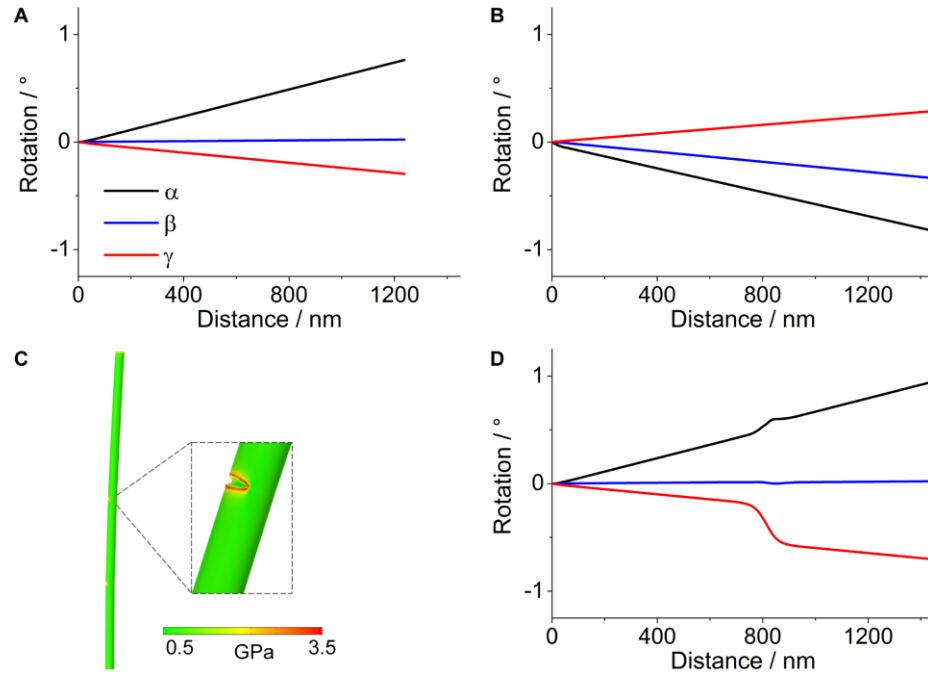


Figure 4.14 A and B show the results of the finite element calculations for nanowires with orientations similar to those shown in Figure 4.11 A and B, respectively, applied with a homogenous 10 Nm^{-1} surface stress. C shows the model used for the calculations in the presence of surface notches and D displays the results of the calculations for twist and bend as a function of position on a nanowire identified on the nanowire with a growth direction close to $[20\ 4\ -1]$. Image provided by Alexander Côté, Robert Darkins and Dorothy Duffy from the Department of Physics and Astronomy, University College London.

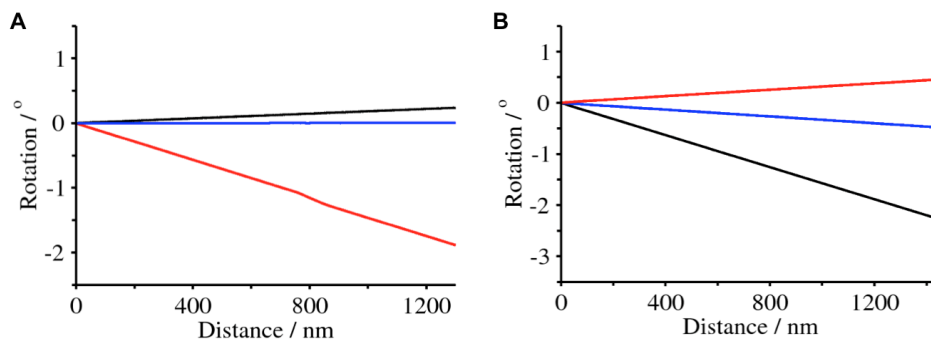


Figure 4.15 The calculated rotations (α : twist (black), β : out of plane bending (red) and γ : in plane rotation (blue)) as a function of the position along the nanowire for (A) a surface stress of 2 Nm^{-1} oriented along the wire on one side and 0.7 Nm^{-1} on the opposite side for a wire orientation corresponding to the one shown in Figure 4.11A. (B) an anisotropic, surface stress with principal components of magnitudes 2 Nm^{-1} and 1 Nm^{-1} , oriented 30° and 120° to the axis of a nanowire orientated as in Figure 4.11B. In both cases the rotations agree well with the observed values. Image provided by Alexander Côté, Robert Darkins and Dorothy Duffy from the Department of Physics and Astronomy, University College London.

Although the polycarbonate track etch membranes have a smooth glass-like surface film, on the nanoscale imperfections could lead to localised stress on the nanowires.

Lastly by employing linear elasticity theory to investigate the exact nature of the strain fields involved in causing the nanowires to bend and twist, it was found that, regardless of crystal orientation, twisting is primarily caused by shear stress and bending by tensile stress [166].

Summary of the results

Single crystal calcite nanowires with diameters of approximately 70 and 250 nm and random crystal growth orientation were grown from confined spaces of nanoporous membranes. The thin nanowires had significant lattice rotations along their longitudinal axis, caused by anisotropic surface stresses which were enhanced at surface irregularities seen as notches. Shear stress causes twisting, whereas tensile stress results in bending [166]. The thick (250 nm) wires were not consistently single crystal calcite. Some polycrystalline wires were observed, which often consisted of vaterite. Interestingly they exhibited a development in increased alignment toward a more single crystalline nature, along the wires' long axis. No lattice rotations were observed in the thick single crystal calcite wires, emphasizing the size-dependence of this phenomenon.

4.3 CONFINEMENT AND CALCITE CRYSTAL GROWTH

The shape and size of calcium carbonate crystals (i.e. calcite, aragonite and vaterite) formed by organisms often dramatically differs from synthetic bulk crystallisation and their geological counterparts. Crystallisation is highly dependent on reaction kinetics and the diffusion layer around the growing crystal, as is shown

in synthetic experiments where stirring or shaking speeds influence the polymorph selection and crystal morphology [96]. Confinement itself has also been shown to impact the stability of the formed phase, amorphous or crystalline, polymorph selection and morphology and thus the resulting surface structure [182].

In the first part of this chapter the crystal ultrastructure of the coccolithophore species *R. clavigera* was described in detail. Two properties of the *R. clavigera* exoskeleton are structurally impressive: 1) the precise arrangement of simple {104} calcite rhombohedra crystals in intricate staircase formations along a central axis, and 2) the complex shaped crystals of the rim of the coccolith disk. About the first aspect we hypothesised a relation to a templating mechanism similar to the proto-coccolith ring in the V/R structure model described by Young *et al.*, (1999) [105]. This was linked to the observed core-platelet structure seen in transmission tomography images, and was discussed in section 4.1.2. The second aspect: the complex shaped rim crystals, is particularly interesting from the perspective of crystallisation within confined spaces. Previous studies, using polarised light, scanning electron microscopy and cytological transmission electron microscopy have shown that the coccoliths are formed within intracellular golgi-derived vesicles with growth commencing with nucleation of a 'proto-coccolith ring' of minute crystallites with alternating crystallographic orientation, probably controlled by an organic template. Subsequently these crystallites grow and interlock to form the elaborate final coccolith morphologies after which the coccolith vesicle migrates to the edge of the cell and merges with the cell membrane resulting in the expulsion (exocytosis) of the coccolith and its addition to the coccosphere [102, 171].

From this we can deduce that the primary crystals, the rim crystals, are formed under highly controlled conditions, both by a template and within a membrane confined space. The later crystal phases; filling in the centre of the disk and in some species centrally protruding features are partly guided by that 'first order' crystal growth. In all coccoliths these rim crystals (V and R elements) are single crystal calcite, but complex shaped with kinks and bends, as is shown for *R. clavigera* (Figure 4.2). The surface facets of coccoliths do however seem to be mostly low

energy crystal faces but in other biominerals curved faces have been recorded [18]. From our synthetic study of calcite nanowires we can conclude that 'moulding' within an organic membrane is a very effective way of producing curved, non-geometric crystal morphologies. Applying specific surface strain in FEM showed that it could easily result in bending and twisting of the single crystal calcite nanowire. This behaviour could be interpreted as a pathway through which organisms can control crystal shape, and explain how coccolithophores amongst others create such bended and kinked single crystal units, and curved crystalline surfaces such as in calcite spicules of the sponge *Sycon* [18] in particular. Biomineralisation is however far too complex and varied a phenomenon to claim a singular explanation for the extensive assemblage of end products. Aragonite crystal needles in stony corals for example, seem to resemble their geological complements in general terms, the spherulitic growth is also reproducible in synthetic CaCO_3 systems. However these crystals form in an extracellular environment, probably guided by a nucleation site, but then filling in a space until it meets the next spherulite, and growing via a common thermodynamic reaction pathway, influenced by a diurnal chemistry cycle. But the nanocrystalline phase in corals does seem to have been further influenced by the high abundance of organics at certain times within this 24 hour cycle.

5. DISCUSSION & CONCLUSIONS

In this chapter the results and interpretations from the experimental investigation of biogenic and bio-inspired aragonite and calcite structures will be discussed, compared and summarised. Three main subjects will be highlighted; the effects on the calcium carbonate crystal growth by the *local carbonate chemistry*, the *organic additives* and precipitation in *bulk versus confinement*. These subjects will be discussed in the light of the results of this study and the current literature, and the impacts on existing understandings within this field will be explored.

In the last part of this chapter an outlook on future experimental work related to this study within the framework of biomineralisation research will be presented.

5.1 IMPACT OF THE CRYSTALLISATION ENVIRONMENT

5.1.1 LOCAL CARBONATE CHEMISTRY

The effects of seawater conditions

This study recognises that the composition of the seawater is of fundamental importance for polymorph selection in marine calcifying organisms. Polymorph selection is not always independently controlled by the organism. Throughout geological time (i.e. the Phanerozoic) there have been transitions in polymorph mineralogy in the fossil record of reef-building corals, coccolithophores and other calcereous organisms as well as abiotic CaCO_3 precipitates, correlated to tectonically induced variations in the Mg/Ca ratio of seawater [36]. Global rates of tectonic activity drive the exchange of Mg^{2+} and Ca^{2+} along zones of ocean crust production. The variations thus caused are commonly called *aragonite seas* (molar Mg/Ca > 2) and *calcite seas* (molar Mg/Ca < 2) [36]. We are currently in an aragonite sea condition.

Experiments have shown that, when the Mg/Ca ratio is lowered in experimental seawaters, aragonite accreting organisms start producing an increased proportion of the calcite polymorph [36]. This leads to the conclusion that biomineralogical control can be partially overridden by ambient seawater Mg/Ca conditions. It is therefore suggested that modern aragonite-secreting organisms, such as reef building corals, may have produced a mixture of aragonite and low Mg calcite, and that modern high Mg calcite producing organisms probably secreted low Mg calcite, in past calcite sea conditions [36].

The incorporation of Mg into the calcite crystal lattice has long been known to slow down the calcite crystal growth rate [186-188]. Davis *et al.*, (2000) [189] have demonstrated that the step-geometry of calcite crystals is altered so that solubility increases, thus reducing its net growth rate, by Mg-incorporation. They concluded

that, in aragonite, Mg content, geometry and growth rates are less influenced by solution Mg/Ca ratios, and that aragonite precipitation is thus kinetically favourable when Mg/Ca ratios are high.

The influence of supersaturation levels

In the study of Holcomb *et al.*, (2009) [164], the morphology and composition of abiotic aragonites precipitated experimentally from supersaturated seawater and coral aragonite spherulites were compared. Interestingly, the synthetic aragonite crystals precipitated from the solution as spherulites of approximately 20-100 μm in diameter, with granular submicron material at the centre and elongated needle-like (acicular) crystals radiating out to the edges. This is very similar to the morphology of coral spherulites albeit at a larger scale. The study showed that the formation of the granular centres could be associated with high fluid pH and saturation state, and in contrast the acicular growth occurred at lower pH and saturation state. Furthermore, the study showed that both the granular phase in the abiotic crystals as well as in corals had significantly higher Mg/Ca and Ba/Ca ratios than the acicular crystal phase. They proposed that the coral skeletal growth can be interpreted as a cyclical process by changes in the saturation state of the coral's calcifying fluid. During high saturation states, granular crystals are precipitated at the edge of the existing skeleton, thus forming the COCs, subsequently when the saturation state lowers, aragonite needles form in bundles that radiate out of these centres [164].

This work has built upon those fundamental observations and found that the granular phase at the centre of the COC in adult scleractinian corals consists of porous disordered nanocrystals of dimensions of 50-70 nm, followed by imperfectly co-oriented nanocrystal stacks with individual crystals of a similar size. The aragonite needles are dense bundles of acicular single crystals (several hundred nm across by several μm in length), which are transected by thin bands (a few hundred nm) of the reoccurring porous nanocrystal stacks. This microstructural evolution

could be directly correlated to contrast bands in optical images of spherulites and thus be linked to the diurnal cycle, induced by the activity of the photosynthetic zooxanthellae in the coral polyps.

The nutrients provided by the coral's zooxanthellae directly impact the production of ATP molecules which serves as the coral's energy source. The ATP then allows calcification regulation at two levels: 1) the regulation of the carbonate supersaturation in the calcifying fluid by a proton pump mechanism, and 2) the production and secretion of organic molecules (the coral skeletal organic matrix) into the calcifying fluid which directly interact with the crystal formation at the solid/liquid interface.

Here we concentrate on that first level of control: the supersaturation levels in the calcifying fluid or the *Extracellular Calcifying Medium* (ECM) of the coral. The supersaturation has been measured to be high during the day ($\Omega > 100$ [4], pH ~ 9 [2]), enabling so called *light-enhanced calcification rates*, and subsequently falls during the night ($\Omega < 10$ [4], pH ~ 8 [2]).

The supersaturation level of a calcifying solution is known to greatly affect the crystallisation pattern or morphology, in proportion to the distance from the equilibrium state [190]. The further away from equilibrium, the higher the saturation state, the higher the driving force for crystallisation. Highly symmetric, single crystal polyhedral forms result from crystal growth near the equilibrium state. In this scenario the reaction is kinetically controlled [190], i.e. the reaction rate is smaller than the mass transport rates, which means there is abundant material to precipitate around all reactive sites. But when the reaction driving force increases, crystal morphologies tend towards less-organised, skeletal (e.g. hopper crystals) and ultimately polycrystalline dendritic and spherulitic shapes [190], as depicted in Figure 5.1. Imai (2007)[190] states that at higher driving forces (i.e. high saturation state and far from equilibrium) the crystal growth rate is determined by mass diffusion, rather than being kinetically controlled. Diffusion-controlled reactions occur so rapidly, that the reaction rate is limited by the *rate of transport* of the reactants through the solution.

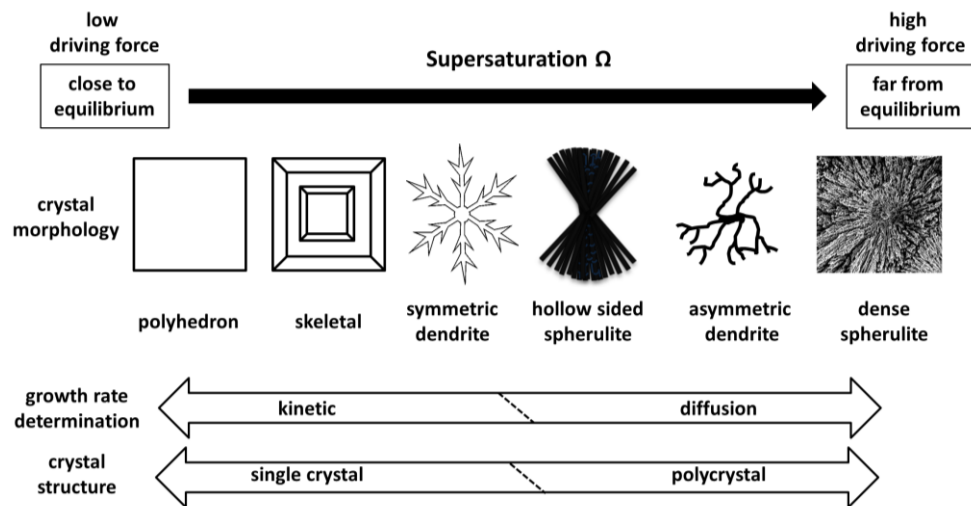


Figure 5.1 Schematic representing crystal morphology and structure variations as a function of the distance from the reaction equilibrium and the strength of the crystallization driving force. Image inspired by Figure 3 in Imai (2007) [190].

In other words, ions are transported to the reaction site at a lower rate than the reaction rate. As a consequence of this, those regions with higher reactant concentrations will have higher reaction rates: this will predominantly be at the corners of crystals and less so at the centre [156]. In that way a skeletal or branching structure formation is encouraged.

It was experimentally shown that, when the density of a gel-matrix reaction medium increases, the resultant crystal morphology changed from single crystal polyhedrons to dendritic forms with irregular branched polycrystalline aggregates [191]. The reaction rate is dependent on the concentration of the reactants, while the diffusion rate depends on the concentration *gradient* and the *viscosity* of the reaction medium (according to Fick's law and the Einstein-Stokes equation). An increase of viscosity decreases the diffusion rate (ion mobility goes down), and thus the reaction rate will be higher than the diffusion rate, making it a diffusion-limited reaction. As such, increased medium viscosity promotes the formation of diffusion controlled crystal morphologies [191]. The coral calcifying fluid is believed to consist of a hydrogel-like environment [63, 66] and is hence likely to provide a diffusion-controlled medium for crystallisation.

Cohen and McConnaughey (2003) [4] proposed a model for coral diurnal aragonite accretion in which the granular centres (COCs) are formed at night during low supersaturation state, and are therefore low density granular aggregates. The dense aragonite single crystal needles in contrast, are thought to form during the day at high supersaturation state and growth rates. This does not agree with the results of Holcomb *et al.*, (2009) [164], who find that the granular phase is related to high saturation states.

Following our detailed structural characterisation of the coral spherulites and the results of Holcomb *et al.*, (2009) [164], we propose an altered and somewhat more complex model, as described in Figure 3.26. We find that the coral microstructural evolution actually contains *three* distinct crystal morphologies, as was described above. From this we surmise that the highly disordered nanocrystal phase at the COC is actually formed during rapid growth, before sunset, when the supersaturation and organic levels have had time to build up during the day (high illumination). This is supported by the results of Holcomb *et al.*, (2009)[164] and the study of Imai (2007), which states that polycrystalline asymmetric aggregates are prone to form at extremely high saturation levels and under rapid growth rates. The following arrangement and increased order of the nanocrystals into stacks can occur during the night, when supersaturation is lowered and crystal growth rates have decreased (under low illumination). The crystallography switches to spherulitic, single crystal growth morphology – it is unclear exactly when this happens – and single crystal acicular bundles are elongated during the day, when growth rates increase again (under high illumination) in correlation with a higher supersaturation state. As the supersaturation state reaches critically high levels again (at the end of the day), the acicular phase is interrupted by a rapid nucleation event of the polycrystalline phase, resulting in the porous nanocrystalline bands. This model is, at this stage, phenomenological, as higher time resolved measurements of the saturation state of the calcifying fluid are elementary in providing unambiguous evidence for such a process.

In summary, at high supersaturation levels, the aragonite precipitation in corals is a probably a diffusion limited reaction, resulting in disordered polycrystalline growth before sunset. During the night, supersaturation decreases and the reaction shifts towards a more kinetic-controlled reaction promoting arrangement into stacks and ultimately single crystalline acicular crystals. The latter phase is extended with increasing growth rates during the day.

5.1.2 ORGANIC ADDITIVES: STABILISING CRYSTAL FACETS AND POLYMORPH SELECTION

Above we discussed the supersaturation cycle as a key player in the microstructural evolution within a spherulite. In this section we elaborate on the role of the skeletal organic matrix. We have determined from our study and the literature that a prominent component within the coral skeletal organic matrix is the functional hydroxyl-group. OH-groups are abundant in both sugars and proteins (such as in the amino acid residues cysteine and threonine), both of which are key ingredients of the coral skeletal organic matrix (e.g. [82, 143]). Therefore, a comparison with a controlled biomimetic carbonate system focused on OH-group additives has been carried out.

The three coral spherulite crystal morphologies are correlated to the change in supersaturation state and the change in *abundance of organics*, most likely boosted by the daily activity cycle of the zooxanthellae, which react to illumination levels, as they are photosynthetic organisms. At the end of the day, the organic molecule levels have built up and this is correlated to the disordered and rapid nucleation of nanocrystals. When the organic matrix levels decrease after sunset, nucleation and growth also slow down, the nanocrystals have time to partly align in a stack wise fashion and preferentially orient along the [001] direction. This aligned stacked growth is subsequently followed, during low organic matrix levels, by densely

packed, elongated single crystals arranged in bundles radiating out from the centre forming the spherulitic appearance.

In the comparative synthetic system we investigated the precipitation in bulk volume from a mixture of super saturated solutions (0.1 M CaCl_2 and 0.1 M Na_2CO_3) in the presence of variable ethanol levels. We found that aragonite in the form of large bundles of needle-like crystals precipitate preferentially relative to calcite and vaterite at high ethanol (35-50 vol%) concentrations. With lower ethanol ratios (≤ 15 vol%) large single crystal {104} calcite rhombohedra are the dominant crystal phase. The dominance of one crystal phase over the other is gradual and often all three polymorphs occur in a single sample. However, there is a clear shift of abundance in calcite rhombohedra (some of Hopper-type) with a few vaterite *cauliflower* or dendritic crystals and some small aragonite bundles towards an abundance of large aragonite sheaf-shaped bundles with a few small calcite rhombohedra (mostly of Hopper-type) and some vaterite, with increasing ethanol percentages (Figure 5.2). Similar results, but with the added impact of slow/fast shaking have been previously published by Sand *et al.*, 2011 [96].

The resulting aragonite bundles precipitated at high ethanol ratios were shown to consist of stacked nanocrystals, in a similar size range and the same crystal growth orientation as in the granular crystal bands of adult corals. In Figure 5.2, the combined results of the coral and the synthetic system are depicted as a schematic and a correlation can be made of selected parameters to crystal morphology. From this scheme it can be deduced that increased levels of organic molecules in both systems promote polycrystallinity over single-crystallinity.

Furthermore, the organic additives appear to promote alignment of nanocrystals in aragonite along the c-axis. However, geological aragonite also predominately extends in the c-axis orientation. Therefore, the influence of the additives may be limited to the change in supersaturation state and thus to the nucleation and growth rates of the system. Finally, in the synthetic system the crystal morphologies seem to shift from highly symmetric polyhedrons to more disordered branching shapes.

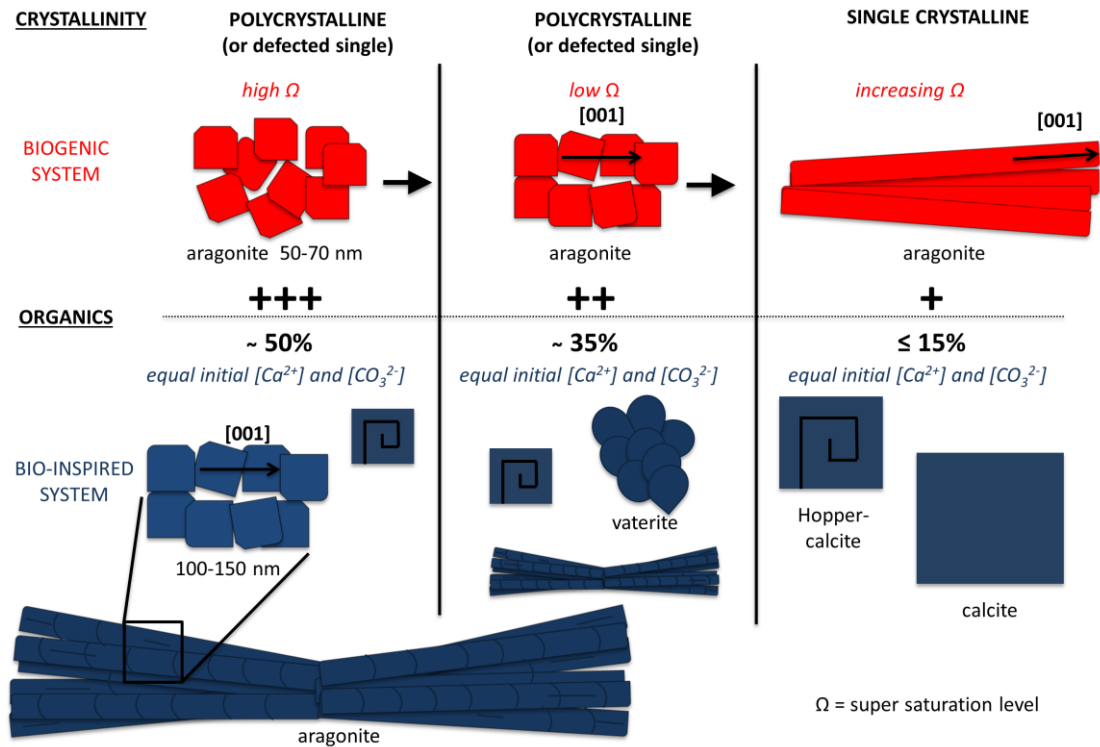


Figure 5.2 Schematic of simplified relation between the amount of organic additives present at the time of precipitation (low (+) to high (+++) in the biogenic system and 15-50 % of water/alcohol ratio in the bio-inspired system) and resulting crystal phase and morphology in adult Scleractinian corals (biogenic) and CaCO_3 precipitated in the presence of ethanol (bio-inspired). The drawing is not to scale, Ω is the supersaturation state.

The effect of OH-groups

Following these observations we discuss through what mechanism the OH-groups can influence crystal morphology and CaCO_3 polymorph selection. The abundance of small calcite Hopper crystals and aragonite bundles consistent of nanocrystalline stacks, when ethanol is present, even after a lengthy maturing time – the observed time scales of several hours in this study to several months in Sand *et al.*, 2011 [96]) – indicates that Ostwald ripening is slow. Ostwald ripening describes the process of the transformation of an inhomogeneous structure, i.e. small crystals, dissolving and re-depositing onto larger crystals over time [192]. The MD simulations in combination with AFM studies performed by Cooke *et al.*, (2010) [95] and Sand *et al.*, (2010) [59], showed that ethanol binds more tightly to the crystal surface (of {104} calcite) than water and that it also displaces absorbed water. It was

found that ethanol binds to the crystal surface through the OH-group so that the CH₃ group points away from the surface. This creates a hydrophobic layer at the crystal-solution interface which causes the water structure to break up around it, thus making the crystal surface less accessible to charged particles. A study using X-ray reflectivity supports these results [193]. Such behaviour stabilises the existing crystal surfaces and inhibits water aided ion transport, thus slowing down the rate of recrystallization. This could help explain the predominance of small and polycrystalline morphologies at high ethanol ratios over large single crystals at low ethanol ratios.

The actual polymorph selection mechanism is more difficult to explain. How are thermodynamically less-favourable polymorphs (e.g. aragonite and vaterite) produced and stabilised in biogenic and biomimetic systems? Chen *et al.* (2006) [194], suggest that, although the surface energies of aragonite and calcite are similar, they are not equally affected by changes in solvent composition, as their atomic arrangements exposed at the crystal surface, greatly differ. It is likely that certain organic molecules have more affinity with/bond more easily to particular atomic surface arrangements, thus providing a possible mechanism for promoting or inhibiting certain structures. This also applies for the promotion of particular crystal facets within a certain polymorph, such as the [001] aragonite. Atomistic modelling has shown that the aragonite [001] surface has low attachment energies and that as such it would be expected to be expressed in the growth morphology [195]. Indeed {001} aragonite is common in both biogenic and abiogenic crystals e.g. [15, 51, 196].

Complex growth condition effects and interface dynamics, underpinned in this work, are intensively studied by both modelling and experimental studies, e.g. [59, 95, 197, 198] but many uncertainties about the principal formation mechanism of biogenic and biomimetic minerals persist.

Another important factor in polymorph selection and crystal morphology in relation to OH-group additives is the driving force of the crystallisation, as was discussed in the section above, *The influence of supersaturation levels*. In general,

crystal morphology is affected by the distance of the solution from equilibrium, which is primarily a function of the supersaturation level [190], see Figure 5.1. When the supersaturation is very high, the driving force of the reaction is high and the precipitates tend towards less-ordered/asymmetric morphologies and polycrystallinity. Thus morphologies like polycrystalline dendrites and spherulites are favoured [190]. Chen *et al.*, (2007) [194], suggested that the addition of alcohol to solutions with calcium and carbonate ions would increase the saturation index of the solution. This would lead to higher supersaturation and thus a higher reaction driving force, promoting polycrystalline spherulitic growth. Our synthetic experiments support this: we see a tendency towards large polycrystalline aragonite bundles that are ordered like *wheat sheafs* or hollow-sided spherulites with increasing ethanol ratios. It remains however unclear through what effect ethanol increases the solution's saturation index, be it through increased activity of calcium and carbonate ions or by decreased solubility of the polymorphs in the alcohol solution [96]. For corals this would imply that an enhanced effect of supersaturation – due to the built up of organics before sunset – is superimposed on the existing diurnal proton pump driven supersaturation cycle. It has to be noted that this has been investigated for ethanol, but not for other OH-group containing molecules, such as polysaccharides and proteins.

In summary, organic additives like ethanol, containing OH-groups could affect the crystal morphology and the polymorph selection in biomimetic and biogenic systems in three ways: 1) by slowing down the rate of recrystallization, possibly by forming ordered hydrophobic layers at the crystal surface, thus stabilising the existing crystal surfaces and inhibiting water aided ion transport, 2) by promoting certain atomic surface arrangements and 3) by enhancing the driving force of the reaction, thus making particular crystal morphologies more favourable. In corals this results in dense spherulitic growth of {001} aragonite, with a polycrystalline centre and diurnal bands, correlated to high organic molecule levels and extreme high supersaturation conditions.

This implies that future conservation studies of reef building corals should not only focus on the change in seawater chemistry - ocean acidification - , but also on other parameters affecting the survival of the zooxanthellae which drive the supersaturation and skeletal organic matrix secretion such as temperature [7, 199] and sedimentation from terrestrial runoff [200].

As a last remark on polymorph selection in biogenic systems, it has been shown that seawater conditions are influential and can partly override biological controlled processes, as was discussed in the section above on *The effects of seawater*. It appears that biomineralising organisms can strictly control their crystallography within a certain range of conditions, but are bound to thermodynamic effects when conditions surpass their comfort thresholds.

The amorphous surface layer on coccolith crystals

Comprehensive studies, using polarised light, scanning electron microscopy and cytological transmission electron microscopy have shown that the coccoliths are formed within intracellular golgi-derived vesicles with growth commencing with nucleation of a *protococcolith ring* of minute crystallites with alternating crystallographic orientation, probably controlled by an organic template [101, 102]. Supersaturation enabling rapid mineralisation has been found, in some species, to be regulated by acidic polysaccharides that bind Ca^{2+} , which are transported into the vesicle [40, 102]. After the coccolith is fully formed the remaining polysaccharide complexes disintegrate and the organic residues bind to the crystals forming a surface coating [102].

A 25 nm homogenous amorphous coating was indeed observed on crystal elements of *R. clavigera*, in this study. The layer contained no calcium according to the EELS low loss spectrum, thus ruling out the possibility of it consisting of amorphous calcium carbonate. However, higher energy core-loss edges should be investigated to better characterise this layer. ACC has often been observed as a precursor phase in biomineral systems [29, 30, 169, 170], but has not been observed in coccoliths. It is therefore reasonable to assume that the amorphous layer is related to the polysaccharides observed in other coccolith species.

The role of this outer layer may also be related to the findings of Cooke *et al.* (2010) [95] and Sand *et al.*, (2010) [59] described above. A stable and highly ordered organic layer attached to the {104} calcite face by OH-groups would make it difficult for incoming ions to penetrate to the crystal surface. The organic coating, therefore, may help to prevent recrystallization on the {104} surface and decrease direct calcite/seawater interactions, acting as a protective layer.

The crystal elements of the *R. clavigera* spine were found to be simple single crystal calcite {104} rhombohedra, similar to crystals precipitated in bulk without or with little organic additives. The organism must regulate the location and size of the crystal elements, but the crystals themselves seem to have grown via a kinetically controlled reaction mechanism.

5.1.3 MINERALISATION IN CONFINEMENT: SHAPING CRYSTALS

Biominingalising organisms often form their mineral skeletons or shells within a confined space. This can be intracellular and in direct contact with the cell membrane (e.g. coccoliths), or at the interface between the mineral and organic matrices (e.g. coral's Extracellular Calcifying Medium). Such conditions drastically differ from precipitation of minerals out of bulk solutions and show the ability of an organism to form complex nanostructures [178]. Furthermore, organisms can exert a delicate control over the precipitation chemistry since the outcome of the CaCO_3 crystallization process is highly dependent on reaction kinetics and the diffusion layer around the growing crystal, as was discussed above.

Confinement is thought to have an important impact on crystal shape. As such it provides biominingalising organisms with a powerful tool for controlling their skeletogenesis. An important factor in this process is the difference in free energy in confinement as compared to bulk reactions. An estimate for the free energy for confinement of rigid macromolecules was described by Zhou *et al.*, (2008) [201] and the following discussion on crystal growth makes use of this concept. Although it

has to be noted that crystal formation in bulk is usually limited by the rules of crystal symmetry, different from the structure formation of macromolecules.

If we consider a crystal A that exists in bulk solution and can have a finite number of configuration states (with position coordinates r , and angular coordinate θ), and we transfer this crystal to an equal volume of solution but bound by hard walls in, one, two or three dimensions. Then for crystal A the change of the free energy ΔF_A is given by the statistical-thermodynamic equation [202]:

$$\Delta F_A = -RT \ln \left(\frac{\iint_{\text{allowed}} d\theta dr}{\iint_{\text{all}} d\theta dr} \right) \quad \text{Eq. 20}$$

where R is the molar gas constant and T the absolute temperature. The multiple integral in the denominator is taken over all configuration states possible in bulk solution, and the multiple integral in the numerator is taken over all allowed configuration states in the confined volume (all states in which no part of A intersects with the confinement walls). From this it follows that confinement changes the amount of possible configurations due to static barriers limiting the movement capabilities [201]. The free energy cost of confinement is not necessarily the smallest for conformations that are the most compact, as in having the smallest radius. The change in free energy needs to be minimised and thus, simply put, confinement favours conformations that have a similar *shape* to the confining volume [201]. For example, the preferred shape in a planar pore can be plate-like and in a cylindrical pore it may be rod-like [201]. Allowed configurations can become other than the low-energy crystal facets resulting from precipitation in bulk solution. Rounded surface shapes, *moulded* to the confined space, can become the favourable structure. In general, the magnitude of confinement effects are dependent on the structure of the confining space as well as the material being confined [203].

One extreme example of mineralisation in confined spaces in nature is the growth of single crystal calcite elements in coccoliths. The nucleation and spacing of the individual structural crystalline elements of coccolith rims (V/R model) is highly regulated by the proto-coccolith ring, but the subsequent growth is also tightly controlled [32, 103]. In general two types of elements can be observed as was found in this study for *R. clavigera*, but also reported for other coccolithophore species [32]. Calcite crystals with regular {104} rhombic faces are common in central areas, but the rim often has single crystal calcite grown in non-low energy facets, showing kinks, rounded shapes or with growth concentrated at element tips to create elongated shapes such as in *Emiliana huxleyi*, shown in Figure 5.3. Calcite {104} rhombohedra faces were reported in this study for *R. clavigera* central areas and for *C. pelagicus* and *O. fragilis* by Henriksen *et al.*, (2003) [204].

Cytological studies suggest that there is no precursor matrix present in coccoliths, instead it grows in an expanding vesicle [32]. Therefore, the final structure and arrangement seems primarily determined by the nucleation stage and subsequent growth of crystals, in a predefined space [32].

The rhombic crystals can be explained by inorganic growth from a set nucleation site, until they meet and interlock with their neighbours or fill in the appointed space. However, the rounded shape elements must have additional shaping constraints. It has been suggested that the growth is blocked in certain directions by coccolith-associated polysaccharide coatings [32].

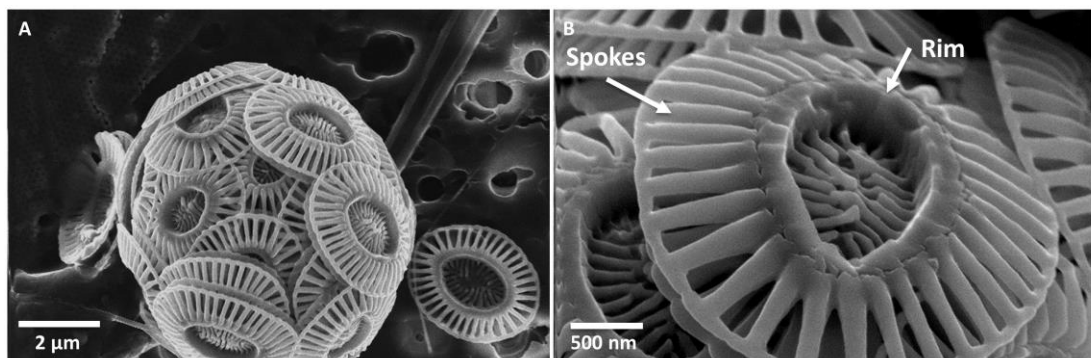


Figure 5.3 SEM images of *Emiliana huxleyi*. A) Complete coccosphere, B) Detail of coccolith with elongated crystals forming a ring of 'spokes' around the outer edge of the rim.

Such coatings have been observed by staining for polysaccharides in TEM specimens [102, 205, 206]. It was suggested that these surface layers can prevent dissolution of coccolith crystal elements [207], and thus it was inferred that they could also act to inhibit crystal growth [32]. Another possible mechanism for shaping coccolith elements in non-crystalline directions is by applying stresses from the surrounding vesicle/membrane/coating to mould it into the required shape.

This study has shown that this can be synthetically emulated and long calcite single crystal rods/wires can be produced using track-etch membranes. The wires consistently had no-low energy or crystallographic faces and random growth orientations, showing that they were shaped by the confining growth conditions.

It was found that thin (< 70 nm diameter) nanowires had lattice rotations throughout the wires' long axes expressed as bending and twisting of the wires. In contrast the larger (< 250 nm diameter) nanowires did not exhibit this lattice rotation behaviour, indicating a size-dependent correlation. By employing linear elasticity theory, it was found that, regardless of crystal orientation, twisting is primarily caused by shear stress and bending by tensile stress [166]. In nanostructures the surface structure and surface stress plays an increasingly important role as the surface area to volume ratio increases and therefore the impact of surface structure can result in bulk distortions [15, 182]. It follows from this that applying external stress to a nanoscale structure is a very effective way of shaping its ultimate structure. As such, shaping crystal elements in coccolith by *cytoskeletal pull* is probably an important part of the skeletogenesis. The cytoskeleton consists of different types of proteins, forming filaments that are dynamic, meaning they can grow and shrink at different locations in the cell and at different rates. Thus the filaments control cell shape, size and movement, as for example during the cell-division process of mitosis, which is aided by a pulling force from the cytoskeleton.

The mineralisation in scleractinian corals seems much less determined by confinement, as the skeletogenesis: 1) does not take place intracellularly, 2) no crystals with non-crystallographic faces are formed and 3) the resulting coral crystal morphology is formed by a combination of a cycle in supersaturation, skeletal

organic matrix input and the gel-like environment of the calcifying fluid. All three factors drive the crystallography towards a diffusion controlled reaction resulting in a branching, polycrystalline (at the highest supersaturation), spherulitic growth. Indeed, experiments performed by Holcomb *et al.*, (2009) showed that a change in pH cycle of supersaturated seawater alone could result in spherulites of aragonite, very similar to the coral's. The width of the coral spherulites is species specific and probably determined by the original nucleation site spacing of the COCs developing simultaneously. Strain contrast was observed in the acicular crystals at spherulite boundaries, which would inhibit further growth. Furthermore, it is unknown what the dimensions of the ECM are, and thus it at this point difficult to draw any conclusions with respect to the possible effects of crystal shaping by external stresses applied by the coral inner tissue layers.

5.2 SUMMARY OF THE CONCLUSIONS

The results of this study on four calcium carbonate systems, combined with information on precipitation environment, derived formation mechanisms and resulting crystallography are summarised in table 5.1.

The microstructural and crystallographic results from this study combined with results from findings by Holcomb *et al.*, (2009) led to the conclusion that at extremely high supersaturation levels, the aragonite precipitation in corals is a diffusion limited reaction. This results in the deposition of a disordered polycrystalline phase before sunset. Subsequently, during the night, supersaturation decreases and the precipitation shifts towards a more kinetic-controlled reaction promoting arrangement of nanocrystals into stacks and ultimately a single crystalline acicular morphology. The latter phase is extended with increasing growth rates during the day. Both the stacks and the acicular crystals preferentially grow in the [001] direction. This microstructural evolution and correlated carbonate saturation cycle is intimately linked to the diurnal activity cycle of the photosynthetic algae (i.e. zooxanthellae) that live in symbiosis with the coral in the upper living tissue layers of the polyps. These algae provide the coral with sugars and oxygen during daylight hours which boost the production of ATP molecules, the energy source of the coral for proton pumping (balancing of the positive Ca^{2+} charge by H^+ out-pumping) to create supersaturation conditions for aragonite accretion. Additionally, the energy is used to secrete the skeletal organic matrix into the calcifying fluid, which interacts with the crystal formation (e.g. [63, 66, 80]). The skeletal organic matrix consists predominantly of proteins and sugars, both of which contain OH-groups (and many other active groups not investigated here).

Therefore a synthetic system was designed to investigate the influence of OH-group containing additives on carbonate crystal morphology. It was found that high ethanol ratios promoted polycrystallinity and shifted the overall crystal morphology from large single crystal calcite polyhedrons (<15 vol% ethanol), to skeletal crystals and asymmetric dendrites (< 35 vol% ethanol) and ultimately to branching *hollow-*

sided spherulites or *sheaf-shaped* bundles (≤ 50 vol% ethanol). The thus precipitated aragonite bundles consisted of needles of stacked nanocrystals, oriented in the [001] growth direction. The co-orientation within stacks only occurred at the nanoscale, similar to the coral nanocrystalline stacks.

From this and a review of the literature it was concluded that organic additives like ethanol, containing OH-groups may affect the crystal morphology and the polymorph selection in three ways: 1) by slowing down the rate of recrystallization, possibly via formation of ordered hydrophobic layers at the crystal surface, thus stabilising the existing crystal surfaces and inhibiting water aided ion transport, 2) by promoting specific atomic surface configurations and 3) by enhancing the driving force of the reaction, thus making particular crystal morphologies more favourable. This should however be verified for other organic additives and in particular for molecules known to be present in coral aragonite mineral.

The OH containing additives could also be present in coccoliths, but as an amorphous surface coating probably made up of polysaccharides. A stable and highly ordered organic layer attached to the {104} calcite face by OH-groups, as seen in synthetic experiments [59, 95], would make it difficult for incoming ions to penetrate to the crystal surface. The organic coating, therefore, may help to prevent recrystallisation on the {104} surface and decrease direct calcite/seawater interactions, acting as a protective layer.

It was also noted that polymorph selection in biogenic systems, is influenced by seawater conditions which can partly override biologically controlled processes. It appears that biomineralising organisms can strictly control their crystallography within a certain range of conditions, but are bound to thermodynamic effects when conditions surpass their comfort thresholds.

Table 5-1 Summary of the results combined with information from literature as described in previous chapters.

Parameters	Scleractinian corals	EtOH-aragonite	Coccolithophores	Nanowires
Crystal polymorph	Aragonite	Aragonite	Calcite	Calcite
System	Biogenic	Bio-inspired	Biogenic	Bio-inspired
Skeletal unit	Spherulites ($\phi = < 30 \mu\text{m}$)	Sheaf-like bundles ($l = > 30 \mu\text{m}$)	Coccoliths ($\phi = 2-10 \mu\text{m}$)	Rods/wires ($\phi = 70 \text{ nm}, l = > 2 \mu\text{m}$)
Mechanisms for obtaining Ω	- Ca^{2+} -ATPase pump - Skeletal organic matrix (OH-groups)	- 0.1 M CaCl_2 + 0.1 M Na_2CO_3 (l) - EtOH 10 - 50%	- Ca^{2+} transport into vesicles by CAPs - Protococcolith ring	- ACC precursor
Location of crystal formation	Extracellular calcifying medium	Bulk	In vesicles (intracellular)	Track-etch membrane
Shaping factors	1) Supersaturation (Ω) cycle 2) Organic additives 3) Hydro-gel like environment	1) Supersaturation (Ω) 2) OH-groups of additive	1) Confinement: External stresses by cytoskeleton 2) Organic crystal growth inhibitors	1) Confinement: External stresses by membrane 2) Precursor phase
Carbonate chemistry	Diffusion controlled (with cyclic switch to more kinetic conditions)	Diffusion controlled at high EtOH ratios (~ 35 -50 %)	Kinetic controlled	Kinetic controlled
Crystal morphology	Polycrystalline spherulites - Disordered nanocrystalline - Stacked nanocrystals [001] - Acicular single crystalline [001]	Polycrystalline hollow-sided spherulites - Stacked nanocrystals [001]	Discrete single crystals - {104} rhombohedra (centre) - Non-crystallographic faces (rim)	Single crystal wires - Random growth orientation - Lattice distortions along length axis - High amount of bend/twist at surface notches

Within the calcite systems investigated here the predominant mechanisms for carbonate accretion and crystal morphology seem to be determined by a kinetically controlled reaction within a confined space with either preordained/limited nucleation sites (coccoliths) or with limited nucleation events (nanowires). The confinement favours conformations that have a similar *shape* to the confining volume [201].

The rhombic coccolith crystals can be explained by inorganic growth of separate units from set nucleation sites, until they meet and interlock with their neighbours or fill in the appointed space. However, the non-crystallographic oriented elements have additional shaping constraints. Polysaccharide coatings were shown to prevent dissolution of coccolith crystal elements [207], and thus it was inferred that they could also act to inhibit crystal growth [32]. Since coccoliths develop within expanding vesicles, we suggest that crystal shaping can be achieved

through mechanical stresses from the surrounding vesicle/membrane/coating to mould it into the required shape. Such phenomena were synthetically emulated and long (several micron) single crystal calcite nanowires (< 70 nm diameter) could be produced using track-etch membranes. The single crystalline nature combined with the large aspect ratio indicates that the nucleation rate is slow as compared to the growth rate under these conditions. The nanowires showed bending and twisting behaviour expressed on the nanoscale as lattice rotations along the longitudinal axis of the wire, this was enhanced in areas where surface distortions (notches) were recorded. It was shown by simulations that bending and twisting is primarily caused by surface tensile and shear stress, respectively.

Thicker nanowires (< 250 nm diameter) produced from wider track-etch membranes did not show lattice distortions and were predominantly polycrystalline. Some of the vaterite polycrystalline wires showed a development towards more aligned, single crystal morphology along the long axis.

5.3 OUTLOOK

The detailed experimental studies of aragonite and calcite biogenic and bio-inspired systems presented here, combining imaging and analytical methods, provides new insights into structural arrangement on the nano- and microscale of these biocomposite materials, as well as their formation mechanism. This forms the basis for further investigations and a better understanding of calcium carbonate formation in biominerals and their synthetic counterparts.

Importantly, although a much better understanding of coral mineralisation and its relation to light-enhanced calcification was achieved, direct structural characterisation of specimens cultivated under stressed conditions (high pH, high/low T) will be imperative to conservational studies. Ideally, a similar structural characterisation of coral spherulites of the same species, both at adult and larval

stages, should be performed using cultured specimens and compared with the data from this study. With such a dataset it will be possible to make predictions about coral reef growth rates and susceptibility to decalcification and bleaching due to ocean acidification and seawater temperature changes, respectively.

Furthermore, the study should be expanded to non-symbiotic corals, which could shed light on the extent of the influence of the photosynthetic cycle of the algae on the crystal microstructure. The microstructure could be directly correlated to the diurnal cycle of the algae, which provide the coral with nutrients. Such a cycle in availability of nutrients need not be restricted to symbiotic photosynthetic algae per se. It could also be realised by the provision of nutrients through ocean currents such as tidal action and thus result in a similar nanostructure.

With regards to synthetically produced aragonite as a comparative system to coral mineralisation, it would be valuable to continue similar precipitation experiments, but with different additives. A recent study has obtained a full sequence of coral mineral specific proteins [153], thus it would be possible to perform a targeted study of the influence of separate proteins or particular protein mixtures on aragonite crystallisation. Experimental studies similar to the one performed by Tong *et al.*, (2004) [208] on the control over crystal phase, shape, size and aggregation of calcium carbonate via L-aspartic acid additive, could be taken further. Similarly, coral specific sugars could be used in the same way. Furthermore, a nanoscale characterisation of synthetic spherulites precipitated from supersaturated seawater, as described in Holcomb *et al.*, (2009)[164] would allow for a better comparison between these features and coral spherulites. As mentioned earlier, these synthetic spherulites were similar to coral's on the microscale, showing a granular centre and outward radiating aragonite needles. In such an experimental set up, the influence of zooxanthellae and the skeletal organic matrix is excluded and the impact of a purely supersaturation state driven reaction can be analysed.

Following the precipitation experiments more modelling studies are necessary to investigate the organic/mineral interface dynamics, binding properties (surface energies) and affinity towards the three calcium carbonate polymorphs and specific

'popular' crystal faces such as aragonite [001] and calcite [104]. Such studies as performed by Sand *et al.*, (2010) [59] on the binding of ethanol on calcite and its relevance to biomineralisation, or Yang *et al.*, (2008) [94] on biological control of calcite crystallisation by polysaccharides, are particularly interesting as they directly combine molecular dynamics simulations with experimentally obtained crystals investigated structurally by electron microscopy.

The structural characteristics of *Rhabdosphaera clavigera* coccolith elements provide the first step towards a better understanding of nanoscale assembly in such biominerals. However, this part of the study in particular, brought up more questions than answers. For example, how is the strict control of size and shape of crystal elements realised by the organism, why do certain coccolith develop spines and some do not within a single specimen, and what are the advantages of such a complex pentameral structure?

It was shown by our experimental nanowire study in collaboration with simulations performed by Alex Coté and colleagues (UCL) that confinement and surface stresses results in moulding of single crystal calcite and that the structure can be bent or twisted according to the type of stress applied. This shows how crystals formed within flexible vesicles could be 'guided' in specific directions. However, the mechanism for such a process is far from resolved. Extensive biochemical and cytological studies of cultured specimens would be required to complement the structural data presented in this thesis.

Additionally the role and positions of the organic coatings of the crystal elements on *R. clavigera* should be further determined by demineralisation studies and subsequent TEM characterisation of the organic 'shells' as was described for *A. robusta* by Probert *et al.*, (2007) [177].

Lastly, one of the most intriguing features of *R. clavigera* is the consistent five-fold chiral symmetry of the spines, see Figure 5.4 below. The symmetry appears to be pre-determined from the crystal nucleation stage, as crystals grow in a regular fashion and interlock at a later stage without changing their growth direction (side panels intergrown with penultimate staircase elements). Also in *Cyrtosphaera* the

papillae at the tip of the spines have a five-fold symmetry. Other calcite biomineralising systems known to have a five-fold symmetry are the echinoderms, for example sea urchins, starfish and brittle stars. However, this symmetry is only superimposed on a primary bilateral symmetry [209]. In nanoparticles, adopting a five-fold symmetry reduces surface energies, which may overcome internal strain caused by some lattice distortions, this is often achieved through multiple twinning, which results from crystal subgrains sharing a common crystallographic plane in a cyclic fashion [210]. On the microscale, synthetic multiple polymeric nano-bristles attached to a substrate, have been shown to naturally assemble in a chiral helical pattern upon drying, by introducing more flexibility (bristle length) and adhesion to the materials [37]. Assembly in a chiral fashion is thought to be energetically advantageous and by introducing a controlled pre-assembly tilt the neighbouring nanostructures can only approach one another from one side and thus induce uniform left-hand or right-hand spiralling depending on the tilt [37].

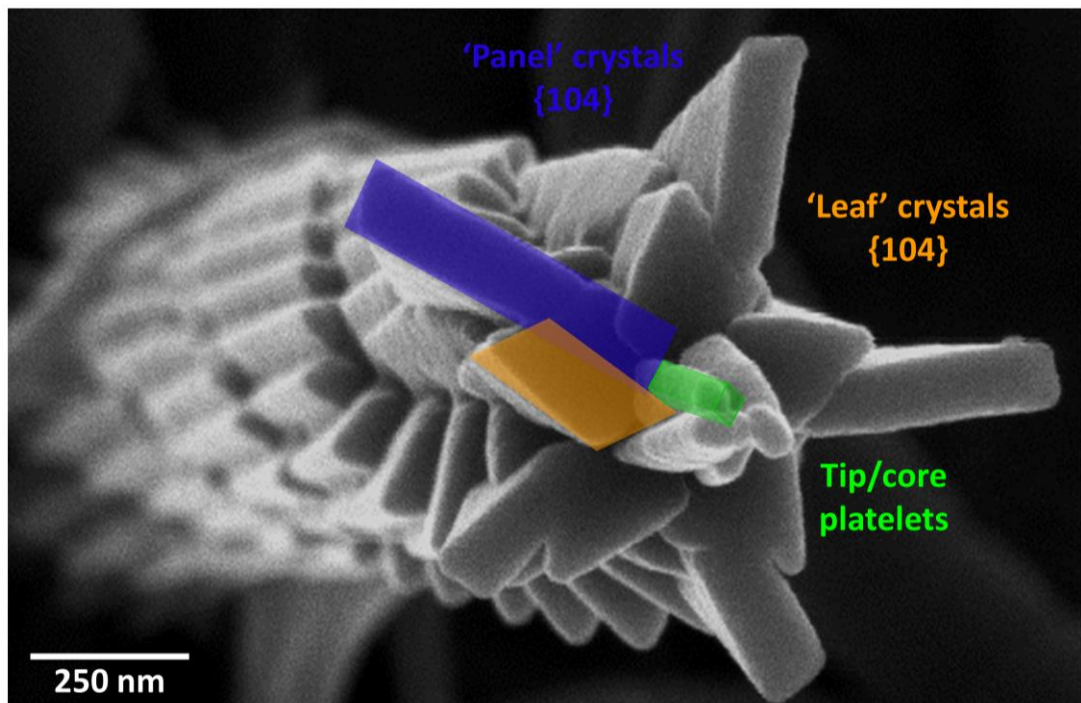


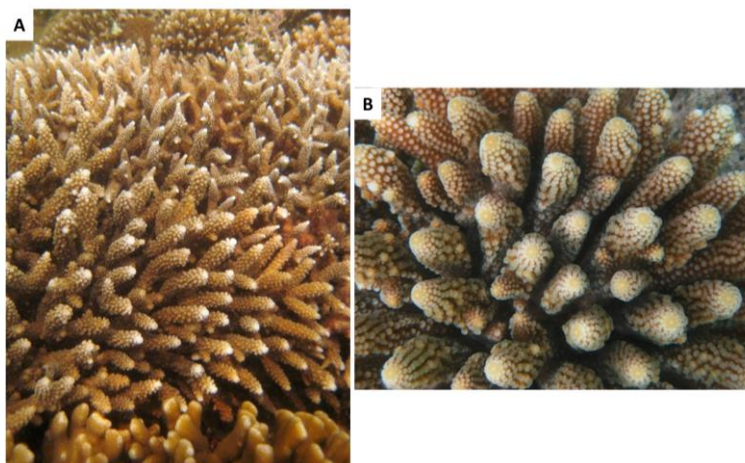
Figure 5.4 SEM micrograph of *R. clavigera* spine with its typical five-fold chiral symmetry and discrete crystal elements, the different tip elements are indicated in colour.

Another study showed that the amount of left-hand to right-hand chiral helical inorganic crystals could be tuned by the addition of chiral molecules, such as D- and L-glutamic acids [211]. The chiral molecules recognised the mirror surface of triclinic crystals and changed the growth behaviour of the helical morphology [211]. Chiral structures thus seem, although their appearance is complex, relatively 'easy' to establish by controlling the initial nucleation template. This issue is still unresolved for *R. clavigera*, although an internal crystal templating mechanism was suggested following the structural analysis. The possible involvement of organic molecules within this process is so far unknown.

APPENDIX A

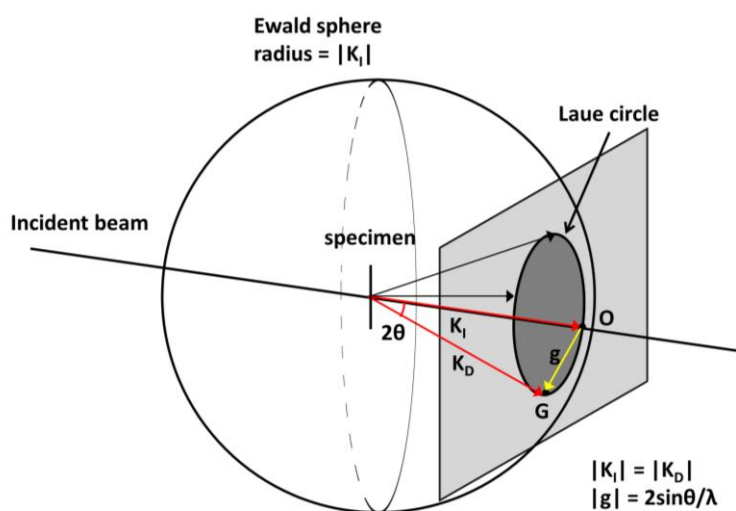
Supplementary data for Chapter 2

Macroscopic images of live coral



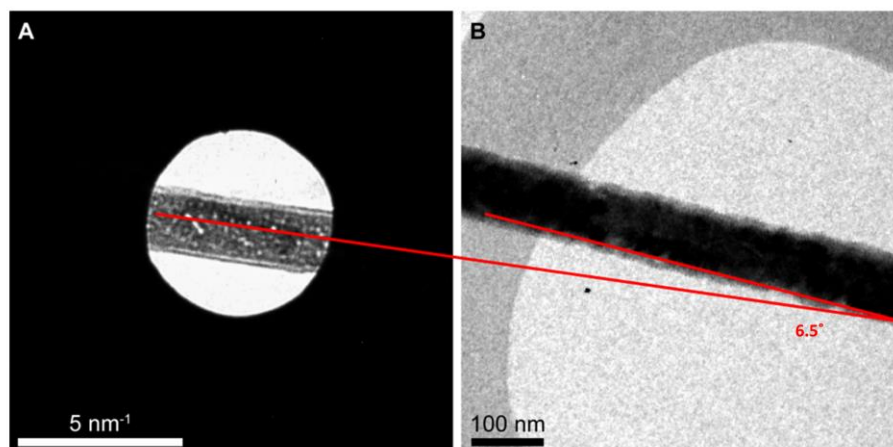
A.1 Photographs of live adult *Acropora sp.* coral. A) A colony. B) Detail of polyps. Images provided by Nikkita Lawton.

Construction of the Ewald sphere



A.2 The Ewald sphere construction, the intersection of surface of the sphere through the origin (O) of the reciprocal lattice is the Laue circle. In geometric terms diffraction spots (i.e. G) will occur only for reciprocal lattice points that lie on the surface of the Ewald sphere, when the origin (O) of the reciprocal lattice is at the tip of K_i .

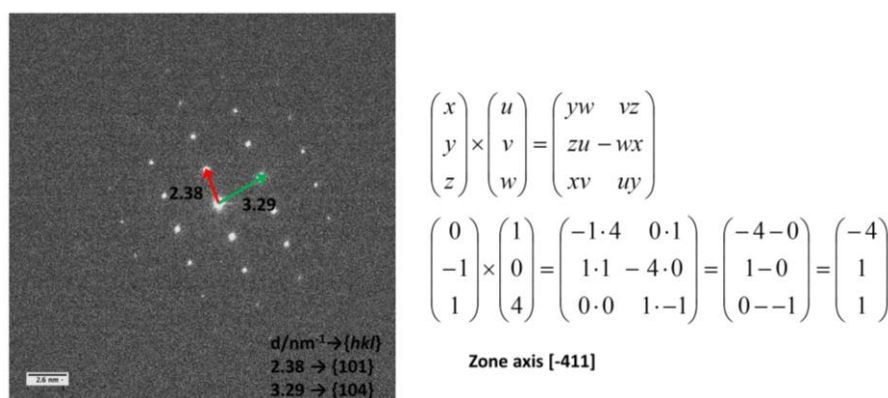
TEM Image rotation determination JEM 2011



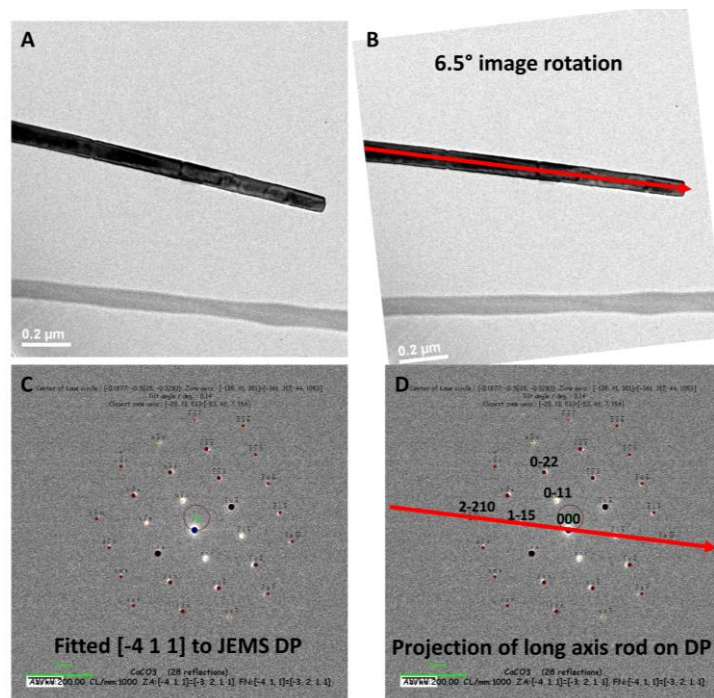
A.3. A) Image of a nanowire as seen in the central beam of a strongly defocused diffraction pattern at a camera length of 20 cm. B) Bright field image corresponding to A. The red lines demonstrate and image rotation of 6.5° between diffraction patterns and the TEM image of the JEOL 2011. Image adapted from Verch *et al.*, (2014) Supplementary data.

Diffraction pattern analysis

Below an example is shown how the TEM bright-field image of a calcite nanowire is linked to the experimental DP and how the zone axis, growth plane and growth direction are obtained.



A.4. Experimental diffraction pattern from a calcite nanowire. Distances are measured in ImageJ and linked to known values for family of planes {hkl}. Combinations of the cross products of the two vectors are calculated using Sarrus' rule and the calculated zone axes are used as input in JEMS for the simulated diffraction pattern, see figure below.



A.5. TEM bright field image (A) with a 6.5 degree image rotation (B) to correct for microscope image rotation between DP and image, red arrow indicates the long axis direction of the rod. C) Simulated DP (dark dots) superimposed on experimental pattern to match calculated zone axis orientation. D) Long axis of rod is projected onto the indexed DP and cuts through (2-2 10) which is the growth plane.

We calculate the growth direction from the growth plane (2-2 10) for calcite:

$$[UVW] = [(2h + k), (h + 2k), \left(l \frac{3}{2} \cdot \frac{\bar{a}}{\bar{c}} \right)^2]$$

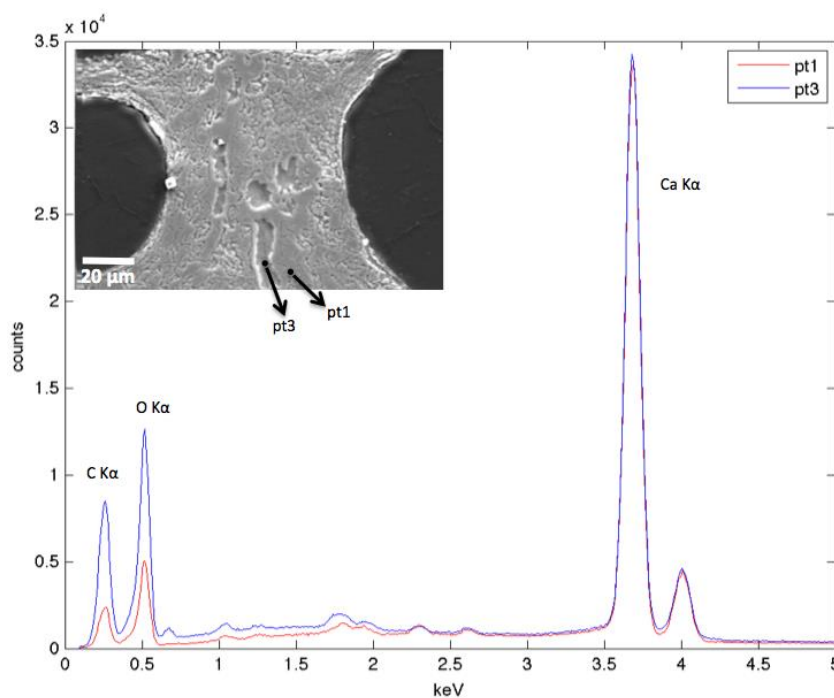
$$[UVW] = [(2 \cdot 2 + -2), (2 + 2 \cdot -2), \left(10 \frac{3}{2} \cdot \frac{0.4999}{1.7061} \right)^2]$$

$$[UVW] = [2, -2, 3.816]$$

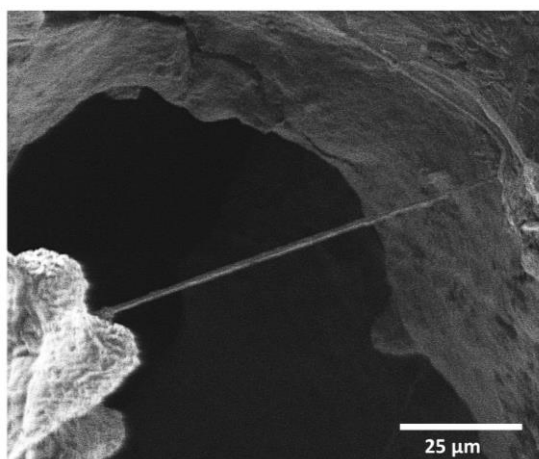
APPENDIX B

Supplementary data for Chapter 3

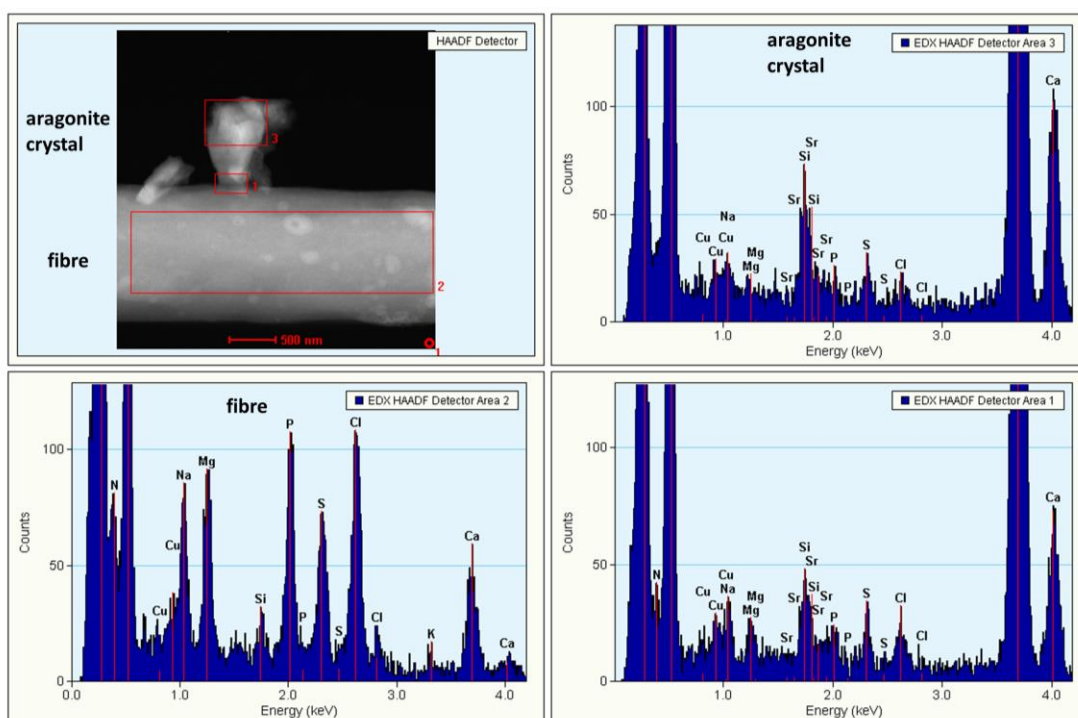
EDX data from coral specimens



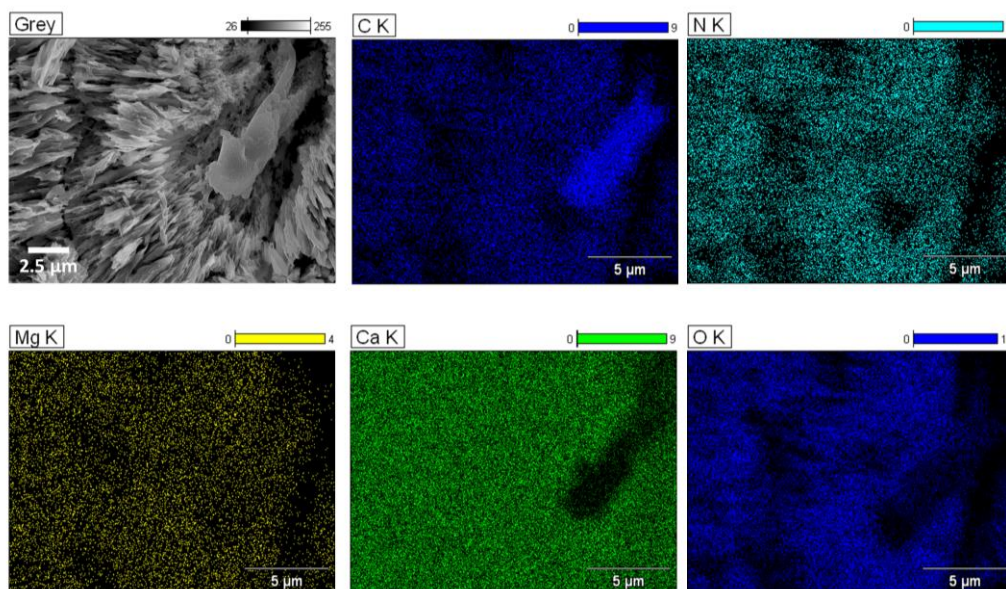
B.1 Graph of EDX point spectra from *Porites sp.* etched specimen (juvenile). Preferentially etched surfaces are the COC's with porous granular crystal morphology (pt 3) as opposed to more resistant densely packed acicular crystals (pt 1).



B.2 SEM micrograph of *P. lutea* (Andaman Islands, Port Blair) corallite surface with attached fibre. Image by Roland Kröger.



B.3 EDX data taken in HAADF STEM of an *in-situ* fibre in *P.lutea* coral partly overgrown with small aragonite crystals. The fibre has an organic composition: high in nitrogen, magnesium, phosphor and sulphur. The aragonite crystal consists as expected of calcium, carbon oxygen and some strontium, which is known to readily substitute for calcium in the crystal lattice. Figure courtesy of Roland Kröger.



B.4 EDX elemental distribution maps of carbon, nitrogen, magnesium, calcium and oxygen of *Porites l.* coral surface with an amorphous feature at the COC. The sample is polished and etched lightly with dilute acetic acid. The amorphous structure is enriched in carbon and depleted in calcium and oxygen

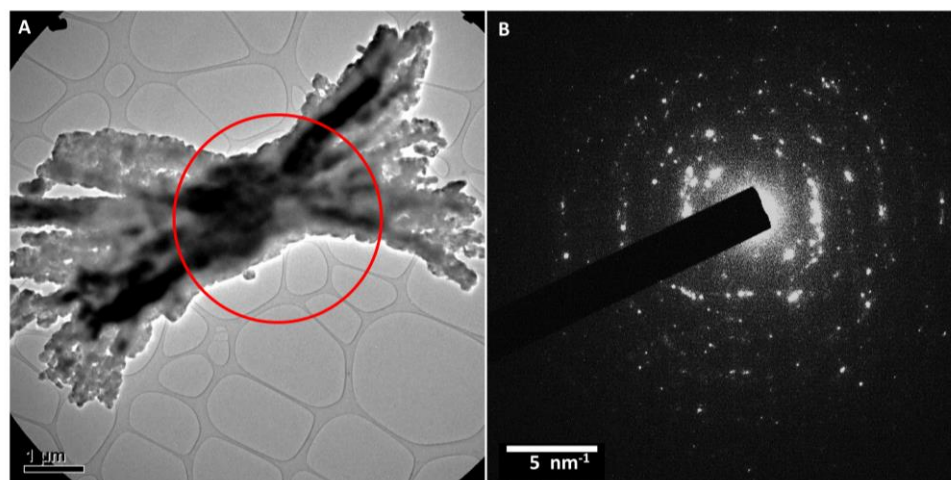
Coral High Performance Liquid Chromatography data (HPLC)

Table B-1 HPLC raw data: pmol amino acid concentration/ per mg sample

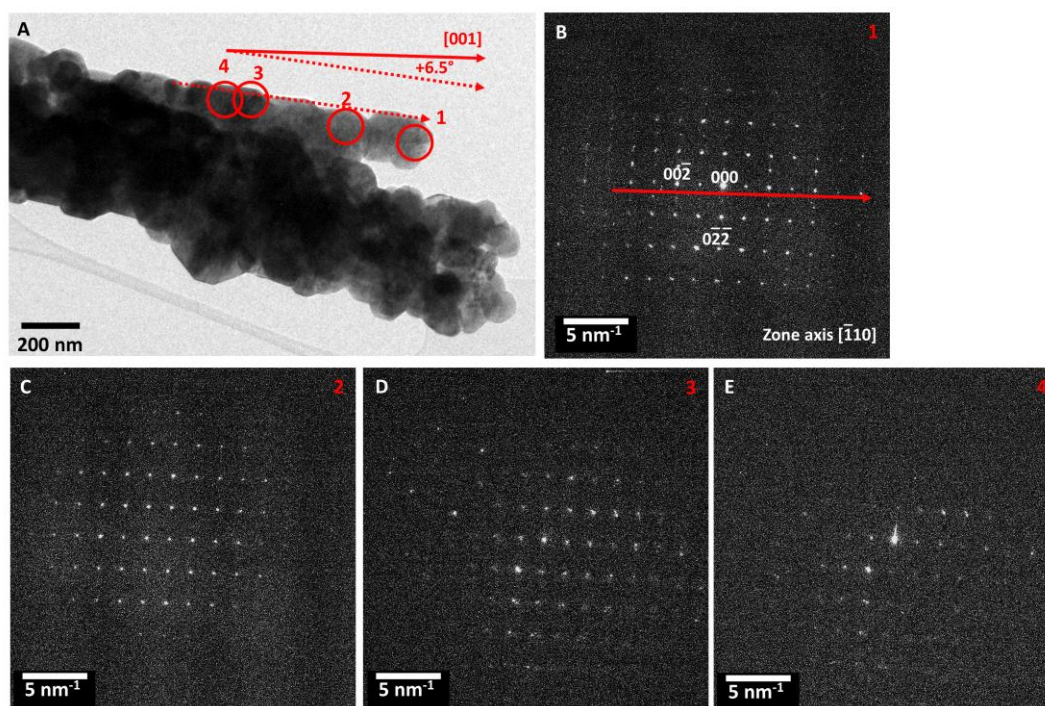
2011 data	Asx	Glx	Ser	L Thr	L His	Gly	L Arg	Ala	Val	Phe	Leu	Ile	total	comments
6812bH*	342	308	220	135	22	414	120	148	164	147	194	101	1775	
6813bH*	696	294	124	81	15	399	49	95	120	131	139	86	1873	
6814bH*	885	211	140	66	12	318	40	83	84	119	111	62	1852	
6815bH*	1167	256	138	66	5	688	45	113	96	126	122	66	2597	
6812aH*	292	455	335	159	36	1825	175	227	193	113	269	144	3532	
6813aH*	1254	836	585	319	79	1511	271	385	392	256	516	317	5386	
6814 dil aH*	5871	5242	2576	2490	409	12871	2192	3679	3222	1829	3543	2571	36022	
6815 dil aH*	6452	5314	4964	3545	213	11519	2418	4767	3861	2174	5085	2989	40499	
6812uH*	1510	2394	1275	640	209	2374	599	957	860	535	1233	676	10241	
6813uH*	2894	1154	557	366	36	1778	221	465	492	259	64	321	9317	
6814uH*	2783	1577	1181	885	185	3027	739	1238	1001	589	2194	893	11625	
6815uH*	2839	1269	661	474	0	2652	313	784	683	269	809	397	9317	
6812fH*	3	5	14	4	2	28	3	5	4	3	10	4	65	not enough sample
6813fH*	1	1	4	1	0	9	0	2	1	1	3	1	20	not enough sample
6814fH*	927	774	514	440	104	1682	354	602	515	312	752	486	5457	
6815fH*	95	51	47	16	7	122	12	26	19	10	36	14	375	not enough sample

2012 data	Asx	Glx	Ser	L Thr	L His	Gly	L Arg	Ala	Val	Phe	Leu	Ile	total	comments
7513bH*	396	173	73	36	213	290	22	96	60	47	74	45	1146	
7514bH*	83	34	28	1	14	213	4	21	5	22	31	7	389	<i>overhydrated</i>
7519uH*	94564	207242	75225	35143	18194	243609	56906	63391	38725	31385	60442	28440	814806	<i>weighing error</i>
7519uH*	83186	179159	70932	32333	18412	244105	54843	59158	34139	28246	54822	25462	757855	<i>weighing error</i>
7526uH*	78	65	71	15	1	262	7	44	11	19	26	9	554	
7515bH*	1631	285	190	69	24	519	45	132	72	56	112	47	2944	
7515bH*	1692	256	196	69	19	369	26	124	70	48	87	44	2802	
7522bH*	861	129	89	30	10	225	18	59	27	23	34	17	1438	
7522bH*	1084	128	83	27	73	99	11	66	30	21	33	17	1529	
7518uH*	4493	1670	1375	699	147	2989	466	1082	644	428	1555	576	13418	
7518uH*	4041	1327	1379	696	98	2726	453	1059	614	404	1073	420	12295	
7525uH*	3821	1393	1145	569	131	3049	354	887	562	390	834	550	11780	
7525uH*	3751	1143	1019	525	108	2075	297	847	535	396	898	389	10192	
7516bH*	2128	451	345	115	35	2346	123	223	111	88	189	67	5842	
7516bH*	2086	424	325	110	27	1606	105	304	100	77	149	59	5059	
7523bH*	953	177	132	46	0	846	32	118	47	28	55	27	2352	
7523bH*	1246	200	84	10	57	326	29	101	64	34	63	36	2061	
7521uH*	3532	1491	1278	520	168	4518	417	938	488	411	730	384	13182	
7521uH*	5472	2079	2055	774	138	5887	519	1420	798	727	1456	635	19004	
7517bH*	840	448	288	144	34	991	112	195	141	97	255	91	3158	
7517bH*	919	421	224	126	29	312	86	195	160	109	225	107	2444	
7524bH*	1122	487	301	134	0	997	96	202	145	101	182	94	3484	
7524bH*	524	210	117	59	19	295	36	93	72	48	82	47	1406	
7520uH*	684	596	309	184	42	1102	191	282	166	134	258	117	3514	
7520uH*	649	461	307	179	32	1072	169	268	164	130	242	116	3269	
7527uH*	1455	608	325	158	19	814	84	247	180	102	205	109	3871	
7527uH*	1489	608	299	151	0	622	74	249	168	80	165	101	3661	

Aragonite bundles precipitated in the presence of ethanol



B.5 A) TEM Bright field micrograph of a bundle of aragonite matured for 4 months after crystallisation, the red circle indicates the position and approximate size of the selected area aperture. B) Diffraction pattern of the bundle in A indicating that the bundle is polycrystalline.

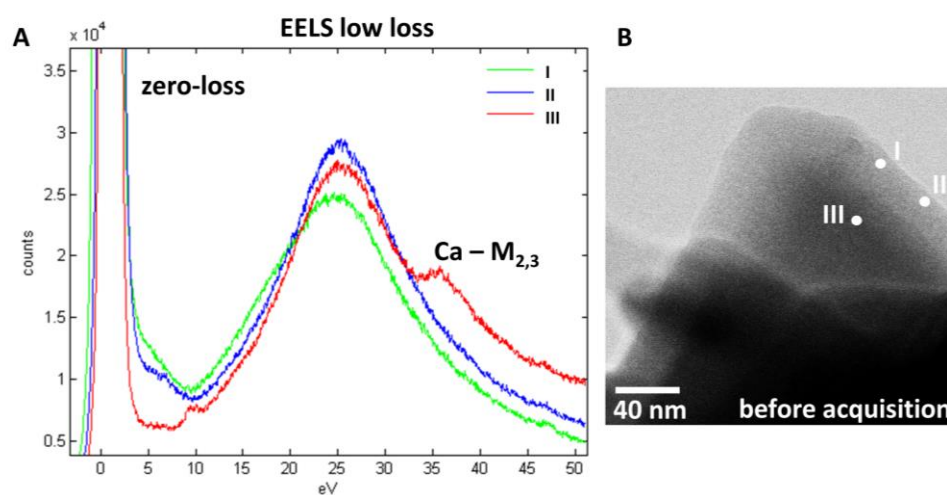


B.6 A) TEM Bright field micrograph of a detail of an aragonite bundle matured for 4 months after crystallisation. The red circles indicate the positions and approximate area size of the selected area aperture. The dotted arrow is the direction of the long axis of the stack, after a 6.5° image rotation correction the growth direction is obtained (solid red arrow). B-E Diffraction pattern series along the stack of grains in the bundle, the red arrow is the growth direction projected on the DP and indicates a [001] orientation.

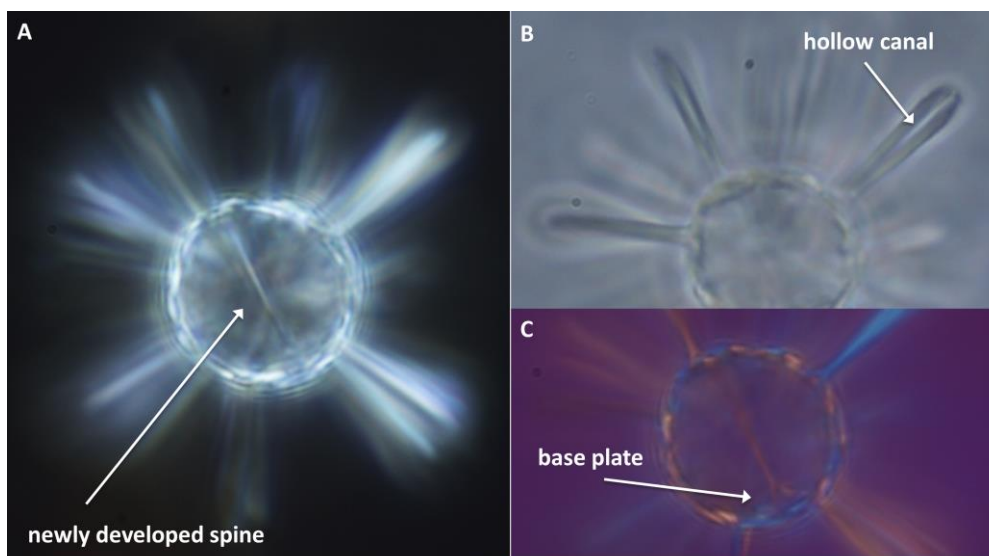
APPENDIX C

Supplementary data for Chapter 4

EELS data and optical images from coccolith specimens



C.1 A) Low loss EELS spectra of three point measurements on a panel crystal from the tip of the spine. Data points I and II were taken from the amorphous layer coating the crystal, point III is from the inner side of the panel. Only the latter shows a characteristic Ca M_{2,3} edge, therefore no Ca is present in the amorphous layer. The broad peaks at ca. 10 and 25 eV are not caused by inner shell electron bonds, but valence bonds. To better characterise the amorphous layer higher energy core loss edges should be obtained instead of the plasmon resonance range. B) TEM bright field micrograph of the analysed crystal.



C.2 Light microscope images of *R. clavigera* showing a fully developed spine-bearing coccolith inside the coccosphere before exocytosis. A) Cross polarised light image. B) Phase contrast image, the hollow canal in the spine is particularly clear in this image. C) Image taken with a gypsum plate (1λ-plate).

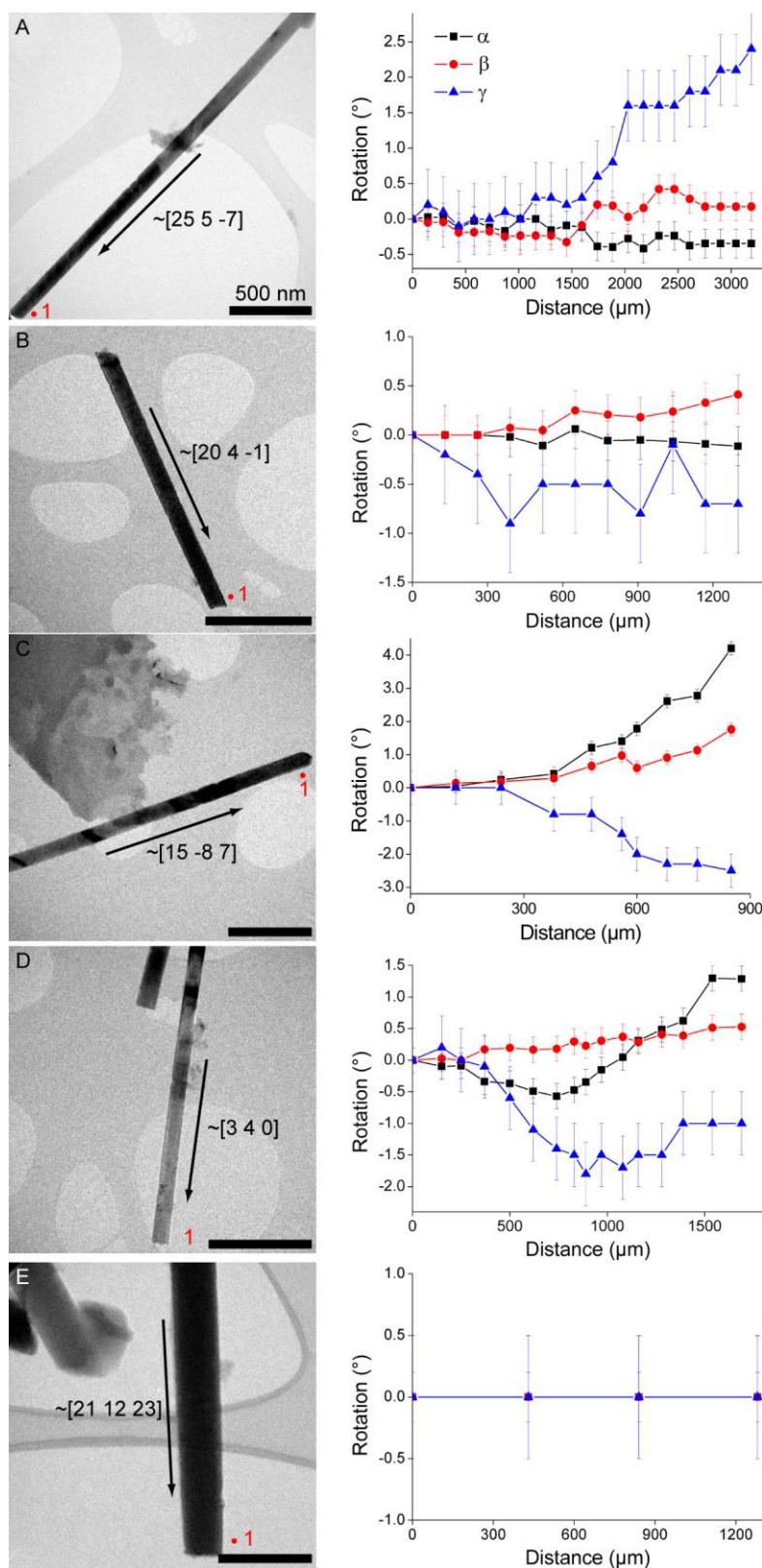
Comparison in ultrastructure of *R. clavigera* and *A. robusta*.

Table C-1. Summary of the crystal elements present in heterococcoliths of *R. clavigera* and *A. robusta*, in the base plate and the central disjunct area. The radial cycle of spoke-like elements in the central area seen in *A. robusta* is 'missing' in *R. clavigera*, it is likely that the lamellar cycle in *A. robusta* is equivalent to the imbricated tile cycle in *R. clavigera*.

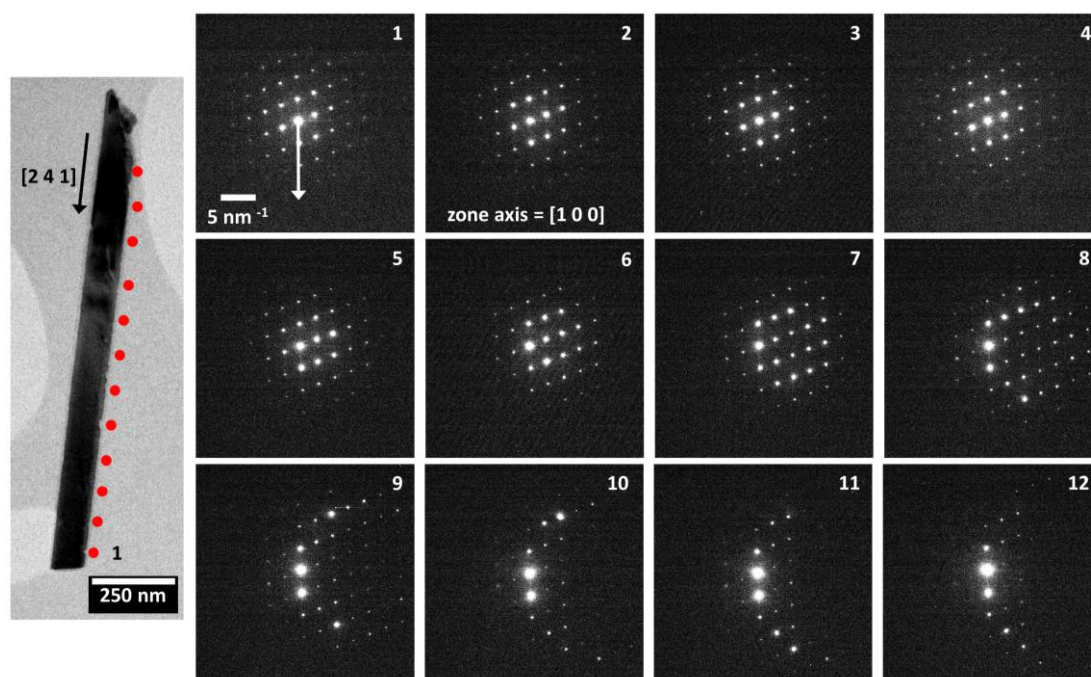
	<i>R. clavigera</i>	<i>A. Robusta</i> (Probert et al., 2007)
Base plate	<p><u>Rim conform V/R model</u> Planolith: rim is not significantly elevated 1) Complex shaped upper rim elements (V-units) 2) Lower rim elements (R-units): interlinked with upper rim</p> <p><u>Central area</u> 3) Radial cycle of imbricated tiles: anticlockwise spiral 4) Central most imbricated tiles: push one another up to form small crest/base of the spine</p>	<p><u>Rim conform V/R model</u> Planolith: rim is not significantly elevated 1) Upper rim elements (V units ?) 2) Lower rim elements (R units ?): interlinked with upper rim</p> <p><u>Central area</u> 3) Radial cycle of horizontal spokes 4) Lamellar cycle of vertical platelets: base of the hood 5) Irregular proximal laths</p>
Central protrusion	<p><u>Spine</u> 1) Staircase platelets: 5 topmost form the 'leaf' elements of tip 2) Five side panels extended in lateral plane of the tip of the spine 3) Five long platelets extended in longitudinal plane of the tip: these extend downward on all sides of the inner spine void.</p>	<p><u>Hood</u> 1) Thin imbricated outer cover tiles: anticlockwise spiral 2) Oblique rods: obliquely to long axis and slope upwards 3) Vertical rods: placed on both sides of the hood's of inner void.</p>

Additional DP series for the 70 and 250 nm calcite nanowires

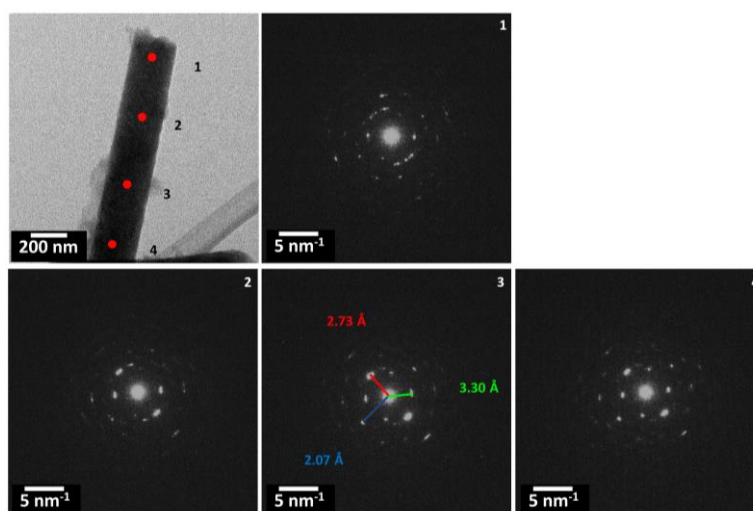
(See next page)



C.3 TEM bright field images of calcite nanowires with on the right side accompanying evaluation of twist (α , black), out-of-plane bending (β , red) and in-plane bending (γ , blue). A-D) Nanowires from 50 nm track-etch membrane pores. E) Nanowires from 200 nm track-etch membrane pores. Figure by courtesy of Andreas Verch.



C.4 TEM bright field image of ~ 70 nm diameter calcite nanowire as shown in Figure 4.8B,C with accompanying SAED pattern series (SA aperture has an approximate 30 nm area size). A dramatic change in lattice orientation occurs from position 9 just near a notch. More notches are present, but not all induce strong lattice distortions.



C.5 TEM bright field image of a ~ 250 nm calcite nanowire with accompanying SAED series. The first and second DPs have characteristic polycrystalline rings, DP three and four show many more discrete reflections as the structure develops into a single crystalline phase. The d-spacings correlate with vaterite.

LIST OF ABBREVIATIONS

Acronyms

ACC	Amorphous Calcium Carbonate
ASEM	Atmospheric Scanning Electron Microscope
BF	Bright Field
BSE	Backscattered Electrons
COC	Centre of Calcification
Cs	Spherical Aberration Coefficient
DF	Dark Field
DP	Diffraction Pattern
ECM	Extracellular Calcifying Medium
EDX	Energy Dispersive X-ray
EELS	Electron Energy Loss Spectroscopy
EM	Electron Microscopy
EtOH	Ethanol
FEG	Field Emission Gun
FEM	Finite Element Modelling
FFT	Fast Fourier Transform
FIB	Focussed Ion Beam
HPLC	High Performance Liquid Chromatography
HRTEM	High Resolution Transmission Electron Microscopy
LhArg	L-homoarginine

MD	Molecular dynamics
pAA	Poly(acrylic acid)
pAsp	Poly(aspartic acid)
PILP	Polymer Induced Liquid Precursor
RP-HPLC	Reverse Phase High Performance Liquid Chromatography
SA	Selected Area
SAED	Selected Area Electron Diffraction
SE	Secondary Electrons
SEM	Scanning Electron Microscopy
STEM	Scanning Transmission Electron Microscopy
TE	Track-Etch
TEM	Transmission Electron Microscopy

Symbols and units

$\bar{\mathbf{a}} \ \bar{\mathbf{b}} \ \bar{\mathbf{c}}$	Base lattice vectors
$\bar{\mathbf{a}}' \ \bar{\mathbf{b}}' \ \bar{\mathbf{c}}'$	Base reciprocal lattice vectors
d_{hkl}	Distance between crystal planes (hkl)
E_0	Energy of the electron beam
E_c	Critical ionisation energy
ΔF_A	Change in Free Energy
$\bar{\mathbf{G}}$	Reciprocal lattice vector
(hkl)	Miller indices of crystal plane
λ	Wavelength
λ_0	Wavelength of incident beam

λ_s	Wavelength of scattered beam
M	Molar
θ_B	Bragg angle
$\bar{\mathbf{R}}$	Lattice vector
R	Molar gas constant
$[uvw]$	Indices of crystal direction (zone axis)
$\tilde{\nu}$	Wavenumber
$\Delta\tilde{\nu}$	Raman shift
ν_0	Frequency of incident beam
ν_m	Vibrational frequency of a molecule
Ω	Saturation state

BIBLIOGRAPHY

1. Meyers, M.A., P.Y. Chen, A.Y.M. Lin, *et al.*, *Biological materials: Structure and mechanical properties*. Progress in Materials Science, 2008. **53**(1): p. 1-206.
2. Al-Horani, F., S. Al-Moghrabi, D. De Beer, *The mechanism of calcification and its relation to photosynthesis and respiration in the scleractinian coral Galaxea fascicularis*. Marine Biology, 2003. **142**(3): p. 419-426.
3. Beniash, E., J. Aizenberg, L. Addadi, *et al.*, *Amorphous calcium carbonate transforms into calcite during sea urchin larval spicule growth*. Proceedings of the Royal Society B: Biological Sciences, 1997. **264**(1380): p. 461.
4. Cohen, A.L., T.A. McConnaughey, *Geochemical perspectives on coral mineralization*, in *Biom mineralization*, P.M. Dove, J.J. DeYoreo, and S. Weiner, Editors. 2003, Mineralogical Soc Amer: Chantilly. p. 151-187.
5. Weiner, S., *Biom mineralization: A structural perspective*. Journal of structural biology, 2008. **163**(3): p. 229-234.
6. Kleypas, J.A., R.A. Feely, V.J. Fabry, *et al.*, *Impacts of Ocean Acidification on Coral Reefs and Other Marine Calcifiers: A Guide for Future Research, report of a workshop held 18–20 April 2005, St. Petersburg, FL, sponsored by NSF, NOAA, and the U.S. Geological Survey, 88 pp.* 2006.
7. Hoegh-Guldberg, O., P. Mumby, A. Hooten, *et al.*, *Coral reefs under rapid climate change and ocean acidification*. Science, 2007. **318**(5857): p. 1737-1742.
8. Bijma, J., B. Honisch, R. Zeebe, *Impact of the ocean carbonate chemistry on living foraminiferal shell weight: Comment on Carbonate ion concentration in glacial-age deep waters of the Caribbean Sea by WS Broecker and E. Clark*. Geochemistry geophysics geosystems, 3 (11), 2002. **1064**.
9. Fine, M., D. Tchernov, *Scleractinian coral species survive and recover from decalcification*. Science, 2007. **315**(5820): p. 1811.
10. Dissard, D., G. Nehrke, G.J. Reichart, *et al.*, *Impact of seawater pCO₂ on calcification and Mg/Ca and Sr/Ca ratios in benthic foraminifera calcite: results from culturing experiments with Ammonia tepida*. Biogeosciences, 7., 2010. **81**.
11. Fratzl, P., R. Weinkamer, *Nature's hierarchical materials*. Progress in Materials Science, 2007. **52**(8): p. 1263-1334.
12. Cusack, M., *Biom mineralization: elemental and organic influence in carbonate systems*. Chemical Reviews, 2008.

13. Schmidt, W., *Die Bausteine des Tierkörpers in polarisiertem Licht*. 1924. *Protoplasmamonographien* 11, 1937.
14. Vincent, J., *Structural biomaterials*. 2012: Princeton University Press.
15. Lowenstam, H.A., S. Weiner, *On biomineralization*. 1989: Oxford University Press.
16. Weiner, S., L. Addadi, *Design strategies in mineralized biological materials*. *Journal of Materials Chemistry*, 1997. **7**(5): p. 689-702.
17. Fratzl, P., O. Paris, K. Klaushofer, et al., *Bone mineralization in an osteogenesis imperfecta mouse model studied by small-angle x-ray scattering*. *Journal of Clinical Investigation*, 1996. **97**(2): p. 396.
18. Aizenberg, J., M. Ilan, S. Weiner, et al., *Intracrystalline macromolecules are involved in the morphogenesis of calcitic sponge spicules*. *Connective Tissue Research*, 1996. **34**(4): p. 255-261.
19. Falini, G., S. Albeck, S. Weiner, et al., *Control of aragonite or calcite polymorphism by mollusk shell macromolecules*. *Science*, 1996. **271**(5245): p. 67-69.
20. Tang, Z., N.A. Kotov, S. Magonov, et al., *Nanostructured artificial nacre*. *Nature materials*, 2003. **2**(6): p. 413-418.
21. Hench, L.L., *Bioceramics: from concept to clinic*. *Journal of the American Ceramic Society*, 1991. **74**(7): p. 1487-1510.
22. Mann, S., *Biomineralization: principles and concepts in bioinorganic materials chemistry*. Vol. 5. 2001: Oxford University Press.
23. Weiner, S., P.M. Dove, *An overview of biomineralization processes and the problem of the vital effect*. *Reviews in mineralogy and geochemistry*, 2003. **54**(1): p. 1-29.
24. Michel, F.M., J. MacDonald, J. Feng, et al., *Structural characteristics of synthetic amorphous calcium carbonate*. *Chemistry of Materials*, 2008. **20**(14): p. 4720-4728.
25. Ogino, T., T. Suzuki, K. Sawada, *The formation and transformation mechanism of calcium carbonate in water*. *Geochimica et Cosmochimica Acta*, 1987. **51**(10): p. 2757-2767.
26. Wray, J.L., F. Daniels, *Precipitation of calcite and aragonite*. *Journal of the American Chemical Society*, 1957. **79**(9): p. 2031-2034.
27. De Yoreo, J., *Crystal nucleation: more than one pathway*. *Nature materials*, 2013. **12**(4): p. 284-285.
28. Weiner, S., Y. Levi-Kalisman, S. Raz, et al., *Biologically formed amorphous calcium carbonate*. *Connective Tissue Research*, 2003. **44**(1): p. 214-218.

29. Weiss, I.M., N. Tuross, L. Addadi, *et al.*, *Mollusc larval shell formation: amorphous calcium carbonate is a precursor phase for aragonite*. *Journal of Experimental Zoology*, 2002. **293**(5): p. 478-491.
30. Addadi, L., S. Raz, S. Weiner, *Taking Advantage of Disorder: Amorphous Calcium Carbonate and Its Roles in Biomineralization*. *advanced materials*, 2003. **15**(12).
31. Wehrmeister, U., D. Jacob, A. Soldati, *et al.*, *Amorphous, nanocrystalline and crystalline calcium carbonates in biological materials*. *Journal of Raman Spectroscopy*, 2011. **42**(5): p. 926-935.
32. Young, J.R., K. Henriksen, *Biomineralization within vesicles: the calcite of coccoliths*. *Reviews in mineralogy and geochemistry*, 2003. **54**(1): p. 189-215.
33. Eiden-Assmann, S., M. Viertelhaus, A. Heiss, *et al.*, *The influence of amino acids on the biomineralization of hydroxyapatite in gelatin*. *Journal of inorganic biochemistry*, 2002. **91**(3): p. 481-486.
34. Wu, Y., G. Cheng, K. Katsov, *et al.*, *Composite mesostructures by nanoconfinement*. *Nat Mater*, 2004. **3**(11): p. 816-822.
35. Kim, Y.Y., N.B. Hetherington, E.H. Noel, *et al.*, *Capillarity Creates Single-Crystal Calcite Nanowires from Amorphous Calcium Carbonate*. *Angewandte Chemie*, 2011. **123**(52): p. 12780-12785.
36. Ries, J., *Review: geological and experimental evidence for secular variation in seawater Mg/Ca(calcite-aragonite seas) and its effects on marine biological calcification*. *Biogeosciences*, 2010. **7**(9): p. 2795-2849.
37. Aizenberg, J., *New Nanofabrication*. *MRS BULLETIN*, 2010.
38. Aizenberg, J., P. Fratzl, *Biological and biomimetic materials*. *Advanced Materials*, 2009. **21**(4): p. 387-388.
39. Williams, D.B., C.B. Carter, *Transmission electron microscopy: a textbook for materials science*. 2009: Springer.
40. Marsh, M., *Regulation of CaCO₃ formation in coccolithophores*. *Comparative Biochemistry and Physiology Part B: Biochemistry and Molecular Biology*, 2003. **136**(4): p. 743-754.
41. Da Silva, J.F., R.J.P. Williams, *The biological chemistry of the elements: the inorganic chemistry of life*. 2001: Oxford University Press.
42. Wada, K., T. Fujinuki, *Biomineralization in bivalve molluscs with emphasis on the chemical composition of the extrapallial fluid*. *The Mechanisms of Mineralization in Invertebrates and Plants*, 1976: p. 175-190.
43. Lowenstam, H.A., *Minerals formed by organisms*. *Science*, 1981. **211**(4487): p. 1126-1131.
44. Mann, S., *Mineralization in biological systems*, in *Inorganic Elements in Biochemistry*. 1983, Springer. p. 125-174.

45. Fortin, D., F. Ferris, T. Beveridge, *Surface-mediated mineral development by bacteria*. Reviews in mineralogy and geochemistry, 1997. **35**(1): p. 161-180.
46. Mann, S., *Biom mineralization: the form (id) able part of bioinorganic chemistry!**. Journal of the Chemical Society, Dalton Transactions, 1997(21): p. 3953-3962.
47. Wegst, U., M. Ashby, *The mechanical efficiency of natural materials*. Philosophical Magazine, 2004. **84**(21): p. 2167-2186.
48. Veron, J.E.N., M. Stafford-Smith, *Corals of the World*. 2000.
49. Blow, D.M., *Outline of crystallography for biologists*. 2002: Oxford University Press, USA.
50. De Graef, M., *Introduction to conventional transmission electron microscopy*. 2003: Cambridge Univ Pr.
51. Bragg, W., *The structure of aragonite*. Proceedings of the Royal Society of London. Series A, 1924. **105**(729): p. 16.
52. Caspi, E., B. Pokroy, P. Lee, *et al.*, *On the structure of aragonite*. Acta Crystallographica Section B: Structural Science, 2005. **61**(2): p. 129-132.
53. Bevan, D., E. Rossmann, D. Mylrea, *et al.*, *On the structure of aragonite-Lawrence Bragg revisited*. Acta Crystallographica Section B: Structural Science, 2002. **58**(3): p. 448-456.
54. Przenioslo, R., J. Stolarski, M. Mazur, *et al.*, *Hierarchically structured scleractinian coral biocrystals*. Journal of Structural Biology, 2008. **161**(1): p. 74-82.
55. Abramovitch-Gottlieb, L., D. Dahan, Y. Golan, *et al.*, *Effect of light regimes on the microstructure of the reef-building coral *Fungia simplex**. Materials Science & Engineering C-Biomimetic and Supramolecular Systems, 2005. **25**(1): p. 81-85.
56. Weiner, S., *Organization of organic matrix components in mineralized tissues*. American Zoologist, 1984. **24**(4): p. 945-951.
57. Weiner, S., *Aspartic acid-rich proteins: major components of the soluble organic matrix of mollusk shells*. Calcified Tissue International, 1979. **29**(1): p. 163-167.
58. Gilbert, P., M. Abrecht, B.H. Frazer, *The organic-mineral interface in biominerals*. Reviews in mineralogy and geochemistry, 2005. **59**(1): p. 157-185.
59. Sand, K., M. Yang, E. Makovicky, *et al.*, *Binding of ethanol on calcite: The role of the OH bond and its relevance to biomineralization*. Langmuir, 2010. **26**(19): p. 15239-15247.
60. Muscatine, I., P. Falkowski, J. Porter, *et al.*, *Fate of photosynthetic fixed carbon in light-and shade-adapted colonies of the symbiotic coral *Stylophora pistillata**. Proceedings of the Royal Society of London Series B-Biological Sciences, 1984. **B 222**: p. 181-202.

61. Davies, P.E.a.P., P Edmunds and P Davies. *An energy budget for porites porites (scler- actinia)*. Marine Biology, 1986. **92**(3): p. 339–347.
62. Lawton, N., *Biomineralisation, First Year Dissertation*. 2010, Department of Physics: York, U.K.
63. Allemand, D., E. Tambutte, D. Zoccola, et al., *Coral calcification, cells to reefs*. Coral reefs: an ecosystem in transition, 2011: p. 119-150.
64. Moya, A., L. Huisman, E. Ball, et al., *Whole Transcriptome Analysis of the Coral Acropora millepora Reveals Complex Responses to CO₂-driven Acidification during the Initiation of Calcification*. Molecular Ecology, 2012. **21**: p. 2440-2454.
65. Veron, J.E.N., *Corals of Australia and the Indo-Pacific*. 1986: University of Hawaii Press.
66. Tambutte, S., M. Holcomb, C. Ferrier-Pages, et al., *Coral biomineralization: From the gene to the environment*. Journal of Experimental Marine Biology and Ecology, 2011.
67. Enmar, R., M. Stein, M. Bar-Matthews, et al., *Diagenesis in live corals from the Gulf of Aqaba. I. The effect on paleo-oceanography tracers*. Geochimica et Cosmochimica Acta, 2000. **64**(18): p. 3123-3132.
68. Ogilvie, M., *Microscopic and systematic study of madreporarian types of corals*. Philosophical Transactions of the Royal Society of London. Series B, Containing Papers of a Biological Character, 1896. **187**: p. 83-345.
69. Martin, D.,A. Le Tissier, *The growth and formation of branch tips of Pocillopora damicornis (Linnaeus)*. Journal of Experimental Marine Biology and Ecology, 1988. **124**(2): p. 115-131.
70. Cohen, A.L., G.D. Layne, S.R. Hart, et al., *Kinetic control of skeletal Sr/Ca in a symbiotic coral: Implications for the paleotemperature proxy*. Paleoclimatology, 2001. **16**(1): p. 20-26.
71. Bryan, W.,D. Hill. *Spherulitic crystallization as a mechanism of skeletal growth in the hexacorals*. 1941.
72. Gladfelter, E.H., *Skeletal development in Acropora cervicornis: II. Diel patterns of calcium carbonate accretion*. Coral Reefs, 1983. **2**(2): p. 91-100.
73. Barnes, D.,D. Taylor, *In situ studies of calcification and photosynthetic carbon fixation in the coral Montastrea annularis*. Helgoland Marine Research, 1973. **24**(1): p. 284-291.
74. Cuif, J.,Y. Dauphin, *The two-step mode of growth in the scleractinian coral skeletons from the micrometre to the overall scale*. Journal of structural biology, 2005. **150**(3): p. 319-331.
75. Benzerara, K., N. Menguy, M. Obst, et al., *Study of the crystallographic architecture of corals at the nanoscale by scanning transmission X-ray microscopy and transmission electron microscopy*. Ultramicroscopy, 2011. **111**(8): p. 1268-1275.

76. Gautret, P.,J. Cuif..., *Organic components of the skeleton of scleractinian corals-evidence from in situ acridine orange staining*. Acta Palaeontologica Polonica, 2000.
77. Towe, K.M., *Invertebrate shell structure and the organic matrix concept*. Biomineralization, 1972. **4**: p. 1-14.
78. Johnston, I.S., *The ultrastructure of skeletogenesis in hermatypic corals*. International Review of cytology, 1980. **67**: p. 171-214.
79. Young, S., J. O'Connor,L. Muscatine, *Organic material from scleractinian coral skeletons--II. Incorporation of ¹⁴C into protein, chitin and lipid*. Comparative Biochemistry and Physiology Part B: Comparative Biochemistry, 1971. **40**(4): p. 945-958.
80. Allemand, D., E. Tambutte, J.P. Girard, *et al.*, *Organic matrix synthesis in the scleractinian coral Stylophora pistillata: role in biomineralization and potential target of the organotin tributyltin*. Journal of experimental biology, 1998. **201**(13): p. 2001.
81. Clode, P.,A. Marshall, *Low temperature FESEM of the calcifying interface of a scleractinian coral*. Tissue and Cell, 2002. **34**(3): p. 187-198.
82. Puverel, S., E. Tambutté, L. Pereira-Mouries, *et al.*, *Soluble organic matrix of two Scleractinian corals: partial and comparative analysis*. Comparative Biochemistry and Physiology Part B: Biochemistry and Molecular Biology, 2005. **141**(4): p. 480-487.
83. Fukuda, I., S. Ooki, T. Fujita, *et al.*, *Molecular cloning of a cDNA encoding a soluble protein in the coral exoskeleton*. Biochemical and Biophysical Research Communications, 2003. **304**(1): p. 11-17.
84. Teng, H.H., P.M. Dove, C.A. Orme, *et al.*, *Thermodynamics of calcite growth: baseline for understanding biomineral formation*. Science, 1998. **282**(5389): p. 724-727.
85. Watanabe, T., I. Fukuda, K. China, *et al.*, *Molecular analyses of protein components of the organic matrix in the exoskeleton of two scleractinian coral species*. Comparative Biochemistry and Physiology Part B: Biochemistry and Molecular Biology, 2003. **136**(4): p. 767-774.
86. Tambutté, S., E. Tambutté, D. Zoccola, *et al.*, *Characterization and role of carbonic anhydrase in the calcification process of the azooxanthellate coral Tubastrea aurea*. Marine Biology, 2007. **151**(1): p. 71-83.
87. Nakata, K., N. Shimomura, N. Shiina, *et al.*, *Kinetic study of catalytic CO₂ hydration by water-soluble model compound of carbonic anhydrase and anion inhibition effect on CO₂ hydration*. Journal of Inorganic Biochemistry, 2002. **89**(3): p. 255-266.
88. Ichikawa, K., *Buffering dissociation/formation reaction of biogenic calcium carbonate*. Chemistry-A European Journal, 2007. **13**(36): p. 10176-10181.

89. Cuif, J., Y. Dauphin, A. Denis, *et al.*, *The organo-mineral structure of coral skeletons: a potential source of new criteria for Scleractinian taxonomy*. Bulletin de l'Institut océanographique, 1996: p. 359-367.
90. Dauphin, Y., J. Cuif, P. Massard, *Persistent organic components in heated coral aragonitic skeletons-Implications for palaeoenvironmental reconstructions*. Chemical Geology, 2006. **231**(1-2): p. 26-37.
91. Dauphin, Y., J. Cuif, C. Williams, *Soluble organic matrices of aragonitic skeletons of Merulinidae (Cnidaria, Anthozoa)*. Comparative Biochemistry and Physiology Part B: Biochemistry and Molecular Biology, 2008. **150**(1): p. 10-22.
92. Colombo-Pallotta, M., A. Rodriguez-Roman, R. Iglesias-Prieto, *Calcification in bleached and unbleached Montastraea faveolata: evaluating the role of oxygen and glycerol*. Coral Reefs, 2010. **29**(4): p. 899-907.
93. Goldberg, W.M., *Acid polysaccharides in the skeletal matrix and calicoblastic epithelium of the stony coral *Mycetophyllia reesi**. Tissue and Cell, 2001. **33**(4): p. 376-387.
94. Yang, M., S.S. Stipp, J. Harding, *Biological control on calcite crystallization by polysaccharides*. Crystal Growth and Design, 2008. **8**(11): p. 4066-4074.
95. Cooke, D.J., R.J. Gray, K.K. Sand, *et al.*, *Interaction of ethanol and water with the {1014} surface of calcite*. Langmuir, 2010. **26**(18): p. 14520-14529.
96. Sand, K., J. Rodriguez-Blanco, E. Makovicky, *et al.*, *Crystallization of CaCO₃ in Water-Alcohol Mixtures: Spherulitic Growth, Polymorph Stabilization, and Morphology Change*. Crystal Growth & Design, 2011. **12**(2): p. 842-853.
97. Schüller, T., W. Tremel, *Versatile wet-chemical synthesis of non-agglomerated CaCO₃ vaterite nanoparticles*. Chemical Communications, 2011. **47**(18): p. 5208-5210.
98. Ghosal, S., M. Rogers, A. Wray, *The Effects of Turbulence on Phytoplankton*. 2002.
99. Young, J.R., K. Henriksen, *Biom mineralization within vesicles: The calcite of coccoliths*, in *Biom mineralization*, P.M.D.J.J.W.S. Dove, Editor. 2003. p. 189-215.
100. Thierstein, H.R., J.R. Young, *Coccolithophores: from molecular processes to global impact*. 2004: Springer Verlag.
101. Van Der Wal, P., E. De Jong, P. Westbroek, *et al.*, *Polysaccharide localization, coccolith formation, and golgi dynamics in the coccolithophorid Hymenomonas carterae*. Journal of ultrastructure research, 1983. **85**(2): p. 139-158.
102. Marsh, M.E., *Polyanion-mediated mineralization, assembly and reorganization of acidic polysaccharides in the Golgi system of a coccolithophorid alga during mineral deposition*. Protoplasma, 1994. **177**(3-4): p. 108-122.
103. Young, J.R., J.M. Didymus, P.R. Brown, *et al.*, *Crystal assembly and phylogenetic evolution in heterococcoliths*. Nature, 1992. **356**(6369): p. 516-518.

104. Young, J., *The description and analysis of coccolith structure*. Nannoplankton Research. Hamrsmid B, Young JR (eds) ZPZ, Knihovnicna, 1993: p. 35-71.
105. Young, J.R., S.A. Davis, P.R. Bown, *et al.*, *Coccolith ultrastructure and biomineralisation*. Journal of Structural Biology, 1999. **126**(3): p. 195-215.
106. Chen, Z., C. Majidi, D.J. Srolovitz, *et al.*, *Tunable helical ribbons*. Applied Physics Letters, 2011. **98**(1).
107. Wang, J.-S., X.-Q. Feng, G.-F. Wang, *et al.*, *Twisting of nanowires induced by anisotropic surface stresses*. Applied Physics Letters, 2008. **92**(19): p. 191901-191901-3.
108. Diao, J.K., K. Gall, M.L. Dunn, *Atomistic simulation of the structure and elastic properties of gold nanowires*. Journal of the Mechanics and Physics of Solids, 2004. **52**(9): p. 1935-1962.
109. Gall, K., J.K. Diao, M.L. Dunn, *The strength of gold nanowires*. Nano Letters, 2004. **4**(12): p. 2431-2436.
110. Qiao, L., X. Zheng, *Effect of surface stress on the stiffness of micro/nanocantilevers: Nanowire elastic modulus measured by nano-scale tensile and vibrational techniques*. Journal of Applied Physics, 2013. **113**(1): p. 013508-9.
111. Hirsch, P.B., A. Howie, R. Nicholson, *et al.*, *Electron microscopy of thin crystals*. Vol. 320. 1965: Butterworths London.
112. Horiuchi, S., T. Hanada, M. Ebisawa, *et al.*, *Contamination-free transmission electron microscopy for high-resolution carbon elemental mapping of polymers*. ACS nano, 2009. **3**(5): p. 1297-1304.
113. Mitchell, J., in *Unpublished PhD 1st year report*. 2009: University of York, York.
114. Kremer, J.R., D.N. Mastrorade, J.R. McIntosh, *Computer visualization of three-dimensional image data using IMOD*. Journal of structural biology, 1996. **116**(1): p. 71-76.
115. Stadelmann, P., *Electron Microscopy Software - Java Version (Jems)*, CIME-EPFL, Editor. 1999-2011: Switzerland: Lausanne.
116. Edington, J.W., *Practical electron microscopy in materials science*. 1976: Van Nostrand Reinhold Co.
117. Nehrke, G., H. Poigner, D. Wilhelms-Dick, *et al.*, *Coexistence of three calcium carbonate polymorphs in the shell of the Antarctic clam Laternula elliptica*. Geochemistry Geophysics Geosystems, 2012. **13**(null): p. Q05014.
118. Ferraro, J.R., *Introductory raman spectroscopy*. 2002: Academic press.
119. Long, D.A., *Quantum Mechanical Theory of Rayleigh and Raman Scattering*. 2002: Wiley Online Library.
120. White, S.N., *Laser Raman spectroscopy as a technique for identification of seafloor hydrothermal and cold seep minerals*. Chemical Geology, 2009. **259**(3): p. 240-252.

121. Kaufman, D.S., W.F. Manley, *A new procedure for determining DL amino acid ratios in fossils using reverse phase liquid chromatography*. Quaternary Science Reviews, 1998. **17**(11): p. 987-1000.
122. Penkman, K.E.H., *Amino acid geochronology: a closed system approach to test and refine the UK model*. 2005, University of Newcastle: Newcastle.
123. Hill, R.L., *Hydrolysis of proteins*. Advances in Protein Chemistry, 1965. **20**: p. 37.
124. Demarchi, B., *Geochronology of coastal prehistoric environments: a new closed system approach using amino acid racemisation*. , in *PhD Thesis*. 2009: University of York, York, UK.
125. Bourne, G.C., *Memoirs: Studies on the Structure and Formation of the Calcareous Skeleton of the Anthozoa*. Quarterly Journal of Microscopical Science, 1899. **2**(164): p. 499-547.
126. Bourne, G.C., *Memoirs: On the Anatomy of Mussa and Euphyllia, and the Morphology of the Madreporarian Skeleton*. Quarterly Journal of Microscopical Science, 1887. **2**(109): p. 21-51.
127. Cuif, J., Y. Dauphin, J. Doucet, et al., *XANES mapping of organic sulfate in three scleractinian coral skeletons*. Geochimica et cosmochimica acta, 2003. **67**: p. 75-83.
128. Cuif, J.P., G. Lecointre, C. Perrin, et al., *Patterns of septal biomineralization in Scleractinia compared with their 28S rRNA phylogeny: a dual approach for a new taxonomic framework*. Zoologica Scripta, 2003. **32**(5): p. 459-473.
129. Koch, v.G., *Über die entwicklung des kalkskeletes von Asterodes calycularis und dessen morphologische bedeutung*. Mitt. Zool. Stn., 1882. **3**: p. 284-292.
130. Barnes, D.J., *Coral skeletons: an explanation of their growth and structure*. Science, 1970. **170**(3964): p. 1305-1308.
131. Risk, M., T. Pearce, *Interference imaging of daily growth bands in massive corals*. Nature, 1992. **358**: p. 572-573.
132. Van de Locht, R., A. Verch, M. Saunders, et al., *Microstructural evolution and nanoscale crystallography in scleractinian coral spherulites*. Journal of structural biology, 2013.
133. Cöelfen, H., M. Antonietti, *Mesocrystals and nonclassical crystallization*. 2008: John Wiley & Sons.
134. Gladfelter, E.H., *Skeletal development in Acropora palmata (Lamarck 1816): a scanning electron microscope (SEM) comparison demonstrating similar mechanisms of skeletal extension in axial versus encrusting growth*. Coral Reefs, 2007. **26**(4): p. 883-892.
135. Urmos, J., S.M. Sharma, FT, *Characterization of some biogenic carbonates with Raman spectroscopy*. American Mineralogist, 1991. **76**: p. 641-646.

136. Wall, M.,G. Nehrke, *Reconstructing skeletal fiber arrangement and growth mode in the coral *Porites lutea* (Cnidaria, Scleractinia): a confocal Raman microscopy study*. Biogeosciences, 2012. **9**: p. 4885-4895.
137. Mudalige, A.,J.E. Pemberton, *Raman spectroscopy of glycerol/D₂O solutions*. Vibrational Spectroscopy, 2007. **45**(1): p. 27-35.
138. Zhang, F., W. Cai, J. Zhu, *et al.*, *In situ Raman spectral mapping study on the microscale fibers in blue coral (*Heliopora coerulea*) skeletons*. Analytical Chemistry, 2011. **83**(20): p. 7870-7875.
139. Perrin, C.,D.C. Smith, *Decay of skeletal organic matrices and early diagenesis in coral skeletons*. Comptes Rendus Palevol, 2007. **6**(4): p. 253-260.
140. Kaczorowska, B., A. Hacura, T. Kupka, *et al.*, *Spectroscopic characterization of natural corals*. Analytical and Bioanalytical Chemistry, 2003. **377**(6): p. 1032-1037.
141. Wainwright, S., *Skeletal organization in the coral, *Pocillopora damicornis**. Quarterly Journal of Microscopical Science, 1963. **3**(66): p. 169-183.
142. Bergmann, W.,D. Lester, *Coral-reefs and the formation of petroleum*. Science, 1940. **92**(2394): p. 452-453.
143. Constantz, B.,S. Weiner, *Acidic macromolecules associated with the mineral phase of scleractinian coral skeletons*. Journal of Experimental Zoology, 1988. **248**(3): p. 253-258.
144. Dauphin, Y., *Comparative studies of skeletal soluble matrices from some Scleractinian corals and Molluscs*. International Journal of Biological Macromolecules, 2001. **28**(4): p. 293-304.
145. Cuif, J., Y. Dauphin, A. Freiwald, *et al.*, *Biochemical markers of zooxanthellae symbiosis in soluble matrices of skeleton of 24 Scleractinia species*. Comparative Biochemistry and Physiology-Part A: Molecular & Integrative Physiology, 1999. **123**(3): p. 269-278.
146. Cuif, J., Y. Dauphin,P. Gautret, *Compositional diversity of soluble mineralizing matrices in some recent coral skeletons compared to fine-scale growth structures of fibres: discussion of consequences for biomineralization and diagenesis*. International Journal of Earth Sciences, 1999. **88**(3): p. 582-592.
147. Ingalls, A.E., C. Lee,E.R. Druffel, *Preservation of organic matter in mound-forming coral skeletons*. Geochimica et Cosmochimica Acta, 2003. **67**(15): p. 2827-2841.
148. Helman, Y., F. Natale, R.M. Sherrell, *et al.*, *Extracellular matrix production and calcium carbonate precipitation by coral cells in vitro*. Proceedings of the National Academy of Sciences, 2008. **105**(1): p. 54.
149. Falini, G., M. Reggi, S. Fermani, *et al.*, *Control of aragonite deposition in colonial corals by intra-skeletal macromolecules*. Journal of structural biology, 2013.

150. Goffredo, S., P. Vergni, M. Reggi, *et al.*, *The skeletal organic matrix from Mediterranean coral *Balanophyllia europaea* influences calcium carbonate precipitation*. PloS one, 2011. **6**(7): p. e22338.
151. Wheeler, A.P., C.S. Sikes, *Regulation of carbonate calcification by organic matrix*. American Zoologist, 1984. **24**(4): p. 933-944.
152. Addadi, L., S. Weiner, *Control and design principles in biological mineralization*. Angewandte Chemie International Edition in English, 1992. **31**(2): p. 153-169.
153. Ramos-Silva, P., J. Kaandorp, L. Huisman, *et al.*, *The skeletal proteome of the coral *Acropora millepora*: the evolution of calcification by cooption and domain shuffling*. Molecular Biology and Evolution, 2013.
154. Bentis, C.J., L. Kaufman, S. Golubic, *Endolithic fungi in reef-building corals (Order: Scleractinia) are common, cosmopolitan, and potentially pathogenic*. Biological Bulletin, 2000. **198**(2): p. 254-260.
155. Huang, S., K.C. Zhou, Z. Li, *Inhibition mechanism of aspartic acid on crystal growth of hydroxyapatite*. Transactions of Nonferrous Metals Society of China, 2007. **17**(3): p. 612-616.
156. Philips, F.C., ed. *An Introduction to Crystallography*. 1963, Longmans: London.
157. Barnes, D., *The structure and formation of growth-ridges in scleractinian coral skeletons*. Proceedings of the Royal Society of London. Series B, Biological Sciences, 1972. **182**(1068): p. 331-350.
158. Kuebel, C., K. Gries, R. Kröger, *et al.*, *Microstructure of aragonite platelets in nacre*. Microscopy and Microanalysis, 2009. **15**(S2): p. 900-901.
159. Duerden, J.E., *The coral *Siderastrea radians* and its postlarval development*. 1904: The Carnegie Institution.
160. Kawaguti, S., D. Sakumoto, *The effect of light on the calcium deposition of corals*. Bull. Oceanogr. Inst. Taiwan, 1948. **4**: p. 65-70.
161. Goreau, T.F., *The physiology of skeleton formation in corals. I. A method for measuring the rate of calcium deposition by corals under different conditions*. Biological Bulletin, 1959: p. 59-75.
162. Barnes, D., B. Chalker, *Calcification and photosynthesis in reef-building corals and algae*. Ecosystems of the World, 1990. **25**: p. 109-131.
163. Kulh, M., Y. Cohen, T. Dalsgaard, *et al.*, *Microenvironment and photosynthesis of zooxanthellae in scleractinian corals studied with microsensors for O₂, pH and light*. Marine Ecology Progress Series, 1995. **117**: p. 159-172.1995.
164. Holcomb, M., A.L. Cohen, R.I. Gabitov, *et al.*, *Compositional and morphological features of aragonite precipitated experimentally from seawater and biogenically by corals*. Geochimica et Cosmochimica Acta, 2009. **73**(14): p. 4166-4179.

165. van de Locht, R., T.J. Slater, A. Verch, *et al.*, *Ultrastructure and Crystallography of Nanoscale Calcite Building Blocks in Rhabdosphaera clavigera Cocolith Spines*. *Crystal growth & design*, 2014. **14**(4): p. 1710-1718.
166. Verch, A., A.S. Côté, R. Darkins, *et al.*, *Correlation between Anisotropy and Lattice Distortions in Single Crystal Calcite Nanowires Grown in Confinement*. *Small* (In press), 2014.
167. Kleijne, A., *Extant Rhabdosphaeraceae (coccolithophorids, class Prymnesiophyceae) from the Indian Ocean, Red Sea, Mediterranean Sea and North Atlantic Ocean*. 1992: Nationaal Natuurhistorisch Museum.
168. Aubry, M.P., ed. *Handbook of Cenozoic Calcerous Nannoplankton, Book 5, Heliolithae (Zygoliths and Rhabdoliths)*. 1999, Micropaleontology Press: New York. 1-368.
169. Beniash, E., J. Aizenberg, L. Addadi, *et al.*, *Amorphous calcium carbonate transforms into calcite during sea urchin larval spicule growth*. *Proceedings of the Royal Society of London. Series B: Biological Sciences*, 1997. **264**(1380): p. 461.
170. Cartwright, J.H., A.G. Checa, J.D. Gale, *et al.*, *Calcium Carbonate Polyamorphism and Its Role in Biomineralization: How Many Amorphous Calcium Carbonates Are There?* *Angewandte Chemie International Edition*, 2012. **51**(48): p. 11960-11970.
171. Van der Wal, P., E. De Jong, P. Westbroek, *et al.*, *Ultrastructural polysaccharide localization in calcifying and naked cells of the coccolithophorid Emiliana huxleyi*. *Protoplasma*, 1983. **118**(2): p. 157-168.
172. Henriksen, K., S. Stipp, J. Young, *et al.*, *Biological control on calcite crystallization: AFM investigation of coccolith polysaccharide function*. *American Mineralogist*, 2004. **89**(11-12): p. 1709-1716.
173. Godoi, R.H.M., K. Aerts, J.r.m. Harlay, *et al.*, *Organic surface coating on Coccolithophores Emiliana huxleyi: Its determination and implication in the marine carbon cycle*. *Microchemical Journal*, 2009. **91**(2): p. 266-271.
174. Halldal, P., J. Markali, *Electron microscope studies on coccolithophores from the Norwegian Sea, the Gulf Stream and the Mediterranean*. *Avh Norske VidenskAkad Oslo*, 1955. **1**: p. 1-30.
175. Young, J.R., K. Henriksen, I. Probert, *Structure and morphogenesis of the coccoliths of the Codonet species*, in *Coccolithophores*. 2004, Springer. p. 191-216.
176. Marsh, M., *Coccolith crystals of Pleurochrysis carterae: Crystallographic faces, organization, and development*. *Protoplasma*, 1999. **207**(1-2): p. 54-66.
177. Probert, I., J. Fresnel, C. Billard, *et al.*, *Light and electron microscope observations of Algirosphaera robusta (Prymnesiophyceae)*. *Journal of Phycology*, 2007. **43**(2): p. 319-332.

178. Addadi, L., D. Joester, F. Nudelman, *et al.*, *Mollusk shell formation: a source of new concepts for understanding biomineralization processes*. *Chemistry–A European Journal*, 2006. **12**(4): p. 980-987.
179. Liu, J., J. Duan, M. Toimil-Molares, *et al.*, *Electrochemical fabrication of single-crystalline and polycrystalline Au nanowires: the influence of deposition parameters*. *Nanotechnology*, 2006. **17**(8): p. 1922.
180. Dresselhaus, M.S., Y.-M. Lin, O. Rabin, *et al.*, *Nanowires*, in *Springer Handbook of Nanotechnology*. 2010, Springer. p. 119-167.
181. Meyer, H., *Struktur und Fehlordnung des Vaterits**. *Zeitschrift für Kristallographie*, 1969. **128**(3-6): p. 183-212.
182. Stephens, C.J., S.F. Ladden, F.C. Meldrum, *et al.*, *Amorphous calcium carbonate is stabilized in confinement*. *Advanced Functional Materials*, 2010. **20**(13): p. 2108-2115.
183. Chen, Z., C. Majidi, D. Srolovitz, *et al.*, *Tunable helical ribbons*. *Applied Physics Letters*, 2011. **98**(1): p. 011906-011906-3.
184. Diao, J., K. Gall, M. L. Dunn, *Atomistic simulation of the structure and elastic properties of gold nanowires*. *Journal of the Mechanics and Physics of Solids*, 2004. **52**(9): p. 1935-1962.
185. Gall, K., J. Diao, M.L. Dunn, *The strength of gold nanowires*. *Nano Letters*, 2004. **4**(12): p. 2431-2436.
186. De Groot, K.E. Duyvis, *Crystal form of precipitated calcium carbonate as influenced by adsorbed magnesium ions*. 1966.
187. Folk, R.L., *The natural history of crystalline calcium carbonate; effect of magnesium content and salinity*. *Journal of Sedimentary Research*, 1974. **44**(1): p. 40-53.
188. Lahann, R.W., *A chemical model for calcite crystal growth and morphology control*. *Journal of Sedimentary Research*, 1978. **48**(1): p. 337-347.
189. Davis, K.J., P.M. Dove, J.J. De Yoreo, *The role of Mg²⁺ as an impurity in calcite growth*. *Science*, 2000. **290**(5494): p. 1134-1137.
190. Imai, H., *Self-organized formation of hierarchical structures*, in *Biomineralization I*. 2007, Springer. p. 43-72.
191. Oaki, Y., H. Imai, *Experimental demonstration for the morphological evolution of crystals grown in gel media*. *Crystal growth & design*, 2003. **3**(5): p. 711-716.
192. Ostwald, W., *Lehrbuch der Allgemeinen Chemie; Leipzig, Germany, 1896; Vol. 2, Part 1*. There is no corresponding record for this reference.
193. Pasarín, I., M. Yang, N. Bovet, *et al.*, *Molecular ordering of ethanol at the calcite surface*. *Langmuir*, 2012. **28**(5): p. 2545-2550.
194. Chen, S.-F., S.-H. Yu, J. Jiang, *et al.*, *Polymorph discrimination of CaCO₃ mineral in an ethanol/water solution: Formation of complex vaterite superstructures and aragonite rods*. *Chemistry of Materials*, 2006. **18**(1): p. 115-122.

195. de Leeuw, N.H., S.C. Parker, *Surface structure and morphology of calcium carbonate polymorphs calcite, aragonite, and vaterite: An atomistic approach*. The Journal of Physical Chemistry B, 1998. **102**(16): p. 2914-2922.
196. Nassif, N., N. Pinna, N. Gehrke, *et al.*, *Amorphous layer around aragonite platelets in nacre*. Proceedings of the National Academy of Sciences of the United States of America, 2005. **102**(36): p. 12653-12655.
197. Verch, A., I.E. Morrison, R. van de Locht, *et al.*, *In situ electron microscopy studies of calcium carbonate precipitation from aqueous solution with and without organic additives*. Journal of structural biology, 2013.
198. Fenter, P., N.C. Sturchio, *Calcite (104)-Water Interface Structure, Revisited*. Geochimica et Cosmochimica Acta, 2012.
199. Saxby, T., W.C. Dennison, O. Hoegh-Guldberg, *Photosynthetic responses of the coral Montipora digitata to cold temperature stress*. Marine Ecology Progress Series, 2003. **248**: p. 85-97.
200. Rogers, C.S., *Responses of coral reefs and reef organisms to sedimentation*. Marine ecology progress series. Oldendorf, 1990. **62**(1): p. 185-202.
201. Zhou, H.-X., G. Rivas, A.P. Minton, *Macromolecular crowding and confinement: biochemical, biophysical, and potential physiological consequences*. Annual review of biophysics, 2008. **37**: p. 375.
202. Giddings, J.C., E. Kucera, C.P. Russell, *et al.*, *Statistical theory for the equilibrium distribution of rigid molecules in inert porous networks. Exclusion chromatography*. The Journal of Physical Chemistry, 1968. **72**(13): p. 4397-4408.
203. Minton, A.P., *Confinement as a determinant of macromolecular structure and reactivity*. Biophysical Journal, 1992. **63**(4): p. 1090-1100.
204. Henriksen, K., S. Stipp, J. Young, *et al.*, *Tailoring calcite: Nanoscale AFM of coccolith biocrystals*. American Mineralogist, 2003. **88**(11-12): p. 2040-2044.
205. Outka, D., D. Williams, *Sequential coccolith morphogenesis in Hymenomonas carterae*. Journal of Eukaryotic Microbiology, 1971. **18**(2): p. 285-297.
206. Klaveness, D., *Emiliana huxleyi (Lohmann) Hay & Mohler. III. Mineral deposition and the origin of the matrix during coccolith formation*. Protistologica, 1976. **12**: p. 217-224.
207. Henriksen, K., J. Young, P. Bown, *et al.*, *Coccolith biomineralisation studied with atomic force microscopy*. Palaeontology, 2004. **47**(3): p. 725-743.
208. Tong, H., W. Ma, L. Wang, *et al.*, *Control over the crystal phase, shape, size and aggregation of calcium carbonate via a l-aspartic acid inducing process*. Biomaterials, 2004. **25**(17): p. 3923-3929.
209. Cuif, J.-P., Y. Dauphin, J.E. Sorauf, *Biominerals and fossils through time*. 2011: Cambridge University Press.

210. Hofmeister, H., *Fivefold twinned nanoparticles*. Encyclopedia of nanoscience and nanotechnology, 2004. **3**: p. 431.
211. Oaki, Y.,H. Imai, *Amplification of chirality from molecules into morphology of crystals through molecular recognition*. Journal of the American Chemical Society, 2004. **126**(30): p. 9271-9275.